Università degli Studi di Napoli 'Federico II'

FACOLTÀ DI SCIENZE MATEMATICHE FISICHE E NATURALI
Corso di Laurea in Fisica

Tesi di Laurea in Fisica

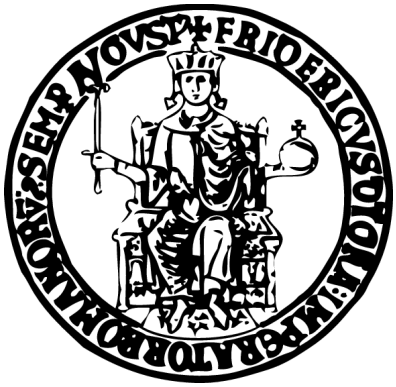

Study of $\mathbf{Z \to \mu^+\mu^-}$ decays and measurement of the inclusive cross section $\mathbf{p + p \to Z + X \to \mu^+\mu^- + X}$ with the CMS experiment at CERN

Candidato:
Salvatore Di Guida
Matricola 60/779

Relatori:
Ch.mo prof. Crisostomo Sciacca

dott. Luca Lista

dott. Davide Piccolo

Anno Accademico 2007–2008

Il grande Galileo ha detto che Dio ha scritto il libro della natura nella forma del linguaggio matematico. Lui era convinto che Dio ci ha donato due libri: quello della Sacra Scrittura e quello della natura. E il linguaggio della natura — questa era la sua convinzione — è la matematica, quindi essa è un linguaggio di Dio, del Creatore. Riflettiamo ora su cos'è la matematica: di per sé è un sistema astratto, un'invenzione dello spirito umano, che come tale nella sua purezza non esiste. È sempre realizzato approssimativamente, ma — come tale — è un sistema intellettuale, è una grande, geniale invenzione dello spirito umano. La cosa sorprendente è che questa invenzione della nostra mente umana è veramente la chiave per comprendere la natura, che la natura è realmente strutturata in modo matematico e che la nostra matematica, inventata dal nostro spirito, è realmente lo strumento per poter lavorare con la natura, per metterla al nostro servizio, per strumentalizzarla attraverso la tecnica.

Mi sembra una cosa quasi incredibile che una invenzione dell'intelletto umano e la struttura dell'universo coincidano: la matematica inventata da noi ci dà realmente accesso alla natura dell'universo e lo rende utilizzabile per noi. Quindi la struttura intellettuale del soggetto umano e la struttura oggettiva della realtà coincidono: la ragione soggettiva e la ragione oggettivata nella natura sono identiche. Penso che questa coincidenza tra quanto noi abbiamo pensato e il come si realizza e si comporta la natura, siano un enigma ed una sfida grandi, perché vediamo che, alla fine, è "una" ragione che le collega ambedue: la nostra ragione non potrebbe scoprire quest'altra, se non vi fosse un'identica ragione a monte di ambedue.

In questo senso mi sembra proprio che la matematica — nella quale come tale Dio non può apparire — ci mostri la struttura intelligente dell'universo. [...] E così vediamo che c'è una razionalità soggettiva e una razionalità oggettivata nella materia, che coincidono. Naturalmente adesso nessuno può provare — come si prova nell'esperimento, nelle leggi tecniche — che ambedue siano realmente originate in un'unica intelligenza, ma mi sembra che questa unità dell'intelligenza, dietro le due intelligenze, appaia realmente nel nostro mondo. E quanto più noi possiamo strumentalizzare il mondo con la nostra intelligenza, tanto più appare il disegno della Creazione.

Alla fine, per arrivare alla questione definitiva, direi: Dio o c'è o non c'è. Ci sono solo due opzioni. O si riconosce la priorità della ragione, della Ragione creatrice che sta all'inizio di tutto ed è il principio di tutto — la priorità della ragione è anche priorità della libertà — o si sostiene la priorità dell'irrazionale, per cui tutto quanto funziona sulla nostra terra e nella nostra vita sarebbe solo occasionale, marginale, un prodotto irrazionale — la ragione sarebbe un prodotto della irrazionalità. Non si può ultimamente "provare" l'uno o l'altro progetto, ma la grande opzione del Cristianesimo è l'opzione per la razionalità e per la priorità della ragione. Questa mi sembra un'ottima opzione, che ci dimostra come dietro a tutto ci sia una grande Intelligenza, alla quale possiamo affidarci.

Ma il vero problema contro la fede oggi mi sembra essere il male nel mondo: ci si chiede come esso sia compatibile con questa razionalità del Creatore. E qui abbiamo bisogno realmente del Dio che si è fatto carne e che ci mostra come Egli non sia solo una ragione matematica, ma che questa ragione originaria è anche Amore. Se guardiamo alle grandi opzioni, l'opzione cristiana è anche oggi quella più razionale e quella più umana. Per questo possiamo elaborare con fiducia una filosofia, una visione del mondo che sia basata su questa priorità della ragione, su questa fiducia che la Ragione creatrice è amore, e che questo amore è Dio.

BENEDETTO XVI, *Incontro con i giovani della Diocesi di Roma*, 6 aprile 2006.

CONTENTS

LIST OF FIGURES

LIST OF TABLES

INTRODUCTION

THE Standard Model (SM) of the electroweak interactions, as a fundamental theory of elementary particles and their interactions, has proven to be very succesful: many experimental observations have confirmed its validity. However, one open issue is the origin of the masses of elementary particles. The spontaneous symmetry breaking mechanism, which explains the particles' masses in the SM, requires indeed the existence of a scalar particle, the Higgs boson, which has not yet been found experimentally. Direct searches for the Higgs boson through its decay channels, made at the LEP and Tevatron accelerators, gave no evidence of its existence, setting an exclusion limit to the Higgs boson mass $m_{\mathrm{H}} > 114.4\ \mathrm{GeV/c^2}$. Besides, theoretical arguments based upon self-consistence of the Standard Model fix an upper limit on the Higgs boson mass at $m_{\mathrm{H}} \lesssim 1\ \mathrm{TeV/c^2}$.

The search for the Higgs boson and the possibility of investigating the existence of new physics beyond the Standard Model are among the main reasons which led to the project of the Large Hadron Collider, a proton-proton collider built at CERN, Geneva. This collider, in which the first collisions are foreseen in the next few months, has a design total center-of-mass energy of 14 TeV and a luminosity $\mathscr{L} = 10^{34}\ \mathrm{cm^{-2}\ s^{-1}}$. The Compact Muon Solenoid (CMS) detector is one of the four detectors which will operate at LHC and it is designed not only to search for the Higgs particle, but also to detect other possible sources of new physics, e.g. verifying the Minimal Supersymmetric Standard Model (MSSM) through the search for possible supersymmetric particles, and to study the physics of the heavy quarks t and b in detail.

This thesis presents a study on the inclusive production channel of the Z boson, subsequently decaying into two muons, to determine the inclusive cross section for the process $\mathrm{p} + \mathrm{p} \rightarrow \mathrm{Z} + X \rightarrow \mu^+\,\mu^- + X$ within the CMS

experiment. The inclusive process $\mathrm{p} + \mathrm{p} \rightarrow \mathrm{Z} + X \rightarrow \ell^+ \ell^- + X$ has relatively large cross section, $\simeq 1$ nb, and evident signature; among them, the decay $\mathrm{Z} \rightarrow \mu^+ \mu^-$ has, in addition to a large cross section, the clearest experimental signature, as such events are characterized by two isolated, high-p_t muons with an invariant mass consistent with the Z boson mass. The Z production with subsequent decay into two muons — or, more generally, into leptons — will be studied starting from the LHC startup: it indeed allows not only to calibrate the detector and to check the collider luminosity, but also to discover the new physics beyond the SM through the detection of events with two high energy final state muons. In particular, this channel will be very useful for the detection of Higgs boson: if H has mass $M_H > 182$ GeV/c^2, its decay channel $\mathrm{H} \rightarrow \mathrm{Z}\,\mathrm{Z} \rightarrow 4\mu$ will be the "golden" channel for its discovery. The four muons in the final state make it particularly promising despite the very small cross section, $\sim$ fb. The fully muonic decay of the Higgs boson has indeed the cleanest experimental signature and will allow a very good estimate of the Higgs boson mass.

For this thesis work, the kinematical characteristics of the muons, in which the Z decays, have been analyzed in detail both at Monte Carlo (MC) generator level, and at the end of the simulation of the full reconstruction chain. From this analysis, several fit models for signal events have been studied in order to determine the inclusive Z cross section: to do this, a toolkit that allows to easily define in `C++` function models to be used in fit problems, has been developed within the CMS framework. Several fit models have been tested on a high statistics signal event $\mathrm{Z} \rightarrow \mu^+ \mu^-$ sample, both obtained from MC generator, and reconstructed from data, taking into account the experimental resolution effects. Next, algorithms allowing the identification of signal events and the rejection of backgrounds from other channels with two final state muons have been implemented: from them, an estimate of the number of signal events, and, at the same time, a direct measure of the reconstruction efficiency for the muon candidates from Z can be obtained. Counting the number of selected events and of the estimated background, the reconstruction efficiency and the cross section for the process can be simultaneously extracted, once known the integrated luminosity of the collider. This technique for both analysis and reconstruction is applied directly on the reconstructed data, so, just after the LHC startup, only few pb^{-1} of integrated luminosity will be enough to cross-check MC predictions and to measure the Z inclusive cross section.

In Chapter 1 the basic concepts of this model are introduced starting from the description of the gauge symmetry $SU(2)_{\mathrm{L}} \otimes U(1)_{\mathrm{Y}}$ and how spontaneous breaking of the symmetry yields the massive bosons $\mathrm{W}^{\pm}$ and Z and a yet undiscovered particle, the Higgs boson; their properties are finally reviewed.

In the first part of chapter 2 an overview of the LHC accelerator and of the requirements for the LHC experiments is given. The second part of the chapter is devoted to the description of the CMS detector.

In Chapter 3 the production mechanisms, the decay channels of the Higgs boson at LHC and the search strategies for different mass regions are reported. Some aspects of physics beyond the Standard Model are briefly reviewed. The final part of the chapter is devoted to the Standard Model Z physics.

In Chapter 4 the analysis strategy is described and tested over different samples of signal and background events in order to determine the reconstruction efficiencies and the Z inclusive cross section. A comparison with the values obtained from Monte Carlo models is also performed, in order to check the robustness of the analysis.

CHAPTER 1

THE STANDARD MODEL OF ELECTROWEAK INTERACTIONS

AFTER the discovery that the atomic nuclei are constituted by protons and neutrons, the composition of the matter could be understood in terms of a small number of (so-called) "elementary" particles: the proton, the neutron, the electron, the neutrino and the photon. However, there were precise clues that this picture was not complete. The cosmic rays revealed the existence of new small-lived particles, called baryons (heavier) and mesons (lighter), that could not be included in that scheme (Lattes et al., 1947; Occhialini and Powell, 1947; Rochester and Butler, 1947). Besides, the nuclear interaction between protons and neutrons — the nuclear force — did not appear as simple and fundamental as the electromagnetic one, but, rather, as an expression of more fundamental forces acting inside the nucleon, i.e. between its components, and connected with its internal structure. Finally, particle accelerators showed explicitly that the nucleon was not an elementary particle, and indications about its internal structure were given by the elastic scattering of electrons over nucleons. These measures pointed out that nucleons have a charge radius ~ 0.8 fm (Hofstadter et al., 1953), very similar to what was obtained by the study of the pion-nucleon collisions and by detailed models of the adronic spectra. As it is not an elementary particle, the nucleon, then, must have an internal structure.

The development of particle accelerators allowed to discover new particles: they are created and trasformed into one another in a great variety of interactions and decay processes. The picture obtained is quite simple. There are four kinds of fundamental interactions:

- gravity,

- strong interactions,
- electromagnetic interactions,
- weak interactions.

Particles can be divided up into three families:

Leptons They are spin-1/2 fermions and are grouped into three generations, each one formed by a pair of particles, the former with charge $-e$ — the electron e, the muon μ, the tau τ, the latter neutral — the electron neutrino ν_{e}, the muon neutrino ν_{μ}, the tau neutrino ν_{τ}.

Table 1.1: Lepton generations

e	μ	τ
ν_{e}	ν_{μ}	ν_{τ}

Quarks They are spin-1/2 fermions. There are six different types of quarks, each characterized by a different flavour. They have fractional electric charge in units of e: up u, charm c, top t quarks with charge $+2/3$, down d, strange s, bottom b quarks with charge $-1/3$. They have never been observed as free particles, so are permanently confined into hadrons.

Table 1.2: Quark flavours

u	c	t
d	s	b

Field quanta The fundamental interactions are mediated by fields. The quantum of the electomagnetic interactions is the photon: it is not massive. The eight quanta of the strong field binding quarks to form hadrons are called gluons: they have zero mass. The three quanta of the weak field are called W^{+}, W^{-} and Z: they are massive. All these field quanta are spin-1 bosons.

The constituents of matter, quarks and leptons, then, interact by interchange of bosonic field quanta.

1.1 The $SU(2)_{\mathbf{L}} \otimes U(1)_{\mathbf{Y}}$ gauge group of the electroweak interactions

The best known description of elementary particles and their fundamental interactions (excluding gravitational effects) is provided by a quantum field theory known as the Standard Model (SM) (Aitchison and Hey, 2002; Ryder, 1996). The description of the SM interactions is implemented by a gauge theory based on $SU(3)_{\mathrm{c}} \otimes SU(2)_{\mathrm{L}} \otimes U(1)_{\mathrm{Y}}$ symmetry. Gauge symmetry provides bosons, which serve as interaction mediators. Local gauge invariance makes the theory renormalizible and requires the gauge bosons to be massless. At the same time we know that Z and $\mathrm{W}^{\pm}$ bosons have masses. The solution of the problem in the SM is the Higgs mechanism (Higgs, 1964a,b, 1966), which spontaneously breaks the gauge symmetry by adding to the Lagrangian a scalar potential that generates the vector boson and fermion masses in a gauge invariant way. Spontaneous breaking of gauge symmetries was the crucial new ingredient in the model of unified weak and electromagnetic interactions constructed independently by Glashow (1961), Weinberg (1967) and Salam (1968).

The Dirac Lagrangian (1.1):

$$\hat{\mathscr{L}} = \hat{\bar{\psi}}(\mathrm{i}\partial\!\!\!/ - m)\hat{\psi} \tag{1.1}$$

becomes simply:

$$\hat{\mathscr{L}} = \hat{\bar{\psi}}\mathrm{i}\partial\!\!\!/\hat{\psi}$$

when $m = 0$. Introducing the chirality projection operators:

$$P_{\mathrm{L}} = \left(\frac{1-\gamma^5}{2}\right) \qquad P_{\mathrm{R}} = \left(\frac{1+\gamma^5}{2}\right)$$

so that the chirality eigenstate components of the Dirac field are:

$$\hat{\psi}_{\mathrm{L}} = \left(\frac{1-\gamma^5}{2}\right)\hat{\psi} \qquad \hat{\psi}_{\mathrm{R}} = \left(\frac{1+\gamma^5}{2}\right)\hat{\psi} \qquad .$$

It follows that:

$$\hat{\bar{\psi}}\mathrm{i}\partial\!\!\!/\hat{\psi} = \hat{\bar{\psi}}_{\mathrm{R}}\mathrm{i}\partial\!\!\!/\hat{\psi}_{\mathrm{R}} + \hat{\bar{\psi}}_{\mathrm{L}}\mathrm{i}\partial\!\!\!/\hat{\psi}_{\mathrm{L}},$$

since γ^5 anticommutes with γ^μ. The electron, muon and tau have L and R components, but, in the 2-component neutrino theory (Halzen and Martin,

1984), $\nu_{\rm e}$, ν_μ and ν_τ have L components only[1]. The lepton Lagrangian is then:

$$\begin{aligned}\hat{\mathscr{L}}_{\rm lep} = {} & \hat{\bar{e}}_{\rm R}{\rm i}\partial\!\!\!/\hat{e}_{\rm R} + \hat{\bar{e}}_{\rm L}{\rm i}\partial\!\!\!/\hat{e}_{\rm L} + \hat{\bar{\nu}}_e{\rm i}\partial\!\!\!/\hat{\nu}_e + \\ & + \hat{\bar{\mu}}_{\rm R}{\rm i}\partial\!\!\!/\hat{\mu}_{\rm R} + \hat{\bar{\mu}}_{\rm L}{\rm i}\partial\!\!\!/\hat{\mu}_{\rm L} + \hat{\bar{\nu}}_\mu{\rm i}\partial\!\!\!/\hat{\nu}_\mu + \\ & + \hat{\bar{\tau}}_{\rm R}{\rm i}\partial\!\!\!/\hat{\tau}_{\rm R} + \hat{\bar{\tau}}_{\rm L}{\rm i}\partial\!\!\!/\hat{\tau}_{\rm L} + \hat{\bar{\nu}}_\tau{\rm i}\partial\!\!\!/\hat{\nu}_\tau .\end{aligned} \tag{1.2}$$

Now we consider the internal symmetries in (1.2). We therefore write the 'isospinors':

$$\hat{L}_{\rm e} = \begin{pmatrix}\hat{\nu}_{\rm e}\\ \hat{e}_{\rm L}\end{pmatrix} \qquad \hat{L}_\mu = \begin{pmatrix}\hat{\nu}_\mu\\ \hat{\mu}_{\rm L}\end{pmatrix} \qquad \hat{L}_\tau = \begin{pmatrix}\hat{\nu}_\tau\\ \hat{\tau}_{\rm L}\end{pmatrix} \tag{1.3}$$

and assign to this doublet a non-Abelian charge — the weak isospin — $T_{\rm W} = \frac{1}{2}$. ν_ℓ has a third component $T^3_{\rm W} = \frac{1}{2}$, and $\ell_{\rm L}$ has $T^3_{\rm W} = -\frac{1}{2}$, where $\ell = {\rm e}$, μ, τ. The remaining particles

$$\hat{R}_{\rm e} = \hat{e}_{\rm R} \qquad R_\mu = \hat{\mu}_{\rm R} \qquad R_\tau = \hat{\tau}_{\rm R} \tag{1.4}$$

are isosinglets: $T_{\rm W} = 0$. In summary:

$$T_{\rm W} = \frac{1}{2} \qquad \begin{cases} T^3_{\rm W} = +1/2 \\ T^3_{\rm W} = -1/2 \end{cases} \qquad \begin{pmatrix}\hat{\nu}_{\rm e}\\ \hat{e}_{\rm L}\end{pmatrix} \qquad \begin{pmatrix}\hat{\nu}_\mu\\ \hat{\mu}_{\rm L}\end{pmatrix} \qquad \begin{pmatrix}\hat{\nu}_\tau\\ \hat{\tau}_{\rm L}\end{pmatrix}. \tag{1.5}$$

We have then:

$$\hat{\mathscr{L}}_{\rm lep} = \sum_{\ell={\rm e},\mu,\tau} \left(\hat{\bar{R}}_\ell {\rm i}\partial\!\!\!/ \hat{R}_\ell + \hat{\bar{L}}_\ell i\partial\!\!\!/ \hat{L}_\ell \right) \tag{1.6}$$

and $\hat{\mathscr{L}}_{\rm lep}$ is invariant under

$$\left.\begin{aligned} \hat{L}_\ell &\to e^{-{\rm i}\frac{\boldsymbol{\tau}}{2}\cdot\boldsymbol{\alpha}}\hat{L}_\ell \\ \hat{R}_\ell &\to \hat{R}_\ell \end{aligned}\right\} \tag{1.7}$$

which are rotations in weak isospin space. They generate the group $SU(2)$. The relation between electric charge Q and $T^3_{\rm W}$ is

$$\hat{L}_\ell : \; Q = T^3_{\rm W} - \frac{1}{2} \qquad \hat{R}_\ell : \; Q = T^3_{\rm W} - 1. \tag{1.8}$$

There is, at present, no evidence for any weak interactions coupling to right-handed field components and it is therefore natural — and a basic assumption

[1] In the original SM, the neutrinos were taken to be massless, with no neutrino mixing. It is an excellent approximation to treat the neutrinos as massless, except when discussing experimental situations sensitive to neutrino oscillations.

of the electroweak theory — that all 'R' components are singlets under the weak isospin group. Crucially, however, the 'R' components interact via the $U(1)$ field $\hat{B}^\mu$: this allows electromagnetism to emerge free of parity-violating γ^5 terms.

When we come to gauge this symmetry (i.e. make $\boldsymbol{\alpha}$ a function of the space-time coordinates) we will acquire three massless gauge fields. The photon, however, will not be one of them. The right-handed leptonic components ℓ_{R}, i.e. e_{R}, μ_{R} and τ_{R}, are weak-isospin singlets, so they will not interact with our gauge fields; yet we know that, as leptons are electrically charged particles, they do interact with the photon. However,$SU(2)_{\mathrm{L}}$ is not the maximal symmetry of $\hat{\mathscr{L}}_{\mathrm{lep}}$. We could also have a simple $U(1)$ transformation on $\hat{R}_\ell$

$$U(1):\ \hat{R}_\ell \to e^{-\mathrm{i}\beta}\hat{R}_\ell. \tag{1.9}$$

This transformation can affect $\hat{L}_\ell$ only by an *overall* phase; in other words, ν_ℓ and ℓ_{L} must pick up the same phase (as each other), since otherwise it would be a special case of an $SU(2)$ transformation. This phase, however, is not necessarily the same as that of $\hat{R}_\ell$. We write, therefore,

$$U(1):\ \hat{L}_\ell \to e^{-\mathrm{i}n\beta}\hat{L}_\ell, \tag{1.10}$$

where n is a number, which we must now find. This $U(1)$ symmetry leads to a conserved charge, of which ℓ_{R} possesses one value, and ν_ℓ and ℓ_{L} another value. It is clearly not the electric charge Q (in units of e), since ν_ℓ and ℓ_{L} have different values of Q. In other words, the gauge field we get on gauging $U(1)$ is also not the photon field. Weinberg suggested that this charge is 'weak hypercharge' Y_{W} defined by a Gell-Mann-Nishijima relation:

$$Q = T^3_{\mathrm{W}} + \frac{Y_{\mathrm{W}}}{2}. \tag{1.11}$$

Comparing with (1.8), it's clear that:

$$\hat{L}_\ell \text{ has } Y_{\mathrm{W}} = -1 \tag{1.12a}$$

$$\hat{R}_\ell \text{ has } Y_{\mathrm{W}} = -2 \tag{1.12b}$$

so, in (1.10), $n = \frac{1}{2}$; the left-handed fields couple, with half the strength of the right-handed field, to the hypercharge gauge field. The $U(1)$ transformation is then:

$$U(1):\quad \begin{cases} \hat{L}_\ell \to e^{-\mathrm{i}\frac{\beta}{2}}\hat{L}_\ell \\ \hat{R}_\ell \to e^{-\mathrm{i}\beta}\hat{R}_\ell \end{cases} \tag{1.13}$$

for $\ell = \mathrm{e}, \mu, \tau$. The Lagrangian (1.6) is then invariant under $SU(2)\otimes U(1)$.

We now gauge the theory. Gauging $SU(2)$ means that we introduce three gauge potentials W^i_μ so that, acting on the isospinors $\hat{L}_\ell$, the ordinary derivative is replaced by the covariant derivative:

$$\hat{D}_\mu \hat{L}_\ell = \left(\partial_\mu + \mathrm{i}g\frac{\boldsymbol{\tau}}{2}\cdot\boldsymbol{W}_\mu\right)\hat{L}_\ell, \tag{1.14}$$

where g is the $SU(2)$ coupling constant.
Gauging $U(1)$ introduces another potential B^μ and coupling constant g',

$$\hat{D}_\mu = \partial_\mu + \mathrm{i}\frac{g'}{2}Y_\mathrm{W}\hat{B}_\mu \tag{1.15}$$

and, from (1.13), since $\hat{L}_\ell$ has half the hypercharge of $\hat{R}_\ell$, the covariant derivatives are:

$$\left.\begin{aligned}\hat{D}_\mu\hat{L}_\ell &= \left(\partial_\mu - \mathrm{i}\frac{g'}{2}\hat{B}_\mu\right)\hat{L}_\ell\\ \hat{D}_\mu\hat{R}_\ell &= \left(\partial_\mu - \mathrm{i}g'\hat{B}_\mu\right)\hat{R}_\ell\end{aligned}\right\} \tag{1.16}$$

Putting (1.14) and (1.16) into (1.6), and adding the gauge-field terms:

$$-\frac{1}{4}\hat{\boldsymbol{F}}_{\mu\nu}\cdot\hat{\boldsymbol{F}}^{\mu\nu}, \tag{1.17}$$

where

$$\hat{\boldsymbol{F}}^{\mu\nu} = \partial^\mu\hat{\boldsymbol{W}}^\nu - \partial^\nu\hat{\boldsymbol{W}}^\mu - g\hat{\boldsymbol{W}}^\mu\times\hat{\boldsymbol{W}}^\nu \tag{1.18}$$

is the $SU(2)$ field stregth tensor for the gauge fields $\hat{\boldsymbol{W}}^\mu$, and

$$-\frac{1}{4}\hat{G}_{\mu\nu}\hat{G}^{\mu\nu}, \tag{1.19}$$

where

$$\hat{G}^{\mu\nu} = \partial^\mu\hat{B}^\nu - \partial^\nu\hat{B}^\mu \tag{1.20}$$

is the $U(1)$ field stregth tensor for the gauge field $\hat{B}^\mu$, we obtain the $SU(2)_\mathrm{L}\otimes U(1)_\mathrm{Y}$ gauge-invariant free leptonic Lagrangian:

$$\begin{aligned}\hat{\mathscr{L}}_{\mathrm{G\ lep}} &= \sum_{\ell=\mathrm{e},\mu,\tau}\left[\hat{\bar{L}}_\ell\mathrm{i}\gamma^\mu\left(\partial_\mu + \mathrm{i}g\frac{\boldsymbol{\tau}}{2}\cdot\hat{\boldsymbol{W}}_\mu - \mathrm{i}\frac{g'}{2}\hat{B}_\mu\right)\hat{L}_\ell\right]\\ &\quad+\sum_{\ell=\mathrm{e},\mu,\tau}\left[\hat{\bar{R}}_\ell\mathrm{i}\gamma^\mu\left(\partial_\mu - \mathrm{i}g'\hat{B}_\mu\right)\hat{R}_\ell\right]\\ &\quad-\frac{1}{4}\hat{\boldsymbol{F}}_{\mu\nu}\cdot\hat{\boldsymbol{F}}^{\mu\nu} - \frac{1}{4}\hat{G}_{\mu\nu}\hat{G}^{\mu\nu}\\ &= \sum_{\ell=\mathrm{e},\mu,\tau}\left[\hat{\bar{L}}_\ell i\not{D}\hat{L}_\ell + \hat{\bar{R}}_\ell i\not{D}\hat{R}_\ell\right] - \frac{1}{4}\hat{\boldsymbol{F}}_{\mu\nu}\cdot\hat{\boldsymbol{F}}^{\mu\nu} - \frac{1}{4}\hat{G}_{\mu\nu}\hat{G}^{\mu\nu}.\end{aligned} \tag{1.21}$$

The $SU(2)_{\rm L} \otimes U(1)_{\rm Y}$ covariant derivatives in terms of the gauge fields $\hat{\boldsymbol{W}}^\mu$ and $\hat{B}^\mu$ are:

$$D_\mu = \partial_\mu + \mathrm{i}g\frac{\boldsymbol{\tau}}{2}\cdot\hat{\boldsymbol{W}}_\mu + \mathrm{i}\frac{g'}{2}Y_{\rm W}\hat{B}_\mu \qquad \text{on } \hat{L}\ SU(2) \text{ doublets,} \tag{1.22}$$

$$D_\mu = \partial_\mu + \mathrm{i}\frac{g'}{2}Y_{\rm W}\hat{B}_\mu \qquad \text{on } \hat{R}\ SU(2) \text{ singlets.} \tag{1.23}$$

1.2 Spontaneous breaking of the $SU(2)_{\mathbf{L}} \otimes U(1)_{\mathbf{Y}}$ symmetry with the Higgs mechanism

1.2.1 Spontaneously broken global $SU(2)_{\mathbf{L}} \otimes U(1)_{\mathbf{Y}}$ symmetry

We consider a $SU(2)$ doublet of bosons — 'isodoublet':

$$\hat{\phi} = \begin{pmatrix} \hat{\phi}^+ \\ \hat{\phi}^0 \end{pmatrix} = \begin{pmatrix} \frac{1}{\sqrt{2}}\left(\hat{\phi}_1 + \mathrm{i}\hat{\phi}_2\right) \\ \frac{1}{\sqrt{2}}\left(\hat{\phi}_3 + \mathrm{i}\hat{\phi}_4\right) \end{pmatrix}. \tag{1.24}$$

The Lagrangian we shall use must have an additional $U(1)$ symmetry, so that the full symmetry is $SU(2) \otimes U(1)$. This $U(1)$ symmetry leads, as we have seen, to the conserved quantum number of weak hypercharge $Y_{\rm W}$. We associate the physical charge Q with the eigenvalue $T^3_{\rm W}$ of $SU(2)$ generator $\hat{T}^3$ via the Gell-Mann-Nishijima equation (1.11), so that $Y_{\rm W}(\hat{\phi}^+) = Y_{\rm W}(\hat{\phi}^0) = 1$. The Lagrangian we choose is then:

$$\begin{aligned} \hat{\mathscr{L}}_\Phi &= \left(\partial_\mu\hat{\phi}^\dagger\right)\left(\partial^\mu\hat{\phi}\right) + \mu^2\hat{\phi}^\dagger\hat{\phi} - \frac{\lambda}{4}\left(\hat{\phi}^\dagger\hat{\phi}\right)^2 \\ &= \left(\partial_\mu\hat{\phi}^\dagger\right)\left(\partial^\mu\hat{\phi}\right) - V(\hat{\phi}), \end{aligned} \tag{1.25}$$

where the scalar potential

$$V(\hat{\phi}) = -\mu^2\hat{\phi}^\dagger\hat{\phi} + \frac{\lambda}{4}\left(\hat{\phi}^\dagger\hat{\phi}\right)^2 \tag{1.26}$$

has the 'spontaneous symmetry breaking' choice of sign for the parameter μ^2. Plainly, for the 'normal' sign of μ^2, in which $+\mu^2\hat{\phi}^\dagger\hat{\phi}$ is replaced by $-\mu^2\hat{\phi}^\dagger\hat{\phi}$, with $\mu^2 > 0$ in both cases, the free ($\lambda = 0$) part would describe a complex doublet, each with the same mass μ. For the Lagrangian (1.25) with $\mu^2 > 0$, the minimum of the classical potential is at the point

$$\left(\phi^\dagger\phi\right)_{\rm min} = 2\mu^2/\lambda \equiv v^2/2. \tag{1.27}$$

We interpret (1.27) as a condition on the vacuum expectation value (*vev*) of $\hat{\phi}^\dagger\hat{\phi}$:

$$\langle 0|\,\hat{\phi}^\dagger\hat{\phi}\,|0\rangle = v^2/2, \tag{1.28}$$

where now $|0\rangle$ is the symmetry-breaking ground state. We note that the Lagrangian (1.25) is invariant under global $SU(2)$ transformations

$$\hat{\phi} \to \hat{\phi}' = \exp\left[-\mathrm{i}\boldsymbol{\alpha}\cdot\boldsymbol{\tau}/2\right]\hat{\phi}, \tag{1.29}$$

but also under a separate global $U(1)$ transformation

$$\hat{\phi} \to \hat{\phi}' = \exp\left[-\mathrm{i}\beta\right]\hat{\phi}. \tag{1.30}$$

The full symmetry is then referred to as global $SU(2)\otimes U(1)$ symmetry.

In order to apply the Goldstone theorem (Goldstone, 1961; Goldstone, Salam, and Weinberg, 1962), and so break the symmetry (thus getting a sensitive particle spectrum), we must expand the fields $\hat{\phi}$ not about $\hat{\phi}=0$, but about a point satysfying the stable ground state (vacuum) condition in (1.28). We need then to define $\langle 0|\,\hat{\phi}\,|0\rangle$ and expand about it: the complex doublet (1.24) contains four real fields, as indicated in (1.24), and (1.28) becomes:

$$\langle 0|\,\hat{\phi}_1^2+\hat{\phi}_2^2+\hat{\phi}_3^2+\hat{\phi}_4^2\,|0\rangle = v^2. \tag{1.31}$$

We have a wide margin of freedom in choosing the $\langle 0|\,\hat{\phi}_i\,|0\rangle$ so that (1.31) holds.

Furthermore, in this non-Abelian situation it may happen that the chosen condition $\langle 0|\,\hat{\phi}_i\,|0\rangle \neq 0$ is *invariant* under some subset of the allowed symmetry transformations. This could mean that this particular choice of the vaccum state respected that subset of symmetries, which would therefore not be 'spontaneously broken' after all. Since each broken symmetry is associated with a massless Goldstone boson, we would then get fewer of these bosons than expected. This is exactly what occurred in the present case.

Assuming, then, that we could choose the $\langle 0|\,\hat{\phi}_i\,|0\rangle$ so as to break the $SU(2)\otimes U(1)$ symmetry completely, we would then expect four massless fields. Actually, however, it is not possible to make such a choice. By using the freedom of global $SU(2)\otimes U(1)$ phase changes, an arbitrary $\langle 0|\,\hat{\phi}_i\,|0\rangle$ can be brought to the form:

$$\langle 0|\,\hat{\phi}\,|0\rangle = \begin{pmatrix} 0 \\ v/\sqrt{2}\end{pmatrix}. \tag{1.32}$$

In considering what symmeties are respected or broken by (1.32), it is easier to look at infinitesimal transformations. The particular transformation:

$$\delta\hat{\phi} = -\mathrm{i}\epsilon(1+\tau_3)\hat{\phi} \tag{1.33}$$

(which is a combination of (1.30) and the 'third component' of (1.29)) is still a symmetry of (1.32) since:

$$(1+\tau_3)\begin{pmatrix}0\\ v/\sqrt{2}\end{pmatrix}=\begin{pmatrix}0\\0\end{pmatrix} \tag{1.34}$$

so that:

$$\langle 0|\,\hat{\phi}\,|0\rangle = \langle 0|\,\hat{\phi}+\delta\hat{\phi}\,|0\rangle\,. \tag{1.35}$$

The vacuum is then invariant under (1.33), and when we look at the spectrum of oscillations about that vacuum, we expect to find only three massless bosons and not four.

Oscillations about (1.32) are conveniently parametrized by:

$$\hat{\phi}=\exp\left[-\mathrm{i}\left(\hat{\boldsymbol{\theta}}\cdot\frac{\boldsymbol{\tau}}{2}\right)v\right]\begin{pmatrix}0\\ \frac{1}{\sqrt{2}}\left(v+\hat{H}(x)\right)\end{pmatrix}. \tag{1.36}$$

Inserting (1.36) into (1.25), we see that no mass term is genetated for the $\hat{\theta}_i$ fields, while the $\hat{H}$ field piece is:

$$\hat{\mathscr{L}}_{\mathrm{H}}=\frac{1}{2}\partial_\mu\hat{H}\partial^\mu\hat{H}-\mu^2\hat{H}^2+\text{interactions}, \tag{1.37}$$

showing that $m_{\mathrm{H}}=\sqrt{2}\mu$.

While in the 'normal symmetry' case with the opposite sign for the μ^2 term in the Lagrangian (1.25), the free-particle spectrum consists of a degenerate doublet of four degrees of freedom all with the same mass μ, in the 'spontaneously broken' case, no such doublet structure is to be seen: instead, there is one massive scalar field and three massless scalar fields. The number of degrees of freedom, four, is the same in each case, but the physical spectrum is completely different.

1.2.2 Spontaneously broken local $SU(2)_{\mathbf{L}}\otimes U(1)_{\mathbf{Y}}$ symmetry

In the local gauge invariant version of the Lagrangian, we introduce the three $SU(2)$ gauge fields $\hat{W}_i^\mu(x)$ $(i=1,2,3)$, and the single $U(1)$ gauge field $\hat{B}^\mu(x)$. The Lagrangian is therefore:

$$\hat{\mathscr{L}}_{\mathrm{G}\Phi}=\left(\hat{D}_\mu\hat{\phi}^\dagger\right)\left(\hat{D}^\mu\hat{\phi}\right)+\mu^2\hat{\phi}^\dagger\hat{\phi}-\frac{\lambda}{4}\left(\hat{\phi}^\dagger\hat{\phi}\right)^2-\frac{1}{4}\hat{\boldsymbol{F}}_{\mu\nu}\cdot\hat{\boldsymbol{F}}^{\mu\nu}-\frac{1}{4}\hat{G}_{\mu\nu}\hat{G}^{\mu\nu} \tag{1.38}$$

where

$$D_\mu\hat{\phi}=\left(\partial_\mu+\mathrm{i}g\frac{\boldsymbol{\tau}}{2}\cdot\hat{\boldsymbol{W}}_\mu+\mathrm{i}\frac{g'}{2}\hat{B}_\mu\right)\hat{\phi} \tag{1.39}$$

We must now decide how to choose the non-zero vacuum expectation value that breaks the symmetry. The essential point for electroweak application is that, after symmetry breaking, we should be left with three massive gauge bosons (which will be the $W^{\pm}$ and Z) and one massless gauge boson, the photon. We may reasonably guess that the massless boson will be associated with a symmetry which is unbroken by the *vev*. The choice is

$$\langle 0|\,\hat{\phi}\,|0\rangle = \begin{pmatrix} 0 \\ v/\sqrt{2} \end{pmatrix} \tag{1.40}$$

where $v/\sqrt{2} = \sqrt{2}\mu/\lambda^{1/2}$. Eq. (1.40) implies that the vacuum remains invariant under the combined transformation:

$$\left(\frac{1}{2} + T_3^{(\frac{1}{2})}\right) \langle 0|\,\hat{\phi}\,|0\rangle = 0, \tag{1.41}$$

and hence

$$\langle 0|\,\hat{\phi}\,|0\rangle \rightarrow \Big(\langle 0|\,\hat{\phi}\,|0\rangle\Big)' = \exp\left[\mathrm{i}\alpha\left(\frac{1}{2} + T_3^{(\frac{1}{2})}\right)\right] \langle 0|\,\hat{\phi}\,|0\rangle = \langle 0|\,\hat{\phi}\,|0\rangle \tag{1.42}$$

where $T_3^{(\frac{1}{2})} = \tau_3/2$. We now need to consider oscillations about (1.40) in order to see the physical particle spectrum. We parametrize these conveniently as:

$$\hat{\phi} = \exp\left[-\mathrm{i}\hat{\boldsymbol{\theta}}(x)\cdot\boldsymbol{\tau}/2v\right]\begin{pmatrix} 0 \\ \frac{1}{\sqrt{2}}\Big(v + \hat{H}(x)\Big) \end{pmatrix}. \tag{1.43}$$

We can reduce the phase fields $\hat{\boldsymbol{\theta}}$ to zero by an appropriate gauge transformation, and it is simplest to examine the particle spectrum in this *unitary* gauge. Substituting

$$\hat{\phi} = \begin{pmatrix} 0 \\ \frac{1}{\sqrt{2}}\Big(v + \hat{H}(x)\Big) \end{pmatrix} \tag{1.44}$$

into the Lagrangian (1.38) we obtain:

$$\begin{aligned} \hat{\mathscr{L}}_{\mathrm{G}\Phi} = {} & \frac{1}{2}\partial_\mu \hat{H}\partial^\mu \hat{H} \\ & + \frac{1}{8}g^2\Big(v+\hat{H}\Big)^2\Big(\hat{W}_{1\mu} + \mathrm{i}\hat{W}_{2\mu}\Big)\Big(\hat{W}_1^\mu - \mathrm{i}\hat{W}_2^\mu\Big) \\ & + \frac{1}{8}\Big(v+\hat{H}\Big)^2\Big(g\hat{W}_{3\mu} - g'\hat{B}_\mu\Big)\Big(g\hat{W}_3^\mu - g'\hat{B}^\mu\Big) \\ & - \frac{\mu^2}{2}\Big(v+\hat{H}\Big)^2 + \frac{\lambda}{16}\Big(v+\hat{H}\Big)^4 \\ & - \frac{1}{4}\hat{\boldsymbol{F}}_{\mu\nu}\cdot\hat{\boldsymbol{F}}^{\mu\nu} - \frac{1}{4}\hat{G}_{\mu\nu}\hat{G}^{\mu\nu} \end{aligned} \tag{1.45}$$

and retaining only the terms which are second order in the fields (i.e. kinetic energies or mass terms), we find that:

$$\begin{aligned}\hat{\mathscr{L}}^{\text{free}}_{\text{G}\Phi} = &\frac{1}{2}\partial_\mu \hat{H}\partial^\mu \hat{H} - \mu^2 \hat{H}^2 \\ &- \frac{1}{4}\left(\partial_\mu \hat{W}_{1\nu} - \partial_\nu \hat{W}_{1\mu}\right)\left(\partial^\mu \hat{W}_1^\nu - \partial^\nu \hat{W}_1^\mu\right) + \frac{1}{8}g^2 v^2 \hat{W}_{1\mu}\hat{W}_1^\mu \\ &- \frac{1}{4}\left(\partial_\mu \hat{W}_{2\nu} - \partial_\nu \hat{W}_{2\mu}\right)\left(\partial^\mu \hat{W}_2^\nu - \partial^\nu \hat{W}_2^\mu\right) + \frac{1}{8}g^2 v^2 \hat{W}_{2\mu}\hat{W}_2^\mu \\ &- \frac{1}{4}\left(\partial_\mu \hat{W}_{3\nu} - \partial_\nu \hat{W}_{3\mu}\right)\left(\partial^\mu \hat{W}_3^\nu - \partial^\nu \hat{W}_3^\mu\right) - \frac{1}{4}\hat{G}_{\mu\nu}\hat{G}^{\mu\nu} \\ &+ \frac{1}{8}v^2\left(g\hat{W}_{3\mu} - g'\hat{B}_\mu\right)\left(g\hat{W}_3^\mu - g'\hat{B}^\mu\right).\end{aligned} \tag{1.46}$$

The first row of (1.46) tells us that we have a scalar field, the Higgs boson, whose tree-level mass is

$$m_{\text{H}} = \sqrt{2}\mu = \sqrt{\lambda}v/\sqrt{2} \tag{1.47}$$

where $v/\sqrt{2}$ is the (tree-level) Higgs vacuum value.
The next two rows tell us that the components $\hat{W}_1$ and $\hat{W}_2$ of the triplet $\left(\hat{W}_1,\ \hat{W}_2,\ \hat{W}_3\right)$ acquire a (tree-level) mass:

$$M_1 = M_2 = gv/2 \equiv M_{\text{W}} \tag{1.48}$$

The last two rows show us that the fields $\hat{W}_3$ and $\hat{B}$ are mixed. However, they can be easily unmixed by noting that the last term in (1.46) involves only the combination $g\hat{W}_3^\mu - g'\hat{B}^\mu$, which evidently acquires a mass. This suggests introducing the normalized linear combination:

$$\hat{Z}^\mu = \cos\theta_{\text{W}}\hat{W}_3^\mu - \sin\theta_{\text{W}}\hat{B}^\mu. \tag{1.49}$$

where the 'weak mixing angle' θ_{W} is given by:

$$\cos\theta_{\text{W}} = \frac{g}{(g^2+g'^2)^{1/2}} \quad , \qquad \sin\theta_{\text{W}} = \frac{g'}{(g^2+g'^2)^{1/2}} \tag{1.50}$$

together with the orthogonal combination:

$$\hat{A}^\mu = \sin\theta_{\text{W}}\hat{W}_3^\mu + \cos\theta_{\text{W}}\hat{B}^\mu. \tag{1.51}$$

We then find that the two last lines of (1.46) become:

$$-\frac{1}{4}\left(\partial_\mu \hat{Z}_\nu - \partial_\nu \hat{Z}_\mu\right)\left(\partial^\mu \hat{Z}^\nu - \partial^\nu \hat{Z}^\mu\right) + \frac{1}{8}v^2\left(g^2+g'^2\right)\hat{Z}_\mu \hat{Z}^\mu - \frac{1}{4}\hat{F}_{\mu\nu}\hat{F}^{\mu\nu}, \tag{1.52}$$

where

$$\hat{F}_{\mu\nu} = \partial_\mu \hat{A}_\nu - \partial_\nu \hat{A}_\mu. \tag{1.53}$$

Thus, the (tree-level) mass of the $\hat{Z}$ field is:

$$M_{\mathrm{Z}} = \frac{1}{2}\left(g^2 + g'^2\right)^{1/2} = \frac{M_{\mathrm{W}}}{\cos\theta_{\mathrm{W}}} \tag{1.54}$$

while, for the $\hat{A}$ field:

$$M_{\mathrm{A}} = 0. \tag{1.55}$$

The $\hat{A}^\mu$ field describes a massless particle, to be identified with the photon. Counting the number of degrees of freedom, we originally had 12 in the Lagrangian (1.38) — three massless $\hat{W}$'s and one massless $\hat{B}$ gauge fields, which is eight degrees of freedom in all, together with four $\hat{\phi}$ fields. After symmetry breaking, we have three massive vector gauge fields $\hat{W}_1$, $\hat{W}_2$ and $\hat{Z}$ with nine degrees of freedom, one massless vector gauge field $\hat{A}$ with two, and one massive scalar $\hat{H}$. Comparing this result with the Goldstone model of spontaneously broken *global* $SU(2) \otimes U(1)$ symmetry, the three massless Goldstone bosons have both disappeared in the Higgs model of spontaneously broken *local* symmetry, and three of the massless gauge fields have become massive. In a manner of speaking, we can say that the three gauge fields have eaten a scalar field (the Goldstone massless boson) each and acquired a mass. More properly, we may compare the situation with the Gupta-Bleuler mechanism for the photon field quantized in the Lorentz gauge (Bleuler, 1950; Gupta, 1950). In that mechanism, the longitudinal and timelike components of the photon cancel each other, leaving the two transverse components. Here the timelike component of the massless gauge field is cancelled by the scalar field, leaving three polarisation states for the gauge field, rendering it massive. Spontaneous breaking of $SU(2) \otimes U(1)$ symmetry, then, yields the following particle spectrum, depending on whether the symmetry is global or local.

Goldstone mode (spontaneous breaking of global $SU(2) \otimes U(1)$ symmetry):

$$\text{4 massive scalar fields} \quad \rightarrow \begin{cases} \text{1 massive scalar field} \\ \quad + \text{3 massless scalar fields} \end{cases}$$

Higgs mode (spontaneous breaking of local $SU(2) \otimes U(1)$ symmetry):

$$\left.\begin{array}{l} \text{4 massive scalar fields} \\ \quad + \text{4 massless vector gauge fields} \end{array}\right\} \quad \rightarrow \begin{cases} \text{1 massive scalar field} \\ \quad + \text{3 massive vector fields} \\ \quad + \text{1 massless vector field} \end{cases}$$

Of course, the physical application will be to identify the $\hat{W}$ and $\hat{Z}$ fields with those physical particles mediating the weak interactions, and the $\hat{A}$ field with the massless photon.

The identification of $\hat{A}^\mu$ with the photon field is made clearer if we look at the form of $D_\mu\hat{\phi}$ written in terms of $\hat{A}_\mu$ and $\hat{Z}_\mu$, discarding the $\hat{W}_1$ and $\hat{W}_2$ pieces:

$$\begin{aligned} D_\mu\hat{\phi} = \Bigg\{ & \partial_\mu + \mathrm{i}g\sin\theta_\mathrm{W}\left(\frac{1+\tau_3}{2}\right)\hat{A}_\mu \\ & + \frac{\mathrm{i}g}{\cos\theta_\mathrm{W}}\left[\frac{\tau_3}{2} - \sin^2\theta_\mathrm{W}\left(\frac{1+\tau_3}{2}\right)\right]\hat{Z}_\mu \Bigg\}\hat{\phi}. \end{aligned} \tag{1.56}$$

Now the operator $1+\tau_3$ acting on $\langle 0|\,\hat{\phi}\,|0\rangle$ gives zero, as observed in (1.41), and this is why $\hat{A}_\mu$ does not acquire a mass when $\langle 0|\,\hat{\phi}\,|0\rangle \neq 0$. When a spontaneously broken non-Abelian symmetry is gauged, gauge fields corresponding to symmetries that are broken by the choice of $\langle 0|\,\hat{\phi}\,|0\rangle$ acquire a mass, while those that correspond to *unbroken* simmetries of $\langle 0|\,\hat{\phi}\,|0\rangle$ do not become massive. Although not unique, this choice of $\hat{\phi}$ and $\langle 0|\,\hat{\phi}\,|0\rangle$ in very economical and natural. We are interpreting the zero eigenvalue of $1+\tau_3$ as the electromagnetic charge of the vacuum, which we do not wish to be zero. We then make the identification:

$$e = g\sin\theta_\mathrm{W}. \tag{1.57}$$

The particular form of (1.46) correspond to a *choice of gauge*, namely the unitary one. There is always the possibility of using other gauges: we would return to a general parametrization including 't Hooft gauge-fixing terms.

We consider now with further detail the Higgs Lagrangian (1.45) to take into account the Higgs boson self-coupling and its coupling with vector bosons. Using the relation $v/\sqrt{2} = \sqrt{2}\mu/\lambda^{1/2}$, we find that the Lagrangian containing the Higgs field H is given by:

$$\begin{aligned} \hat{\mathscr{L}}_\mathrm{H} &= \frac{1}{2}\partial_\mu\hat{H}\partial^\mu\hat{H} - \frac{\mu^2}{2}\left(v+\hat{H}\right)^2 + \frac{\lambda}{16}\left(v+\hat{H}\right)^4 \\ &= \frac{1}{2}\partial_\mu\hat{H}\partial^\mu\hat{H} - \frac{\lambda v^2}{4}\hat{H}^2 - \frac{\lambda v}{4}\hat{H}^3 - \frac{\lambda}{16}\hat{H}^4 + \frac{\lambda v^4}{16} \end{aligned} \tag{1.58}$$

where the unrelevant constant factor $\frac{\lambda v^4}{16}$ can be omitted. From this Lagrangian, the Feynman rules[2] for the Higgs self-interaction vertices are given

[2]The Feynman rule for these vertices are obtained by multiplying the term involving the interaction by a factor $-\mathrm{i}$. One includes also a factor $n!$ where n is the number of identical particles in the vertex.

by:

$$g_{\mathrm{HHH}} = (3!)\mathrm{i}\frac{\lambda v}{4} = 3\mathrm{i}\frac{m_{\mathrm{H}}^2}{v}, \qquad g_{\mathrm{HHHH}} = (4!)\mathrm{i}\frac{\lambda}{16} = 3\mathrm{i}\frac{m_{\mathrm{H}}^2}{v^2}. \tag{1.59}$$

As for the Higgs boson couplings to gauge bosons, they were almost derived previously, when the masses of these particles were calculated (cfr eq (1.45)). Indeed, from the Lagrangian describing the gauge boson masses:

$$\mathscr{L}_{M_V} \sim M_V^2 \left(1 + \frac{\hat{H}}{v}\right)^2 \tag{1.60}$$

one obtains also the Higgs boson couplings to gauge bosons and fermions:

$$g_{\mathrm{H}VV} = -2\mathrm{i}\frac{M_V^2}{v}, \quad g_{\mathrm{HH}VV} = -2\mathrm{i}\frac{M_V^2}{v^2}. \tag{1.61}$$

This form of the Higgs couplings ensures the unitarity of the theory.

The model introduced here is the 'Higgs sector' of the SM, without any coupling to fermions. We have seen how, by supposing that the potential in (1.38) has the symmetry-breaking sign of the parameter μ^2, the $\mathrm{W}^{\pm}$ and Z gauge bosons can be given mass. This is an elegant 'mechanism' for arriving at a renormalizable theory of massive vector bosons.

1.2.3 The Leptonic Currents

Eqs (1.48) and (1.54) give the values of some experimental observables, whose measure leads to a direct test of the consistency of the SM. The weak mixing angle θ_{W} can be measured from neutrino-lepton scattering (Commins and Bucksbaum, 1983; Renton, 1990; Winter, 2000): we obtain $\sin^2\theta_{\mathrm{W}} \simeq 0.23$. More precise measurements of θ_{W} depend on the normalization prescription and are sensitive to higher-order corrections, which must be included in comparing the full GSW theory with experiment (Yao et al., 2006).

Consider now the charged leptonic currents. The correct normalization for the charged fields is that $\hat{W}^{\mu} = (\hat{W}_1^{\mu} - \mathrm{i}\hat{W}_2^{\mu})/\sqrt{2}$ destroys the W^+ or creates the W^-. The $\boldsymbol{\tau}\cdot\hat{\boldsymbol{W}}/2$ terms can be written as:

$$\boldsymbol{\tau}\cdot\hat{\boldsymbol{W}}^{\boldsymbol{\mu}}/2 = \frac{1}{\sqrt{2}}\left\{\tau_+\frac{\hat{W}_1^{\mu} - \mathrm{i}\hat{W}_2^{\mu}}{\sqrt{2}} + \tau_-\frac{\hat{W}_1^{\mu} + \mathrm{i}\hat{W}_2^{\mu}}{\sqrt{2}}\right\} + \frac{\tau_3}{2}\hat{W}_3^{\mu} \tag{1.62}$$

where $\tau_{\pm} = (\tau_1 \pm \tau_2)/2$ are the usual raising and lowering operators for the doublets. The $\ell = \mathrm{e}$ contribution to the left-handed term of (1.21) picks out

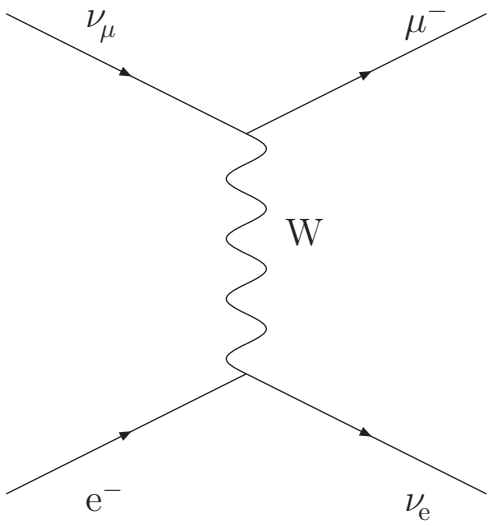

Figure 1.1: W-exchange process in $\nu_\mu + e^- \rightarrow \mu^- + \nu_e$

the process $e^- \rightarrow \nu_e + W^-$ for example, with the result that the corresponding vertex is given by:

$$-i\frac{g}{\sqrt{2}}\gamma^\mu\frac{1-\gamma^5}{2}. \tag{1.63}$$

The 'universality' of the single coupling constant g ensures that (1.63) is also the amplitude for the $\mu-\ \nu_\mu-$ W and $\tau-\ \nu_\tau-$ W vertices.

In particular, the value of v, the *vev* of the neutral component of the Higgs doublet, can be obtained from the value of the Fermi constant G_F measured from muon decay. In order to be consistent with the Fermi theory, the electroweak amplitude has to be equal to the Fermi amplitude in the limit of low transfered momentum. The comparison between the two amplitude leads to:

$$\frac{G_F}{\sqrt{2}} = \frac{g^2}{8M_W}. \tag{1.64}$$

Putting together (1.48) and (1.64), we can deduce:

$$\frac{G_F}{\sqrt{2}} = \frac{1}{2v^2} \tag{1.65}$$

so that, from the known value of G_F (Yao et al., 2006):

$$G_F = 1.6637(1)\cdot 10^{-5}\ \text{GeV}^{-2} \tag{1.66}$$

there follows the value of v:

$$v \simeq 246\ \text{GeV}. \tag{1.67}$$

This parameter sets the scale of electroweak symmetry breaking. However, it is related by (cf eq. (1.27)):

$$v = \frac{2\mu}{\lambda^{1/2}} \tag{1.68}$$

to the parameters λ and μ, whose values cannot be predicted by the theory. Analogously, the dependence of the Higgs boson mass (1.47) from one of the free parameters λ and μ makes it an unpredictable parameter of the theory.

In general, the charge-changing part of (1.21) can be written as:

$$-\frac{g}{\sqrt{2}} \sum_{\ell=\mathrm{e},\mu,\tau} \left\{ \hat{\bar{\nu}}_\ell \gamma^\mu \frac{1-\gamma^5}{2} \hat{\ell} \right\} \hat{W}_\mu + \text{Hermitian conjugate} \tag{1.69}$$

where $\hat{W}^\mu = (\hat{W}_1^\mu - \mathrm{i}\hat{W}_2^\mu)/\sqrt{2}$. Eq. (1.69) has the form:

$$-\hat{j}^\mu_{\mathrm{CC}}(\text{leptons})\hat{W}_\mu - \hat{j}^{\mu\dagger}_{\mathrm{CC}}(\text{leptons})\hat{W}^\dagger_\mu \tag{1.70}$$

where the *leptonic weak charged current* $\hat{j}^\mu_{\mathrm{CC}}(\text{leptons})$ is given by:

$$\hat{j}^\mu_{\mathrm{CC}}(\text{leptons}) = \frac{g}{\sqrt{2}} \sum_{\ell=\mathrm{e},\mu,\tau} \left\{ \hat{\bar{\nu}}_\ell \gamma^\mu \frac{1-\gamma^5}{2} \hat{\ell} \right\}. \tag{1.71}$$

Turning now to the *leptonic weak neutral current*, this will appear via the couplings to the Z, written as:

$$-\hat{j}^\mu_{\mathrm{NC}}(\text{leptons})\hat{Z}_\mu. \tag{1.72}$$

Referring to (1.49) for the linear combination of $\hat{W}_3^\mu$ and $\hat{B}^\mu$ which represents $\hat{Z}^\mu$, we find that:

$$\hat{j}^\mu_{\mathrm{NC}}(\text{leptons}) = \frac{g}{\cos\theta_{\mathrm{W}}} \sum_{\substack{\ell=\mathrm{e},\mu,\tau \\ \nu_\mathrm{e},\nu_\mu,\nu_\tau}} \hat{\bar{\psi}}_\ell \gamma^\mu \left[T_W^{3\ell} \left(\frac{1-\gamma^5}{2} \right) - \sin^2\theta_{\mathrm{W}} Q_\ell \right] \hat{\psi}_\ell. \tag{1.73}$$

For the $Q = 0$ neutrinos with $T^3_{\mathrm{W}} = 1/2$,

$$\hat{j}^\mu_{\mathrm{NC}}(\text{neutrinos}) = \frac{g}{2\cos\theta_{\mathrm{W}}} \sum_{\ell=\mathrm{e},\mu,\tau} \hat{\bar{\nu}}_\ell \gamma^\mu \frac{1-\gamma^5}{2} \hat{\nu}_\ell. \tag{1.74}$$

For the other (negatively charged) leptons, we have both L and R couplings from (1.73), and we can write:

$$\hat{j}^\mu_{\mathrm{NC}}(\text{charged leptons}) = \frac{g}{\cos\theta_{\mathrm{W}}} \sum_{\ell=\mathrm{e},\mu,\tau} \hat{\bar{\ell}} \gamma^\mu \left[c^\ell_{\mathrm{L}} \left(\frac{1-\gamma^5}{2} \right) + c^\ell_{\mathrm{R}} \left(\frac{1-\gamma^5}{2} \right) \right] \hat{\ell} \tag{1.75}$$

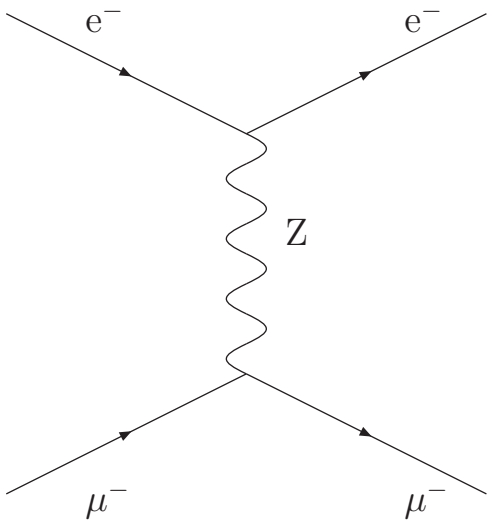

Figure 1.2: Z-exchange process in $e^- + \mu^- \to e^- + \mu^-$

where

$$c_{\rm L}^{\ell} = T_{\rm W}^{3,\ell} - \sin^2\theta_{\rm W} Q_\ell = -\frac{1}{2} + \sin^2\theta_{\rm W} \tag{1.76}$$

$$c_{\rm R}^{\ell} = -\sin^2\theta_{\rm W} Q_\ell = \sin^2\theta_{\rm W}. \tag{1.77}$$

Thus, the Z coupling is not pure $V - A$. In particular, the couplings are independent of ℓ and hence exhibit lepton universality. The alternative notation

$$\hat{j}^{\mu}_{\rm NC}(\text{charged leptons}) = \frac{g}{2\cos\theta_{\rm W}} \sum_{\ell={\rm e},\mu,\tau} \hat{\bar{\ell}}\gamma^{\mu}\left(g_{\rm V}^{\ell} - g_{\rm A}^{\ell}\gamma^5\right)\hat{\ell} \tag{1.78}$$

is often used, where

$$g_{\rm V}^{\ell} = -\frac{1}{2} + 2\sin^2\theta_{\rm W}, \quad g_{\rm A}^{\ell} = -\frac{1}{2}. \tag{1.79}$$

Note that $g_{\rm V}^{\ell}$ vanishes for $\sin^2\theta_{\rm W} = 0.25$. It is customary to define the parameter

$$\rho = M_{\rm W}^2/(M_{\rm Z}^2\cos^2\theta_{\rm W}) \tag{1.80}$$

which is unity at tree level, in absence of loop corrections.

We may also check the electromagnetic current in the theory, by looking for the piece that couples to A^μ. We find that

$$\hat{j}^{\mu}_{\rm em} = -g\sin\theta_{\rm W} \sum_{\ell={\rm e},\mu,\tau} \hat{\bar{\ell}}\gamma^{\mu}\hat{\ell} \tag{1.81}$$

which allows us to identify the electromagnetic charge e as

$$e = g \sin\theta_{\mathrm{W}} \tag{1.82}$$

as already suggested in (1.57). Note that all the γ^5's cancel from (1.81), as required.

1.3 Quark flavour mixing: the CKM matrix

We consider now the quark sector of the SM. The strong interactions between quarks are described by a non-Abelian quantum gauge field theory, in which the gauge group is an $SU(3)_{\mathrm{c}}$, acting on a degree of freedom called 'colour', indicated by the subscript c. This theory is called quantum chromodynamics (QCD). The requirement of local gauge invariance leads to an octet of (massless) gauge fields, called gluons.

Quarks interact also via weak interactions. For them (and their hadronic composites), however, there is the well-known phenomenon of flavour change in weak hadronic processes. In the framework of the $V-A$ theory, Cabibbo (1963) postulated that the strength of the hadronic weak interactions was shared between the $\Delta S = 0$ and $\Delta S = 1$ transitions (where S is the strangeness quantum number), the latter being relatively suppressed as compared to the former. Cabibbo introduced the 'mixed' field

$$\hat{d}' \equiv \cos\theta_{\mathrm{C}}\hat{d} + \sin\theta_{\mathrm{C}}\hat{s}. \tag{1.83}$$

Glashow, Iliopoulos, and Maiani (1970), in order to explain the absence of (first-order) neutral strangeness-changing (or better, flavour-changing) current processes, introduced a fourth quark, called c, the charm quark, with charge $\frac{2}{3}e$. They postulated that c was coupled to the 'orthogonal' d-s combination

$$\hat{s}' \equiv \cos\theta_{\mathrm{C}}\hat{d} + \sin\theta_{\mathrm{C}}\hat{s}. \tag{1.84}$$

The GIM mechanism was experimentally confirmed by the observation of the J/ψ resonance (Aubert et al., 1974; Augustin et al., 1974), interpreted as bound c $\bar{\mathrm{c}}$ state. In the next years, another quark family was discovered. Lederman et al. (1977) discovered the Υ meson, interpreted as the bound $q\,\overline{q}$ state of a new quark flavour, the bottom. In 1994, the t quark (Abachi et al., 1995a,b; Abe et al., 1994a,b, 1995) was discovered through the production of t $\bar{\mathrm{t}}$ pairs at the CDF and D0 detectors at FNAL's Tevatron, in p-$\overline{\mathrm{p}}$ collision at $E_{\mathrm{CM}} = 1.8$ TeV.

Table 1.3: Weak isospin and hypercharge assignments

	$T_{\rm W}$	$T^3_{\rm W}$	$Y_{\rm W}$	Q
$\nu_{\rm eL}$, $\nu_{\mu\rm L}$, $\nu_{\tau\rm L}$	1/2	1/2	-1	0
$\nu_{\rm eR}$, $\nu_{\mu\rm R}$, $\nu_{\tau\rm R}$	0	0	0	0
$\rm e_L$, $\mu_{\rm L}$, $\tau_{\rm L}$	1/2	-1/2	-1	-1
$\rm e_R$, $\mu_{\rm R}$, $\tau_{\rm R}$	0	0	-2	-1
$\rm u_L$, $\rm c_L$, $\rm t_L$	1/2	1/2	1/3	2/3
$\rm u_R$, $\rm c_R$, $\rm t_R$	0	0	4/3	2/3
$\rm d'_L$, $\rm s'_L$, $\rm b'_L$	1/2	-1/2	1/3	-1/3
$\rm d'_R$, $\rm s'_R$, $\rm b'_R$	0	0	-2/3	-1/3
ϕ^+	1/2	1/2	1	1
ϕ^0	1/2	-1/2	1	0

Weak transitions involving charged quarks suggests a doublet structure similar to leptons, involving the 'weak isospin' group. We make these assignments for the left-handed chiral components of quark fields:

$$T_{\rm W} = \frac{1}{2} \qquad \begin{cases} T^3_{\rm W} = +1/2 \\ T^3_{\rm W} = -1/2 \end{cases} \qquad \begin{pmatrix} \hat{u}_{\rm L} \\ \hat{d}'_{\rm L} \end{pmatrix} \qquad \begin{pmatrix} \hat{c}_{\rm L} \\ \hat{s}'_{\rm L} \end{pmatrix} \qquad \begin{pmatrix} \hat{t}_{\rm L} \\ \hat{b}'_{\rm L} \end{pmatrix} \tag{1.85}$$

while the right-handed chiral components of quark fields, for which no weak interaction coupling has been evidenced

$$\hat{u}_{\rm R} \quad \hat{d}'_{\rm R} \quad \hat{c}'_{\rm R} \quad \hat{s}'_{\rm R} \quad \hat{t}_{\rm R} \quad \hat{b}'_{\rm R} \tag{1.86}$$

are singlets under $SU(2)_{\rm L}$ group. With the help of the weak charge formula (1.11) the quark doublets ($\rm u_L$, $\rm d'_L$) etc have $Y_{\rm W} = +\frac{1}{3}$, the 'upper' quark singlets $\rm u_R$ etc $Y_{\rm W} = +\frac{1}{3}$, and the 'lower' ones $\rm d'_R$ etc have $Y_{\rm W} = -\frac{2}{3}$. We obtain, in summary, the assignments in Table 1.3.

The $T^3_{\rm W} = -1/2$ components of the L-doublets have to be understood as the flavour-mixed (weakly interacting states)

$$\begin{pmatrix} \hat{d}' \\ \hat{s}' \\ \hat{b}' \end{pmatrix}_{\rm L} = \begin{pmatrix} V_{\rm ud} & V_{\rm us} & V_{\rm ud} \\ V_{\rm cd} & V_{\rm cs} & V_{\rm cd} \\ V_{\rm td} & V_{\rm ts} & V_{\rm td} \end{pmatrix} \begin{pmatrix} \hat{d} \\ \hat{s} \\ \hat{b} \end{pmatrix}_{\rm L} \tag{1.87}$$

where $\hat{d}$, $\hat{s}$ and $\hat{b}$ are the strongly interacting fields with masses $m_{\rm d}$, $m_{\rm s}$ and $m_{\rm b}$, and the V matrix is the Cabibbo-Kobayashi-Maskawa matrix (Cabibbo, 1963; Kobayashi and Maskawa, 1973), which generalizes the GIM mixing.

1.3.1 The quark currents

The charge-changing quark currents coupled to the $\mathrm{W}^{\pm}$ fields have a form very similar to that of the charged leptonic currents, except that the $T^3_{\rm W} = -\frac{1}{2}$ components of the L-doublets are the weakly interacting states $\hat{d}'$, $\hat{s}'$ and $\hat{b}'$, which are a mixing of the strongly interacting fields $\hat{d}$, $\hat{s}$ and $\hat{b}$ through the CKM matrix. Thus, *the charge-changing weak quark current* is:

$$\hat{j}^{\mu}_{\rm CC}(\text{quarks}) = \frac{g}{\sqrt{2}} \left\{ \hat{\bar{u}}\gamma^{\mu}\frac{1-\gamma^5}{2}\hat{d}' + \hat{\bar{c}}\gamma^{\mu}\frac{1-\gamma^5}{2}\hat{s}' + \hat{\bar{t}}\gamma^{\mu}\frac{1-\gamma^5}{2}\hat{b}' \right\}. \quad (1.88)$$

The neutral currents are diagonal in flavour if the matrix V is unitary (see section 1.3.2). The *neutral weak quark current* is then:

$$\hat{j}^{\mu}_{\rm NC}(\text{quarks}) = \frac{g}{\cos\theta_{\rm W}} \sum_{\substack{q=\mathrm{u,c,t}\\ \mathrm{d,s,b}}} \hat{\bar{q}}\gamma^{\mu}\left[c^q_{\rm L}\left(\frac{1-\gamma^5}{2}\right) + c^q_{\rm R}\left(\frac{1-\gamma^5}{2}\right)\right]\hat{q} \quad (1.89)$$

where

$$c^q_{\rm L} = T^{3,q}_W - \sin^2\theta_{\rm W} Q_q \quad (1.90)$$
$$c^q_{\rm R} = -\sin^2\theta_{\rm W} Q_q. \quad (1.91)$$

As for the charged lepton, we can alternatively write (1.89) as:

$$\hat{j}^{\mu}_{\rm NC}(\text{quarks}) = \frac{g}{2\cos\theta_{\rm W}} \sum_q \hat{\bar{q}}\gamma^{\mu}\left(g^q_{\rm V} - g^q_{\rm A}\gamma^5\right)\hat{q} \quad (1.92)$$

where

$$g^q_{\rm V} = T^{3,q}_W - 2\sin^2\theta_{\rm W} Q_q \quad (1.93)$$
$$g^q_{\rm A} = T^{3,q}_W. \quad (1.94)$$

Reading (1.5) and (1.85) together 'vertically', leptons and quarks are grouped in three *families*, each with two leptons or two quarks. The theoretical motivation for such family grouping is that *anomalies* are cancelled within each complete family. While they can be tolerated in global (non-gauged) currents, they must cancel in the symmetry currents of a gauge theory, or else renormalizability is destroyed. The condition that anomalies cancel in the

gauged currents of the SM is a remarkably simple one (Ryder, 1996, page 374):

$$N_{\rm c}(Q_{\rm u}+Q_{\rm d})+Q_{\rm e}=0 \tag{1.95}$$

where $N_{\rm c}$ is the number of colours, and $Q_{\rm u}$, $Q_{\rm d}$ and $Q_{\rm e}$ are the charges (in units of e) of the 'u', 'd' and 'e' type fields in each family. Clearly, the anomaly-free condition (1.95) is true for the families in (1.5) and (1.85). It appears then to shed some light on lepton-hadron symmetry, but allows for an arbitrary number of generations. Besides, it indicates a remarkable connection between the facts that quarks occur in three families and have charges that are 1/3 fractions. The SM provides no explanation of this connection.

1.3.2 The fermion masses

The fact that $SU(2)_{\rm L}$ gauge group acts only on the L components of the fermion fields, immediately creates a fundamental problem as far as the masses of these particles are concerned. The ordinary 'kinetic' part of a free Dirac fermion does not mix the L and R components of the field:

$$\hat{\bar{\psi}}\not{\partial}\hat{\psi}=\hat{\bar{\psi}}_{\rm R}\not{\partial}\hat{\psi}_{\rm R}+\hat{\bar{\psi}}_{\rm L}\not{\partial}\hat{\psi}_{\rm L}. \tag{1.96}$$

Thus we can, in principle, contemplate 'gauging' the L and R components differently. Weak interactions are parity-violating and the $SU(2)_{\rm L}$ covariant derivative acts only on the second term of (1.96). However, a Dirac mass term has the form:

$$\begin{aligned}
-m\hat{\bar{\psi}}\hat{\psi} &= -m\hat{\psi}^\dagger(P_{\rm L}+P_{\rm R})\gamma^0(P_{\rm L}+P_{\rm R})\hat{\psi}\\
&= -m\hat{\psi}^\dagger(P_{\rm L}\gamma^0P_{\rm L}+P_{\rm L}\gamma^0P_{\rm R}+P_{\rm R}\gamma^0P_{\rm L}+P_{\rm R}\gamma^0P_{\rm R})\hat{\psi}\\
&= -m\hat{\psi}^\dagger(\gamma^0P_{\rm R}P_{\rm L}+\gamma^0P_{\rm R}P_{\rm R}+\gamma^0P_{\rm L}P_{\rm L}+\gamma^0P_{\rm L}P_{\rm R})\hat{\psi}\\
&= -m\hat{\psi}^\dagger(P_{\rm L}\gamma^0P_{\rm R}+P_{\rm R}\gamma^0P_{\rm L})\hat{\psi}\\
&= -m(\hat{\bar{\psi}}_{\rm L}\hat{\psi}_{\rm R}+\hat{\bar{\psi}}_{\rm R}\hat{\psi}_{\rm L})
\end{aligned} \tag{1.97}$$

since γ^5 anticommutes with γ^0: it couples the L and R components. If only $\hat{\bar{\psi}}_{\rm L}$ is subject to a transformation of the form (1.7), then (1.97) is not invariant. Thus, mass terms for Dirac fermions will explicitly break $SU(2)$. This kind of explicit breaking of the gauge symmetry leads to violations of unitarity and then of renormalizability.

However, in a theory with spontaneous symmetry breaking, there is a way of giving masses without introducing an explicit mass term in the Lagrangian. If a fermion has a 'Yukawa'-type coupling to a scalar field which acquires

a *vev*, then this will generate a fermion mass. Consider the electron, for example, and let us hypothesize such a coupling between the electron-type $SU(2)_{\mathrm{L}}$ doublet

$$\hat{L}_{\mathrm{e}} = \begin{pmatrix} \hat{\nu}_{\mathrm{e}} \\ \hat{e} \end{pmatrix}_{\mathrm{L}}, \tag{1.98}$$

the Higgs doublet $\hat{\phi}$ and the R-component of the electron field:

$$\hat{\mathscr{L}}^{\mathrm{e}}_{\mathrm{Yuk}} = -g_{\mathrm{e}} \left(\hat{\bar{L}}_{\mathrm{e}} \hat{\phi} \hat{R}_{\mathrm{e}} + \hat{\bar{R}}_{\mathrm{e}} \hat{\phi}^{\dagger} \hat{L}_{\mathrm{e}} \right). \tag{1.99}$$

In each term of (1.99), the two $SU(2)_{\mathrm{L}}$ doublets are 'dotted together' so as to form an $SU(2)_{\mathrm{L}}$ scalar, which multiplies the $SU(2)_{\mathrm{L}}$ scalar R-component. Thus, (1.99) is $SU(2)_{\mathrm{L}}$-invariant, and the symmetry is preserved, at the Lagrangian level, by such a term. Inserting the vacuum value (1.40) of $\hat{\phi}$ into (1.99), we obtain:

$$\hat{\mathscr{L}}^{\mathrm{e}}_{\mathrm{Yuk}}(\mathrm{vac}) = -g_{\mathrm{e}} \frac{v}{\sqrt{2}} \left(\hat{\bar{e}}_{\mathrm{L}} \hat{e}_{\mathrm{R}} + \hat{\bar{e}}_{\mathrm{R}} \hat{e}_{\mathrm{L}} \right) \tag{1.100}$$

which is exactly a (Dirac) mass term of the form (1.97), allowing us to make the identification:

$$m_{\mathrm{e}} = g_{\mathrm{e}} \frac{v}{\sqrt{2}}. \tag{1.101}$$

Thus, the mass terms for the electron — in general for fermions — are proportional to the Yukawa couplings. When oscillation about the vacuum are considered via the replacement (1.44), the term (1.99) will generate a coupling between the electron and the Higgs field of the form:

$$\begin{aligned} -g_{\mathrm{e}} \hat{\bar{e}} \hat{e} \hat{H} / \sqrt{2} &= -(m_{\mathrm{e}}/v) \hat{\bar{e}} \hat{e} \hat{H} \\ &= -(g m_{\mathrm{e}} / 2 M_{\mathrm{W}}) \hat{\bar{e}} \hat{e} \hat{H} \end{aligned} \tag{1.102}$$

and so the Higgs boson couplings to fermions is given by:

$$g_{\mathrm{H}ff} = \mathrm{i} \frac{m_f}{v} \tag{1.103}$$

ensuring again the unitarity of the theory. The proportionality of the interaction strength to the fermion mass is then a prediction of the theory. At first sight it might seem that this stratagem will only work for the $T^3_{\mathrm{W}} = -\frac{1}{2}$ components of the doublets, because of the form of $\langle 0 | \hat{\phi} | 0 \rangle$. According to the group theory, the $SU(2)$ group is unitarily self-conjugate (Cahn, 1984; Carruthers, 1966): if Ψ is an $SU(2)$ doublet, then the charge conjugate state

$\mathrm{i}\tau_2\Psi^*$ tasforms in exactly the same way under $SU(2)$. Thus, if, in our case, $\hat{\phi}$ is the $SU(2)$ doublet, then the charge conjugate field

$$\hat{\phi}_{\mathbf{C}} \equiv \mathrm{i}\tau_2\hat{\phi}^* = \begin{pmatrix} \frac{1}{\sqrt{2}}(\hat{\phi}_3 + \mathrm{i}\hat{\phi}_4) \\ -\frac{1}{\sqrt{2}}(\hat{\phi}_1 + \mathrm{i}\hat{\phi}_2) \end{pmatrix} \tag{1.104}$$

is also an $SU(2)$ doublet, transforming in just the same way as $\hat{\phi}$. Note that the vacuum value (1.40) will now appear in the upper components of (1.104). With the help of $\hat{\phi}_{\mathbf{C}}$ we can write down another $SU(2)$-invariant coupling in the ν_{e}-e sector:

$$-\, g_{\nu_{\mathrm{e}}} \left(\hat{\bar{L}}_{\mathrm{e}} \hat{\phi}_{\mathbf{C}} \hat{\nu}_{\mathrm{eR}} + \hat{\bar{\nu}}_{\mathrm{eR}} \hat{\phi}^{\dagger}_{\mathbf{C}} \hat{L}_{\mathrm{e}} \right) \tag{1.105}$$

assuming now the existence of the field $\hat{\nu}_{\mathrm{eR}}$. In the Higgs vacuum (1.40), (1.105) then yields:

$$-\, (g_{\nu_{\mathrm{e}}} v/\sqrt{2}) \left(\hat{\bar{\nu}}_{\mathrm{eL}} \hat{\nu}_{\mathrm{eR}} + \hat{\bar{\nu}}_{\mathrm{eR}} \hat{\nu}_{\mathrm{eL}} \right) \tag{1.106}$$

which is precisely a (Dirac) mass for the neutrino, if we set $m_{\nu_{\mathrm{e}}} = g_{\nu_{\mathrm{e}}} v/\sqrt{2}$. We can then arrange for all the fermions, quarks as well as leptons, to acquire a mass by the same 'mechanism'. However, since the couplings are arbitrary, the fermion masses are non calculable parameters of the Standard Model. Besides, there is a certain uneasiness concerning the enormous difference in magnitudes represented by the couplings $g_{\nu_{\mathrm{e}}}, \ldots, g_{\mathrm{e}}, \ldots, g_{\mathrm{t}}$. If $m_{\nu_{\mathrm{e}}} < 1$ eV, then $g_{\nu_{\mathrm{e}}} < 10^{-11}$, while $g_{\mathrm{t}} \sim 1$. Thus, it seems unsatisfactory simply to postulate a different g for each fermion-Higgs interaction. This indicates that we are dealing here with a 'phenomenological model' rather than a 'theory'.

As far as quarks are concerned, there is no *a priori* requirement for the (renormalizable) Yukawa coupling to be diagonal in the weak interaction family index i. The allowed generalization of (1.99) and (1.105) is, therefore, an interaction of the form (summing on repeated indices):

$$\hat{\mathscr{L}}_{\psi\phi} = a_{ij} \hat{\bar{q}}_{\mathrm{L}i} \hat{\phi}_{\mathbf{C}} \hat{u}_{\mathrm{R}j} + b_{ij} \hat{\bar{q}}_{\mathrm{L}i} \hat{\phi} \hat{d}_{\mathrm{R}j} + \mathrm{h.c.} \tag{1.107}$$

where h.c. stands for 'Hermitian conjugate',

$$\hat{q}_{\mathrm{L}i} = \begin{pmatrix} \hat{u}_{\mathrm{L}i} \\ \hat{d}_{\mathrm{L}i} \end{pmatrix}. \tag{1.108}$$

After symmetry breaking, using the gauge (1.44), we find that:

$$\hat{\mathscr{L}}_{f\phi} = -\left(1 + \frac{\hat{H}}{v}\right) [\hat{\bar{u}}_{\mathrm{L}i} m^{\mathrm{u}}_{ij} \hat{u}_{\mathrm{R}j} + \hat{\bar{d}}_{\mathrm{L}i} m^{\mathrm{d}}_{ij} \hat{d}_{\mathrm{R}j} + \mathrm{h.c.}] \tag{1.109}$$

where the 'mass matrices' are:

$$m^{\rm u}_{ij} = -\frac{v}{\sqrt{2}} a_{ij}, \qquad m^{\rm d}_{ij} = -\frac{v}{\sqrt{2}} b_{ij}. \tag{1.110}$$

The $m^{\rm u}$ and $m^{\rm d}$ matrices could involve a γ^5 part as well as a '1' part in Dirac space. It can be shown (Feinberg et al., 1959; Weinberg, 1973) that $m^{\rm u}$ and $m^{\rm d}$ can be made both Hermitian, γ^5-free and diagonal by making four separate unitary transformations on the 'family triplets':

$$\hat{u}_{\rm L} = \begin{pmatrix} \hat{u}_{\rm L1} \\ \hat{u}_{\rm L2} \\ \hat{u}_{\rm L3} \end{pmatrix}, \qquad \hat{d}_{\rm L} = \begin{pmatrix} \hat{d}_{\rm L1} \\ \hat{d}_{\rm L2} \\ \hat{d}_{\rm L3} \end{pmatrix}, \qquad \text{etc} \tag{1.111}$$

via

$$\hat{u}_{{\rm L}\alpha} = (U^{\rm (u)}_{\rm L})_{\alpha i} \hat{u}_{{\rm L}i} \qquad \hat{u}_{{\rm R}\alpha} = (U^{\rm (u)}_{\rm R})_{\alpha i} \hat{u}_{{\rm R}i} \tag{1.112}$$

$$\hat{d}_{{\rm L}\alpha} = (U^{\rm (d)}_{\rm L})_{\alpha i} \hat{d}_{{\rm L}i} \qquad \hat{d}_{{\rm R}\alpha} = (U^{\rm (d)}_{\rm R})_{\alpha i} \hat{d}_{{\rm R}i}. \tag{1.113}$$

In this notation, 'α' is the index of the 'mass diagonal' basis and 'i' is that of the 'weak interaction' basis[3]. Then (1.109) becomes:

$$\hat{\mathscr{L}}_{q\phi} = -\left(1 + \frac{\hat{H}}{v}\right) [m_{\rm u} \hat{\bar{u}} \hat{u} + \ldots + m_{\rm b} \hat{\bar{b}} \hat{b}]. \tag{1.114}$$

The Higgs field couples to each fermion with a strength proportional to the mass of the fermion, divided by $M_{\rm W}$.

To ensure that the neutral current interactions do not change the flavour of the physical (mass eigenstates) quarks, the U in (1.112) matrices must be unitary. The CKM matrix is then obtained from these U matrices through the relation:

$$V_{\alpha\beta} = [U^{\rm (u)}_{\rm L} U^{\rm (d)\dagger}_{\rm L}]_{\alpha\beta}. \tag{1.115}$$

Thus, the CKM matrix is not diagonal, though it is unitary.

1.4 The Higgs Sector

As we have seen, in the SM, the electroweak interactions are described by a gauge field theory based on the $SU(2)_{\rm L} \otimes U(1)_{\rm Y}$ symmetry group. The Higgs mechanism posits a self-interacting complex doublet of scalar fields,

[3] For example, $\hat{u}_{{\rm L}\alpha={\rm t}} = \hat{t}_{\rm L}$, $\hat{d}_{{\rm L}\alpha={\rm s}} = \hat{s}_{\rm L}$, etc.

and renormalizable interactions are arranged such that the neutral component of the scalar doublet acquires a vev which sets the scale of elecroweak symmetry breaking (EWSB). Three massless Goldstone bosons are generated, which are absorbed to give masses to the $W^{\pm}$ and Z gauge bosons. The remaining component of the complex doublet becomes the Higgs boson — a new fundamental scalar particle. The masses of all fermions are also a consequence of EWSB since the Higgs doublet is postulated to couple to the fermions through Yukawa interactions. The Higgs boson mass is given by $m_{\mathrm{H}} = \sqrt{\lambda/2}v$, where λ is the Higgs self-coupling parameter and v is the vacuum expectation value of the Higgs field, $v = (\sqrt{2}G_{\mathrm{F}})^{-1/2} = 246$ GeV, fixed empirically by the Fermi coupling G_{F}. Since λ is presently unknown, the value of the SM Higgs boson mass m_{H} cannot be predicted. The SM Higgs couplings to fundamental fermions are proportional to the fermion masses, and the couplings to bosons are proportional to the squares of the boson masses. In particular, the SM Higgs boson is a CP-even scalar, and its couplings to fermions, gauge bosons and Higgs bosons are given by (Djouadi, 2005):

$$g_{\mathrm{H}f\bar{f}} = \frac{m_f}{v}; \tag{1.116}$$

$$g_{\mathrm{H}VV} = \frac{2m_V^2}{v}, \qquad g_{\mathrm{HH}VV} = \frac{2m_V^2}{v^2}; \tag{1.117}$$

$$g_{\mathrm{HHH}} = \frac{3m_{\mathrm{H}}^2}{v}, \qquad g_{\mathrm{HHHH}} = \frac{3m_{\mathrm{H}}^2}{v^2}. \tag{1.118}$$

where $V = \mathrm{W}^{\pm}$, Z (see also Figure 1.3).

Both theoretical and experimental constraints however exist, including those from direct search at colliders and in particular at LEP (Alcaraz et al., 2006, 2007; Grunewald, 2007).

1.4.1 Theoretical constraints on the Higgs mass

Theoretical constraints can be derived by imposing the energy range in which the Standard Model shall be valid before perturbation theory breaks down and new phenomena emerge. These include constraints from unitarity in scattering amplitude, perturbativity of the Higgs self coupling, stability of the electroweak vacuum and fine tuning (Yao et al., 2006).

The tighter theoretical constraints come from one loop matching conditions relating the particle couplings to their masses (Kane, 1997). Besides the upper bound on the Higgs mass from unitarity constraints (Cornwall et al., 1973, 1974; Lee et al., 1977; Llewellyn Smith, 1974), additional theoretical arguments place upper and lower bounds on m_{H} (Altarelli and Isidori, 1994;

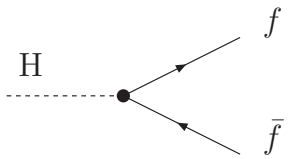

$$g_{\mathrm{H}ff} = m_f/v = (\sqrt{2}G_{\mathrm{F}})^{1/2} m_f \qquad \times \text{ (i)}$$

(a)

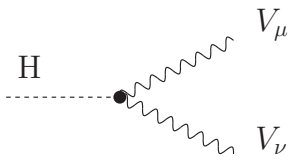

$$g_{\mathrm{H}VV} = 2M_V^2/v = 2(\sqrt{2}G_{\mathrm{F}})^{1/2} M_V^2 \qquad \times (\mathrm{i}g_{\mu\nu})$$

(b)

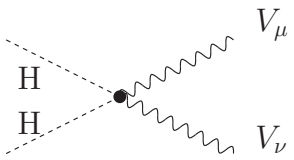

$$g_{\mathrm{HH}VV} = 2M_V^2/v^2 = 2\sqrt{2}G_{\mathrm{F}} M_V^2 \qquad \times (\mathrm{i}g_{\mu\nu})$$

(c)

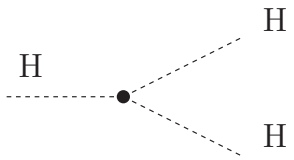

$$g_{\mathrm{HHH}} = 3m_{\mathrm{H}}^2/v = 3(\sqrt{2}G_{\mathrm{F}})^{1/2} m_{\mathrm{H}}^2 \qquad \times \text{ (i)}$$

(d)

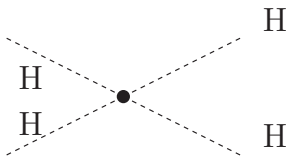

$$g_{\mathrm{HHHH}} = 3m_{\mathrm{H}}^2/v^2 = 3\sqrt{2}G_{\mathrm{F}} m_{\mathrm{H}}^2 \qquad \times \text{ (i)}$$

(e)

Figure 1.3: The Higgs boson couplings to (a) fermions and (b), (c) gauge bosons and (d), (e) the Higgs self-couplings in the SM. The normalization factors of the Feynman rules are also displayed (Djouadi, 2005).

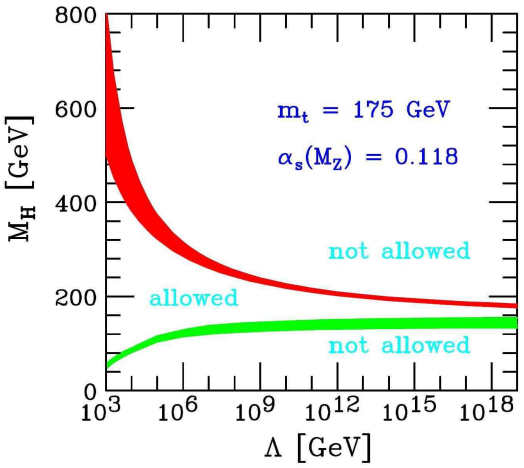

Figure 1.4: The triviality (upper) bound and the vacuum stability (lower) bound on the Higgs boson mass as a function of the new physics or cut-off scale Λ for a top quark mass $m_t = 175 \pm 6$ GeV/c^2 and $\alpha_s(M_Z) = 0.118 \pm 0.002$; the allowed region lies between the bands and the coloured/shaded bands illustrate the impact of various uncertainties (Djouadi, 2005; Hambye and Riesselmann, 1997).

Cabibbo et al., 1979; Casas et al., 1995, 1996; Hambye and Riesselmann, 1997). There is an upper bound based on the perturbativity of the theory up to the scale Λ at which the SM breaks down, and a lower bound derived from the stability of the Higgs potential. If m_H is too large, then the Higgs self-coupling diverges at some scale Λ below the Planck scale $M_{Pl} \sim 10^{19}$ GeV. If m_H is too small, then the Higgs potential develops a second (global) minimum at a large value of the scalar field of order Λ. New physics must enter at a scale Λ or below, so that the global minimum of the theory corresponds to the observed $SU(2)_L \otimes U(1)_Y$ broken vacuum with $v = 246$ GeV. Given a value of Λ, one can compute the minimum and the maximum allowed Higgs boson mass. Conversely, the value of m_H itself can provide an important constraint on the scale up to which the SM remains sucessful as an effective theory.

The allowed upper and lower limits as a function of the cutoff parameter Λ at which the Standard Model is replaced by a higher energy theory are shown in Figure 1.4. The upper limit is obtained requiring that the quartic coupling of Higgs potential remain finite (*triviality*). The lower line limits the region in which the quartic coupling becomes negative and the potential is unbounded from below (*vacuum stability*). The allowed region lies between the two bands which illustrate the theoretical uncertainties. In particular, a Higgs boson with mass in the range $130 \text{ GeV/c}^2 \lesssim m_H \lesssim 180 \text{ GeV/c}^2$ is

consistent with an effective SM description that survives all the way to the Planck scale, although the hierarchy problem between the electroweak scale and $\Lambda = M_{\mathrm{Pl}}$ still persists. The lower bound on m_{H} can be reduced to about 115 GeV/c^2 (Espinosa and Quiros, 1995; Isidori et al., 2001), if one allows for the electroweak vacuum to be metastable, with a lifetime greater than the age of the universe. Conversely, a possible discovery of the Standard Model Higgs boson outside this mass range would be a hint of the presence of a new theory above a certain energy scale.

1.4.2 Experimental constraints on the Higgs mass

Experimental limits on the Higgs mass come both from direct and indirect searches. The existence of the Standard Model Higgs particle has an impact on the value of most electroweak parameters via higher order corrections, which present a logarithmic sensitivity to the Higgs mass (Alcaraz et al., 2006, 2007). The best constraint to the Higgs mass is given by a global fit of all the available electroweak data: all the precision electroweak results obtained by the four LEP experiments (ALEPH, DELPHI, L3 and OPAL) and by other experiments (SLD results at Z peak and top quark mass from CDF and D0 at Tevatron), such as cross sections, masses and various couplings of the heavy electroweak gauge bosons, have been combined together assuming the Standard Model to be the correct theory of nature. The results, updated to July 2008, are reported in Figure 1.5 and the $\Delta\chi^2$ of the fit to all measurements as a function of m_{H}, with the uncertainties on $\Delta\alpha^{(5)}_{\mathrm{had}}(M^2_{\mathrm{Z}})$, $\alpha(M_{\mathrm{Z}})$, $\alpha_{\mathrm{s}}(M_{\mathrm{Z}})$, m_{t} as well as on M_{Z} is shown in Figure 1.6. Among the experimental inputs for the global fit, the W mass has a large impact. The top quark mass also enters the fit as a parameter. The one loop corrections to electroweak parameters have at most logarithmic dependence on m_{H}, as stated by the screening theorem: this explains why the $\Delta\chi^2$ is quadratic with respect to $\log m_{\mathrm{H}}$.

While this is not a proof that the SM Higgs boson actually exists, it does serve as a guideline in what mass range to look for it. Precise electroweak measurements tell us that the mass of the SM Higgs boson is lower than about 160 GeV/c^2 (one-sided 95 percent confidence level upper limit derived from $\Delta\chi^2 = 2.7$ for the blue band, thus including both the experimental and the theoretical uncertainty). This limit increases to 190 GeV/c^2 when including the LEP-2 direct search limit of 114 GeV/c^2 (discussed in the following) shown in yellow. This result is obviously model-dependent, being calculated from loop corrections, that could be circumvented by some new physics contributions. This result is well-grounded only within the Standard Model theory and has always to be confirmed by the direct observation of

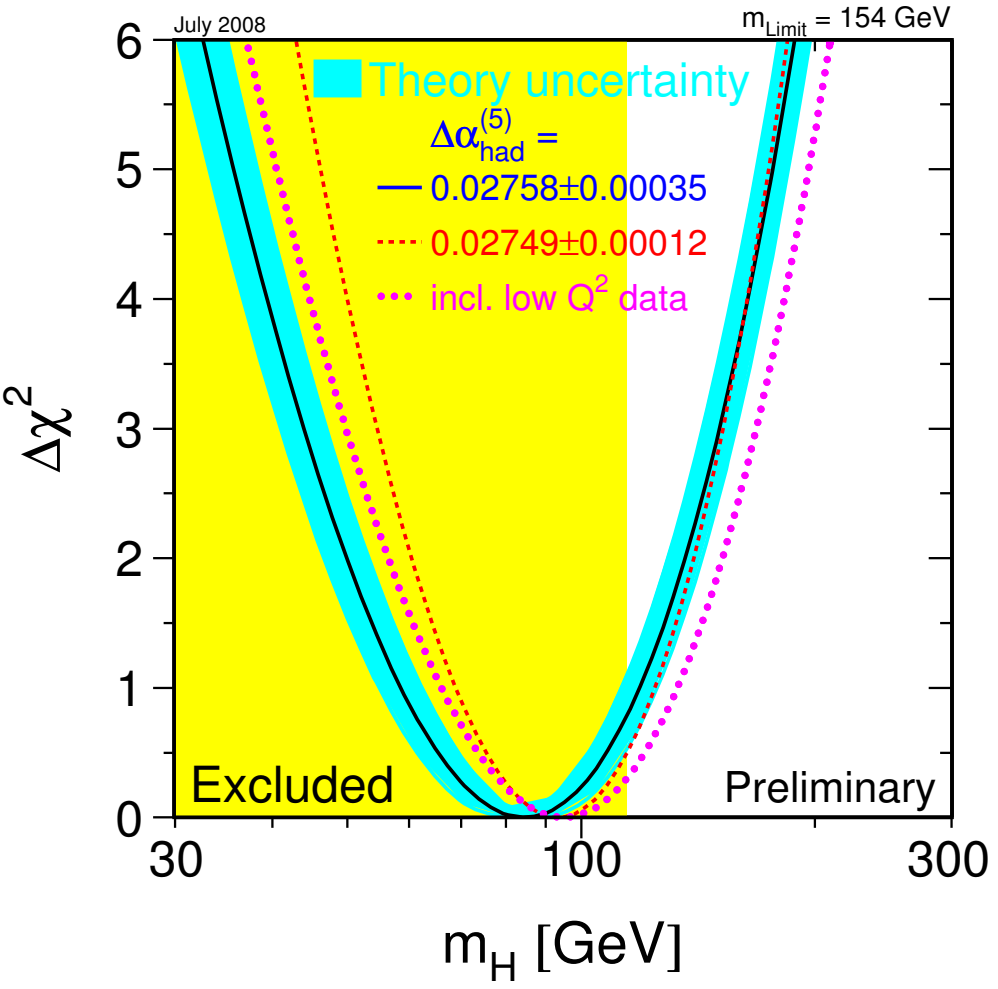

Figure 1.5: $\Delta\chi^2 = \chi^2 - \chi^2_{\rm min}$ curve derived from high-Q^2 precision electroweak measurements, performed at LEP and by SLD, CDF, and D0, as a function of the Higgs-boson mass, assuming the Standard Model to be the correct theory of nature. The line is the result of the fit using all high-Q^2 data; the band represents an estimate of the theoretical error due to missing higher order corrections. The vertical band shows the 95% CL exclusion limit on $m_{\rm H}$ from the direct search. The dashed curve is the result obtained using the evaluation of the contribution of light quarks to the photon vacuum polarization $\Delta\alpha^{(5)}_{\rm had}(M_{\rm Z}^2)$ from (de Trocóniz and Ynduráin, 2002). The dotted curve is the result obatined including also the low-Q^2 data (Alcaraz et al., 2007).

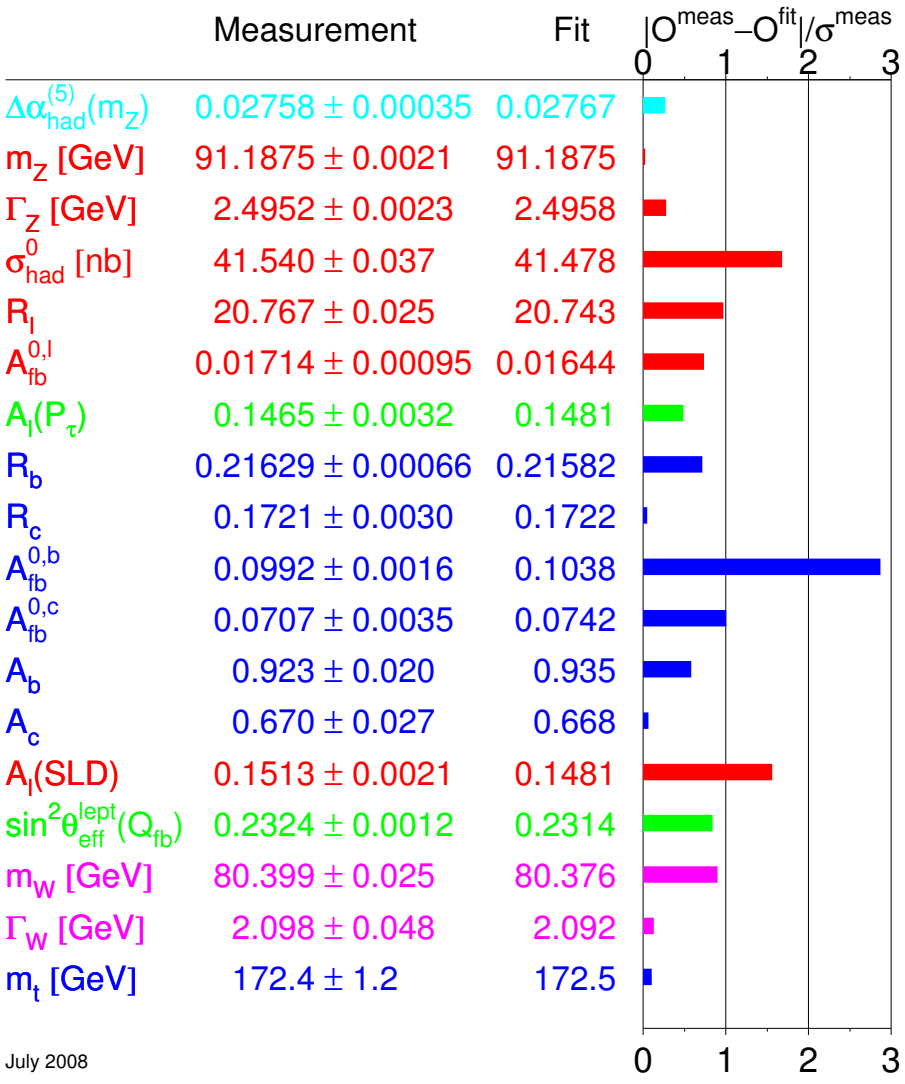

Figure 1.6: Summary of electroweak precision measurements at LEP, SLC and the Tevatron (Alcaraz et al., 2006). The Standard Model fit results and the residuals are also shown.

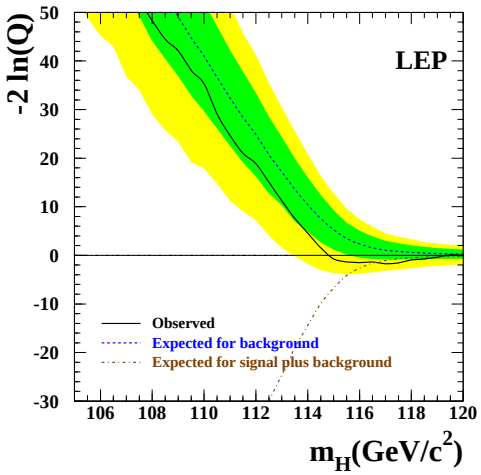

Figure 1.7: Observed and expected behaviour of the test statistics $-2\ln Q$ as a function of the Higgs mass. Q is the ratio between the signal plus background likelihood and the background only likelihood. The result is the combination of the data collected by the four LEP experiments. The solid line is the observed curve, the dashed curve is the median background expectation and the dash-dotted curve is the expectation in the signal plus background hypothesis. The dark and the light shaded bands represent the 68% and 95% probability bounds around the median background expectation. The expected curves and the associated uncertainty bands have been obtained by replacing data by Monte Carlo generated events in a large number of toy experiments (Abbiendi et al., 2003).

the Higgs boson, while a heavier Higgs can enter theories which extend the model.

Of course, the Higgs boson is also searched for directly. Only the direct observation of the Higgs boson constitutes a proof of its existence. The direct searches of the Higgs boson did not show any evidence up to now. The strongest limit comes from the combined results of the four LEP experiments (Abbiendi et al., 2003). The data collected by the four experiments have been examined in a likelihood test for their consistency with the background only hypothesis and the signal plus background hypothesis. The final result, shown in Figure 1.7, gives $m_{\mathrm{H}} > 114.4$ GeV/c^2 as a lower limit on the SM Higgs boson mass at the 95% confidence level.

CHAPTER 2

THE CMS EXPERIMENT AT LHC

As it was discussed in the previous chapter, the Standard Model is not able to answer all the many questions which raise in particle physics, the most burning ones being the problem of the origin of the mass and the possible presence of new physics beyond the Standard Model. This is the main reason which led to the project of a new particle accelerator, the Large Hadron Collider, built at CERN, which will start its operations in July 2008. The Large Hadron Collider (LHC) will collide protons at the design centre of mass energy $\sqrt{s} = 14$ TeV with a design luminosity $\mathscr{L} = 10^{34}\,\mathrm{cm}^{-2}\,\mathrm{s}^{-1}$. The experiments which will take data at LHC will exploit its unique characteristics to cover a wide physics program ranging from the problem of the origin of the mass to the search for new physics beyond the Standard Model. In this chapter, we briefly describe the LHC accelerator and the CMS detector.

2.1 The Large Hadron Collider

The Large Hadron Collider (LHC) is a 27 km circumference particle accelerator sited about 100 m depth underground, inside the already existing LEP tunnel, across the Swiss-French border (The LHC Project, 2004a,b,c). LHC has two counter-rotating proton beams each with an energy of 7 TeV giving a total collision energy ($\sqrt{s}$) of 14 TeV and it is composed by eight curvilinear sections and eight rectilinear sections, where the beams may collide.

Four detectors will be installed in the caverns around the collision points, which are shown in Figure 2.1. Two of them are multipurpose experiments, ATLAS (The ATLAS Collaboration, 1994) and CMS (The CMS Collabo-

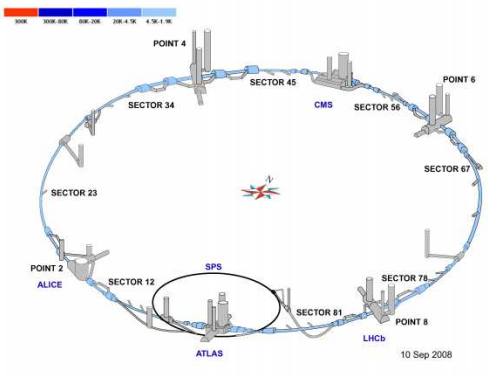

Figure 2.1: The LHC tunnel. The interaction points where the four experiments are installed are also shown. The magnet temperature at the startup is also plotted.

ration, 1994), the other two are dedicated experiments, one to heavy ion physics, ALICE (The ALICE Collaboration, 1995), and the other to B-physics and precision measurements of CP violation, LHCb (The LHCb Collaboration, 1998). The LHC will take advantage of the existing accelerator complex at CERN to create the proton beams and accelerate them. Proton-proton collisions, with a center-of-mass energy $\sqrt{s} = 10$ TeV will start next spring. Heavy ions will be also accelerated up to total energy of 2.76 TeV/nucleon in Pb-Pb collisions. LHC can be seen as a discovery machine with a dynamic range of discovery from energy scales from 5 GeV/c^2, as in the case of B-physics, to a few TeV/c^2, for the discovery of new vector bosons or quark compositeness.

To extend the reach of new physics to as high mass scales as possible and to increase the production cross section of the processes of interest it is important to increase the centre of mass energy as much as possible. However high energy beams need high magnetic bending fields.

The maximum achievable energy at LHC is constrained by the magnetic field B needed to keep beams circulating

$$B = \frac{p}{0.3\rho} \tag{2.1}$$

where p is the particle momentum and ρ is the radius orbit. The requirement that LHC has to fit inside the existing LEP tunnel fixes $\rho = 4.3$ km, therefore, if $p = 7$ TeV/c, from (2.1) $B = 5.4$ T is obtained. However in the LHC tunnel protons are not bent continuously, but the 1232 superconducting magnets act only in the eight curvilinear segments, so they are forced to work at 8.3 T, the highest operational magnetic field for affordable superconducting

magnets. LHC magnet coils, made of copper-clad niobium-titanium cables, are 14 metres long, and will operate at 1.9 K, so they are kept cold with superfluid He.

With the beam energy limited, another way to increase the rate of events with interesting physics is to raise the luminosity. The event rate of a specific process is given by:

$$n_{\text{event}} = \sigma_{\text{event}} \mathscr{L} \tag{2.2}$$

where $\mathscr{L}$ is the luminosity and σ_{event} is the cross section of the process. The luminosity for a p p collider, assuming equal beam parameters for both circulating beams, depends only on the beam parameters and can be written for a Gaussian beam distribution as:

$$\mathscr{L} = \frac{N_{\text{b}}^2 n_{\text{b}} f_{\text{rev}} \gamma_{\text{r}}}{4\pi \epsilon_{\text{n}} \beta^*} F \tag{2.3}$$

where N_{b} is the number of protons in each bunch, n_{b} the number of bunches per beam, f_{rev} the revolution frequency, γ the relativistic Lorentz factor, ϵ_{n} the normalized transverse beam emittance, β^* the beta function at the collision point and F the geometric luminosity reduction factor due to the crossing angle at the IP:

$$F = 1/\sqrt{1 + \left(\frac{\theta_{\text{c}} \sigma_z}{2\sigma^*}\right)^2} \tag{2.4}$$

where θ_{c} is the full crossing angle at the interaction point (IP), σ_z the RMS bunch length and σ^* the transverse RMS beam size at the IP. The exploration of rare events in the LHC collisions therefore requires both high beam energies and high beam intensities. The time between the bunches is limited by the requirement that there should be no additional interactions on each side of the interaction region. For the LHC the bunch crossing time will be 25 ns corresponding to a bunch separation of 7.5 m. The transverse dimensions of the beam at the interaction point can be squeezed down to 15 μm. To be able to fill new bunches into the LHC and operate the beam dump it is necessary to order the proton bunches in trains followed by some empty bunches. In total 2808 of the 3557 available spaces with 25 ns separation will contain protons, corresponding to a fraction of bunch positions actually containing protons $f = 0.80$. The only remaining way to increase the luminosity is to increase the number of protons in each bunch, which is however limited by electromagnetic forces between the colliding bunches. The maximal luminosity achievable will be close to $2 \cdot 10^{34}$ cm^{-2} s^{-1}, but to be in a stable region the nominal luminosity is fixed at 10^{34} cm^{-2} s^{-1}.

Table 2.1: Main technical parameters of LHC (The LHC Project, 2004a).

Parameter	Symbol	Value
Energy per proton	E	7 TeV
Dipole field	B	8.33 T
Design luminosity	$\mathscr{L}$	10^{34} cm^{-2} s^{-1}
Bunch separation		25 ns
Number of bunches	k_{B}	2808
Number of particles per bunch	N_{p}	$1.15 \cdot 10^{11}$
β-value at IP	β^*	0.55 m
RMS beam radius at IP	σ^*	16.7 µm
Luminosity lifetime	τ_{L}	15 h
Number of collisions/crossing	n_{c}	≈ 20

A summary of the main technical features of the LHC collider is provided in Table 2.1.

The number of observed events for a specific process is given as:

$$n_{\mathrm{event}} = L \cdot \sigma_{\mathrm{event}} \cdot \epsilon \tag{2.5}$$

where σ_{event} is the cross section of the process, ϵ the detection efficiency and L the integrated luminosity, defined as:

$$L = \int \mathscr{L}\, dt \tag{2.6}$$

i.e. the integral of the luminosity during the effective time the machine is running. A standard year at the LHC is supposed to give a total running time of $t = 10^7$ s. In the start-up period (the first six months of LHC operation) the proton beams will be accelerated up to 5 TeV each, while the instantaneous luminosity should be increased starting from the value of $2 \cdot 10^{26}$ cm^{-2} s^{-1}. In the very first period only 43 equidistant bunches will circulate to perform a deep test of the accelerator. Then the number of bunches and the luminosity will be gradually increased up to $0.5 \cdot 10^{33}$ cm^{-2} s^{-1}. In this first six months an integrated luminosity of 0.4 fb^{-1} of data should be collected to calibrate the detectors with physics samples. After a shut-down of six months due to hardware improvement, LHC should work, in the next three

years, at $\sqrt{s} = 14$ TeV and $\mathscr{L} = 2 \cdot 10^{33}$ cm^{-2} s^{-1}, the so called low luminosity regime. Then luminosity will be finally increased to 10^{34} cm^{-2} s^{-1} for the high luminosity data taking period. If LHC is assumed fully efficient, 20 fb^{-1} per year during the three years at low luminosity for a total of 60 fb^{-1} should be collected. Nominally the period of high luminosity data taking will last at least five years for a total of 500 fb^{-1}. The high requirement on luminosity is the reason for the choice of a proton-proton collider. While a proton-antiproton collider has the advantage that both counter-rotating beams can be kept in the same beam pipe, the production of the large amounts of antiprotons required for the high luminosity is not realistic and would be more expensive than the proton-proton solution with separate beam pipes. The charge asymmetry introduced with a proton-proton collider is not a serious problem for the physics analysis.

The number of simultaneous proton-proton inelastic interactions which take place in each bunch crossing is given by a Poisson distribution with an average of

$$\langle n \rangle = \frac{L \sigma_{\mathrm{tot}}^{\mathrm{pp}} t}{f} \tag{2.7}$$

where t is the time interval between individual bunches and f the fraction of bunch positions actually containing protons.

The proton-proton cross section as a function of the centre of mass energy is shown in Figure 2.2. The upper and lower estimates are also shown. This gives an average of 25 simultaneous interactions (~ 5 at low luminosity) in each event with an expected value of the total proton-proton cross section $\sigma_{\mathrm{tot}}^{\mathrm{pp}} \simeq 80$ mb (diffractive events are also included). Out of all these interactions, those with production of high mass objects such as vector bosons or Higgs particles are often called physics events. The term is misleading since all interactions of course contain physics but the dominating QCD-jet processes with low energy transfer are believed to contain little unknown physics and are thus regarded as background without new physics information. The difference between the total cross section and the cross section of the interesting physics processes is in many cases greater than ten orders of magnitude. The absolute majority of interactions, called *minimum bias* events, are fusion processes of gluons or quarks with a small energy transfer resulting into events with many hadrons of low momentum and nothing else.

Every time a high p_{t} collision occurs, it is then shadowed on average by 25 low p_{t} events which are called *pile-up*. Pile-up is one the critical issues at LHC and has a big impact in the detector design.

Furthermore the detectors have to face the problem of large QCD backgrounds with cross section orders of magnitude larger than those for inter-

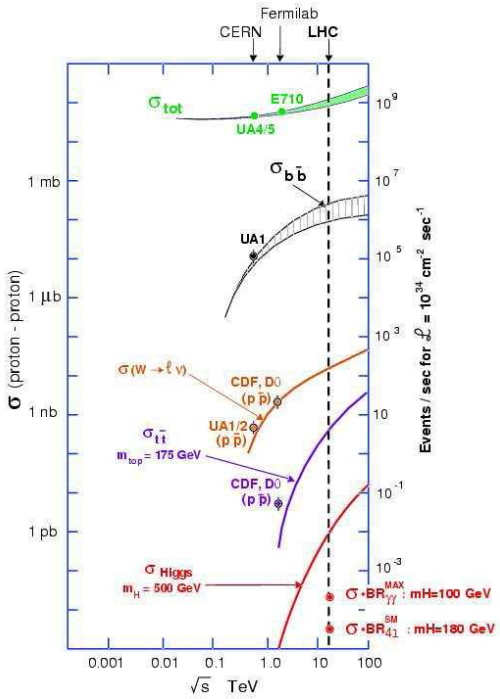

Figure 2.2: Cross sections for different processes in a proton-proton collision as a function of the centre of mass energy.

esting events. Such a difficult environment imposes important requirements on the detector design:

- *fast response*: in order to avoid superpositions between collisions belonging to different bunches (typical response times are $20 \div 50$ ns);
- *fine granularity*: in order to cope with the 20 events and 1000 tracks produced on average per bunch crossing, thus separating the large number of particles, and to minimize the pile-up effects;
- *fast and efficient trigger and data acquisition system*: necessary to manage the high rate of events ($\sim 10^9$ events/s);
- *good radiation resistance* required for all the detector components, due to the high flux of particles, especially in the forward regions.

2.2 The CMS Experiment

CMS (Compact Muon Solenoid) (The CMS Collaboration, 2006) is one of the two general purpose experiments which will tale data at the LHC. Its physics goals range from the search for the Higgs boson to the searches for new physics beyond the Standard Model, to the precision measurements of already known particles and phenomena. To achieve these goals excellent performances in lepton reconstruction and particle identification are necessary. Besides, an optimal hermeticity is required to detect invisible particles through missing energy measurements.

CMS has a several cylindrical layers coaxial to the bean direction (the barrel) closed at both ends by disks which are orthogonal to the beam pipe (the endcaps). The central part of the detector is a 13 m long superconducting solenoid of 6 m diameter, providing a 4 T axial magnetic field.

The overall layout of the detector is shown in Figure 2.3 and the transverse and longitudal views of the barrel region are given in Figure 2.4. A detailed one quarter longitudinal view is plotted in Figure 2.5. The natural coordinate frame to describe the detector is a right handed cartesian system with the x axis pointing toward the centre of the LHC ring, the z axis directed along the beam pipe and the y axis directed upward, as shown in Figure 2.6. Given the cylindrical symmetry of CMS, a convenient coordinate system is given by the triplet (r, ϕ, η), being r the distance from the z axis, ϕ the azimuthal coordinate with respect to the x axis, and $\eta = -\ln(\tan(\theta/2))$ the pseudorapidity, where θ is the polar angle with respect to the z axis.

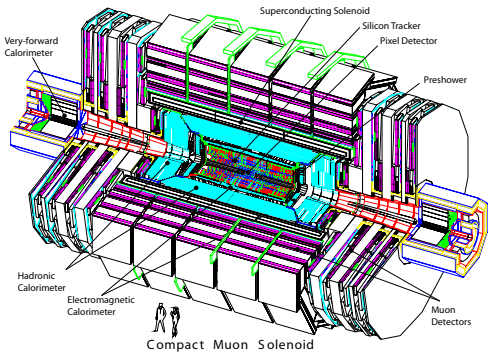

Figure 2.3: An exploded view of the CMS detector.

Another kinematic quantity, frequently used to describe particles in inclusive reactions, is the *rapidity* y, defined as:

$$\begin{aligned} y &= \frac{1}{2}\ln\left(\frac{E+p_z}{E-p_z}\right) \\ &= \tanh^{-1}\left(\frac{p_z}{E}\right) \end{aligned} \tag{2.8}$$

where p_z is the longitudinal momentum along the direction of the colliding particle (i.e. along the z-direction), and E is the energy of the particle. Under a boost in the z-direction to a frame with velocity β, $y \to y' = y - \tanh^{-1}\beta$; thus, differences in rapidity are invariant under a Lorentz boost. For $p \ggg m$, the rapidity, eq. (2.8) may be expanded to obtain

$$\begin{aligned} y &= \frac{1}{2}\ln\frac{\cos^2(\theta/2) + m^2/4p^2 + \ldots}{\sin^2(\theta/2) + m^2/4p^2 + \ldots} \\ &\approx -\ln\tan(\theta/2) \equiv \eta \end{aligned} \tag{2.9}$$

where $\cos\theta = p_z/p$. The pseudorapidity η is approximately equal to the rapidity y for $p \ggg m$, and in any case can be measured when the mass and momentum of the particle is unknown.

CMS consists of different subdetectors. Starting from the beam line there are (see Figure 2.7):

- *the tracker*, to measure the momentum of charged particles in the magnetic field and to identify the interaction vertex and the secondary vertices;
- *the electromagnetic calorimeter* (ECAL), for an accurate measurement of the energy and of the position of photons and electrons;

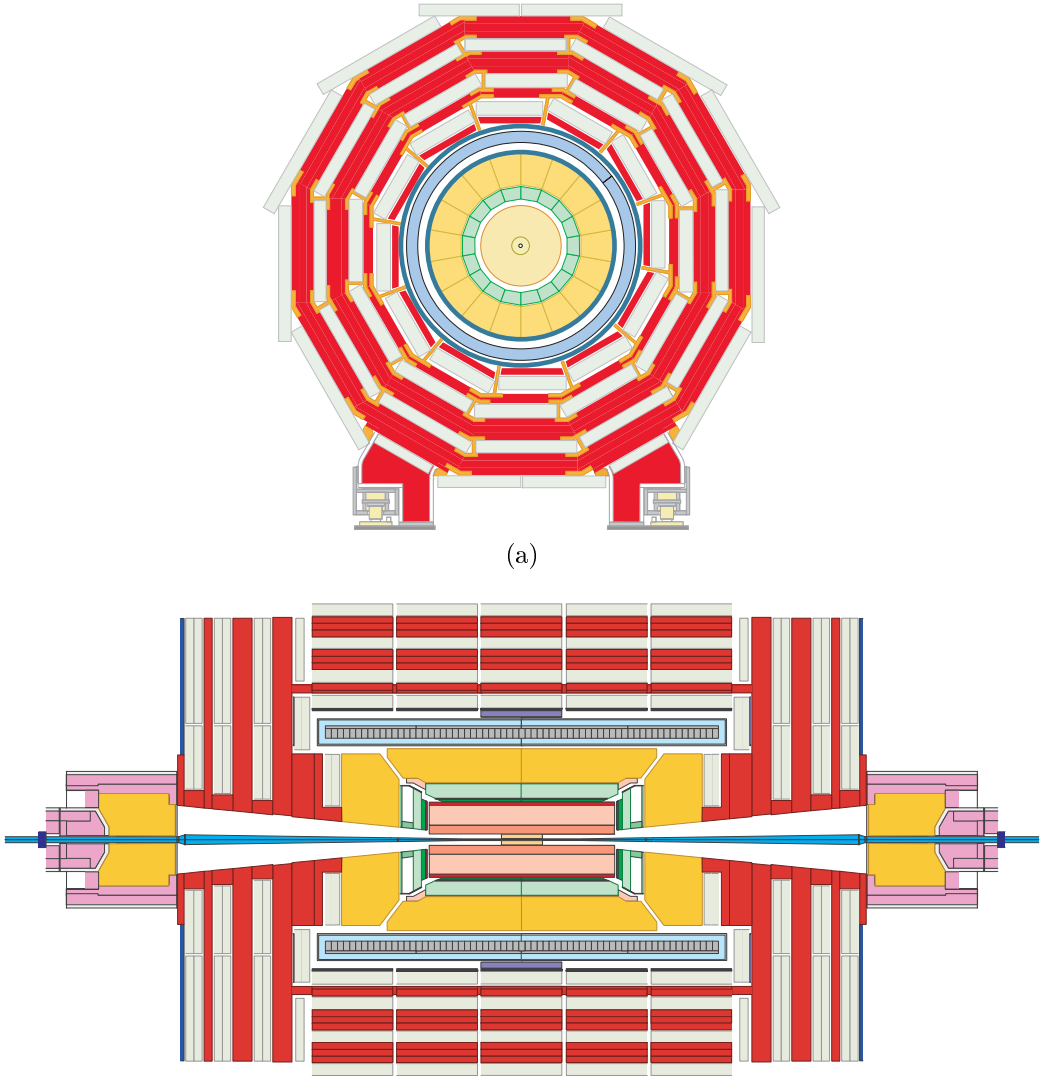

(a)

(b)

Figure 2.4: (a) Cross-sectional and (b) longitudinal views of CMS.

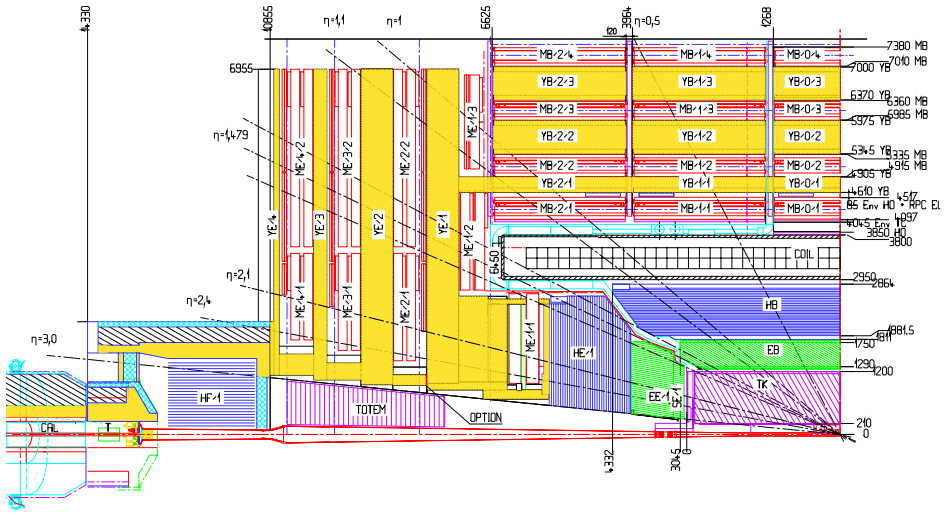

Figure 2.5: One quarter longitudinal view of the CMS Experiment. Dimensions are in units of mm.

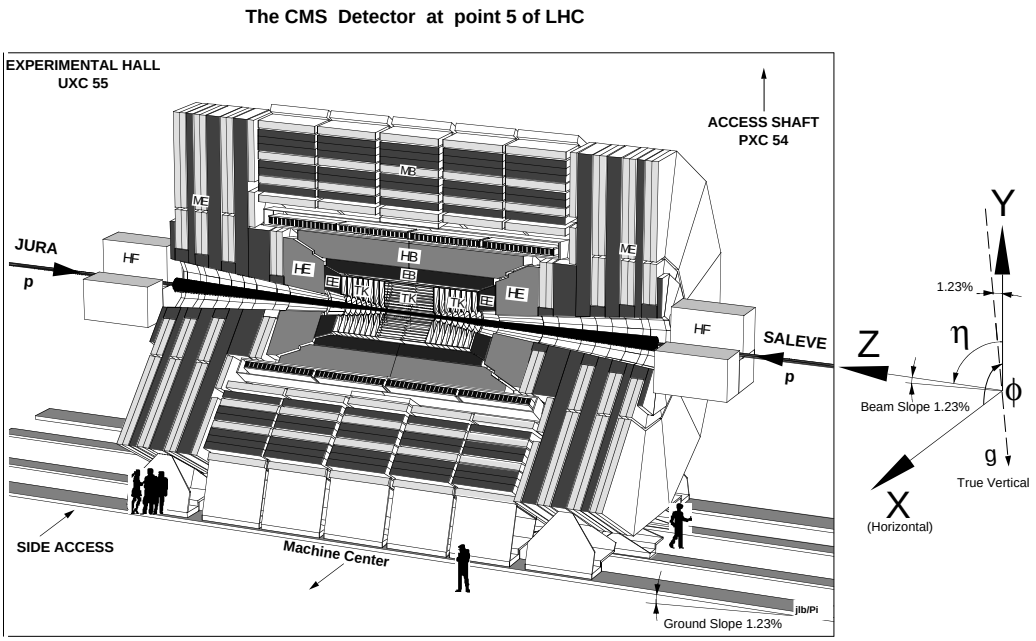

Figure 2.6: Overall view of the CMS detector, showing the coordinate frame.

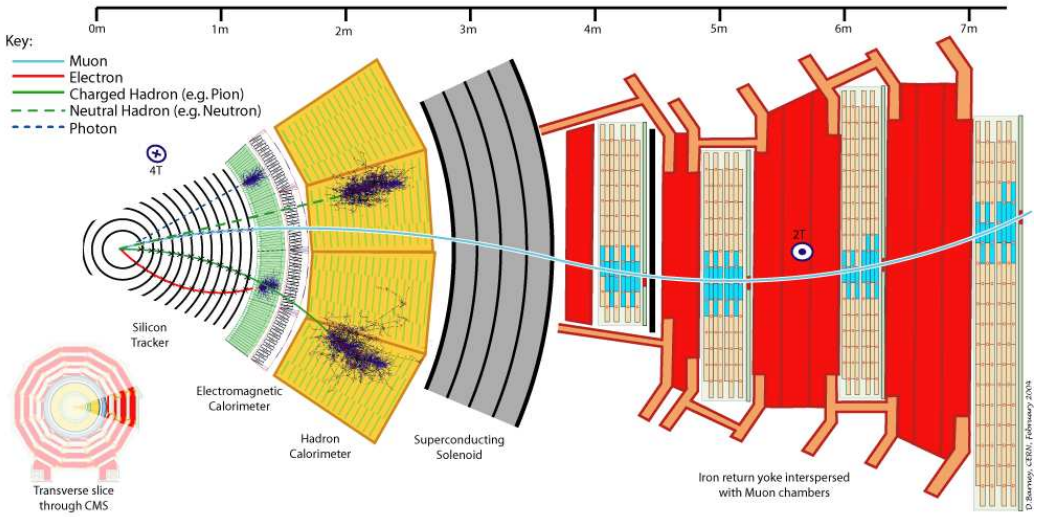

Figure 2.7: Slice through CMS showing particles incident on the different subdetectors.

- *the hadronic calorimeter* (HCAL), to measure the energy of both neutral and charged hadronic particles;
- *the muon system*, to reconstruct the muonic tracks and to measure their momenta from the bending in the magnetic field.

The overall length of the detector is approximately 22 m, its width is 15 m and the total weight is about 12500 t.

2.2.1 The tracker

The tracker, placed within the magnetic field, is the subdetector which is closer to the interaction point. It is dedicated to track and vertex finding. High-p_t charged particles, both isolated and within jets, have to be reconstructed with high efficiency and good momentum resolution; the interaction vertex has to be reconstructed and possible secondary vertices (which can be usefully exploited for jet tagging) have also to be identified.

The silicon technology has been chosen for the whole tracker and different constraints have driven the tracker design. Given the high number of charged tracks which are expected per bunch crossing, the tracker has to provide high granularity and large hit redundancy to perform better the pattern recognition. Severe material budget constraints are imposed by the necessity not to degrade the ECAL performances. Finally, the tracker performances must degrade as least as possible in an environment with high radiation,

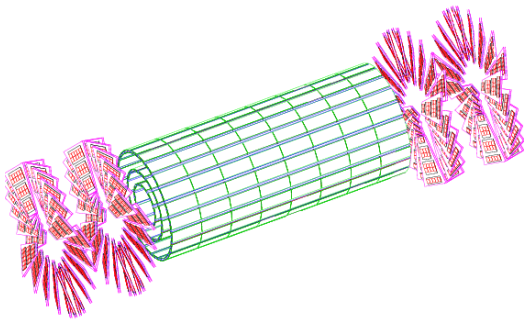

Figure 2.8: The pixel detector. The barrel section and the two disks of the endcaps are visible.

due to the high number of hadrons and back scattered neutrons. Indeed, the irradiation can bring both superficial and bulk damages to the silicon structure. In order to survive for a long time, the tracking system will operate at -10 °C.

The tracker covers the region up to 120 cm in the radial direction and up to $|z| = 270$ cm along the beam. It consists of an inner silicon pixel detector and an outer silicon microstrip system.

The pixel detector

The pixel detector consists of three barrel layers and two endcap disks at each side (Figure 2.8).

The barrel layers, 53 cm long, are positioned at radii of 4.4 cm, 7.3 cm and 10.2 cm. The first layer will be replaced by an outer layer at $r = 13$ cm during the high luminosity phase, to reduce the radiation damage. Each of the endcaps consists of 2 disks with 24 blades arranged in a turbin-like shape, having the inner radius of 6 cm and the outer one of 15 cm. The total area covered with pixels is close to 0.92 m^2.

The inner detector is designed to ensures at least 2 hits for each track having the vertex within $2.2\sigma_z^2$ from the central interaction point in the whole pseudorapidity region $|\eta| < 2.2$. Due to the high density of tracks, a fine granularity is required to assure low occupancy for each cell: 100×150 μm has been chosen. The estimated resolution on the single hit is 10 μm for the (r, θ) coordinate, and 15 μm for z in the barrel, 15 μm and 20 μm respectively in the endcaps.

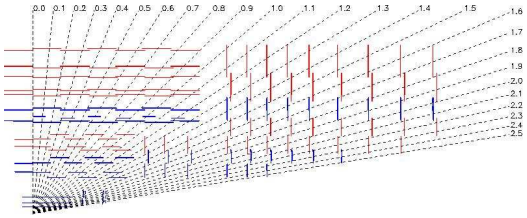

Figure 2.9: Longitudinal view of one quarter of the CMS silicon strip tracking system. The red lines are modules composed of one detector only, the blue lines are detectors composed of two modules.

The silicon strip detector

The silicon strip detector is divided into 2 parts: a TIB (Tracker Inner Barrel) and a TOB (Tracker Outer Barrel). The TIB is made of 4 layers and covers up to $|z| < 65$ cm, using silicon sensors with a thickness of 320 µm and a strip pitch which varies from 80 to 120 µm. The first 2 layers are made with "stereo" modules in order to provide a measurement in both $r - \phi$ and $r - z$ coordinates. A stereo angle of 100 mrad has been chosen. This leads to a single-point resolution of between $23 - 34$ µm in the $r - \phi$ direction and 230 µm in z. The TOB comprises 6 layers with a half-length of $|z| <$ 110 cm. As the radiation levels are smaller in this region, thicker silicon sensors (500 µm) can be used to maintain a good signal-noise ratio for longer strip length and wider pitch. The strip pitch varies from 120 to 180 µm. Also for the TOB the first 2 layers provide a "stereo" measurement in both $r - \phi$ and $r - z$ coordinates. The stereo angle is again 100 mrad and the single-point resolution varies from $35 - 52$ µm in the $r - \phi$ direction and 530 µm in z (Figure 2.9).

The endcaps are divided into the TEC (Tracker End Cap) and TID (Tracker Inner Disks). Each TEC comprises 9 disks that extend into the region 120 cm $< |z| <$ 280 cm, and each TID comprises 3 small disks that fill the gap between the TIB and the TEC. The TEC and TID modules are arranged in rings, centred on the beam line, and have strips that point towards the beam line, therefore having a variable pitch. The first 2 rings of the TID and the innermost 2 rings and the fifth ring of the TEC have "stereo" modules. The thickness of the sensors is 320 µm for the TID and the 3 innermost rings of the TEC and 500 µm for the rest of the TEC.

The entire silicon strip detector consists of almost 15400 modules, which will be mounted on carbon-fibre structures and housed inside a temperature controlled outer support tube. The operating temperature will be around -20 °C.

The performances of the CMS tracker are summarized in Figure 2.10.

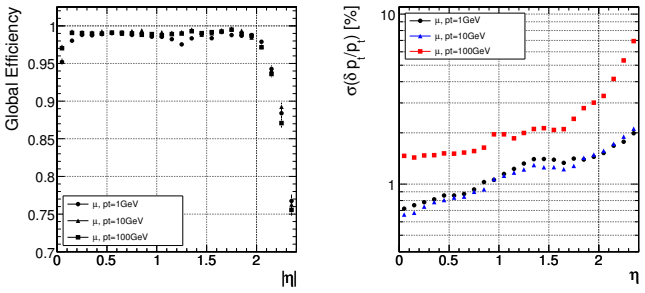

(a) (b)

Figure 2.10: (a) Global efficiency of the tracking algorithm for single muons events as a function of the pseudorapidity ($p_{\mathrm{t}} = 1, 10, 100$ GeV/c); (b) transverse momentum resolution for single muons events as a function of the pseudorapidity ($p_{\mathrm{t}} = 1, 10, 100$ GeV/c).

High energy electrons are reconstructed with efficiency higher than 90%. The reconstruction efficiency for isolated muons with $p_{\mathrm{t}} > 1$ GeV/c is close to 100% in the $|\eta| < 2$ region, and the transverse momentum resolution is better than 3% for $p_t extt \lesssim 100$ GeV/c. The vertex reconstruction can be performed using the pixel detector alone with a spatial resolution between $20 - 70$ μm and efficiency $\sim 95\%$. Such reconstruction is fast enough to be used in the High Level Trigger. The resolution on the vertex position can be improved down to 15 μm by using the information from whole tracking system. This can be usefully exploited in the accurate off-line analysis.

2.2.2 The electromagnetic calorimeter

The main goal of the electromagnetic calorimeter (ECAL) is the precise measurement of the energy of electrons and photons. The design of the ECAL was led by the request imposed by the $\mathrm{H} \rightarrow \gamma\gamma$ channel, which is studied looking for a peak in the photon pair invariant mass distribution. It will be discussed in the next chapter (see section 3.3.1) that in the mass region $m_{\mathrm{H}} < 140$ GeV/c^2 the intrinsic Higgs width is lower than 30 MeV, therefore the invariant mass resolution is dominated by the experimental resolution, which is required to be order of 1%. Besides, an high granularity is necessary, to improve the measurement of the angle between the two photons and to obtain a good π^0/γ separation.

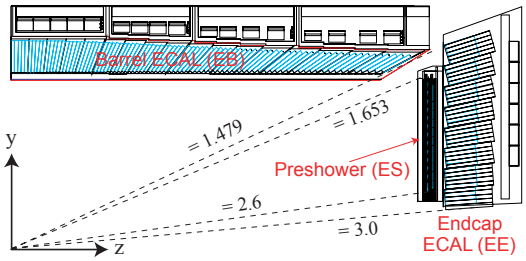

Figure 2.11: Transverse section through the ECAL, showing geometrical configuration.

General structure

An homogeneous calorimeter has been chosen. ECAL consists of almost 76000 Lead Tungstate $PbWO_4$ scintillating crystals divided into a barrel and two endcaps; more precisely, ECAL comprises 61200 $PbWO_4$ crystals mounted in the central barrel part, closed by 7324 crystals in each of the 2 endcaps. A transverse view of the calorimeter is given in Figure 2.11.

The barrel section (EB) has an inner radius of 129 cm. It consists of 36 supermodules, each covering half the barrel length and corresponding to a pseudorapidity interval of $|\eta| < 1.479$. Each supermodule contains 20 crystals in $\phi \times 85$ crystals in η covering an azimuthal arc of 20°. The supermodules are divided along η in 4 modules made of submodules, which are the basic units of the ECAL and which consist of 5×2 crystals each. The geometrical shape of the crystals slightly changes along η and there are 17 types of crystals, with length close to 230 mm and front face area of about 22×22 mm^2. The barrel granularity is $\Delta\phi \times \Delta\eta = 0.0175 \times 0.0175$ the crystals are grouped into 5×5 arrays corresponding to the trigger towers. To avoid that cracks might align with the particles trajectories, the crystal axes are tilted by 3 degrees with respect to the direction from the interaction point, both in ϕ and in η.

The endcaps (EE), at a distance of 314 cm from the vertex, consist of two halves ("Dees") and cover the pseudorapidity region $1.479 < |\eta| < 3$. All the crystals have the same shape ($220 \times 24.7 \times 24.7$ mm^3) and they are grouped in structures of 5×5 crystals called super-crystals. The granularity varies from $\Delta\phi \times \Delta\eta = 0.0175 \times 0.0175$ to $\Delta\phi \times \Delta\eta = 0.05 \times 0.05$. As for the barrel, the crystals have a non pointing geometry. To ensure good hermeticity, an overlap of half crystal between the endcaps and the barrel is obtained by orienting the crystals axis to point 1300 mm beyond the interaction point.

To improve the π^0/γ separation, and the vertex identification, a preshower is designed to cover the region between $|\eta| = 1.6$ and $|\eta| = 2.6$. It consists of two lead converters ($2X_0$ and X_0 thick) followed by silicon strips with a

pitch of less than 2 mm. The strips following the two absorbers are disposed in orthogonal way. The preshower will operate at the temperature of -5 °C.

Different reasons brought to the choice of the $PbWO_4$ as active medium for ECAL:

- Its short radiation length $X_0 = 0.89$ cm and Moliere Radius $R_M = 2.19$ cm allow to build a compact and high granularity calorimeter;
- The fast response ($\sim 80\%$ of the light collected in 25 ns) is comparable with LHC rate;
- $PbWO_4$ has a good intrinsic radiation hardness, which makes it suitable to work in the hard LHC environment.

The main drawback of the $PbWO_4$ crystals is the low light yield ($\sim 80\ \gamma$/MeV), which makes an internal amplification for the photodetectors necessary.

The photodetectors

The low light yield of the $PbWO_4$ makes the use of photodetectors with an intrinsic gain necessary. At the same time, the photodetectors for ECAL have to be radiation hard, fast and able to operate in the strong CMS magnetic field. The devices which match these characteristics and that have been chosen for the electromagnetic calorimeter are the Avalanche PhotoDiodes (APDs) for the barrel and the Vacuum PhotoTriodes (VPTs) for the endcaps. The APDs are silicon detectors. A 5 μm thick p^+ layer acts as photoconverter, the photoelectrons are accelerated and multiplied through the $p-n$ junction and then a n^{++} doped region provides the ohmic contact with the preamplifier. The active area is a 5×5 mm^2 surface. Even if it is quite small, the APDs have a high quantum efficiency ($\sim 75\%$ at 430 nm) which well matches the emission spectrum of the $PbWO_4$; besides, each crystal is equipped with two APDs to increase the acceptance to the scintillation photons.

The APDs affect all the terms of the energy resolution which will be discussed later in the chapter. The statistical fluctuations in the multiplication process influence the stochastic term of the energy resolution. The calorimeter noise is affected by the APD capacitance and by the leakage currents flowing on the surface and in the bulk of the APD. Finally, the sensitivity of the APD gain to the biasing voltage and to the temperature directly influences the constant term in the energy resolution.

The APDs are seriously affected by the radiations. The damage is mainly due to the neutrons which create defects in the silicon increasing the leakage

currents. Since the APDs can ot survive the radiation doses of the end-caps, the technology of the Vacuum PhotoTriodes has been chosen for those regions.

The VPTs are phototubes with a bi-alkali photocathode deposited on a glass window. The electrons emitted from the cathode are accelerated towards a 10 μm thick anode; the fraction of them passing the anode grid impacts on a reflective dynode with a planar geometry and then emits new electrons ($\sim$ 20 secondary electrons are emitted for each impinging electron), which are accelerated back toward the anode. The VPT quantum efficiency is about 15% at the peak of the $PbWO_4$ emission spectrum, but since the active area is $\sim$ 300 mm^2 the total light collection is at the same level as for the APDs. The VPTs operate at gain around 8–10 which is much lower with respect the one of the APDs, but presents very little dependence on the temperature fluctuations and on the biasing voltage. The capacitance is low (few pF), the leakage current is $<$ 2 nA and the excess noise factor around 2.5–3. The VPTs use a radiation hard glass which has been appositely developed and whose transparency is not strongly affected by irradiating particles. Tests have shown that the loss in response can be kept under 10% in ten years of LHC.

The energy resolution

The performance of a supermodule was measured in a test beam. Representative results on the energy resolution as a function of beam energy are shown in Figure 2.12.

The energy resolution, measured by fitting a Gaussian function to the reconstructed energy distributions, has been parameterized as a function of energy:

$$\left(\frac{\sigma_E}{E}\right)^2 = \left(\frac{s}{\sqrt{E}}\right)^2 + \left(\frac{n}{E}\right)^2 + c^2 \qquad (2.10)$$

where s, n and c represent the stochastic, noise and constant term of the energy resolution, respectively. Different effects contribute to each term in eq 2.10; the relative contributions are shown in Figure 2.13.

The stochastic term s includes the contribution of the fluctuations in the number of electrons which are produced and collected. The noise term n includes contributions from the electronic noise, both due to the photodetector and to the preamplifier, and from pile-up events. The contributions change at the different pseudorapidities and with the luminosity of the machine. The constant term c is the dominating term at high energies and it includes many different contributions. Among them, the most important are:

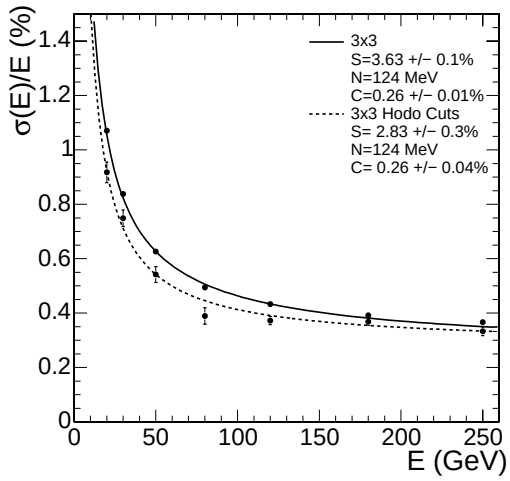

Figure 2.12: ECAL supermodule energy resolution, σ_E/E, as a function of electron energy as measured from a beam test.

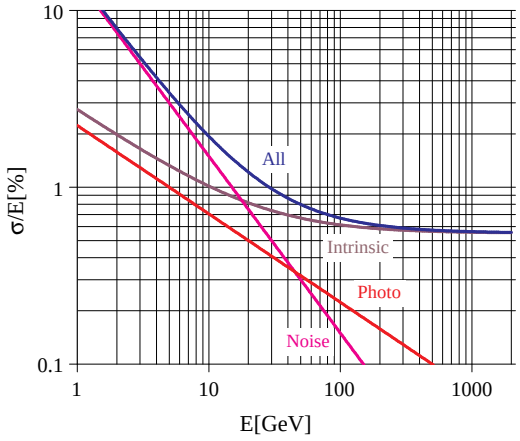

Figure 2.13: The expected ECAL energy resolution versus the energy of the impacting electron. The different contributions are superimposed separately. The term "Intrinsic" includes the shower containment and a constant term (0.55%).

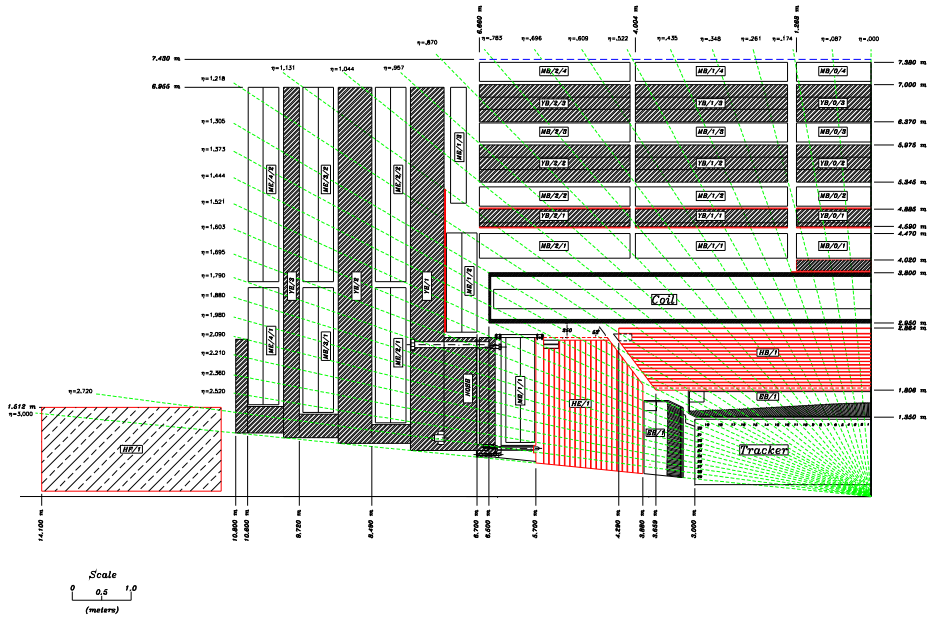

Figure 2.14: One quarter longitudinal view of the HCAL components, labelled in red.

- the stability of the operating conditions, such as the temperature and the high voltage;

- the presence of dead materials between the crystals and the rear and lateral leakage of the electromagnetic shower;

- the longitudinal non uniformity of the crystal light yield: strong focusing effect of the light takes place due to the tronco-pyramidal shape of the crystals and to the high refractive index, so the light collection is not uniform;

- the intercalibration errors;

- the radiation damage of the crystals, which changes their response to a certain amount of deposited energy when exposed to high radiation dose rates.

2.2.3 The hadronic calorimeter

The main goal of the hadron calorimeter HCAL, shown in Figure 2.14, is to contribute to the reconstruction of events which involve both hadrons and invisible particles, by means of jet and missing energy reconstruction. High hermeticity and transverse granularity are necessary, together with a number of hadron interaction lengths sufficient to contain the energetic particles coming from high transverse momentum jets.

The CMS central hadron calorimeter is placed within the magnet. It is a sampling calorimeter with brass layers used as absorbers and plastic scintillators as active medium, while the structural elements are made of stainless steel. The plastic scintillators are divided into tiles which are read out by fibers which act as wavelength shifters. Brass has been chosen as absorber instead of iron because it is easier to machine and it has a 10% shorter hadron interaction length. This is complemented by an additional layer of scintillators, referred to as the hadron outer (HO) detector, lining the outside of the coil.

Hadron barrel

The hadron barrel (HB) part of HCAL consists of 32 towers covering the pseudorapidity region $|\eta| < 1.4$, resulting in 2304 towers with a segmentation $\Delta\phi \times \Delta\eta = 0.0875 \times 0.0875$, which matches the granularity of the ECAL trigger towers and which ensures the required jet separation. The HB is read out as a single longitudinal sampling. There are 15 brass plates, each with a thickness of about 5 cm, plus 2 external stainless steel plates for mechanical strength. Particles leaving the ECAL volume first see a scintillator plate with a thickness of 9 mm rather than 3.7 mm for the other plates. The light collected by the first layer is optimized to be a factor of about 1.5 higher than the other scintillator plates.

Hadron outer

The hadron outer (HO) detector contains scintillators with a thickness of 10 mm, which line the outside of the outer vacuum tank of the coil and cover the region $|\eta| < 1.26$. The tiles sample the energy from penetrating hadron showers leaking through the rear of the calorimeters. They increase the effective thickness of the hadron calorimetry to over 10 interaction lengths, thus reducing the tails in the energy resolution function. The HO also improves the $E_{\mathrm{t}}^{\mathrm{miss}}$ resolution of the calorimeter.

HO is physically located inside the barrel muon system and is hence constrained by the geometry and construction of that system. It is divided

into 5 sections along η, called "rings"-2, -1, 0, 1, and 2. The fixed ring-0 has 2 scintillator layers on either side of an iron absorber with a thickness of about 18 cm, at radial distances of 3.850 m and 4.097 m, respectively. The other mobile rings have single layers at a radial distance of 4.097 m. Each ring covers 2.5 m in z. HO scintillators follow the HCAL barrel tower geometry in η and ϕ.

Hadron endcap

Each hadron endcap (HE) of HCAL consists of 14 η towers with 5° ϕ segmentation, covering the pseudorapidity region $1.3 < |\eta| < 3$, partially overlapping the barrel. For the 5 outermost towers (at smaller η) the ϕ segmentation is 5° and the η segmentation is 0.087. For the 8 innermost towers the η segmentation is 10°, whilst the ϕ segmentation varies from 0.09 to 0.35 at the highest η. The total number of HE towers is 2304.

Hadron forward

To improve the hermeticity, a separate very forward calorimeter is placed outside the magnet yoke. Coverage between pseudorapidities of 3.0 and 5.0 is provided by the steel/quartz fibre Hadron Forward (HF) calorimeter. Since the neutral component of the hadron shower is preferentially sampled in the HF technology, this design leads to narrower and shorter hadronic showers and hence is ideally suited for the congested environment in the forward region. The front face is located at 11 m from the interaction point. The depth of the absorber is 1.65 m. The signal originates from Cerenkov light emitted in the quartz fibres, which is then channeled by the fibres to photomultipliers. The quartz fibres, which run parallel to the beam line, have two different lengths (namely 1.43 m and 1.65 m) which are inserted into grooves, creating 2 effective longitudinal samplings. There are 13 towers in η, all with a size given by $\Delta\eta \approx 0.175$, except for the lowest-η tower with $\Delta\eta \approx 0.1$ and the highest-η tower with $\Delta\eta \approx 0.3$. The ϕ segmentation of all towers is 10°, except for the highest-η one which has $\Delta\eta = 20°$. This leads to 900 towers and 1800 channels in the 2 HF modules.

Performance of the hadron calorimeter

For measuring the performance of the HCAL, it is usual to look at the jet energy resolution and the missing transverse energy resolution. The granularity of the sampling in the 3 parts of the HCAL has been chosen such that the jet energy resolution, as a function of E_t, is similar in all 3 parts. This is illustrated in Figure 2.15. The resolution of the missing transverse energy

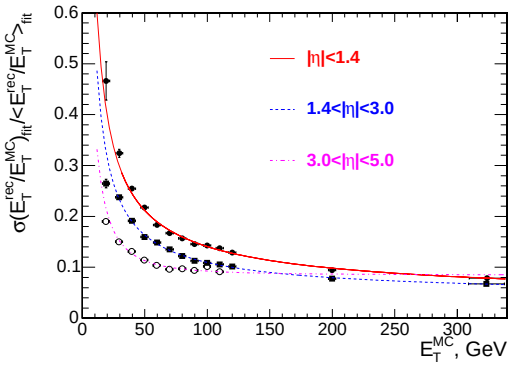

Figure 2.15: The jet transverse energy resolution as a function of the simulated jet transverse energy for barrel jets($|\eta| < 1.4$), endcap jets ($1.3 < |\eta| < 3$) and very forward jets ($3 < |\eta| < 5$). The jets are reconstructed with the iterative cone $R = 0.5$ algorithm.

$E_{\mathrm{t}}^{\mathrm{miss}}$ in QCD dijet events with pile-up is given by $\sigma(E_{\mathrm{t}}^{\mathrm{miss}}) \approx 1.0\sqrt{\sum E_{\mathrm{t}}}$ if energy clustering corrections are not made, while the average $E_{\mathrm{t}}^{\mathrm{miss}}$ is given by $\left\langle E_{\mathrm{t}}^{\mathrm{miss}} \right\rangle \approx 1.25\sqrt{\sum E_{\mathrm{t}}}$.

The CMS calorimetric system is not compensated, being the response to the electromagnetic part of an hadron shower different from the response to the hadron part. The non compensation effects, which degrade both the linearity and the resolution, can be reduced by an appropriate weighting of the response of the ECAL and of the different layers of the HCAL. Detailed Monte Carlo studies and test beam analysis have shown that the energy resolution is only marginally improved by the usage of energy dependent weights; fixed weights have therefore been chosen. The hadronic energy resolution when combining informations from HCAL and ECAL is:

$$\frac{\sigma_E}{E} = \frac{1.00}{E(\mathrm{GeV})} + 0.045 \quad . \tag{2.11}$$

The expected energy resolution for the very forward calorimeter is given for electrons and hadrons by

$$\frac{\sigma_E}{E} = \frac{1.38}{E(\mathrm{GeV})} + 0.05 \qquad \text{for electrons} \tag{2.12}$$

$$\frac{\sigma_E}{E} = \frac{1.82}{E(\mathrm{GeV})} + 0.09 \qquad \text{for hadrons.} \tag{2.13}$$

2.2.4 The magnet

Both the tracker and the two calorimeters are within a 4 T magnetic field which is generated by a solenoidal magnet coaxial to the beam. The presence

Table 2.2: Some properties of the CMS solenoid.

Parameter	Value
Magnetic field at the interaction point	4 T
Coil lenght	12.48 m
Stored energy	$2.70 \cdot 10^9$ J
Magnetic radial pressure	$6.47 \cdot 10^6$ Pa
Axial compressive force at mid plane	$148 \cdot 10^9$ N
Circulating current	20 kA

of the field allows the momentum measurement of the tracker thanks to the use of the curvature radius and at the same time reduces the effect of the pile-up by preventing low energy particles to reach the ECAL barrel. Finally, the magnetic field in the return yoke is used for the reconstruction of the muon tracks in the muon chambers.

The CMS magnet system consists of a superconducting coil housed in a vacuum tank and of a return yoke. The iron return yoke has a 12-sided cylindrical structure. The central part is divided in 5 coaxial rings, each one consisting of three layers where the muon chambers are hosted; the endcaps yokes instead are made of three disks, divided into 12 sectors. The superconducting coil is cooled down by liquid helium. It is housed in a vacuum tank which also works as supporting structure for the ECAL, the HCAL and the tracker. The main parameters of the magnet are given in Table.

The choice of the field intensity is a compromise between trigger efficiency requirements and reconstruction requirements.

2.2.5 The muon system

The muon system is the outermost of the CMS subdetectors. Its main goals are the identification of muons, thanks to their high penetrating power, and a precise measurement of their momentum, with the help of the information coming from the tracker. The muon system also works as trigger for events which involve muons and it provides a precise time measurement of the bunch crossing.

Centrally produced muons are measured 3 times: in the inner tracker, after the coil, and in the return flux. Measurement of the momentum of muons using only the muon system is essentially determined by the muon

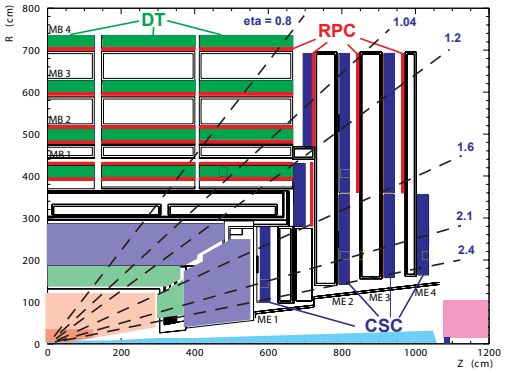

Figure 2.16: Layout of one quarter of the CMS muon system for initial low luminosity running. The RPC system is limited to $|\eta| < 1.6$ in the endcaps, and for the CSC system only the inner ring of the ME4 chambers have been deployed.

bending angle at the exit of the 4 T coil, taking the interaction point (which will be known to ≈20 μm) as the origin of the muon.

The resolution of this measurement (labelled "muon system only" in Figure 2.19) is dominated by multiple scattering in the material before the first muon station up to p_t values of 200 GeV/c, when the chamber spatial resolution starts to dominate. For low-momentum muons, the best momentum resolution (by an order of magnitude) is given by the resolution obtained in the silicon tracker ("inner tracker only" in Figure 2.19). However, the muon trajectory beyond the return yoke extrapolates back to the beam-line due to the compensation of the bend before and after the coil when multiple scattering and energy loss can be neglected. This fact can be used to improve the muon momentum resolution at high momentum when combining the inner tracker and muon detector measurements ("full system" in Figure 2.19).

The CMS muon system relies on three kinds of gaseous detectors: drift tubes, cathode strip chambers and resistive plate chambers. The drift tubes and the cathode strip chambers provide an excellent spatial resolution and the resistive plate chambers have a very good timing. The active parts of the muon system are hosted into stations which are interleaved by the iron layers of the return yoke of the magnet. The longitudinal view of a quarter of the muon system is given in Figure 2.16. The barrel extends up to $|\eta| < 1.3$, the endcaps up to $|\eta| < 2.5$.

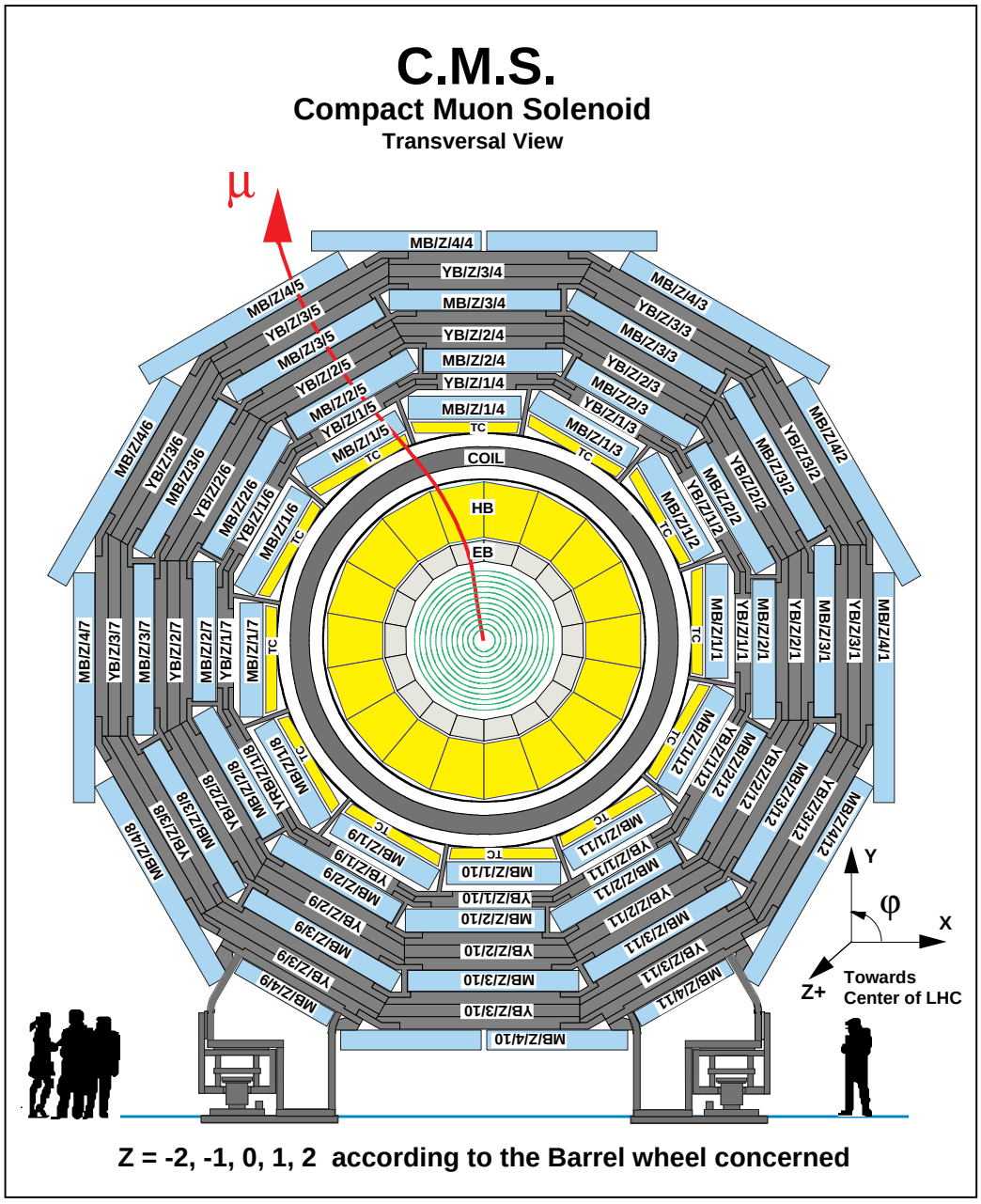

Figure 2.17: Transversal view of the CMS detector, with the labels for the different muon stations; the trajectory of a muon into the whole detector is also plotted.

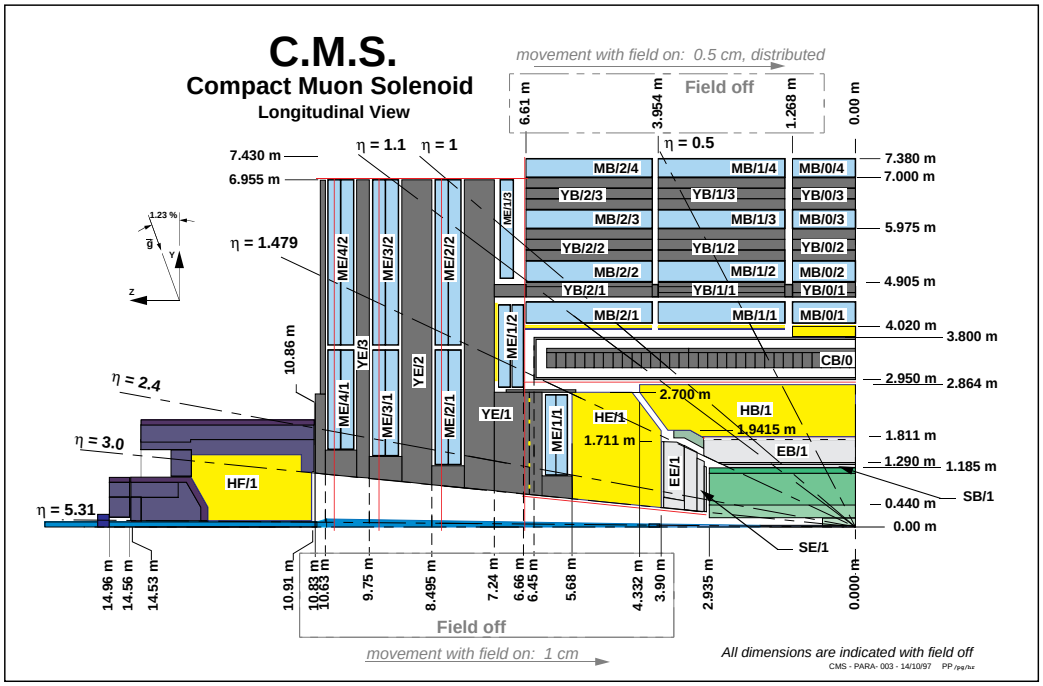

Figure 2.18: One quarter longitudinal view of the CMS detector, with labels for the different muon stations; the mechanical effect of the intense magnetic field is also taken into account.

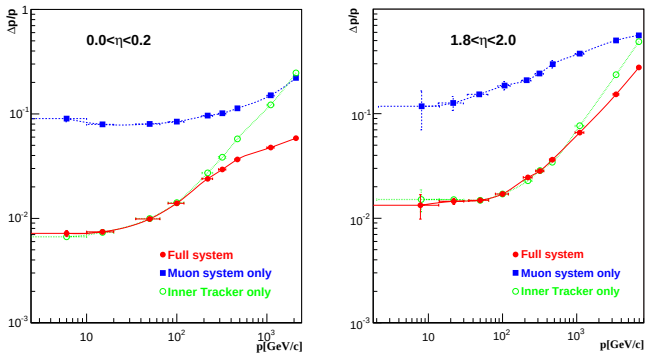

(a) (b)

Figure 2.19: The muon momentum resolution versus p using the muon system only, the inner tracker only, or both ("full system"). a) barrel, $|\eta| < 0.2$; b) endcap, $1.8 < |\eta| < 2.0$.

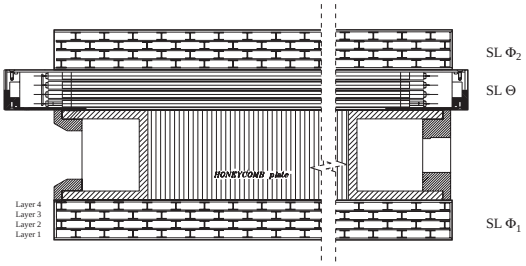

Figure 2.20: The layout of a DT chamber inside a muon barrel station.

The drift chambers

The drif tube chambers can very well operate in the barrel region, where the track occupancy is low, the neutron presence is negligible and the residual magnetic field is not too high thanks to the presence of the magnet return joke.

The basic element of a drift tube chamber is the drift cell, which is shown in Figure 2.20. A stainless steel anode wire is placed between two parallel aluminium layers; two 'I'-shaped electrodes, which define the boundaries of the cell, work as cathodes and shape the electric field. The distance of the track from the wire is measured by the drift time of the electrons and the chosen mixture of 80% Ar and 20% CO_2 ensures a good space-time linearity. The single cell, which works in condition of saturated drift velocity, has efficiency around 99.8% and spatial resolution ~ 180 μm.

Four layers of parallel staggering drift cells are glued together to form a superlayer. This allows to solve the left-right ambiguity of a single layer. Each muon station consists of three superlayers; the central one measures z and the other two the azimuthal coordinate ϕ. Despite the long drift time of a single layer, the combination of the responses of the four layers ensures a good time resolution.

Cathode strip chambers

The cathode strip chambers, shown in Figure 2.21, are multi-wire proportional chambers.

Being able to work also in a high radiation environment and in presence of inhomogeneus magnetic field, they have been chosen as detectors for the two endcaps. The chambers are composed of six layers, each one consisting of an array of anode wires between two cathode planes, one of which is segmented in the radial direction to provide the ϕ measurements. The region among the cathodes is filled with a mixture of 30% Ar, 50% CO_2 and 20%

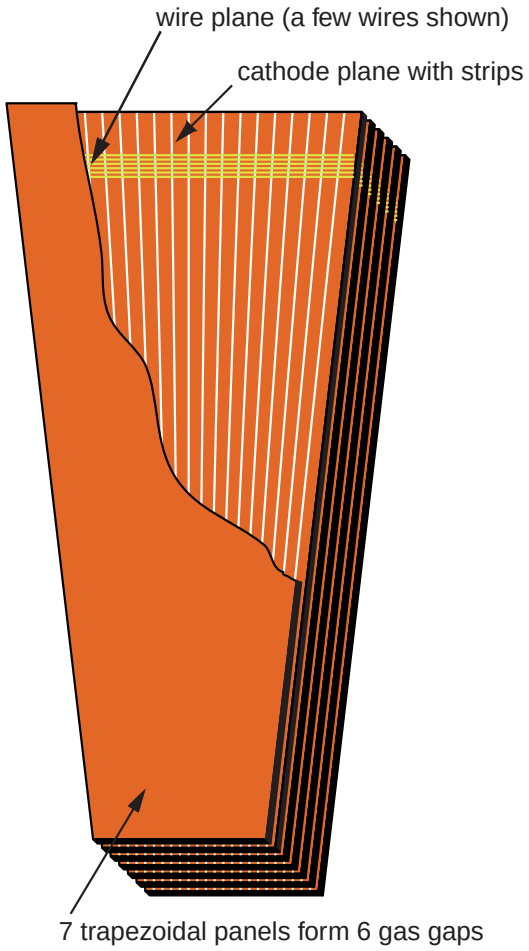

Figure 2.21: Schematic view of a CSC chamber.

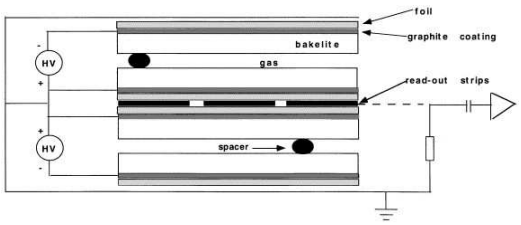

Figure 2.22: Schematic view of the RPC double-gap structure. The read-out strips in the Barrel chambers run along the beam direction.

CF_4. The passage of a particle induces a signal on many wires and strips and the particle position is obtained by an interpolation, with a resolution $50 - 100$ μm for the ϕ measurements, done by the strips, and about 5 mm for r, measured by the wires. In each endcap station, the presence of six layers of cathode strip chambers improves the timing and gives an efficiency better than 99%.

Resistive plate chambers

The resistive plate chambers, shown in Figure 2.22 are used both in the barrel and in the endcaps to provide a fast answer which is suitable for triggering purposes.

The RPCs have four bakelite electrodes forming two coupled gaps. They are filled with a gas mixture of freon ($C_2H_2F_4$, 95%) and isobutane (i-C_4H_10, 5%). The outer face of the bakelite planes is covered with graphite to distribute the high voltage over the whole surface. The RPCs operate in the avalanche mode instead of the streamer mode, to better sustain the high flux of particles; the amplitude of the signal is smaller since the gas multiplication is reduced, but this is compensated by an electronic amplification. The readout is made by aluminium strips. The main characteristic of the RPCs is their excellent time resolution, which is better than 2 ns.

2.2.6 The trigger

At the nominal LHC luminosity, a total event rate of 10^{12} Hz is expected. Given the typical size of a raw event ($\sim$ 1 MB), it is impossible to record the information corresponding to all the events; the rate has therefore to be reduced to the order of 100 Hz, which is the upper limit for storing events. The rate is dominated by low transverse momentum events. The trigger system therefore must have a huge reduction factor and at the same time it must maintain high efficiency on interesting events. This requires for the trigger a

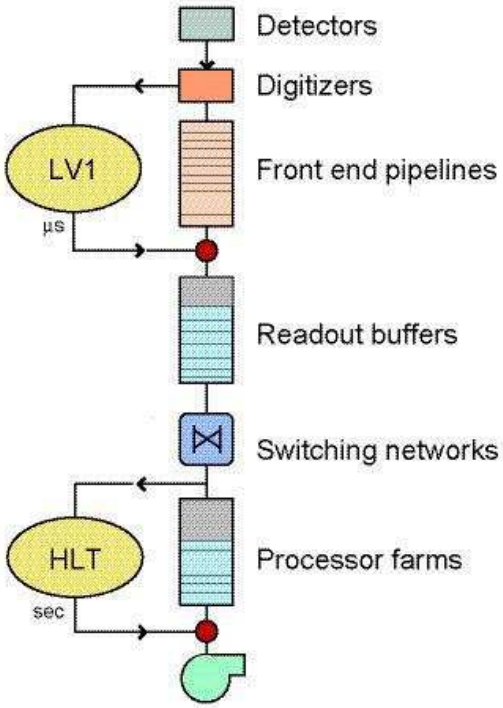

Figure 2.23: Data flow in the Trigger/DAQ system.

level of complexity which is comparable with the offline reconstruction and at the same time the necessity to work fast. This is done in two main steps.

The Level 1 trigger (L1) reduces the rate to about 50 kHz (100 kHz) for the low (high) luminosity phase. At a first level, the full data are stored in pipelines of processing elements, each one taking a decision in less than 25 ns. At each bunch crossing, each element passes its results to the following one and it receives new informations. The L1 decision about taking or discarding data from a particular bunch crossing has to be taken in 3.2 μs. If the first level trigger accepts the event, the data are moved to be processed by the HLT.

To deal with the 25 ns bunch crossing rate, the L1 trigger has to take decisions in a time which is too short to read all the raw data from the whole detector, therefore it uses the calorimetric and muons information only. It is organized in a Calorimeter Trigger and a Muon Trigger; they both pass the information to the Global Trigger which takes a global decision. The Calorimetric Trigger consists of trigger towers which match the granularity of ECAL and which are grouped in regions of 4×4 trigger towers. Four categories of objects (electrons and photons, central jets, forward jets and τ jets) are analized and the best four candidates of each class are passed to

the Global Trigger together with the missing E_{t}. The Muon Trigger analizes separately the three different detectors of the muon system and then it passes the four best muon candidates to the Global Trigger. The Global Trigger uses a logical combination of the data with the corresponding thresholds and it takes a decision. The estimate output rate is almost a factor 3 lower than the sustainable one.

The High Level Trigger (HLT) reduces the output rate down to 100 Hz. The idea behind the HLT software is the regional reconstruction on demand, i.e. only the objects which are in useful regions are reconstructed and the not interesting events are rejected as soon as possible. The HLT can be splitted into three logical levels. At the first one, only the full information of the muon system and of the calorimeters is used; at the second level the information from the tracker hits is added and finally, at a third level, the full information is available.

CHAPTER 3

PHYSICS AT CMS

We now turn our attention on the production mechanisms, on the decay channels of the Higgs boson at LHC, and on the search strategies for different mass regions (The CMS Collaboration, 2007).

3.1 Higgs boson production

For all possible Higgs boson masses the dominating Higgs boson production mechanism at the LHC is the gluon fusion process whose Feynman diagram is shown in Figure 3.1.

The other processes shown in Figure 3.1 are also of interest because of the special signatures they can provide for the identification of the Higgs boson. In Figure 3.2 the cross section is shown as a function of the Standard Model Higgs boson mass. At the higher masses a significant part of the cross section is from vector boson fusion.

3.1.1 Gluon fusion

The gluon fusion process for Higgs boson production, shown in Figure 3.1, can be calculated from the width of the $H \to gg$ decay and the gluon structure function. The loop is totally dominated by the top quark because of the strong Higgs boson coupling to the heavy top quark. The cross section for the basic gluon to Higgs boson process is (Georgi et al., 1978):

$$\sigma(gg \to H) = \frac{G_F \alpha_S^2(\mu_R^2)}{288\sqrt{2}\pi} \left| \frac{3}{4} \sum_q A_{1/2}^H(\tau_q) \right|^2 \tag{3.1}$$

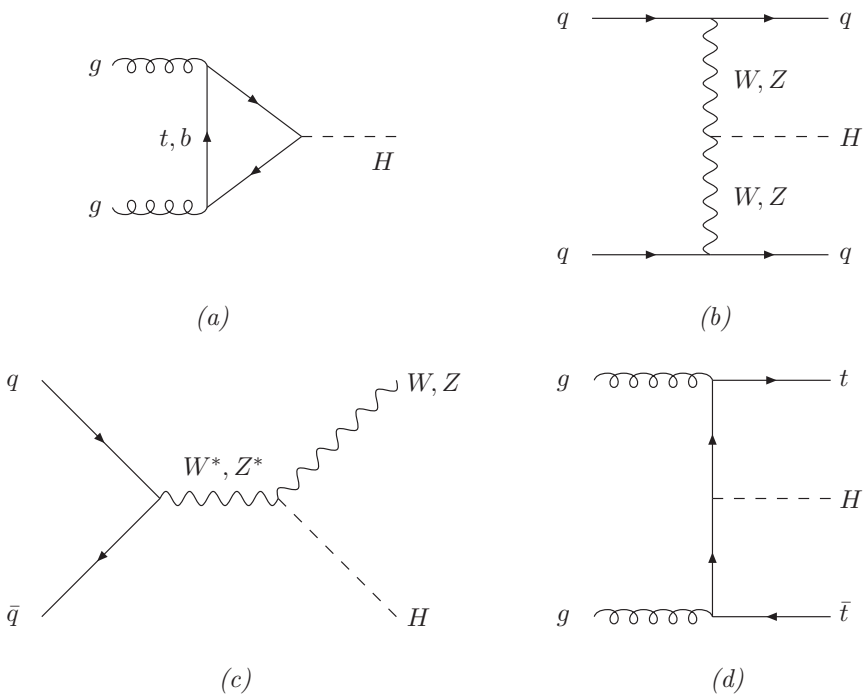

Figure 3.1: Typical diagrams for all relevant Higgs boson production mechanisms at leading order: (a) gluon fusion, (b) vector boson fusion, (c) Higgs-strahlung, (d) Higgs bremsstrahlung off top quarks.

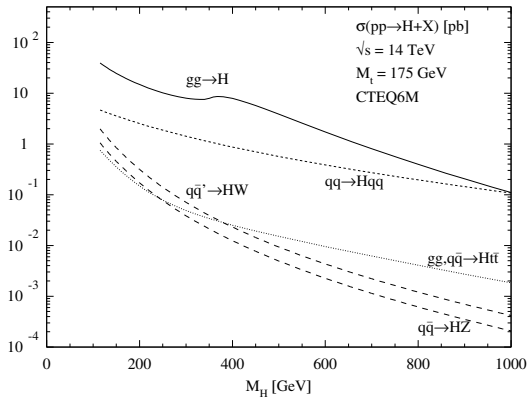

Figure 3.2: Production cross section of the Standard Model Higgs boson as a function of its mass for the main processes. The cross sections are calculated using HIGLU and other programs (Spira, 1995); they contain higher order corrections and the `CTEQ6M` (Tung et al., 2007) p.d.f. has been adopted.

where $A^{\mathrm{H}}_{1/2}(\tau_{\mathrm{Q}})$, with $\tau_q = M^2_{\mathrm{H}}/4m^2_q$ is a form factor (Djouadi, 2005). The lowest order cross section has large corrections from higher order QCD diagrams. The increase in cross section from higher order diagrams is conventionally defined as the k-factor:

$$k = \frac{\sigma_{\mathrm{HO}}}{\sigma_{\mathrm{LO}}} \tag{3.2}$$

where LO (HO) refer to lowest (higher) order results. The value of the cross section including the k-factor has two main uncertainties. The first is from the gluon structure function which still has large uncertainty in the low x region. The cross section using a large set of todays best available structure functions was calculated by (Kramer et al., 1998) and the results differ by around 20% which can be taken as the theoretical unertainty from gluon structure function. At the time of data taking for LHC it can be expected to have much better structure functions available with data from HERA and the Tevatron.

The second uncertainty in the gluon fusion cross section is from corrections above the next-to-leading order. The cross section changes with the renormalization scale μ as an effect of un-calculated higher order diagrams. By changing μ between $M_{\mathrm{H}}/2$ and $2M_{\mathrm{H}}$ it can be guessed that the remaining uncertainties from higher order effects are below 15% (Ravindran et al., 2003).

The production of the Higgs boson through gluon fusion is sensitive to a fourth generation of quarks. Because the Higgs boson couples in proportion to the fermion mass, a heavier generation of quarks is not suppressed in the process as would be expected for a loop process with a heavier particle in the loop. The inclusion of a fourth generation of very heavy quarks will more than double the cross section. Therefore, the Higgs boson cross section is sensitive to a fourth generation of quarks even if the quarks are too heavy for a direct discovery at the LHC.

3.1.2 Vector boson fusion

The process of Higgs boson production through vector boson fusion shown in Figure 3.1 is important only for high Higgs boson masses where the coupling to longitudinal polarized vector bosons is strong. At the high energies where a heavy Higgs particle is created, the vector bosons act essentially as massless particles and can be treated as particles present inside the colliding protons. With this simplification the full process in Figure 3.1 can be separated into a calculation of the vector boson structure function in the proton and a calculation of Higgs boson production in colliding vector boson beams.

The method is called the effective W approximation. The production of a Higgs boson is dominated by the longitudinal polarized state and the small contribution from the transverse polarized state can be ignored. Following the derivation by Kane et al. (1984) the cross section for production of a Higgs boson in the fusion of two vector bosons can be written as

$$\sigma(q_1 q_2 \to q_1' q_2' \mathrm{H}) = \frac{16\pi^2}{\hat{s} M_\mathrm{H}} \sum_{V=\mathrm{W,Z}} \int_{M_\mathrm{H}^2/\hat{s}}^1 \frac{dx}{x} F_\mathrm{V}(x) F_\mathrm{V}(M_\mathrm{H}^2/\hat{s}x) \Gamma_\mathrm{V}(\mathrm{H} \to \mathrm{VV}) \tag{3.3}$$

where F_V is the structure function for the vector boson V with partial width $\Gamma_\mathrm{V}$in the longitudinal polarized state and $q_1' q_2'$ denoting the two outgoing quarks.

To get the full cross section for the Higgs boson from vector boson fusion the cross section above has to be convoluted with the structure functions of the incoming quarks. For all possible values of the Higgs boson mass the cross section is below the gluon fusion process, but with the additional signature of the two outgoing quarks participating in the process the identification could be easier in this production channel.

3.1.3 Higgs-strahlung

In the Higgs-strahlungh process, whose digram is plotted in Figure 3.1, the Higgs is produced in association with a W or Z boson, whose decay products can be used to tag the event. The cross section is orders of magnitude smaller with respect to the gluon fusion one (Glashow et al., 1978). For a Higgs boson mass of 150 GeV/c^2 the production cross section is around 1 pb or 4% of the gluon fusion cross section. With the present structure functions available, due to the large QCD corrections, the uncertainty in the cross section is around 30%.

3.1.4 Associated production

The associated production with a t $\bar{\mathrm{t}}$ pair, plotted in Figure 3.1, is the last production mechanism for the Higgs boson (Kunszt, 1984). For Higgs boson masses below 200 GeV/c^2 the cross section is about a factor 5 below the cross section for associated production with a W, while for masses above 500 GeV/c^2 it is greater than the W H cross section but is still far below the gluon fusion cross section. The size of the QCD corrections depends sensitively on the choice of the scale and on the parton distributions functions. However, as for the Higgs-strahlungh case, the presence of a t $\bar{\mathrm{t}}$ pair in the final state can be exploited to tag the event.

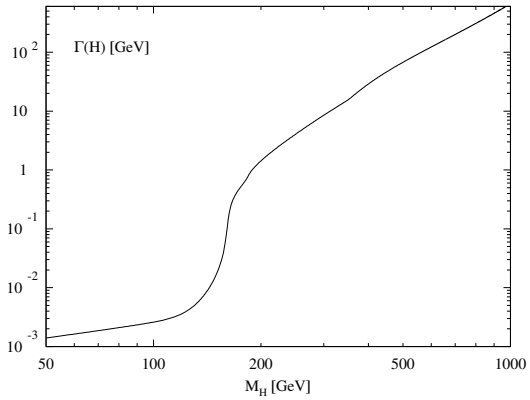

Figure 3.3: The Standard Model Higgs boson total decay width as a function of M_{H}.

3.2 Higgs boson decay

With the Higgs boson decaying directly into pairs of all massive particles and through loop diagrams even into pairs of massless gluons and photons, the spectrum of Higgs boson signatures is large. After a discovery of a Higgs particle it will be important to detect it in several decay channels to check if the coupling strength is proportional to the fermion mass as the Standard Model predicts.

The total width and the branching ratios, including the dominant higher order corrections, are plotted in Figure 3.3 and Figure 3.4. They are calculated with the program `HDECAY` (Djouadi et al., 1997) which includes the dominant higher order corrections to the decay width.

As shown in Figure 3.4, the branching ratios change dramatically across the possible range of the Higgs boson mass requiring different strategies for the Higgs particle identification depending on its mass.

As shown in Figure 3.4, the branching ratios change dramatically across the possible range of the Higgs boson mass requiring different strategies for the Higgs particle identification depending on its mass.

3.2.1 Fermionic decays

In the Born approximation, the partial width of the Higgs boson decay into fermion pairs, whose diagram is shown in Figure 3.5, is given by (Ellis et al., 1976):

$$\Gamma_{\mathrm{Born}}(\mathrm{H} \to f\bar{f}) = \frac{G_{\mathrm{F}} N_{\mathrm{c}}}{4\sqrt{2}\pi} M_{\mathrm{H}} m_f^2 \beta_f^3 \tag{3.4}$$

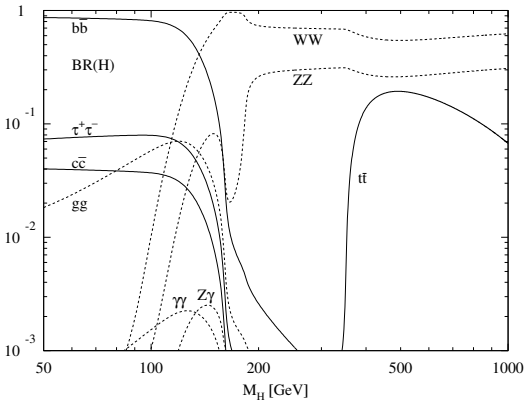

Figure 3.4: The decay branching ratios of the Standard Model Higgs boson into the main channels as a function of its mass.

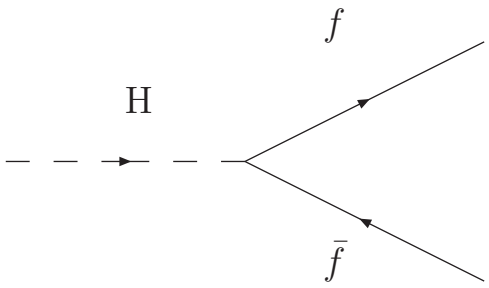

Figure 3.5: Leading order Feynman diagram for the decay process of the Standard Model Higgs boson into a pair of fermions.

with $\beta_f = (1 - 4m_f^2/M_{\mathrm{H}}^2)^{1/2}$ being the velocity of the fermions in the final state and $N_{\mathrm{c}} = 3(1)$ is the colour factor for quarks (leptons).

The Higgs particle couples to all fermions proportionally to their mass so the coupling to a pair of top quarks is by far the strongest. If the Higgs boson mass is below twice the top mass the dominant fermionic decay will be to bottom quarks. In the lepton case, only decaysinto τ^+ τ^- pair and, to a much lesser extent, decays into muons pair are relevant.

In the case of the hadronic decays of the Higgs boson, the QCD corrections turn out to be quite large and therefore must be included. At one loop level the gluon exchange and the emission of a gluon in the final state should be included. The Feynman diagrams for these corrections are shown in Figure 3.6.

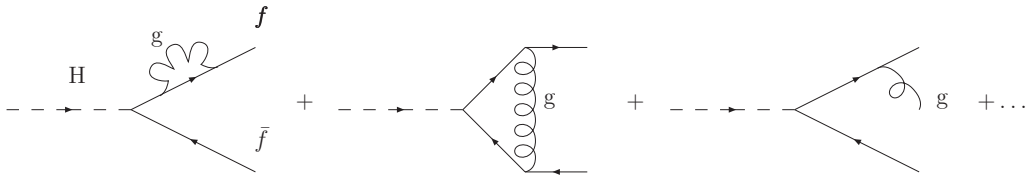

Figure 3.6: Some of the higher order corrections to the decay channel of the Standard Model Higgs boson into two fermions.

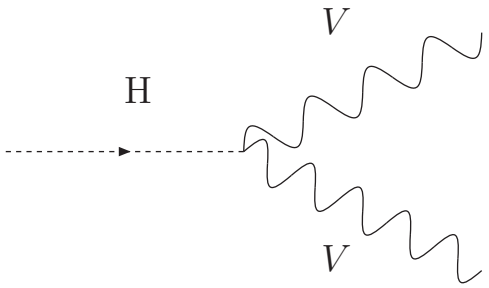

Figure 3.7: Leading order Feynman diagram for the decay process of the Standard Model Higgs boson into two vector bosons.

3.2.2 Vector boson decay

Above the W W and Z Z kinematical thresholds, the Higgs boson decays mainly into pairs of massive gauge bosons, the corresponding diagrams being that in Figure 3.7.

The decay widths are directly proportional to the H VV couplings. The widths are given by (Resnick et al., 1973):

$$\Gamma(\mathrm{H} \to \mathrm{VV}) = \frac{G_\mathrm{F} M_\mathrm{H}^3}{16\sqrt{2}\pi} \delta_\mathrm{V} \sqrt{1-4x} \left(1 - 4x + 12x^2\right) \tag{3.5}$$

where $x = M_\mathrm{V}^2/M_\mathrm{H}^2$, $\delta_\mathrm{W} = 2$ and $\delta_\mathrm{Z} = 1$. For large enough Higgs boson masses, when the phase space factors can be ignored, the decay width into W W bosons is two times larger than the decay width into ZZ bosons and the branching ratios for the decays are approximately 2/3 and 1/3 for energies below the t $\bar{\mathrm{t}}$ threshold.

3.2.3 Two photon decay

Since the photon is massless there is no coupling between the Standard Model Higgs boson and the photon. However, the decay is possible through loop

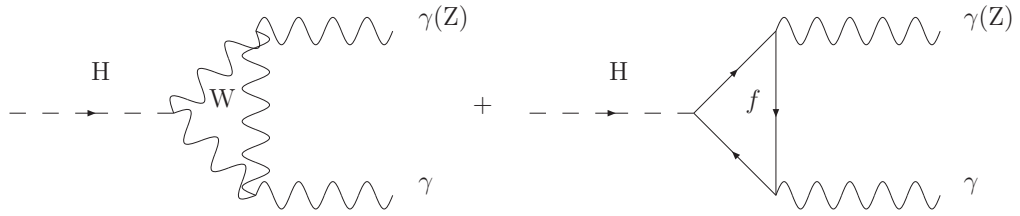

Figure 3.8: Leading order Feynman diagrams for the decay process of the Standard Model Higgs boson into two photons.

processes with either fermions or bosons in the loop. Feynman diagrams for the lowest order processes are shown in Figure 3.8.

The calculation of the matrix element for the decay is rather difficult and involves dimensional regularization of the infinities arising from the loop. The final result for the squared matrix element is (Vainshtein et al., 1979):

$$|M| = \frac{g^2 M_{\mathrm{H}}^4}{32\pi^2 M_{\mathrm{W}}^2} \left| \sum_i \alpha N_{\mathrm{c}} e_i^2 F_i \right|^2 \tag{3.6}$$

with the sum over all scalars, fermions and bosons in the loop with charge e_i and colour factor N_{c}. The factors F_i depend on the particles in the loop. They disappear for small values of the fermion mass, so that light quarks and leptons are insignificant. The only fermion participating is the top quark. For bosons the loop only contains the charged W. The width of the $\mathrm{H} \to \gamma\gamma$ decay is:

$$\Gamma(\mathrm{H} \to \gamma\gamma) = \frac{\alpha^2 g^2 M_{\mathrm{H}}^3}{1024\pi^3 M_{\mathrm{W}}^2} \left| \sum_i N_{\mathrm{c}} e_i^2 F_i \right|^2 \tag{3.7}$$

which always gives a branching ratio below 0.3% due to the much larger width of the $\mathrm{H} \to \mathrm{b\bar{b}}$ decay. The two photon signature is, however, clean and is an important decay channel at the LHC. The radiative corrections to the $\mathrm{H} \to \gamma\gamma$ decay width are relatively simple as they only affect the top quark loop and neither the W loop nor the final state photons. The corrections are below 3%, thus of limited importance.

3.3 Higgs boson search

Higgs boson production cross section is greater than 1 pb in the whole mass range 100 GeV/c^2–1 TeV/c^2. More than two thousands events are therefore expected in one year of data taking at the nominal low luminosity $\mathscr{L} =$

$2 \cdot 10^{33}$ cm^{-2} s^{-1} with an increase of a factor five in the high luminosity regime $\mathscr{L} = 10^{34}$ cm^{-2} s^{-1}. Fully hadronic events are the most copious final states from Higgs boson decays. These decays can not be easily resolved when merged in QCD background, therefore topologies with leptons or photons are preferred, even if they have smaller branching ratio. Similarly signatures of the associated production, with a leptonically decaying particle, can be searched for. As decay branching ratios depend on the Higgs boson mass, search strategies change accordingly.

3.3.1 Low mass region

The region $M_{\mathrm{H}} < 130$ GeV/c^2 is the hardest to be explored. The best way to detect a light Higgs boson would be in the dominant H $\rightarrow$ b$\overline{\mathrm{b}}$ channel. The large cross section (28 pb) for $M_{\mathrm{H}} = 115$ GeV/c^2 is however overwhelmed by the di-jet rate (more than six orders of magnitude higher).

A more favorable situation can be obtained by either looking at associate production (t $\overline{\mathrm{t}}$ H, W H or Z H) or at one of the rare decays.

The most promising way of identifying a Higgs boson in the low mass region is to select the decay H $\rightarrow \gamma\gamma$. The channel suffers from a branching ratio around 10^{-3}but the backgrounds are much lower than in the case of the H $\rightarrow$ b$\overline{\mathrm{b}}$ decay thanks to the clear signature of two isolated photons in the final state. The main backgrounds are from direct photon production and jets faking photons. The expected signal to background ratio is 10^{-2}, which make this channel much more attractive than the b $\overline{\mathrm{b}}$ decay.

3.3.2 Intermediate mass region

In the mass region between 130 GeV/c^2 $< M_{\mathrm{H}} < 2M_{\mathrm{Z}}$ the branching ratio to vector bosons reaches significant levels. The decay channels are then H $\rightarrow$ WW* $\rightarrow \ell^+\nu_\ell\ell^{-\prime}\overline{\nu}_\ell{}'$ and H $\rightarrow$ ZZ* $\rightarrow \ell^+\ell^-\ell^{+\prime}\ell^{-\prime}$ with only one vector boson on-shell. The WW* decay mode has to be extracted from a background mainly due to non resonant W W production and t$\overline{\mathrm{t}}$ $\rightarrow$ W$^+$W$^-$b$\overline{\mathrm{b}}$.

The fully leptonic decay H $\rightarrow$ ZZ $\rightarrow 4\ell$ has the cleanest experimental signature, particularly in the four muon channel. The signal selection is based on the mass constraint which can be made on one of the lepton pairs. The main irreducible background is continuum Z Z production while reducible backgrounds are t $\overline{\mathrm{t}}$ and Z b $\overline{\mathrm{b}}$. Looking at Figure 3.4 a particular shape of the branching ratio to Z bosons can be seen for Higgs boson masses in the interval 130 GeV/c^2 $< M_{\mathrm{H}} <$ 130 GeV/c^2. It is caused by a threshold effect where the decay to two W bosons on the mass shell becomes possible while

still at least one of the Z bosons needs to be below the mass shell in the concurrent $H \rightarrow ZZ^*$ decay.

3.3.3 High mass region

If the Standard Model Higgs boson has a mass above twice the Z mass the discovery will be easy through the decay channel $H \rightarrow ZZ \rightarrow \ell^+\ell^-\ell^+\ell^-$: this is indeed the golden channel for the Higgs boson discovery at LHC. Both lepton pairs will have an on-shell Z mass which makes possible to reduce many types of backgrounds. The upper mass limit for detecting the Higgs boson in this decay channel is given by the reduced production rate and the increased width of the Higgs boson. As an example fewer than 200 Higgs particles with $M_H = 700\,\mathrm{GeV/c^2}$ decay in the $H \rightarrow ZZ \rightarrow 4\ell$ channel in year at high luminosity and the large width of such a heavy Higgs boson makes it very difficult to observe a mass peak. A selective decay channel like the four lepton channel is thus no longer sufficient for the highest Higgs boson masses. With the decays to vector bosons totally dominating, the only possible detection channels left are with at least one of the vector bosons decaying to neutrinos or jets. The decay channel $H \rightarrow WW \rightarrow \ell\nu_\ell jj$ where j denotes a jet from a quark in the W decay, has a branching ratio just below 30%, yielding a rate some 50 times higher than the four lepton channel from $H \rightarrow ZZ$ decays. The decay channel $H \rightarrow ZZ \rightarrow \ell^+\ell^-\nu_{\ell'}\overline{\nu}_{\ell'}$ which has a six times larger branching ratio than the four lepton channel could also be interesting.

3.4 Physics beyond the Standard Model

Although the SM is very successful, there exist some hints to physics beyond the Standard Model. The theoretical and phenomenological landscape of beyond the standard model searches extends to a multitude of exotic tendencies today in collider physics. Most are conceived within one kind or another of extra dimensions and supersymmetric scenarios. The strict or loose dualities between different frameworks for physics "beyond the standard model" have a direct experimental consequence: the final states and signatures of the models are very similar. This renders the characterisation of an excess or a deviation a fine and probably long challenge. The results from all the collider data to date, together with the as yet unobserved Higgs and including the data on the neutrino masses and the composition of the universe, impose a wide program of searches that the CMS experiments is preparing for. In general the SM can only be valid up to energies of the order of the

Planck scale (10^{19} GeV) where one has to include gravity because at such distances the strength of gravity is comparable to the strength of the three other forces. There are open question in the SM:

- the origin of CP-violation and matter-antimatter asymmetry;
- the origin of the hierarchy of the fermion masses;
- the origin of the three generations of both quarks and leptons;
- the possible compositeness of quarks and leptons.

Another desired feature of a theory would be the unification of gauge couplings. This requires that the gauge couplings meet at a high scale, when the couplings are evolved following the renormalization group (RG) equations. In the SM this is not possible, but in the Minimal Supersymmetric Standard Model (MSSM) the unification is possible. In addition, supersymmetric models provide a mechanism to solve the so-called Higgs hierarchy problem.

The hierarchy problem

The mass of the Higgs-boson receives enormous quantum corrections from every particle that couples to the Higgs field. At one-loop level this correction is shown in Figure 3.9.

The correction of the first graph to the Higgs mass yields

$$\Delta M_{\mathrm{H}}^2 = -\frac{|\lambda_f|^2}{8\pi^2}\Lambda_{\mathrm{UV}}^2 + \dots \tag{3.8}$$

where λ_f is the Yukawa coupling of the Higgs field to the fermion fields, and Λ_{UV}^2 is an ultraviolet momentum cutoff to regularize the loop integral. This cutoff represents the scale where new physics enters the theory. The problem arises when Λ_{UV}^2 is of the order of $M_{\mathrm{P}} = 10^{19}$ GeV, because the quantum corrections are 34 orders of magnitude larger than the actual value ΔM_{H}^2. Although a quadratical correction only occurs in the loop correction to the Higgs boson mass, all particles are influenced by this correction because they obtain their masses via the Higgs mechanism. For the corrections of the boson loops in the second graph, we obtain

$$\Delta M_{\mathrm{H}}^2 = \frac{|\lambda_s|^2}{16\pi^2}\left[\Lambda_{\mathrm{UV}}^2 - 2m_s^2 \ln(\Lambda_{\mathrm{UV}}/m_s)\right] + \dots \tag{3.9}$$

which has a different sign, so that the corrections partially cancel out (λ_s is the Yukawa coupling of the boson s and m_s its mass). But since in the

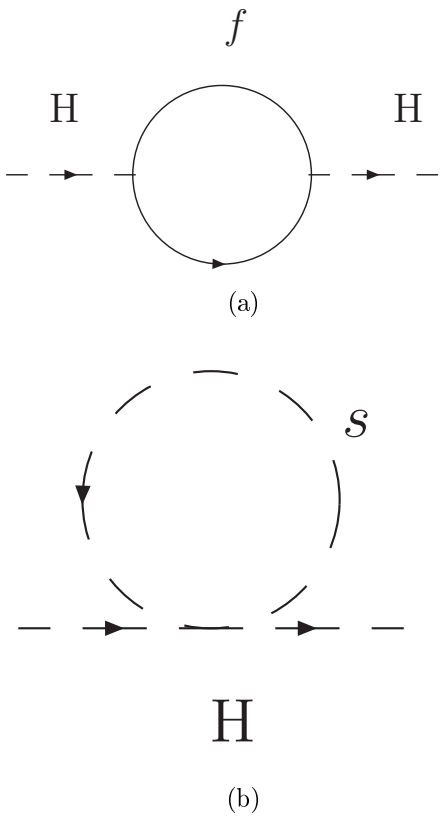

Figure 3.9: (a) Fermion and (b) boson corrections to the Higgs propagator at one loop level.

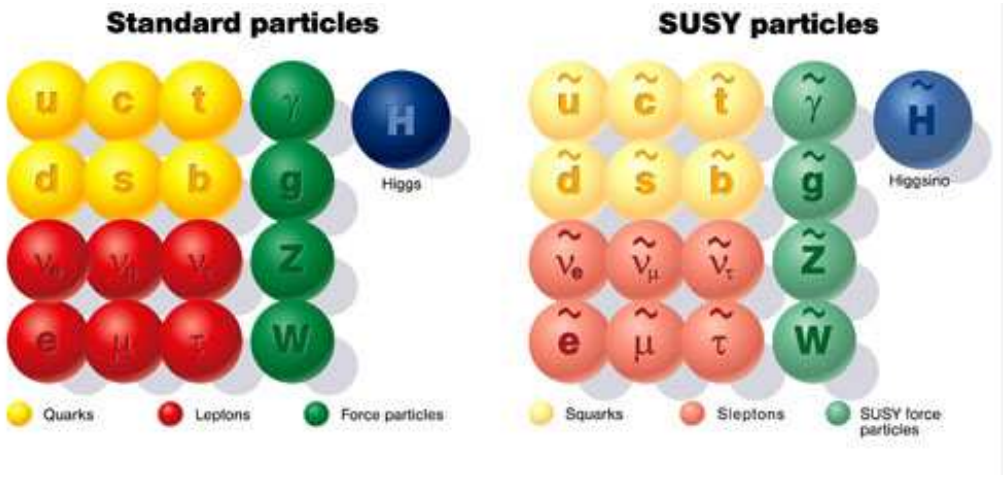

Figure 3.10: SM particles and their MSSM partners

SM the number of fermions and bosons is very different there remain very large corrections. If there was a bosonic particle to each SM fermion and vice versa, and the couplings $\lambda_s = |\lambda_f|^2$ were equal, all corrections would cancel out and one would remain with a logarithmic correction only. Even in case of a broken symmetry, where the masses of the corresponding particles are different, the dependence on the scale Λ_{UV} still cancels out.

Supersymmetry

Supersimmetry (Martin, 2006) is the symmetry between fermions and bosons. A supersymmetric transformation Q turns a bosonic state into a fermionic state ($Q\,|\text{boson}\rangle = |\text{fermion}\rangle$) and vice versa. Each SM particle is transformed into its superpartner, which differs in spin by 1/2. None of these superpartners has been observed until now. The particles included in the Minimal Supersymmetric Standard Model (MSSM) are listed in Figure 3.10.

The MSSM contains a minimal number of new particles. Supersymmetric particles are commonly called *sparticles* (supersymmetric particles). The partners of the fermions (sfermions) get a prefix s- (scalar particle, e.g. squarks, sleptons ...), while the superpartners of the bosons (gauginos) get a suffix -ino (e.g. gluino, wino ...). The MSSM particles shown in Figure 3.10 represent the gauge eigenstates in the theory. The experimentally observed mass eigenstates are formed by mixing of these eigenstates.

Actually there exist four neutral gauginos, called neutralinos ($\widetilde{\chi}^0_1$, $\widetilde{\chi}^0_2$, $\widetilde{\chi}^0_3$, $\widetilde{\chi}^0_4$), which are mixed states of the neutral gauge particles (wino, bino, neutral higgsinos). The four charged gaugino mass eigenstates are called charginos ($\widetilde{\chi}^{\pm}_1$, $\widetilde{\chi}^{\pm}_2$) and are obtained by mixing of the charged gauginos

(charged winos, charged higgsinos). These particles are ordered by their mass, indicated by the index of the particle, where the mass increases with index.

In supersymmetric models a new multiplicative quantum number is introduced, which allows to distinguish SM and supersymmetric particles. It is called R-parity (or matter parity) and is defined as follows:

$$P_{\mathrm{R}} = (-1)^{3(B-L)+2s} \tag{3.10}$$

where B is the baryon number, L the lepton number and s the spin of the particle. This quantum number yields +1 for a SM particle and -1 for the supersymmetric partners.

The decays of supersymmetric particles, such as squarks and gluinos, involve cascades that, if R-parity is conserved, always contain the lightest SUSY particle (LSP). The latter is expected to interact very weakly, thus leading to significant $E_{\mathrm{t}}^{\mathrm{miss}}$ in the final state. The rest of the cascade results in an abundance of leptons and jets (particularly b-jets and/or τ-jets).

3.4.1 Extra dimensions and new vector boson high mass states

Additional heavy neutral gauge bosons (Z′) are predicted in many superstring-inspired (Cvetic and Langacker, 1996) and grand unified theories (GUTs) (Leike, 1999), as well as in dynamical symmetry breaking (Hill and Simmons, 2003) and "little Higgs" (Han et al., 2003) models. There are no reliable theoretical predictions, however, of the Z′ mass scale. Current lower limits on the Z′ mass are (depending on the model) of the order of $600 - 900$ GeV/c^2 (Yao et al., 2006). The LHC offers the opportunity to search for Z′ bosons in a mass range significantly larger than 1 TeV/c^2.

The detector requirements for high momenta can be determined by considering decays of high-mass objects such as $\mathrm{Z}' \rightarrow \mathrm{e}^+\mathrm{e}^-$ and $\mu^+\,\mu^-$. The discovery of an object like a Z′ boson will, very likely, be limited by the statistical significance of the signal. Ways of distinguishing between different models involve the measurement of the natural width and the forward-backward asymmetry, both of which require sufficiently good momentum resolution at high p_{t} ($\Delta p_{\mathrm{t}}/p_{\mathrm{t}} < 0.1$ at $p_{\mathrm{t}} \approx 1$ TeV/c) to determine the sign of the leptons and a pseudorapidity coverage up to $\eta = 2.4$.

Randall-Sundrum models

Randall-Sundrum (RS) models refer to a class of scenarios, also known as warped extra dimensions models, originated by Lisa Randall and Raman

Sundrum (Randall and Sundrum, 1999). In these scenarios there is one extra spatial dimension, and the five-dimensional geometry is "warped" by the presence of one or more branes. The branes extend infinitely in the usual three spatial dimensions, but are sufficiently thin in the warped direction that their profiles are well-approximated by delta functions in the energy regime of interest.

Most collider physics phenomenology done with warped extra dimensions so far is based upon one very specific model, the original simple scenario called RSI. In this model the extra dimension is compactified to a circle of circumference $2L$, and then further orbifolded by identifying points related by $y \to -y$. The fifth dimension then consists of two periodically identified mirror copies of a curved 5d space extending from $y = 0$ to $y = L$.

In RSI, the Standard Model is replaced at the TeVscale by a new effective theory in which gravity is still very weak, but there are exotic heavy spin-two particles, the Kaluza-Klein (KK) gravitons. At the LHC the KK gravitons of RSI would be seen as difermion or dibosons resonances.

3.4.2 Technicolour theories

Technicolour (TC) provides an alternative to the elementary Higgs mechanism of the Standard Model. It introduces a new strong interaction (Lane) providing a dynamical nature to Electroweak Symmetry Breaking. Technicolour is a QCD-like force, acting on technifermions at an energy scale $\Lambda_{\mathrm{TC}} \simeq v = 246$ GeV. A number N_D of technifermion doublet condensates yield the pseudo-Goldstone bosons π_{TC}, together with a wide spectroscopy of excited technimesons. The colour-singlet sector includes the spin-zero π_{TC} and the spin-one technimesons ρ_{TC} and ω_{TC}. The decay cross section of the ρ_{TC} is expressed as an admixture of π_{TC} and the Standard Model Z and W bosons. The decay channel $\rho_{\mathrm{TC}} \to \mathrm{W} + \mathrm{Z}$ is the subject of the CMS analysis.

3.5 Standard Model and Z physics at CMS

3.5.1 Tree-level predictions

Before the discovery of the W and Z particles, the then known data were consistent with a single value of θ_{W} given (using a modern value) by $\sin\theta_{\mathrm{W}}^2 \simeq 0.23$. Using eqs. (1.64) and (1.82) we may then predict the value of M_{W}:

$$M_{\mathrm{W}} = \left(\frac{\pi\alpha}{\sqrt{2}G_{\mathrm{F}}}\right)^{1/2} \frac{1}{\sin\theta_{\mathrm{W}}} \simeq 77.73 \text{ GeV/c}^2. \tag{3.11}$$

Similarly, using eq. (1.54) we predict

$$M_{\rm Z} = \frac{M_{\rm W}}{\cos\theta_{\rm W}} \simeq 88.58 \text{ GeV/c}^2. \tag{3.12}$$

These predictions of the theory at lowest order indicate the power of the underlying symmetry to tie together many apparently unrelated quantitites, which are all determined in terms of a few basic parameters. The width for $\rm W^- \to e^- \overline{\nu}_e$ can be calculated using the vertex (1.63):

$$\Gamma(\rm W^- \to e^- \overline{\nu}_e) = \frac{1}{12}\frac{g^2}{4\pi} M_{\rm W} \simeq 205 \text{ MeV} \tag{3.13}$$

using (3.11). The widths to $\mu^-\ \overline{\nu}_\mu$ and $\tau^-\ \overline{\nu}_\tau$ are the same. Neglecting GIM-type flavour mixing among the two energetically allowed quark channels $\overline{\rm u}$ d and $\overline{\rm c}$ s, their widths would also be the same, apart from a factor of three for the different colour channels. The total W width for all these channels will therefore be about 1.85 GeV. In making these estimates, we have neglected all fermion masses.

The width $\rm Z \to \nu\overline{\nu}$ can be found from eq. (3.13) by replacing $g/\sqrt{2}$ by $g/(2\cos\theta_{\rm W})$ and $M_{\rm W}$ by $M_{\rm Z}$, giving

$$\Gamma(\rm Z \to \nu\overline{\nu}) = \frac{1}{24}\frac{g^2}{4\pi}\frac{M_{\rm Z}}{\cos^2\theta_{\rm W}} \simeq 152 \text{ MeV} \tag{3.14}$$

using eq. (3.12). Charged lepton pairs couple with both $c^\ell_{\rm L}$ and $c^\ell_{\rm R}$ terms, leading, with neglect of lepton masses, to

$$\Gamma(\rm Z \to \ell\overline{\ell}) = \left(\frac{|c^\ell_{\rm L}|^2 + |c^\ell_{\rm R}|^2}{6}\right)\frac{g^2}{4\pi}\frac{M_{\rm Z}}{\cos^2\theta_{\rm W}}. \tag{3.15}$$

The values $c^\nu_{\rm L} = \frac{1}{2}$, $c^\nu_{\rm R} = 0$ in eq. (3.15) reproduce (3.14). With $\sin\theta^2_{\rm W} \simeq 0.23$, we find that

$$\Gamma(\rm Z \to \ell\overline{\ell}) \simeq 76.5 \text{ MeV}. \tag{3.16}$$

Quark pairs couple as in eq. (1.89), the GIM mechanism ensuring that all flavour-changing terms cancel. The total width to u $\overline{\rm u}$, d $\overline{\rm d}$, c $\overline{\rm c}$, s $\overline{\rm s}$ and b $\overline{\rm b}$ channels (allowing three for colour and neglecting masses) is then 1538 MeV, producing an estimated total width $\Gamma_{\rm Z}(\text{total}) \simeq 2.22$ GeV. QCD corrections increase these estimates by a factor$\sim$ 1.1. The branching ratio to charged leptons is $\sim 3.4\%$, to three (invisible) neutrino channels 20.5% and to hadrons (via hadronization of the $q\ \overline{q}$ channels) $\sim 69.3\%$.

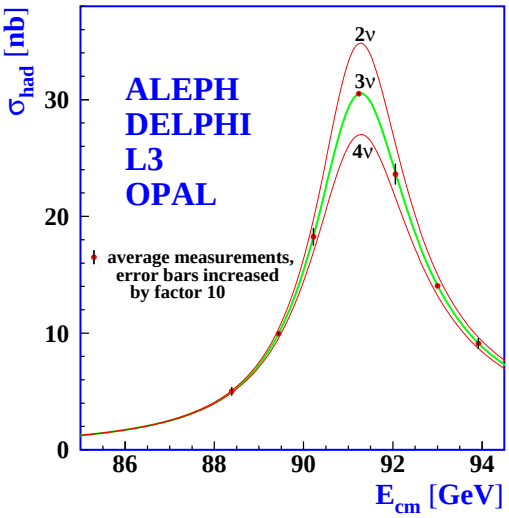

Figure 3.11: The cross section $e^+ e^- \rightarrow$ hadrons around the Z mass (The ALEPH Collaboration et al., 2006). The three different lines are the predictions of the Standard Model assuming two, three or four massless neutrino species respectively.

The total Z width Γ_Z is an interesting quantity. If we assume that, for any fermion family additional to th three known ones, only the neutrinos are significantly less massive than $M_Z/2$, we have

$$\Gamma_Z \simeq 2.5 + 0.16 \Delta N_\nu \text{ GeV} \tag{3.17}$$

where ΔN_ν is the number of additional light neurinos (i.e. beyond ν_e, ν_μ, ν_τ) which contribute to the width through the process $Z \rightarrow \nu\overline{\nu}$. Thus eq. (3.17) can be used as an important measure of such neutrinos (i.e. generations) if Γ_Z can be determined accurately enough. The advent of LEP provided precision checks on Γ_Z value: at the cost of anticipating some experimental results, in Figure 3.11 we show data from LEP collaborations (The ALEPH Collaboration et al., 2006), which established $N_\nu = 3$.

Particularly precise determinations of the SM parameters were made at $e^+ e^-$ colliders, LEP and SLC. Consider the process $e^+e^- \rightarrow f\bar{f}$, where f =e, μ, τ, at energies where the lepton masses can be neglected in the final answers. In the lowest order, the process is mediated by both γ and Z annihilation, as shown in Figure 3.12.

The differential cross section (Budny, 1975) for the scattering of unpolarized e^- and e^+ is given by

$$\frac{d\sigma}{d\cos\theta} = \frac{\pi\alpha^2}{2s}[(1+\cos^2\theta)A + \cos\theta B] \tag{3.18}$$

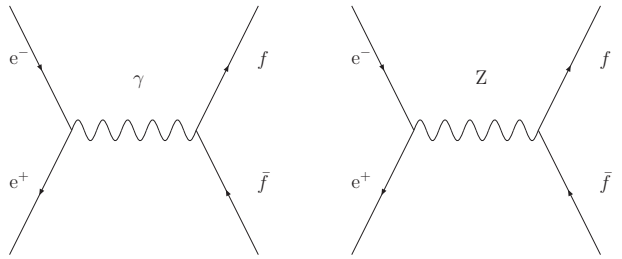

Figure 3.12: (a) One-γ and (b) one-Z annihilation graphs in $e^+e^- \to f\bar{f}$.

where θ is the CM scattering angle of the final state lepton, $s = (p_{e^-} + p_{e^+})^2$ and

$$A = 1 + g_V^e g_V^f \,\mathrm{Re}\,\chi(s) + [(g_A^e)^2 + (g_V^e)^2][(g_A^f)^2 + (g_V^f)^2]|\chi(s)|^2 \tag{3.19a}$$

$$B = 4 g_A^e g_A^f \,\mathrm{Re}\,\chi(s) + 8 g_A^e g_V^e g_a^f g_V^f |\chi(s)|^2 \tag{3.19b}$$

$$\chi(s) = s/[4\sin^2\theta_W \cos^2\theta_W (s - M_Z^2 + i\,\Gamma_Z M_Z)] \tag{3.19c}$$

The term surviving when all the g's are zero is the pure single photon contribution from QED. The presence of the $\cos\theta$ term leads to the forward-backward asymmetry.

The forward-backward asymmetry A_{FB} is defined as

$$A_{FB} \equiv \frac{N_F - N_B}{N_F + N_B} \tag{3.20}$$

where N_F is the number scattered into the forward hemisphere $0 \le \cos\theta \le 1$ and N_B that into the backward hemisphere $-1 \le \cos\theta \le 0$. Integrating eq. 3.18 we find that

$$A_{FB} = 3B/8A. \tag{3.21}$$

For $\sin^2\theta_W = 0.25$ we noted after eq. 1.79 that the g_V^ℓ vanish, so they are very small for $\sin^2\theta_W \sim 0.23$. The effect is controlled essentially by the first term in eq. 3.19b. At $\sqrt{s} = 29$ GeV, for example, the asymmetry is $A_{FB} \sim -0.063$.

However, QED alone produces a small positive A_{FB}, through interference between 1γ and 2γ annihilation processes, which have different charge conjugation parity), as well as between initial and final state bremsstrahlung correction to Figure 3.12a. Indeed, *all* one-loop radiative effects must clearly be considered, in any comparison with modern high precision data.

Many such measurements have been made 'on the Z peak', i.e. at $s = M_Z^2$ in the parametrization 3.19c. In that case, A_{FB} becomes

$$A_{FB}(\text{Z peak}) = \frac{3 g_A^e g_V^e g_A^f g_V^f}{[(g_A^e)^2 + (g_V^e)^2][(g_A^f)^2 + (g_V^f)^2]}. \tag{3.22}$$

Another important asymmetry observable is that involving the difference of the cross section for left and right handed incident electrons:

$$A_{\mathrm{LR}} \equiv \frac{\sigma_{\mathrm{L}} - \sigma_{\mathrm{R}}}{\sigma_{\mathrm{L}} + \sigma_{\mathrm{R}}} \tag{3.23}$$

for which the tree-level prediction is

$$A_{\mathrm{LR}} = \frac{2 g_{\mathrm{V}}^{\mathrm{e}} g_{\mathrm{A}}^{\mathrm{e}}}{[(g_{\mathrm{V}}^{\mathrm{e}})^2 + (g_{\mathrm{A}}^{\mathrm{e}})^2]}. \tag{3.24}$$

A similar combination of the g's for the final state leptons can be measured by forming the 'L-R F-B' asymmetry

$$A_{\mathrm{LRFB}} \equiv \frac{(\sigma_{\mathrm{LF}} - \sigma_{\mathrm{LB}}) - (\sigma_{\mathrm{RF}} - \sigma_{\mathrm{RB}})}{\sigma_{\mathrm{R}} + \sigma_{\mathrm{L}}} \tag{3.25}$$

for which the tree-level prediction is

$$A_{\mathrm{LRFB}} = \frac{2 g_{\mathrm{V}}^{f} g_{\mathrm{A}}^{f}}{(g_{\mathrm{V}}^{f})^2 + (g_{\mathrm{A}}^{f})^2}. \tag{3.26}$$

The quantity on the right-hand side of eq. 3.26 is usually denoted by A_f.

The asymmetry A_{FB} is not, in fact, direct evidence for parity violation in $\mathrm{e^+e^-} \to \mu^+\mu^-$, since we see from eqs. 3.19a and 3.19b that it is even under $g_{\mathrm{A}}^{\ell} \to -g_{\mathrm{A}}^{\mathrm{e}}$, whereas a true parity-violating effect would involve terms odd (linear) in g_{A}^{ℓ}.

3.5.2 Electroweak Precision Measurements at LEP

Precision measurements at the Z-boson resonance using electron-positron colliding beams began in 1989 at the SLC and at LEP. During 1989-95, the four LEP experiments (ALEPH, DELPHI, L3, OPAL) made high-statistics studies of the production and decay properties of the Z. Although the SLD experiment at the SLC collected much lower statistics, it was able to match the precision of LEP experiments in determining the effective electroweak mixing angle $\sin^2\bar{\theta}_{\mathrm{W}}$ and the rate of Z decay into b and c quarks.

The standard 'lineshape' parameters of the Z are determined from an analysis of the production cross sections of these final states in $\mathrm{e^+\ e^-}$ collisions (Yao et al., 2006, Z mini-review, and references therein). The $\mathrm{Z} \to \nu\overline{\nu}(\gamma)$ state is identified directly by detecting single photon production and indirectly by subtracting the visible partial widths from the total width. Inclusion in this analysis of the forward-backward asymmetry of charged

leptons, $A_{\rm FB}^{(0,\ell)}$, of the τ polarization $P(\tau)$, and its forward-backward asymmetry $P(\tau)^{\rm fb}$ enables the separate determination of the effective vector $\bar{g}_{\rm V}$ and axial vector $\bar{g}_{\rm A}$ couplings of the Z to these leptons and the ratio $\bar{g}_{\rm V}/\bar{g}_{\rm A}$ which is related to the effective electroweak mixing $\sin^2\bar{\theta}_{\rm W}$. LEP was run at energy points on and around the Z mass ($88-94$ GeV) constituting an energy 'scan'. The shape of the cross section variation around the Z peak can be described by a Breit-Wigner ansatz with an energy-dependent total width (Berends et al., 1989; Borrelli et al., 1990; Cahn, 1987). The three main properties of this distribution, the position of the peak, the width of the distribution, and the height of the peak, determine respectively the values of $M_{\rm Z}$, $\Gamma_{\rm Z}$ and $\Gamma(\mathrm{e^+e^-}) \times \Gamma(f\bar{f})$, where $\Gamma(\mathrm{e^+e^-})$ and $\Gamma(f\bar{f})$ are the electron and fermion partial widths of the Z. The quantitative determination of these parameters is done by writing analytic expressions for these cross sections in terms of the parameters, and fitting the calculated cross sections to the measured ones by varying these parameters, taking properly into account all the errors. In principle, a $\mathrm{Z} \to \ell^+\ell^-$ is indistinguishable from a $\gamma^* \to \ell^+\ell^-$ event. This means that also exist quantum-mechanical interference terms in the cross section. Here the * is used to denote that the photon *must* be off mass-shell in order to decay. Single-photon exchange σ_γ^0 and γ-Z interference $\sigma_{\gamma\,\mathrm{Z}}^0$ are included, and the large ($\sim 25\%$) initial-state radiation (ISR) effects are taken into account by convoluting the analytic expressions over a 'Radiator Function' (Bardin and Passarino; Bardin et al., 1990, 1991a,b, 2001; Berends et al., 1989; Borrelli et al., 1990; Cahn, 1987) $H(s,s')$ (see Figure 3.13).

Thus, for the process $\mathrm{e^+e^-} \to f\bar{f}$:

$$\sigma_f(s) = \int H(s,s')\sigma_f^0(s')ds' \tag{3.27}$$

$$\sigma_f^0(s) = \sigma_{\rm Z}^0 + \sigma_\gamma^0 + \sigma_{\gamma\,\mathrm{Z}}^0 \tag{3.28}$$

$$\sigma_{\rm Z}^0 = \frac{12\pi}{M_{\rm Z}^2}\frac{\Gamma(\mathrm{e^+e^-})\Gamma(f\bar{f})}{\Gamma_{\rm Z}^2}\frac{s\Gamma_{\rm Z}^2}{(s-M_{\rm Z}^2)^2+s^2\Gamma_{\rm Z}/M_{\rm Z}^2} \tag{3.29}$$

$$\sigma_\gamma^0 = \frac{4\pi\alpha^2(s)}{3s}Q_f^2N_{\rm c}^f \tag{3.30}$$

$$\sigma_{\gamma\,\mathrm{Z}}^0 = -\frac{2\sqrt{2}\alpha^2(s)}{3}(Q_fG_{\rm F}N_{\rm c}^f\mathcal{G}_{\rm V}^{\mathrm{e^-}}\mathcal{G}_{\rm V}^f)\frac{(s-M_{\rm Z}^2)M_{\rm Z}^2}{(s-M_{\rm Z}^2)^2+s^2\Gamma_{\rm Z}/M_{\rm Z}^2} \tag{3.31}$$

where Q_f is the charge of the fermion, $N_{\rm c} = 3(1)$ for quarks (leptons), and $\mathcal{G}_{\rm V}^f$ is the vector coupling of the Z to the fermion-antifermion pair $f\bar{f}$. Since $\sigma_{\gamma\,\mathrm{Z}}^0$ is expected to be much less than $\sigma_{\rm Z}^0$, the LEP Collaborations have generally calculated the interference term in the framework of the Standard Model.

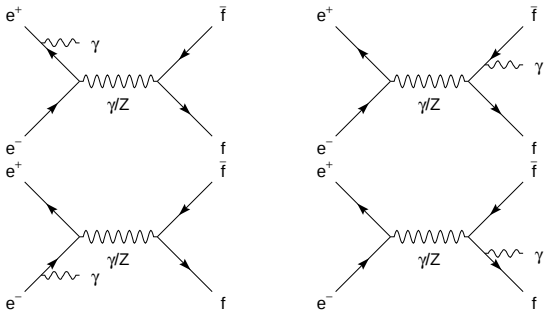

(a) *Radiative corrections.*

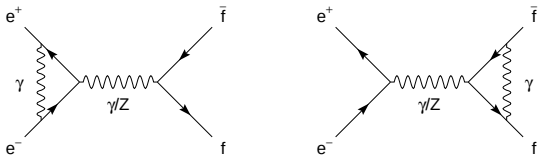

(b) *Vertex corrections.*

Figure 3.13: Some of the lowest order QED corrections to the fermion pair production. Together with photonic box diagrams, which give much smaller contributions, these form a gauge-invariant subset included in the radiator function H.

This fixing of $\sigma^0_{\gamma\,\mathrm{Z}}$ leads to a tighter constraint on M_Z and consequently a smaller error on its fitted value. In the above framework, the QED radiative corrections have been explicitly taken into account by convoluting over the ISR and allowing the electromagnetic coupling constant to run (Burgers et al., 1989): $\alpha(s) = \alpha/(1 - \Delta\alpha)$. On the other hand, weak radiative corrections that depend upon the assumptions of the electroweak theory and on the values of M_t and M_H are accounted for by absorbing them into the couplings, which are then called the effective couplings $\mathcal{G}_\mathrm{V}$ and $\mathcal{G}_\mathrm{A}$. $\mathcal{G}_\mathrm{V}$ and $\mathcal{G}_\mathrm{A}$ are complex numbers with small imaginary parts. As experimental data does not allow simultaneous extraction of both real and imaginary parts of the effective couplings, the convention g^f_A and g^f_V is used. From the definition of A_f

$$A_f = \frac{2 g^f_\mathrm{V} g^f_\mathrm{A}}{(g^f_\mathrm{V})^2 + (g^f_\mathrm{A})^2} \tag{3.32}$$

the lowest-order expressions for the various lepton-related asymmetries on the Z pole are $A^{(0,\ell)}_\mathrm{FB} = (3/4) A_\mathrm{e} A_f$, $P(\tau) = -A_\tau$, $P(\tau)^{fb} = -(3/4) A_\mathrm{e}$, $A_\mathrm{LR} = A_\mathrm{e}$.

The definition of the partial decay width of the Z to $f\bar{f}$ includes the effects of QED and QCD final state corrections, as well as the contribution

due to the imaginary parts of the couplings:

$$\Gamma(f\bar{f}) = \frac{G_{\mathrm{F}} M_{\mathrm{Z}}^3}{6\sqrt{2}\pi} N_{\mathrm{c}}^f \left(|\mathcal{G}_{\mathrm{A}}^f|^2 R_{\mathrm{A}}^f + |\mathcal{G}_{\mathrm{V}}^f|^2 R_{\mathrm{V}}^f \right) + \Delta_{\mathrm{ew/QCD}} \tag{3.33}$$

where R_{V}^f and R_{A}^f are radiator factors to account for final state QED and QCD corrections, as well as effects due to nonzero fermion masses, and $\Delta_{\mathrm{ew/QCD}}$ represents the non-factorizable electroweak/QCD corrections.

Unlike other $f\bar{f}$ decay final state of the Z, the e^+ e^- final state has a contribution not only from the s-channel but also from the t-channel and $s-t$ interference.

The LEP Collaborations have chosen the following primary set of parameters for fitting: M_{Z}, Γ_{Z}, $A_{\mathrm{FB}}^{(0,\ell)}$, $\sigma_{\mathrm{hadron}}^0$, R(lepton), where R(lepton) = Γ(hadrons)/Γ(lepton), $\sigma_{\mathrm{hadron}}^0 = 12\pi\Gamma(\mathrm{e^+e^-})\Gamma(\mathrm{hadrons})/M_{\mathrm{Z}}^2\Gamma_{\mathrm{Z}}^2$. With a knowledge of these fitted parameters and their covariance matrix, any other parameter can be derived. The main advantage of these parameters is that they form a physics motivated set of parameters with much reduced correlations. Thus, the most general fit carried out to cross section and asymmetry data determines the nine parameters: M_{Z}, Γ_{Z}, $\sigma_{\mathrm{hadron}}^0$, $R(\mathrm{e})$, $R(\mu)$, $R(\tau)$, $A_{\mathrm{FB}}^{(0,\mathrm{e})}$, $A_{\mathrm{FB}}^{(0,\mu)}$, $A_{\mathrm{FB}}^{(0,\tau)}$. Assumption of lepton universality leads to a five-parameter fit determining M_{Z}, Γ_{Z}, $\sigma_{\mathrm{hadron}}^0$, R(lepton), $A_{\mathrm{FB}}^{(0,\ell)}$. Combining results from LEP and SLC experiments, the Particle Data Group (Yao et al., 2006) has obtained:

$$M_{\mathrm{Z}} = 91.1876 \pm 0.0021 \text{ GeV/c}^2 \tag{3.34}$$

$$\Gamma_{\mathrm{Z}} = 2.4952 \pm 0.0023 \text{ GeV}. \tag{3.35}$$

The result of the fit to the hadronic cross section is plotted in Figure 3.14.

3.5.3 Electroweak measurements at CMS

The energies achievable in circular colliders are limited by the size of the ring and the strength of the magnetic fields which hold the beam in place. The Large Hadron Collider will operate in a 27 km circumference ring, accelerating protons to 7 TeV.

Another factor limits the energies achievable. The LHC tunnel was previously used by the Large Electron Position collider, which reached a maximum centre of mass energy of 210 GeV. In this case, bremsstrahlung radiation losses limited the energy that the beams could reach. These losses fall with the fourth power of the mass, so are much less significant for protons than electrons. While they can reach higher energies, proton colliders (also known

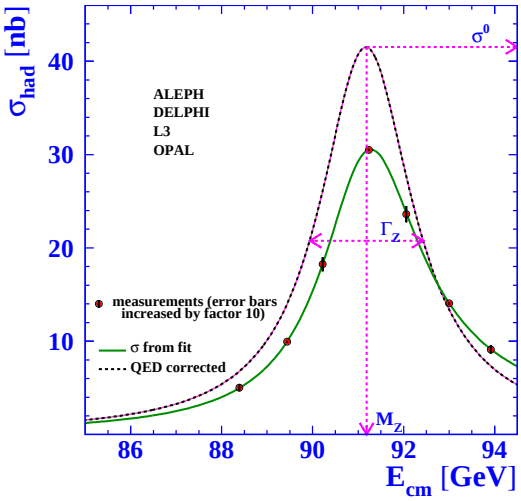

Figure 3.14: Average over measurements of the hadronic cross sections by the four LEP expriments, as a function of center-of-mass energy. The full line represents the result of model-independent fit to the measurements. Correcting for QED photonic effects yields the dashed curve.

as hadron colliders) have one significant disadvantage from the experimental point of view, in that the proton is a composite particle. At the simplest level, it consists of three valence quarks: u u d. The quarks are bound together by gluons, which carry a significant fraction of the proton momentum. There are also short-lived quark anti-quark pairs, known as the quark sea. The gluons, valence and sea quarks are referred to as 'partons'. Proton-proton collisions can then be classified in two ways. First, diffractive collisions, in which one of the protons (or both) remain intact. Diffractive collisions do not contribute to the analysis carried out in this thesis and are not discussed further. The main type of collision of interest here results in both protons dissociating. Dissociative collisions contain two processes: the 'main' collision or hard scattering in such an event, which is in fact a parton-parton collision; the remains of the protons typically continue close to the original beam direction, and form what is known as the underlying event. There is no way to know in advance the fraction of the proton's momentum carried into the hard scattering by each parton. So while the LHC design collision energy is 14 TeV, each hard scattering contains less than this. The probability to find a parton with a certain momentum fraction is given by the parton distribution functions, which are measured experimentally.

The major advantage of electron-positron accelerators is that electrons are (as far as we know) fundamental particles, so carry all of their energy into each collision. Thus, the collision energy can be precisely controlled. So,

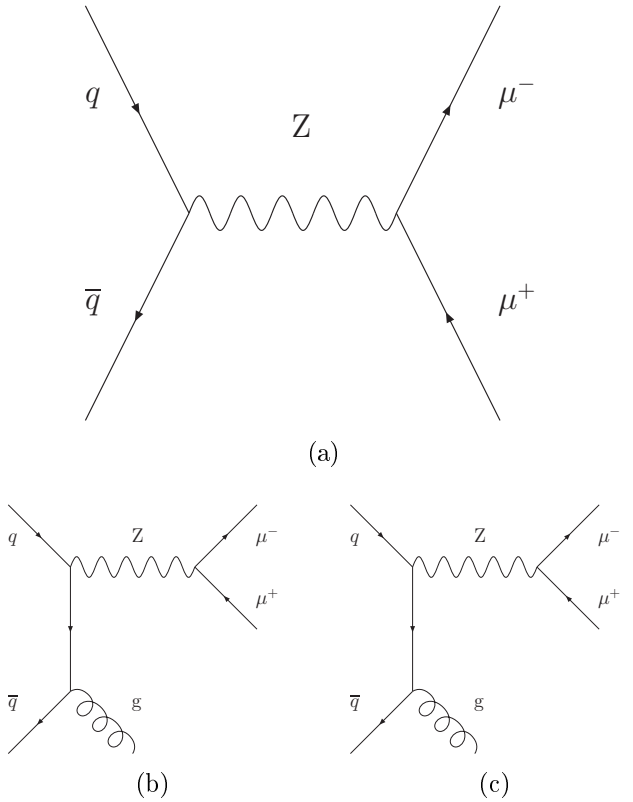

Figure 3.15: Feynman diagrams showing (a) the leading order, (b) and (c) two higher order Z production mechanisms in p $\overline{\text{p}}$ collisions. The muon decay mode of Z is shown.

while electron-positron colliders cannot reach the energies of hadron colliders, they can make detailed studies of a particular particle by running with a collision energy equal to the mass of that particle. The LEP accelerator, as discussed above, collected significant amounts of data around the Z mass, and, as a result, the Z is one of the best understood particles in the Standard Model.

At the LHC collision energy 14 TeV, Z production is dominated by leading order quark anti-quark annihilation (the Drell-Yan process (Drell and Yan, 1971)), shown in Figure 3.15.

The higher order processes in Figure 3.15 contain an additional gluon or quark in the final state, which will appear as a 'jet' of hadrons.

In a hadron collider such as the LHC, the electron and muon Z decay channels are experimentally the easiest to identify, with significant backgrounds to the quark Z decay channels from other (mainly QCD) processes. The muon channel is used in this thesis. In the laboratory rest frame Z bosons

will be produced with a range of momenta, determined by the momenta of the colliding partons. In the Z rest frame, each muon will carry away energy equivalent to half of the Z mass, a signal for the production and decay of a Z thus being the presence of two high energy muons. By measuring the 4-momenta of these muons, it is possible to reconstruct the mass of the Z and many of its other properties. Therefore, to study the Z, CMS must be able to identify and measure its decay products, such as muons.

Although precision measurements of the Z can be performed at CMS, the Z parameters, like mass and width have already been measured at LEP to a much higher precision that could be expected from hadron colliders. There is one exception, namely the forward-backward asymmetry A_{FB} of the lepton pairs in the process $q\overline{q} \rightarrow \mathrm{Z}\gamma \rightarrow \overline{\ell}\ell$. A non-zero A_{FB} arises from the presence of both vector and axial couplings of electroweak bosons to fermions. The Z-quark couplings can be extracted from the distribution of A_{FB} as a function of the invariant mass of the lepton pair. Besides, a measurement of the Z production rate at a hadron collider such as the LHC is an important test of our understanding of the strong force and the composition of the proton, in terms of the parton distribution functions.

Efficiency estimates with tag and probe analysis

A clean sample of muons is necessary to accurately measure from data the tracking and muon identification efficiencies. To keep potential backgrounds and biases under control, the diagnostic sample must be selected with a simple set of cuts. These efficiencies can be analyzed in more detail by using the tag-and-probe methods as a function of several kinematic variables (p_{t}, η and so on).

In actual experimental data taking, $\mathrm{Z} \rightarrow \mu^{+}\mu^{-}$ events constitute an ideal sample to determine muon efficiencies at medium-high momenta ($\gtrsim$ 20 GeV/c). Requiring the selected dimuon invariant mass to be close to M_{Z} yields a high-purity and almost unbiased sample of probe muons. This remains true even if one of the muons is not associated to a track in the central tracker or is not identified in the muon system and fails to meet the trigger requirements. The remaining background can be controlled by tightening the selection cuts on the tag and probe sides of the event.

The event selection requires evidence that a pair of high p_{t} muons is produced. One muon, the *tag muon*, is identified by requiring a track in the central detectors that is matched to a track in the muon detectors, with transverse momentum larger than a chosen value; in our case $p_{\mathrm{t}} > 30$ GeV/c. This ensures that the tag muon is of high confidence and well reconstructed. The second muon, the *probe muon*, can be either a muon reconstructed in

the muon detectors or a tracker track. The muon probe reconstructed in the muon stations is used to calculate the tracker efficiency, while the tracker track probe will be used to calculate the efficiency of the muon reconstruction in the muon system. To further minimize the background, additional cuts on kinematical quantities as well as on transverse momentum are applied to the probe candidate.

Luminosity measurements

The luminosity measurement is used to monitor the LHC's performance in real time and to provide an overall normalization for physics analyses. The design goal for the real time measurement is to determine the average luminosity with a 1% statistical accuracy in 0.1 s. For offline analyses, the design goal is a systematic accuracy of 5%, although every reasonable effort will be made to produce a more accurate result. Both of these requirements must be met over a very large range of luminosities, extending from roughly 10^{28} cm^{-2} s^{-1} to 10^{34} cm^{-2} s^{-1}.

The normalization of physics analyses will ultimately depend on careful measurements of known cross sections such as the p p total cross section or the production rates for W's and Z's. Since the precision pp total cross section measurement can only be done at low luminosities, $\mathscr{L} = 10^{28}$ cm^{-2} s^{-1}, it will be useful to have a normalization technique that is based on production data taking. The production rate for W's and Z's provides just such a "standard candle". Moreover, the rates are high enough — at design luminosity, the raw rate for $Z \to \ell^+\ell^-$ is 30 Hz— such that datasets of only several minutes can be normalized with good statistical accuracy, even when realistic trigger and reconstruction efficiencies are taken into account.

Measurement of the production rate for vector bosons can be done at all luminosities, but requires that all elements of the detector be operating and well understood. Moreover, the statistical accuracy of this method will fall well short of what is required to meet the 1% in 0.1 s goal.

CHAPTER 4

INCLUSIVE CROSS SECTION $\mathrm{p} + \mathrm{p} \rightarrow \mathrm{Z} + X \rightarrow \mu^+ + \mu^- + X$

We consider now the process $\mathrm{p} + \mathrm{p} \rightarrow \mathrm{Z} + X \rightarrow \mu^+ + \mu^- + X$ at $\sqrt{s} =$ 14 TeV. This inclusive process has relatively large cross section and a clear experimental signature, since the muons from Z decay have large transverse momentum and are isolated (see 4.5). The Z production with subsequent decay into two muons will be studied starting from the LHC startup. Indeed, it allows:

- to monitor the LHC collider luminosity assuming that the cross section is well known from theory;
- to calibrate the CMS detector providing a clear sample of unbiased muons ("tag and probe" method);
- possibly, to discover the new physics beyond the SM through the detection of events with two muons with high invariant mass peaking at a given mass resonance (e.g. Z′ resonance).

In this chapter, we deal with an analysis that, for a given integrated luminosity, will lead us to measure the inclusive cross section and the reconstruction efficiencies directly from the real data with no assumption taken from Monte Carlo. This data-driven analysis gives some advantages:

- it can be performed just after the LHC startup, with only few pb^{-1} of integrated luminosity;
- it is independent of Monte Carlo models, thus reducing systematic uncertainties deriving from simulation inaccuracies.

The method used for our analysis follows these steps:

1. Detailed study of $\mathrm{Z} \rightarrow \mu^+\mu^-$ decay for Monte Carlo generated event samples, in order to build a detailed model of the Z mass peak shape;

2. Study of the Monte Carlo generated background samples;

3. Detailed study of the Monte Carlo mass resolution, in order to take into account resolution effects for real data, and to test several fit models;

4. Construction of algorithms allowing the rejection of backgrounds from other channels with two final state muons and the identification of signal events, from which, through a robust fit model, both the number of signal events and the reconstruction efficiences can be determined.

5. For a given integrated luminosity, the counting of the number of signal events, corrected by the reconstruction efficiencies, allows to measure the Z inclusive cross section.

4.1 Physics processes and their generation

Large Monte Carlo samples have been generated with the leading order (LO) generator `PYTHIA` (Sjöstrand et al., 2006). The `MC@NLO` (Frixione and Webber, 2002; Frixione et al., 2003) package, which makes use of the `HERWIG` (Corcella et al., 2001, 2002) Monte Carlo generator, is used to perform next-to-leading order (NLO) calculations, in order to study variations in the acceptance and systematic effects in the LO-NLO transition. Both `PYTHIA` and `MC@NLO` generated samples are simulated and reconstructed using the official CMS software package, `CMSSW`. We concentrate our study on the `PYTHIA` samples, while `MC@NLO` has been used for more detailed generator studies.

4.1.1 Monte Carlo study of the $\mathrm{Z} \rightarrow \mu^+\mu^-$ signal

Details on Monte Carlo signal events, generated by imposing an invariant mass for the muon pair larger than 40 GeV/c^2, are given in Table 4.1.

We note in particular that no cuts have been imposed on muon p_{t}, while the cut on muon η takes into account that the muon reconstruction is performed in this region of the detector, in which the muon detectors are situated.

The distribution for the Z most relevant kinematic quantities are plotted in Figure 4.1.

Table 4.1: Monte Carlo signal samples used in this study: σ is the LO cross section for $m_{\mu^+\mu^-} > 40$ GeV/c^2, ϵ_{gen} is the generator filter efficiency for the cuts applied (listed in the last column), N_{sample} is the number of generated events used in our study and L is the equivalent integrated luminosity.

Sample	σ (nb)	ϵ_{gen}	N_{sample}	L (pb^{-1})	Generator cuts
$Z(\gamma) \to \mu^+\mu^-$	1.795	0.465	146k	175	$\lvert\eta_\mu\rvert < 2.5$

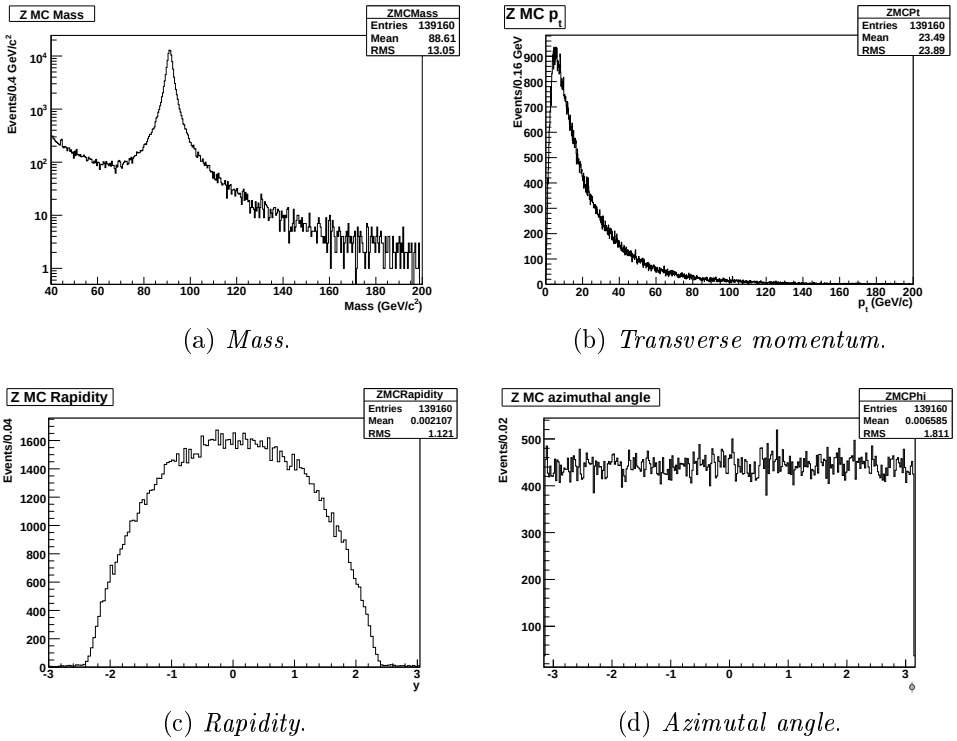

(a) *Mass.* (b) *Transverse momentum.*

(c) *Rapidity.* (d) *Azimutal angle.*

Figure 4.1: Distributions of the kinematic variables for the generated Z.

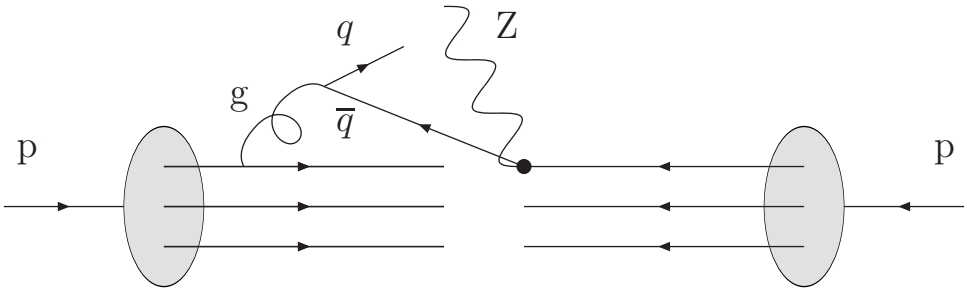

Figure 4.2: Z creation from the annihilation of a "valence" quark and a "sea" antiquark.

The Z creation involves a quark-antiquark $q\ \overline{q}$ pair: while $\overline{q}$ is always a "sea" antiquark, q can be either a "valence" or a "sea" quark; in the latter case (Figure 4.2) q has, on average, a greater momentum than $\overline{q}$, so the Z created in the collision will have a longitudinal component of the momentum different from zero, on average, in the former one, the colliding partons have similar momentum distributions.

We consider now the generated final state muons coming from the Z decay: possibly, they have emitted photons as final state radiation (FSR). In Figure 4.3 the kinematic variable distributions for generated final state muons from Z are plotted: in particular, as for transverse momentum p_{t}, pseudorapidity η and azimutal angle ϕ, the contributions of muons with smaller and larger p_{t} are distinguished with different colors. As far as the muon pair invariant mass is concerned, the step at $m_{\mu^+\mu^-} = 40$ GeV/c^2 is due to the generator cut 40 GeV/c^2 onto the muon invariant mass. The muons are preferably emitted around $\eta = 0$, i.e. orthogonally to the beam axis; we can clearly see the generator cut for $|\eta_\mu| < 2.5$.

Finally, the energy spectrum of the photons emitted as FSR is plotted in Figure 4.4. It has the typical decreasing shape of radiative processes: for high energies it has an exponential shape, while for low energies it points out the presence of an infrared divergence.

Di-muon invariant mass shape model

We now determine a parametric model for the shape of the muon pair invariant mass distribution by a binned χ^2 fit to the mass distribution for the Z. This is the first step of the analysis defined above.

If N_0 is the signal yield and N_{Z} is the number of generated Z, we have:

$$N_0 = N_{\mathrm{Z}}.$$

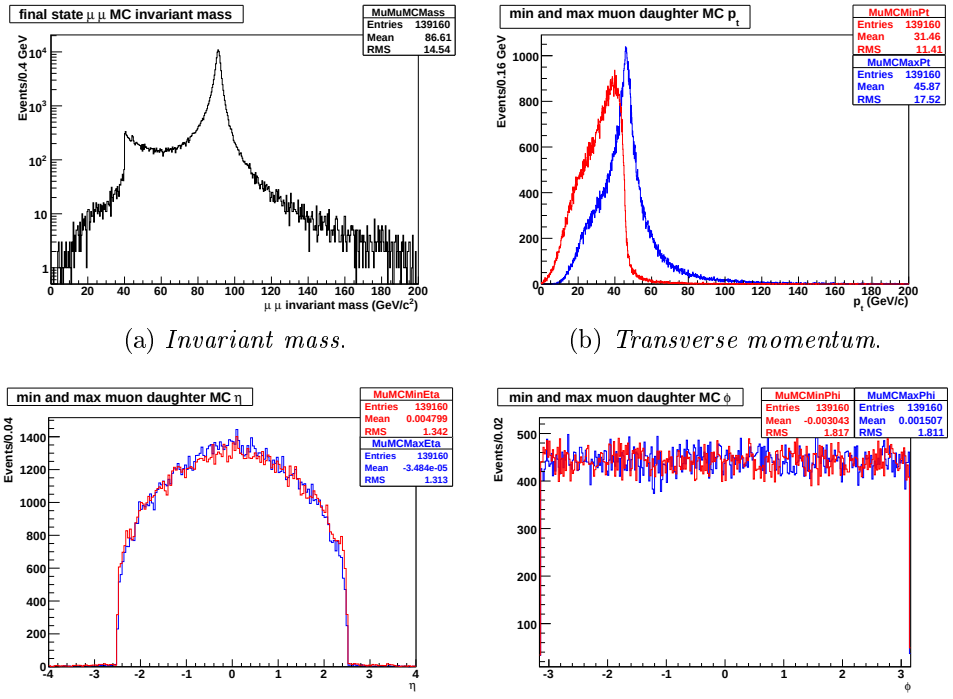

(a) *Invariant mass.* (b) *Transverse momentum.*

(c) *Pseudorapidity.* (d) *Azimutal angle.*

Figure 4.3: Distributions of the kinematic variables for the generated final state muons from Z, with minimum (red) and maximum (blue) transverse momentum.

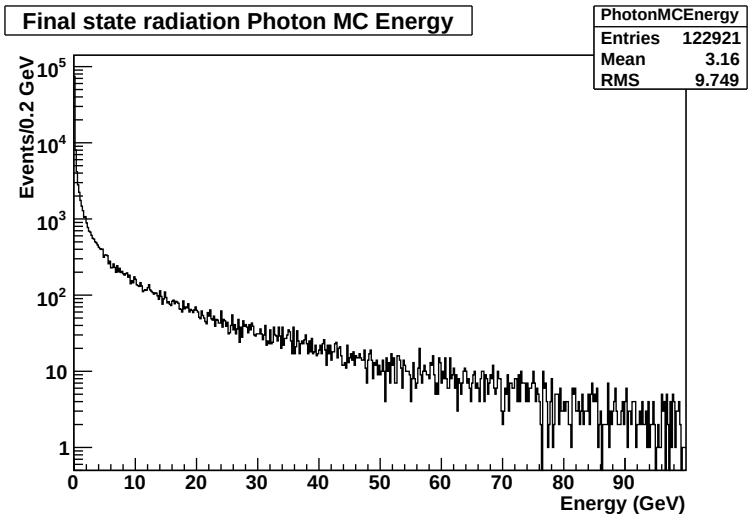

Figure 4.4: Final state radiation emitted by generated muons.

As a first ansatz, we model the signal distribution with the function $H(m)$, which is a linear combination of a relativistic Breit-Wigner (BW), f_{Z}, centered at the Z resonance mass, M, with a width Γ, of Z/γ interference term $f_{\mathrm{Z}/\gamma}$ and of photon propagator f_γ:

$$H(m) = C(M,\Gamma)\left[\alpha \cdot f_{\mathrm{Z}}(m;M,\Gamma) + \beta \cdot f_{\mathrm{Z}/\gamma}(m;M,\Gamma) + \delta \cdot f_\gamma(m)\right] \tag{4.1}$$

with $\alpha+\beta+\delta = 1$, where $C(M,\Gamma)$ is a normalization factor such that $H(m)$ is normalized to unity in the fit range, and

$$f_{\mathrm{Z}}(m;M,\Gamma) = \frac{2}{\pi} \cdot \frac{\Gamma^2 M^2}{(m^2-M^2)^2 + m^4(\Gamma^2/M^2)} \tag{4.2a}$$

$$f_{\mathrm{Z}/\gamma}(m;M,\Gamma) = M \cdot \frac{(m^2-M^2)^2}{(m^2-M^2)^2 + m^4(\Gamma^2/M^2)} \tag{4.2b}$$

$$f_\gamma(m) = \frac{1}{m^2}. \tag{4.2c}$$

We have chosen the complete mass range, between $m_{\min} = 40\ \mathrm{GeV/c^2}$ and $m_{\max} = 200\ \mathrm{GeV/c^2}$ for the fit. The binning of the histogram has been chosen in order to assure a sufficient statistics in each bin. In Table 4.2 we report the mass range, the binning and the bin interval for the fitted histogram.

Table 4.2: Mass range $[m_{\min}, m_{\max}]$, binning N_{bins} and bin width ΔI for the generated Z mass fit.

Histogram	$m_{\min}(\mathrm{GeV/c^2})$	$m_{\max}(\mathrm{GeV/c^2})$	N_{bins}	$\Delta I(\mathrm{GeV/c^2})$
$m_{\mu\mu}$	40	200	400	0.4

If N_0 is the signal yield, the fit function is then:

$$F_{\mathrm{Z}} = N_0 H(m). \tag{4.3}$$

In eq. (4.4) we report the results of the fit.

$$\chi^2 = 2342.71/389 = 6.0224 \tag{4.4a}$$

$$N_0 = 136600 \pm 400 \tag{4.4b}$$

$$M = 91.235 \pm 0.005\ \mathrm{GeV/c^2} \tag{4.4c}$$

$$\Gamma = 2.466 \pm 0.010\ \mathrm{GeV/c^2} \tag{4.4d}$$

$$\beta = -0.001205 \pm 0.000018 \tag{4.4e}$$

$$\delta = 0.799 \pm 0.002. \tag{4.4f}$$

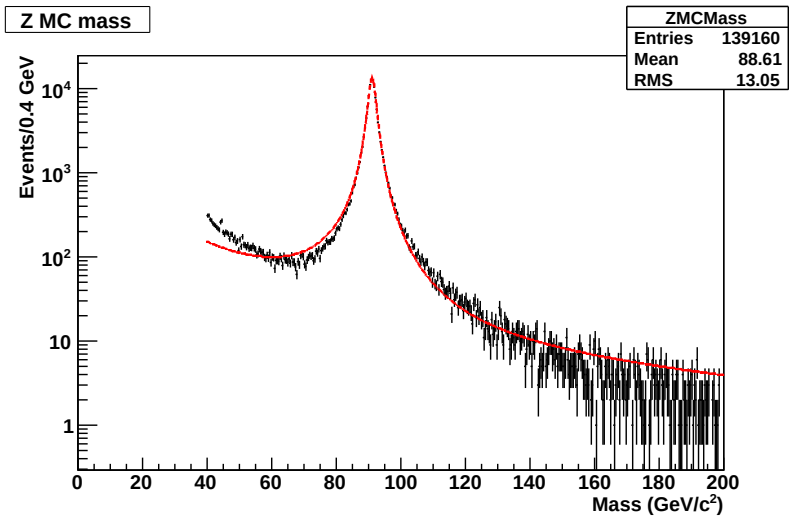

Figure 4.5: Fit of the generated Z mass to the linear combination a relativistic Breit-Wigner (BW), of Z/γ interference term and of photon propagator.

The function obtained from fit, superimposed to the mass distribution of the generated Z, is shown in Figure 4.5.

As Figure 4.5 and the χ^2 show, the fit is not sufficiently accurate. This is due to the need to take into account the contribution of the colliding parton distribution functions, relative to all the possible quark-antiquark pairs (the former relative to a valence or sea quark, the latter relative to a sea antiquark). To model this contribution, we multiply the function $H(m)$ used in the previous fit by a decreasing exponential, considered here as an "effective PDF" term. The signal distribution is then modeled with the function $H'(m)$:

$$H'(m) = C(M,\Gamma,\lambda)e^{-\lambda m} \left[\alpha \cdot f_{\mathrm{Z}}(m;M,\Gamma) + \beta \cdot f_{\mathrm{Z}/\gamma}(m;M,\Gamma) + \delta \cdot f_{\gamma}(m)\right] \tag{4.5}$$

where $C(M,\Gamma,\lambda)$ is a normalization factor such that $H'(m)$ is normalized to unity in the fit range. Choosing again the complete mass range for the fit,

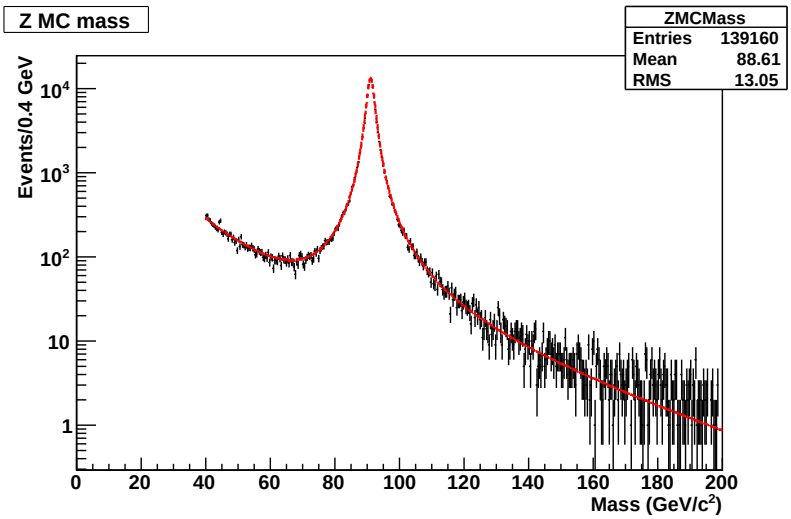

Figure 4.6: Fit of the generated Z mass to the product of a negative exponential with a linear combination a relativistic Breit-Wigner, of Z/γ interference term and of photon propagator.

we obtain:

$$\chi^2 = 422.741/388 = 1.08954 \tag{4.6a}$$
$$N_0 = 138500 \pm 400 \tag{4.6b}$$
$$\lambda = 0.0205 \pm 0.0005\ (\mathrm{GeV/c^2})^{-1} \tag{4.6c}$$
$$M = 91.172 \pm 0.005\ \mathrm{GeV/c^2} \tag{4.6d}$$
$$\Gamma = 2.500 \pm 0.011\ \mathrm{GeV/c^2} \tag{4.6e}$$
$$\beta = (22 \pm 4) \cdot 10^{-5} \tag{4.6f}$$
$$\delta = 0.755 \pm 0.004. \tag{4.6g}$$

The function obtained from fit, superimposed to the mass distribution of the generated Z, is shown in Figure 4.6.

The χ^2 is good, and the Z mass and width are now consistent with their PDG values (see eq. (3.34)). We have thus obtained a satisfactory fit model, for the generated Z by including, besides the relativistic Breit-Wigner and the Z/γ interference term, an exponential term.

Finally, we consider the final state muon pair invariant mass. This distribution differs from the Z invariant mass since we now deal with muons that have possibly emitted FSR photons. We fit this distribution to the function $H'(m)$ in the complete mass range, between $m_{\mathrm{min}} = 40\ \mathrm{GeV/c^2}$ and $m_{\mathrm{max}} = 200\ \mathrm{GeV/c^2}$, choosing a binning for the histogram that ensures a sufficient statistics in each bin.

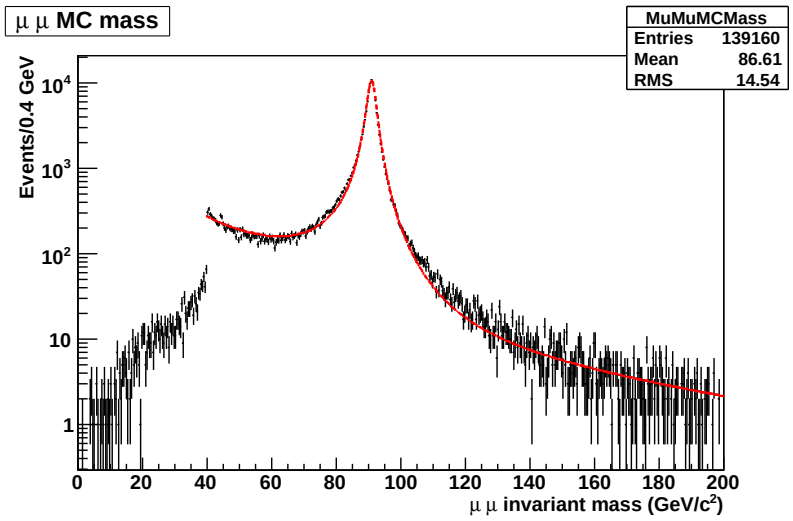

Figure 4.7: Fit of the generated final state $\mu^+ \mu^-$ pair invariant mass to the product of a negative exponential with a linear combination a relativistic Breit-Wigner, of Z/γ interference term and of photon propagator.

The fit yields:

$$\chi^2 = 1160.61/380 = 3.05423 \tag{4.7a}$$
$$N_0 = 136700 \pm 400 \tag{4.7b}$$
$$\lambda = 0.0056 \pm 0.0005 \ (\mathrm{GeV/c^2})^{-1} \tag{4.7c}$$
$$M = 91.089 \pm 0.007 \ \mathrm{GeV/c^2} \tag{4.7d}$$
$$\Gamma = 2.986 \pm 0.014 \ \mathrm{GeV/c^2} \tag{4.7e}$$
$$\beta = -0.00143 \pm 0.00002 \tag{4.7f}$$
$$\delta = 0.848 \pm 0.003. \tag{4.7g}$$

The function obtained from fit, superimposed to the invariant mass distribution of the generated final state $\mu^+ \mu^-$ pair, is shown in Figure 4.7.

As the not good χ^2 shows, the model we have chosen for the muon pair invariant mass distribution is not accurate enough: in particular, looking at Figure 4.7, we can see that the off-peak regions are not sufficiently modeled. Besides, the effect of FSR is clearly visible: the width Γ is larger than the PDG value. This implies that, in our model, we have to take the presence of FSR into account.

In conclusion, we can consider the parametrization obtained by this fit as an effective description of the final state muon pair invariant mass, without the attempt to give interpretation of the fitted "Z mass" and "Z width" as the physical Z boson parameters. We do not attempt a better description

of this model, since the remaining effect of the finite detector resolution will have more impact on the fit model, as described in section 4.2.

4.1.2 The backgrounds

Several Monte Carlo samples are used to estimate the background contamination in $Z \to \mu^+\mu^-$ selected events: they are listed in Table 4.3.

$W \to \mu\nu$, generated at the LO, is considered a background in $Z \to \mu^+\mu^-$ analysis. This sample has only one muon in the final state; however, a pair of muons, the former coming from the W decay, the latter from decay of a charged hadron (like B, π, K) in the underlying event — i.e. soft interaction processes deriving from parton fragments of the colliding protons not involved in the hard scattering —, can give an invariant mass in the range we study in our analysis. The contribution from $\tau \to \mu\nu_\tau$ decays is estimated with $Z \to \tau^-\tau^+$ sample generated with `PYTHIA` by imposing an invariant mass for the tau pair $70\ \mathrm{GeV/c^2} < M < 130\ \mathrm{GeV/c^2}$. The sample of $t\ \bar{t}$ events containing muons is inclusive. The efficiencies mentioned in Table 4.3 are not filter efficiencies, but "generation efficiencies", i.e. the fraction of generated events in which the muons pass the kinematic cuts imposed; therefore they do not need to be taken into account in calculating the luminosity corresponding to the various samples. A large sample of QCD events containing muons is used to simulate the kinematics and approximate rate of inclusive muon events. For the last two samples, the generation of multi-parton processes in hadronic collisions has been performed by the package `ALPGEN` (Mangano et al., 2003), interfaced to `PYTHIA` for the development of the parton shower and for the calculation of the partonic distribution functions (PDF), using the dedicated packages `CTEQ6L` (Pumplin et al., 2002) and `CTEQ6.5M` (Tung et al., 2007).

4.2 Monte Carlo matching truth

In order to compare data from generated and reconstructed particles, a Monte Carlo truth matching between generated and reconstructed particles has been implemented. The MC matching is based on a distance defined in terms of the pseudorapidity η and of the azimutal angle ϕ. A final state reconstructed particle (i.e. a particle seen by the detector) is associated to a particle from the MC generator if the distance

$$\Delta R = \sqrt{(\Delta\eta)^2 + (\Delta\phi)^2} \tag{4.8}$$

Table 4.3: Monte Carlo background samples used in this study: σ is the cross section, ϵ_{gen} is the generator filter efficiency for the cuts applied (listed in the last column), N_{sample} is the number of generated events used in our study and L is the equivalent integrated luminosity.

Sample	Generator	σ (nb)	ϵ_{gen}	N_{sample}	L (pb^{-1})	Generator cuts
$W \rightarrow \mu\nu$	PYTHIA	17.17	0.6418	1M	90	$\lvert\eta_\mu\rvert < 2.5$
$Z(\gamma) \rightarrow \tau\tau$	PYTHIA	1.596	1.0	1M	600	70 GeV/c^2 $< M <$ 130 GeV/c^2
$t\bar{t}$ + 0 jets	ALPGEN + PYTHIA	0.619	0.0174	1.2M	2000	no cuts
$t\bar{t}$ + 1 jet	ALPGEN + PYTHIA	0.176	0.00593	350k	2000	no cuts
$t\bar{t}$ + 2 jets	ALPGEN + PYTHIA	0.034	0.000412	70k	2000	no cuts
$t\bar{t}$ + 3 jets	ALPGEN + PYTHIA	0.006	0.000343	12k	2000	no cuts
$t\bar{t}$ + 4 jets	ALPGEN + PYTHIA	0.0015	0.000269	3k	2000	no cuts
QCD $pp \rightarrow \mu X$	ALPGEN + PYTHIA	$8199 \cdot 10^3$	0.00028	2M	0.05	$\hat{p}_t > 20$ GeV/c, $p_{t,\,\mu} > 15$ GeV/c

is smaller than a 0.15, where $\Delta\eta$ and $\Delta\phi$ are the differences in pseudorapidity and azimutal angle between the vertexes of the trajectory of the particles.

The Monte Carlo truth matching of a composite object, like a reconstructed $Z \rightarrow \mu^+\mu^-$ is done in two steps:

1. Matching of final state particles to final state generator particles (in this case the muons);
2. Matching of reconstructed composite objects to composite MC parents (in this case the Z).

4.2.1 Z Monte Carlo mass resolution

Using MC truth association, we can determine the mass resolution for the Z candidate reconstructed from muon pairs. For this analysis, we use the raw alignment conditions expected for the first data-taking period. As a first step, we define the MC mass resolution as the difference between the reconstructed Z candidate and the generated Z mass. Only reconstructed Z candidates matched to a Monte Carlo one are used in the analysis, in order to avoid combinatorial background. With this definition, actually, we compare the invariant mass of the final state reconstructed muons with a generated Z particle before the simulation of the final state radiation photon. Thus, we find, as we can see in Figure 4.8, a radiative tail, due to final state radiation, on the left of the peak.

The mass resolution is then determined as the difference between the mass of the reconstructed Z candidate (i.e. the invariant mass of the reconstructed muon pair) and the invariant mass of the generated final state muon pair (after possible final state radiation) from Z decay. Again, only reconstructed Z candidates matched to a Monte Carlo particle are used in this analysis, in order to avoid combinatorial background. Doing so, we eliminate the asymmetric tail due to final state radiation. The MC mass resolution is modeled with three different fit functions:

- Gaussian:

$$G(\Delta M; \mu, \sigma) = \frac{1}{\sqrt{2\pi}\sigma} \exp\left[-\frac{(\Delta M - \mu)^2}{2\sigma^2}\right]; \tag{4.9}$$

- Linear combination of two Gaussians: the 2 Gaussians have the same mean and different widths

$$\begin{aligned} G_{1,2}(\Delta M; \mu, \sigma_1, \sigma_2) = \cdot \Bigg\{ & a \cdot \frac{1}{\sqrt{2\pi}\sigma_1} \exp\left[-\frac{(\Delta M - \mu)^2}{2\sigma_1^2}\right] \\ & + (1-a) \cdot \frac{1}{\sqrt{2\pi}\sigma_2} \exp\left[-\frac{(\Delta M - \mu)^2}{2\sigma_2^2}\right] \Bigg\} \end{aligned} \tag{4.10}$$

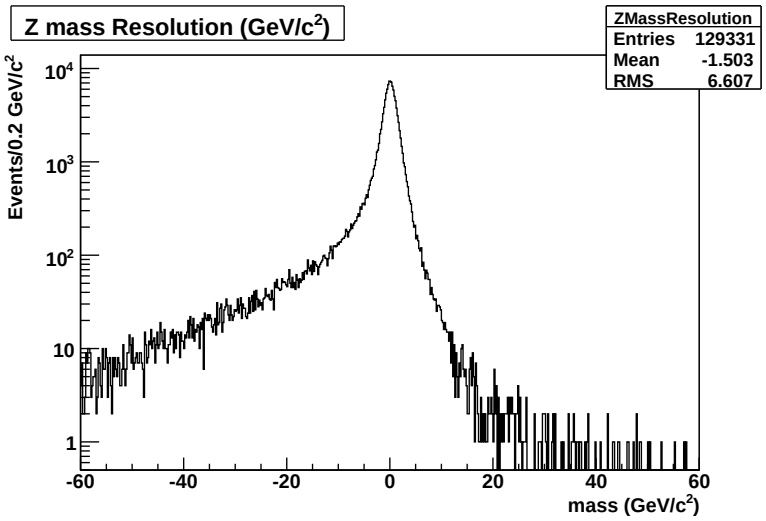

Figure 4.8: Distribution of the MC mass resolution, defined as the difference between the reconstructed Z candidate and the generated Z mass. The asymmetric tail on the left is clearly visible.

- Linear combination of three Gaussians: the 3 Gaussians have different mean values and widths

$$\begin{aligned} G_{1,2,3}(\Delta M;\mu_1,\mu_2,\mu_3,\sigma_1,\sigma_2,\sigma_3) = \cdot \Bigg\{ & a\cdot\frac{1}{\sqrt{2\pi}\sigma_1}\exp\left[-\frac{(\Delta M-\mu_1)^2}{2\sigma_1^2}\right] \\ & + b\cdot\frac{1}{\sqrt{2\pi}\sigma_2}\exp\left[-\frac{(\Delta M-\mu_2)^2}{2\sigma_2^2}\right] \\ & +(1-a-b)\cdot\frac{1}{\sqrt{2\pi}\sigma_3}\exp\left[-\frac{(\Delta M-\mu_3)^2}{2\sigma_3^2}\right]\Bigg\} \end{aligned} \tag{4.11}$$

We have chosen the mass resolution range, between $\Delta M_{\min} = -10$ GeV/c^2 and $\Delta M_{\max} = 10$ GeV/c^2 for the fit. The binning of the histogram has been chosen in order to assure a sufficient statistics in each bin. In Table 4.4 we report the mass resolution range, the binning and the bin interval for the fitted histogram.

If N_0 is the resolution yield, the fit functions are then:

$$F_1 = N_0 G(\Delta M;\mu,\sigma) \tag{4.12a}$$
$$F_{1,2} = N_0 G_{1,2}(\Delta M;\mu,\sigma_1,\sigma_2) \tag{4.12b}$$
$$F_{1,2,3} = N_0 G_{1,2,3}(\Delta M;\mu_1,\mu_2,\mu_3,\sigma_1,\sigma_2,\sigma_3). \tag{4.12c}$$

Table 4.4: Mass resolution range $[\Delta M_{min}, \Delta M_{max}]$, binning N_{bins} and bin width ΔI for the Z MC mass resolution fits.

Histogram	$\Delta M_{min}(GeV/c^2)$	$\Delta M_{max}(GeV/c^2)$	N_{bins}	$\Delta I(GeV/c^2)$
ΔM_Z	-10	10	100	0.2

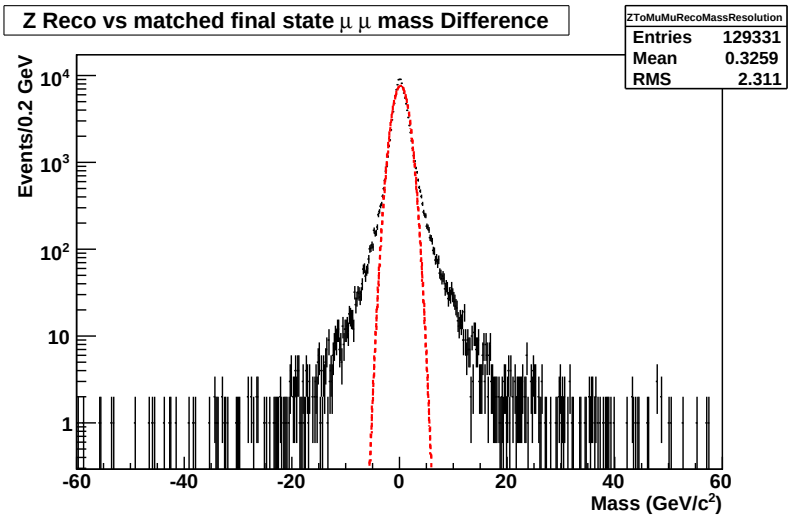

Figure 4.9: Fit of the Z mass resolution to a Gaussian.

In eq. (4.13) we report the results of the fit to the simple Gaussian.

$$\chi^2 = 8640.13/97 = 89.0735 \tag{4.13a}$$
$$N_0 = 119900 \pm 300 \tag{4.13b}$$
$$\mu = 0.243 \pm 0.004 \text{ GeV/c}^2 \tag{4.13c}$$
$$\sigma = 1.269 \pm 0.004 \text{ GeV/c}^2. \tag{4.13d}$$

The function obtained from fit, superimposed to the Z mass resolution, is shown in Figure 4.9.

The χ^2 is not good, and the mean value μ is not consistent with zero. The muon resolution is a function of η, so it cannot be well represented as a single Gaussian if averaged over the whole η range.

In eq. (4.14) we report the results of the fit to the linear combination of

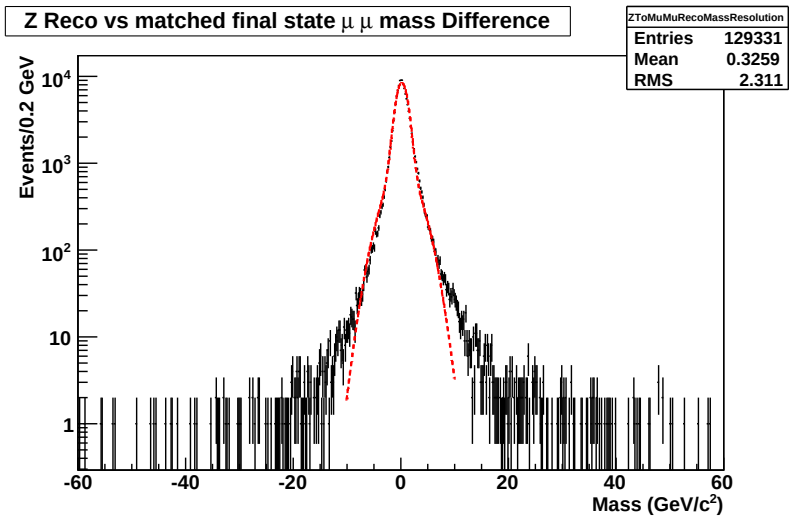

Figure 4.10: Fit of the Z mass resolution to a linear combination of two Gaussians.

two Gaussians.

$$\chi^2 = 1420.26/95 = 14.9501 \tag{4.14a}$$
$$N_0 = 127100 \pm 400 \tag{4.14b}$$
$$a = 0.228 \pm 0.005 \tag{4.14c}$$
$$\mu = 0.233 \pm 0.004 \text{ GeV/c}^2 \tag{4.14d}$$
$$\sigma_1 = 2.94 \pm 0.03 \text{ GeV/c}^2 \tag{4.14e}$$
$$\sigma_2 = 1.027 \pm 0.006 \text{ GeV/c}^2. \tag{4.14f}$$

The function obtained from fit, superimposed to the Z mass resolution, is shown in Figure 4.10.

The χ^2 improves, but is not fully satisfactory yet. The mean value μ is still not consistent with zero.

In eq. (4.15) we report the results of the fit to the linear combination of three Gaussians, having different average values to take into account the

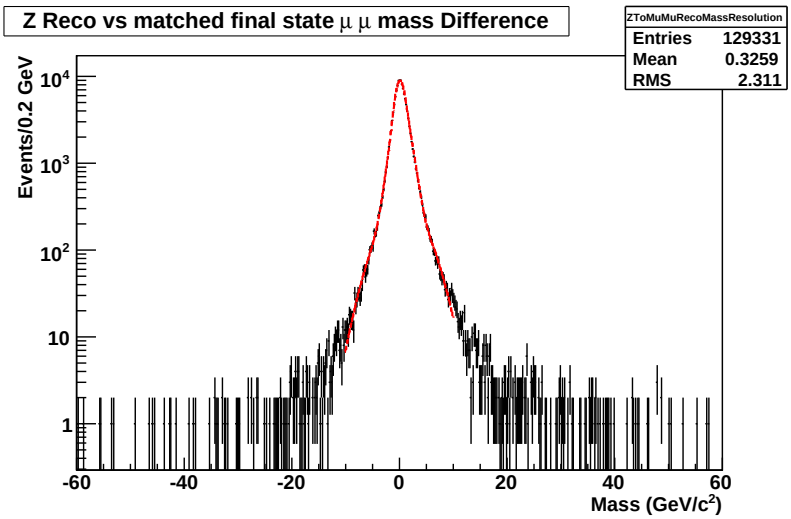

Figure 4.11: Fit of the Z mass resolution to a linear combination of three Gaussians.

asymmetry of the data.

$$\chi^2 = 189.247/91 = 2.07964 \tag{4.15a}$$
$$N_0 = 128500 \pm 400 \tag{4.15b}$$
$$a = 0.42 \pm 0.02 \tag{4.15c}$$
$$b = 0.458 \pm 0.019 \tag{4.15d}$$
$$\mu_1 = 0.113 \pm 0.009 \text{ GeV/c}^2 \tag{4.15e}$$
$$\mu_2 = 0.385 \pm 0.015 \text{ GeV/c}^2 \tag{4.15f}$$
$$\mu_3 = 0.67 \pm 0.04 \text{ GeV/c}^2 \tag{4.15g}$$
$$\sigma_1 = 0.782 \pm 0.016 \text{ GeV/c}^2 \tag{4.15h}$$
$$\sigma_2 = 1.53 \pm 0.04 \text{ GeV/c}^2 \tag{4.15i}$$
$$\sigma_3 = 3.84 \pm 0.08 \text{ GeV/c}^2. \tag{4.15j}$$

The function obtained from fit, superimposed to the Z mass resolution, is shown in Figure 4.11.

The χ^2 improves again, but is not fully satisfactory. No mean values μ_i, $i = 1, 2, 3$ are consistent with zero.

In conclusion, the resolution function is expected to have significant outlier tails with respect to the simple gaussian model.

4.3 Z reconstruction algorithm

Z candidates are reconstructed starting from the final state muons revealed

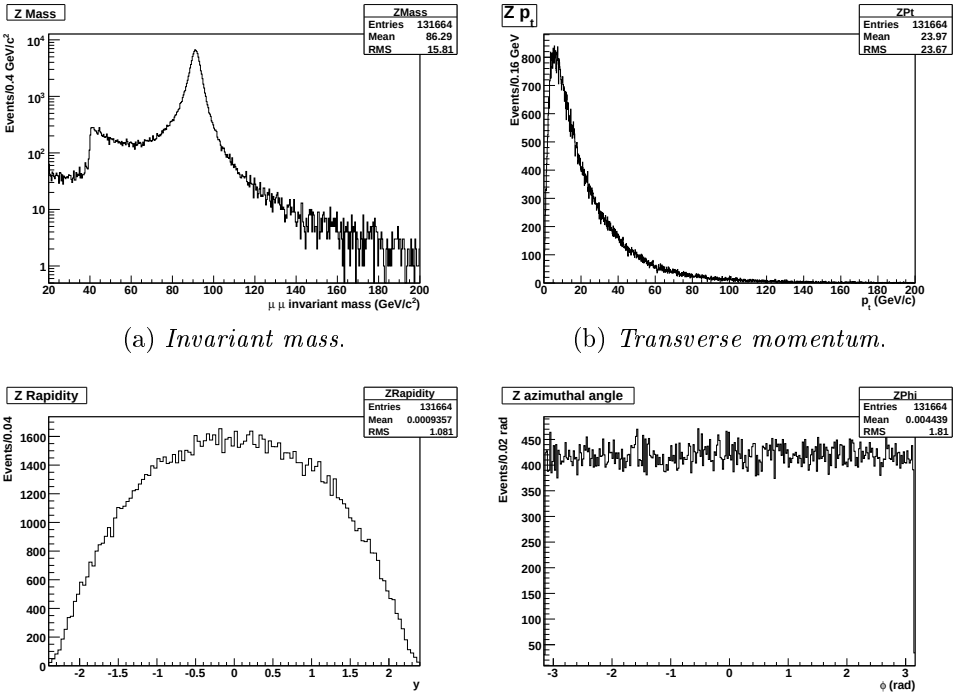

(a) *Invariant mass.* (b) *Transverse momentum.*

(c) *Rapidity.* (d) *Azimutal angle.*

Figure 4.12: Distributions of the kinematic variables for the reconstructed Z.

in the detector. The $Z \rightarrow \mu^+\mu^-$ candidates are built from the combination of pairs of particles with opposite charges with an invariant mass $M_{\mu\mu} > 20$ GeV/c^2; besides, $|\eta| < 2.5$ is required for both muons. This wide invariant mass range allows to take events with a virtual Z (possibly interfering with a virtual photon) into account.

The distribution for the most relevant kinematic quantities of the Z reconstructed from the analyzed samples of $Z \rightarrow \mu^+\mu^-$ signal events are plotted in Figure 4.12. The Z mass peak is clearly visible in the muon pair invariant mass; in good agreement with the Monte Carlo distributions, we find that the Z transverse momentum rapidly increases from zero to the maximum value at ~ 10 GeV/c.

A muon can be reconstructed as a track in the central tracker (*track candidate*) or as a track in the muon detector (*standalone muon* or *standalone candidate*). The muon reconstruction provides also an algorithm to match internal and external tracks: if the matching is successful, the two tracks are combined and a *global muon* is built.

Therefore, three categories of $Z \rightarrow \mu^+\mu^-$ candidates are built, according to type of input muons used in the reconstruction:

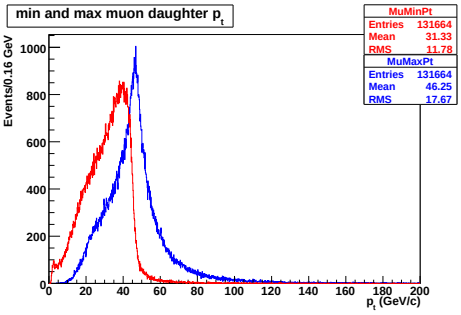

(a) *Transverse momentum.*

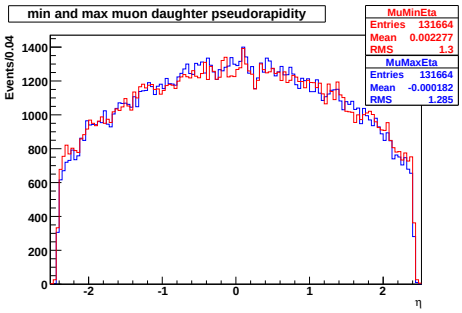

(b) *Pseudorapidity.*

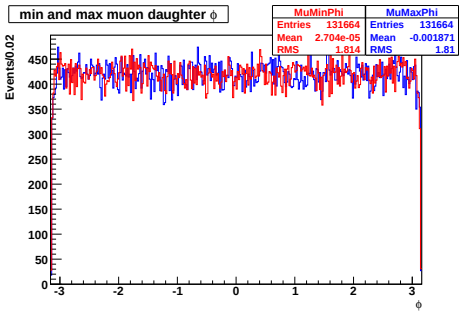

(c) *Azimutal angle.*

Figure 4.13: Distributions of the kinematic variables for the final state muons from which Z is reconstructed in the collection $Z_{\mu\,\mu}$, with minimum (red) and maximum (blue) transverse momentum.

- $Z_{\mu\,\mu}$ candidates, built from pairs of global muon candidates;
- $Z_{\mu\,t}$ candidates, built from a global muon and a track candidate;
- $Z_{\mu\,s}$ candidates, built from a global muon and a standalone candidate.

In Figure 4.13 the kinematic variable distributions for muons from the collection $Z_{\mu\,\mu}$ are plotted: in particular, as for transverse momentum, rapidity and azimutal angle, the contributions of muons with smaller and larger p_t are distinguished. The muons are mainly emitted for $\eta = 0$, that is orthogonally to the beam axis; we can clearly see the generator cut for $|\eta_\mu| < 2.5$.

4.3.1 Efficiency of the Z reconstruction algorithm

Plotting in Figure 4.14 , for $Z \rightarrow \mu^+\mu^-$ events, the number of Z candidates, taken from the collection $Z_{\mu\,\mu}$, reconstructed for each event, we see that:

- In most cases, the algorithm reconstructs correctly one Z from the muon pair per event;

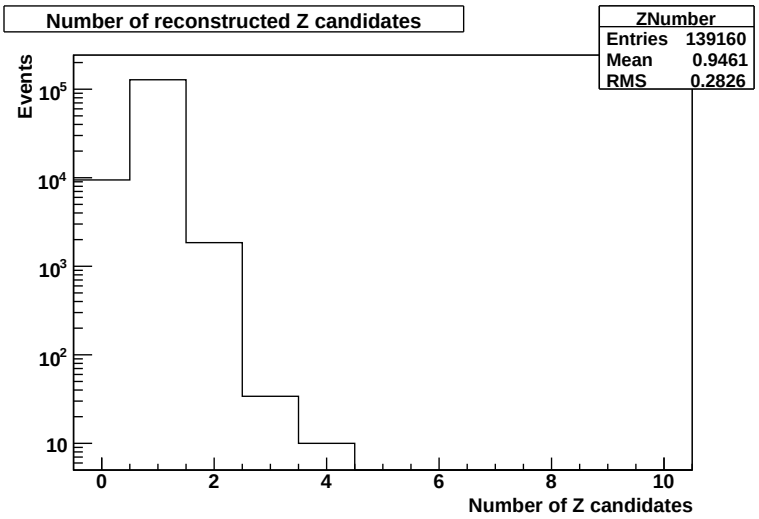

Figure 4.14: Number of $Z_{\mu\ \mu}$ candidates reconstructed per each event.

- In some cases, the algorithm fails, and no Z particles are reconstructed;
- Finally, the algorithm reconstructs two or more Z candidates per event, even if the MC truth ensures the presence of only one Z in the event ($\sim$ at percent level).

In the last case, we obtain events in which, besides a Z reconstructed correctly, there is one or more fake Z candidates, coming from the random combination of a muon pair with invariant mass greater than 20 GeV/c^2. These fake Z cannot be associated to a generated Z. They can be then identified looking for Z candidates not associated to generated Z. The number of fake Z gets hardly reduced when the isolation cut is applied (see section 4.5). In Figure 4.15 we plot the most relevant kinematic quantities for the fake Z taken from the collection $Z_{\mu\ \mu}$. The invariant mass distribution is peaked at low mass values, and decreases rapidly for increasing mass, the transverse momentum distrution rapidly increases from zero to the peak, at $\sim$ 40 GeV/c and equally rapidly decreases, and, finally, the maximum value of the η distribution is zero.

4.4 Fit of the Z $\rightarrow \mu^+\mu^-$ signal

We now build and test a fit model for Z mass peak shape obtained from the invariant mass distribution of the reconstructed muon pairs. In doing so, we have to take into account the parametrization of the Z mass peak

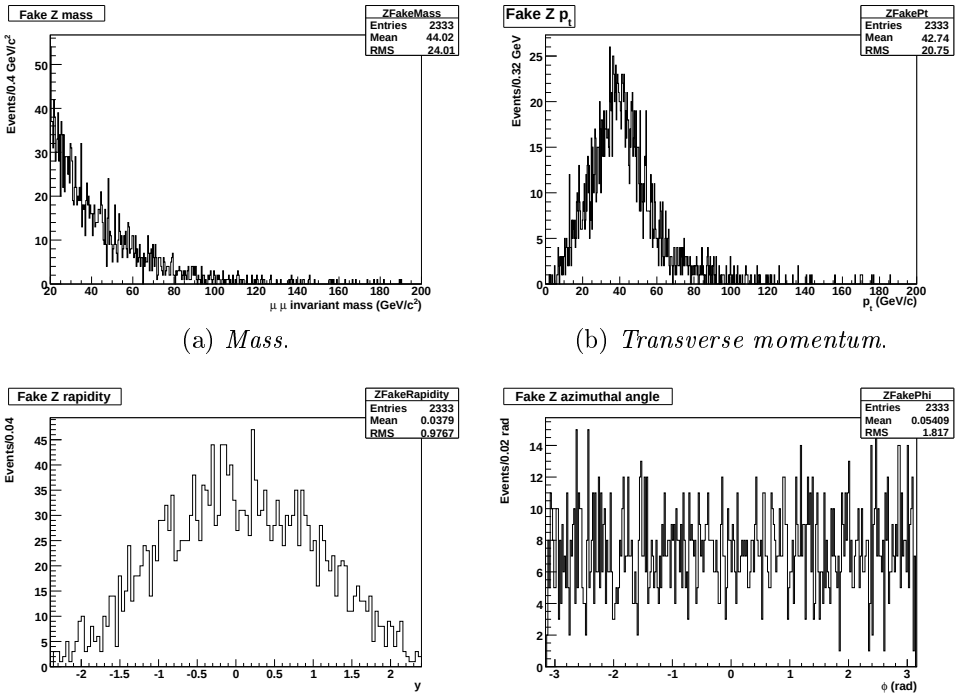

(a) *Mass.* (b) *Transverse momentum.*

(c) *Rapidity.* (d) *Azimutal angle.*

Figure 4.15: Distributions of the kinematic variables for the fake Z.

shape obtained in the detailed Monte Carlo studies in section 4.1.1, and the Monte Carlo mass resolution defined in section 4.2.1. Thus, we try to fit the reconstructed Z $\rightarrow \mu^+\mu^-$ mass distribution, for candidates taken from the collection $Z_{\mu\,\mu}$, to the convolution of the function that models the generated invariant mass with one of the resolution functions, i.e. the Gaussian (4.9) and the linear combination of two (4.10) and three Gaussians (4.11). Actually, we need higher statistics for the muon pair invariant mass distribution in order to determine correctly the resolution parameters of more than one Gaussian. Thus, the fit function is the convolution of the product of an exponential with the linear combination of the relativistic Breit-Wigner, of Z/γ^* interference term and of photon propagator $H'(m)$ (4.5), with a Gaussian:

$$P(m) = C(M, \Gamma, \lambda, \mu, \sigma) \int H'(m') \cdot G(m - m'; \mu, \sigma) dm' \qquad (4.16)$$

where $C(M, \Gamma, \lambda, \mu, \sigma)$ is a normalization factor such that $P(m)$ is normalized to unity in the fit range. We have chosen the complete mass range, between $m_{\min} = 40$ GeV/c^2 and $m_{\max} = 200$ GeV/c^2, for the fit. Besides, to better model the reconstructed Z mass peak shape, we perform a fit to the convolution of linear combination of the relativistic Breit-Wigner, of Z/γ^* interference term and of photon propagator $H(m)$ (4.1) with a Gaussian:

$$P(m) = C(M, \Gamma, \mu, \sigma) \int H(m') \cdot G(m - m'; \mu, \sigma) dm' \qquad (4.17)$$

in the mass range between $m_{\min} = 60$ GeV/c^2 and $m_{\max} = 120$ GeV/c^2, in order to neglect the contribution from the negative exponential, considered as an effective PDF. The binning of the histogram has been chosen in order to assure a sufficient statistics in each bin. In Table 4.5 we report the mass range, the binning and the bin interval for the fitted histogram.

Table 4.5: Mass range $[m_{\min}, m_{\max}]$, binning N_{bins} and bin width ΔI for the reconstructed Z mass fit.

Histogram	$m_{\min}$(GeV/c^2)	$m_{\max}$(GeV/c^2)	N_{bins}	ΔI(GeV/c^2)
$m_{\mu\mu}$	40	200	400	0.4
$m_{\mu\mu}$	60	120	150	0.4

The parameters M and Γ modeling the Z mass peak shape are not to be interpreted as the physical Z mass and width (see the discussion in section 4.1.1): they should be intended as phenomenological parameters, left

floating in the fit in order to take into account the effect of final state radiation. When taking into account the resolution effects, the mean value μ of the Gaussian is fixed to 0, and the standard deviation σ is left as a free parameter in the fit. If N_0 is the signal yield, the fit function is then:

$$F_{\mathrm{Z}} = N_0 P(m). \tag{4.18}$$

In eq. (4.19) we report the results of the fit over the wide mass range.

$$\chi^2 = 462.288/385 = 1.20075 \tag{4.19a}$$
$$N_0 = 127500 \pm 400 \tag{4.19b}$$
$$\lambda = 0.0105 \pm 0.0008 \ \mathrm{GeV}^{-1}\mathrm{c}^2 \tag{4.19c}$$
$$M = 91.337 \pm 0.011 \ \mathrm{GeV/c}^2 \tag{4.19d}$$
$$\Gamma = 4.05 \pm 0.03 \ \mathrm{GeV/c}^2 \tag{4.19e}$$
$$\beta = -0.00164 \pm 0.00004 \tag{4.19f}$$
$$\delta = 0.805 \pm 0.006 \tag{4.19g}$$
$$\mu = 0 \quad \text{(fixed)} \tag{4.19h}$$
$$\sigma = 0.81 \pm 0.04 \ \mathrm{GeV/c}^2. \tag{4.19i}$$

The function obtained from fit, superimposed to the mass distribution of the reconstructed Z, is shown in Figure 4.16.

The fit appears to model the Z mass peak with sufficient accuracy, as the quite good χ^2 shows. Besides, the value of the width for the Gaussian resolution function is consistent with the value obtained from MC resolution within 1σ. However, the effect of the wider Gaussian constributions to the invariant mass resolution are absorbed in the parameters of the Breit-Wigner, by increasing the values of the parameters M and Γ.

If we restrict the invariant mass range, we obtain:

$$\chi^2 = 144.334/144 = 1.00232 \tag{4.20a}$$
$$N_0 = 118200 \pm 300 \tag{4.20b}$$
$$M = 91.363 \pm 0.011 \ \mathrm{GeV/c}^2 \tag{4.20c}$$
$$\Gamma = 4.11 \pm 0.04 \ \mathrm{GeV/c}^2 \tag{4.20d}$$
$$\beta = -0.00196 \pm 0.00008 \tag{4.20e}$$
$$\delta = 0.839 \pm 0.006 \tag{4.20f}$$
$$\mu = 0 \quad \text{(fixed)} \tag{4.20g}$$
$$\sigma = 0.77 \pm 0.04 \ \mathrm{GeV/c}^2. \tag{4.20h}$$

Figure 4.17 shows the function obtained from fit, superimposed to the mass distribution of the reconstructed Z.

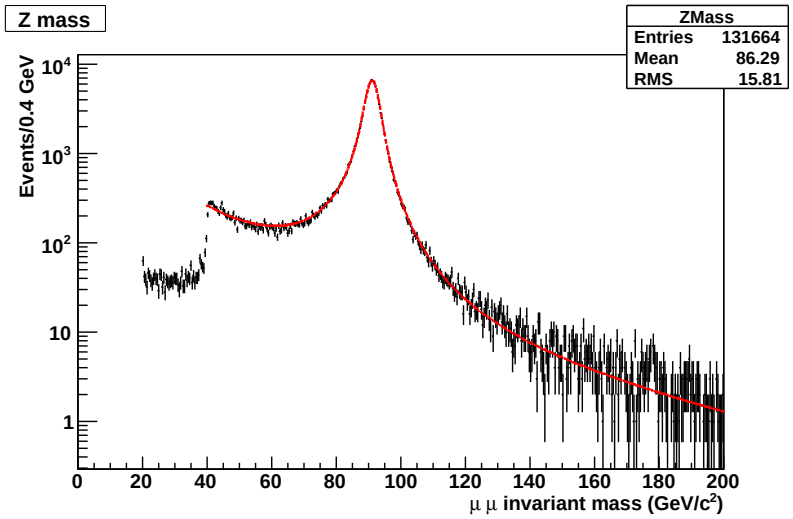

Figure 4.16: Fit of the reconstructed Z mass to the convolution of the product between a negative exponential and the linear combination a relativistic Breit-Wigner (BW), of Z/γ interference term and of photon propagator with a Gaussian in the mass range $[40, 200]$ GeV/c^2.

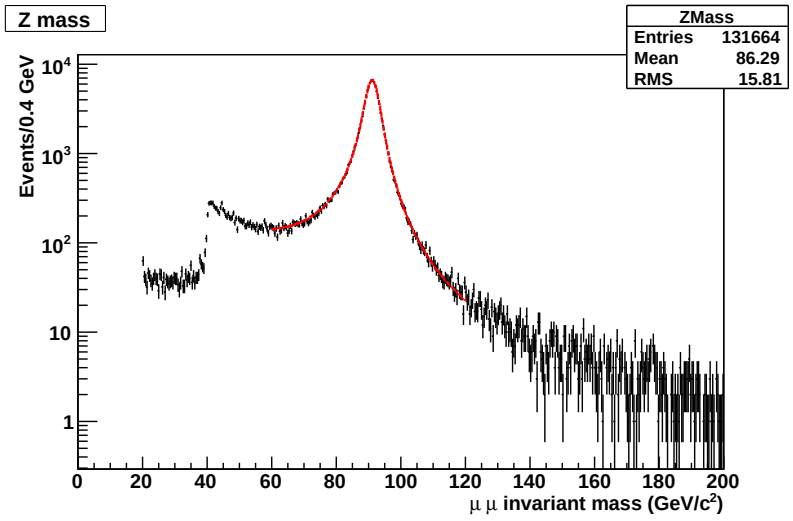

Figure 4.17: Fit of the reconstructed Z mass to the convolution of the linear combination a relativistic Breit-Wigner (BW), of Z/γ interference term and of photon propagator with a Gaussian in the mass range $[60, 120]$ GeV/c^2.

The fit appears to satisfactorily model the Z mass peak, as the very good χ^2 shows, and the value of the width for the Gaussian resolution function is consistent with the value obtained from MC resolution within 2σ. Again, mass M and width Γ are larger than PDG values.

In conclusion:

- These fits are very robust, and with very good χ^2;
- The functional parametrization found is very adequate to model the invariant mass distribution, provided that we just do not consider the Breit-Wigner parameters as physics Z parameters, and the standard deviation of the resolution can be considered as the core contribution to the experimental muon pair invariant mass resolution.

4.5 Muon isolation

In the momentum range relevant for triggering (p_{t} threshold in the range $10 - 30$ GeV/c), the main sources of muons are from b and c decays. Another important contribution, mostly for low-p_{t} muons, is given by muonic K and π decays. All of these muons are produced in (usually soft) jets and are thus accompanied by nearby particles. Only for p_{t} above approximately 30 GeV/c muons from W and Z decays become dominant. Muons from W, Z, and other heavy objects are accompanied only by particles from pile-up and by uncorrelated particles from the underlying event. Muon isolation is a tool to distinguish between the muons produced in jets, in our case background events, and those coming from the decays of heavy objects, like Z decays.

The isolation algorithms that have been developed rely on the comparison of the total energy deposited in a cone around the muon with a predefined threshold. The deposit can be transverse energy in a calorimeter or the sum of transverse momenta of reconstructed charged-particle tracks. The cone axis is chosen according to the muon direction with a procedure that is tailored to the specific properties of each algorithm. The geometrical definition of the cone is given by the condition

$$\Delta R \leqslant \Delta R_{\mathrm{max}}, \tag{4.21}$$

where

$$\Delta R = \sqrt{(\Delta\eta)^2 + (\Delta\phi)^2} \tag{4.22}$$

with $\Delta\eta$ and $\Delta\phi$ being the distances in pseudorapidity and azimuthal angle between the deposit and the cone axis, respectively. A schematic illustration of the isolation cone is shown in Figure 4.18. The energy deposit ($\sum p_{\mathrm{t}}$,

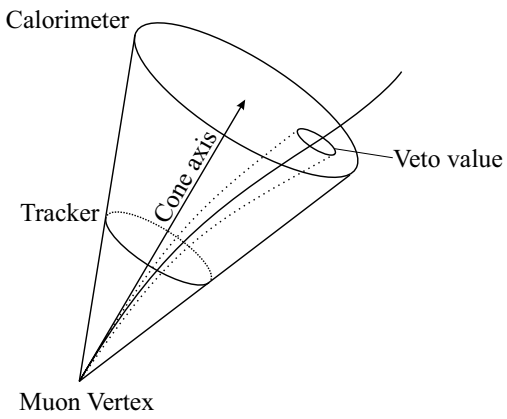

Figure 4.18: Schematic illustration of the isolation cone: the muon direction at the vertex defines the cone axis.

$\sum E_{\mathrm{t}}^{\mathrm{weighted}}$) in the cone is computed, and the muon contribution is removed by excluding the small area around the muon (the "veto value") from the cone. Comparison of the deposit in the cone with a predefined threshold determines the muon isolation.

The algorithm used in this study is based on the scalar sum of transverse momentum from all tracks in the tracker reconstructed in a cone around the direction of the muon at the vertex, removing the contribution from the muon itself. In this algorithm, the tracks are reconstructed using regional tracking. The isolation cone defines the tracking region, with the vertex constraint coming from the isolated muon. Thus, the influence of tracks from pile-up is minimized. Since the direction resolution is good, the veto cone is very small ($\Delta R \approx 0.015$). The tracker isolation is then defined as:

$$\mathrm{iso} = \sum_{\substack{\Delta R_{\mathrm{min}} \leqslant \Delta R_i \leqslant \Delta R_{\mathrm{max}}, \\ p_{\mathrm{t},i} > p_{\mathrm{t,\,min}}}}^{\Delta R_i \leqslant \Delta R_{\mathrm{max}}} p_{\mathrm{t},i} \tag{4.23}$$

where the sum is done for particles with transverse momentum larger than a chosen threshold $p_{\mathrm{t,\,min}}$, in order to reject the large number of low-p_{t} secondary particles detected in the tracker. The cuts imposed to the isolation algorithm are listed in eq. 4.24:

$$p_{\mathrm{t,\,min}} = 1.5 \text{ GeV/c} \tag{4.24a}$$
$$\Delta R_{\mathrm{min}} = 0.015 \tag{4.24b}$$
$$\Delta R_{\mathrm{max}} = 0.3 \quad . \tag{4.24c}$$

In Figure 4.19 the distribution of the tracker isolation for global muons from

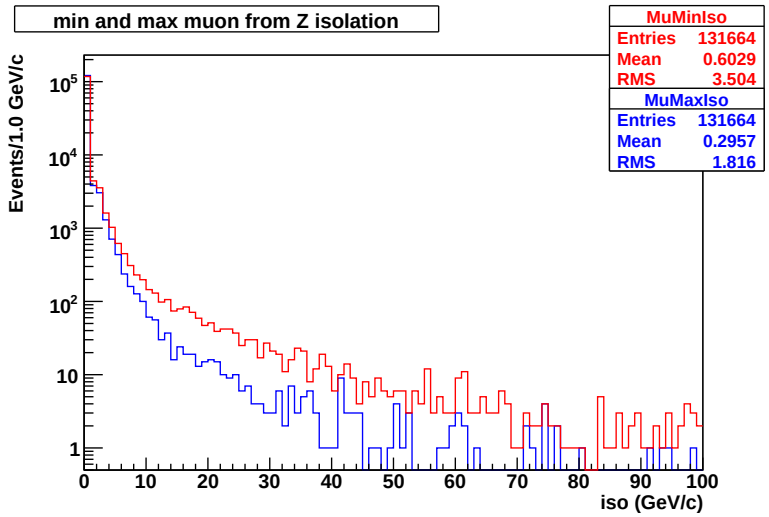

Figure 4.19: Distribution of the tracker isolation for the final state muons from which Z is reconstructed in the collection $Z_{\mu\,\mu}$, with minimum (red) and maximum (blue) transverse momentum.

which a Z candidate is reconstructed and stored in the collection $Z_{\mu\,\mu}$ has been plotted.

4.6 Selection cuts and efficiency measurements for signal and backgrounds

Up to now, we have studied only the signal coming from the $Z \rightarrow \mu^+\mu^-$ decay. We consider now also the backgrounds already defined in section 4.1.2: in real p p collisions, the signal and the backgrounds cannot be distinguished. To select the signal, we can impose some kinematic cuts on muons coming from the Z decay, according to the features we studied above (see 4.3 and 4.5):

- Invariant mass of the dimuon system between 40 GeV/c^2 and 200 GeV/c^2

$$40 \text{ GeV/c}^2 < M_{\mu^-\mu^+} < 200 \text{ GeV/c}^2. \tag{4.25}$$

  This invariant mass range is so wide that we can well describe both the background distribution and the contributions coming from the γ propagator as well as the Z/γ^* interference term.

- Both muons have transverse momentum larger than 20 GeV/c

$$p_t > 20 \text{ GeV/c}. \tag{4.26}$$

This cut comes from the fact that muons from Z decay have large tranverse momentum.

- Both muons have absolute value of pseudorapidity smaller than 2.0

$$|\eta| < 2.0 \quad . \tag{4.27}$$

This cut is useful in order to minimize the effects due to the regions where the muon traverses cracks in the geometry.

- Both muons have tracker isolation smaller than 3.0 GeV/c

$$\text{iso} < 3.0 \text{ GeV/c} \quad . \tag{4.28}$$

This cut must reduce the backgrounds as much as possible, without eliminating significantly the signal events.

Next, both signal and background samples must be normalized to a given equivalent integrated luminosity. For our analysis, we choose $L \equiv \int \mathscr{L}\, dt = 10\ \text{pb}^{-1}$: this value corresponds to the integrated luminosity expected for the first data-taking period. In order to reproduce the invariant mass distributions as they will appear on data, we have summed up the signal and background distributions determined from Monte Carlo samples (`CSA07` production) with $L = 10\ \text{pb}^{-1}$ equivalent luminosity.

We analyze a sample of 11000 $Z \to \mu^+\mu^-$ events, corresponding to $L = 10\ \text{pb}^{-1}$. The three Z collections defined in section 4.3 are not independent. Indeed, a true $Z \to \mu^+\mu^-$ decay will be reconstructed in all the three categories, unless any inefficiency in the detector leads to track candidates that are not matched to standalone candidates or viceversa. Thus, for our analysis we consider the following collections of events:

- events with a $Z_{\mu\,\mu}$ candidate;
- events with a $Z_{\mu\,\text{t}}$ candidate where no corresponding $Z_{\mu\,\mu}$ candidate has been found;
- events with a $Z_{\mu\,\text{s}}$ candidate where no corresponding $Z_{\mu\,\mu}$ has been found.

These three event samples are statistically independent.

4.6.1 Monte Carlo tracking efficiencies

We are now able to estimate the Monte Carlo reconstruction efficiencies, i.e. the mean reconstruction efficiencies obtained through the matching to generated particles. In order to determine the MC tracking efficiency, we use the collection $\mathrm{Z}_{\mu\ \mathrm{s}}$ as a control sample. First we verify if the Z reconstructed from the pair made by a global and a standalone muon is matched to a generated Z (see section 4.2). After checking that both the global and the standalone muon pass the kinematic and isolation cuts described in eqs. (4.25), (4.26), (4.27), (4.28), we control if the standalone muon overlaps to a muon candidate from the collection of muon candidates stored in the event, matched to a generated muon: if they overlap, then the reconstruction in the tracker has been efficient.

Analogously, we start from the collection $\mathrm{Z}_{\mu\ \mathrm{t}}$ of Z reconstructed from the pair made by a global and a track muon, here used as a control sample, and their matching to generated Z, for determining the MC standalone efficiency. We repeat the same steps used for the Z reconstructed from a global and a standalone muon, but considering now the track muon instead of the standalone muon.

We obtain:

$$\epsilon_{\mathrm{Tk}}^{\mathrm{MC}} = 0.9963 \pm 0.0006 \tag{4.29a}$$

$$\epsilon_{\mathrm{Sa}}^{\mathrm{MC}} = 0.9880 \pm 0.0009 \quad , \tag{4.29b}$$

where the errors are given by the binomial error relation:

$$\sigma(\epsilon) = \sqrt{\frac{\epsilon(1-\epsilon)}{N}} \quad . \tag{4.30}$$

As far as the backgrounds are concerned, we consider different samples for an equivalent integrated luminosity $L = 10\ \mathrm{pb}^{-1}$:

- 140k $\mathrm{W} \rightarrow \mu\nu_\mu$ events;
- 16k $\mathrm{Z} \rightarrow \tau\tau$ events;
- $\mathrm{t}\,\bar{\mathrm{t}} + n$ jets, scaled to the chosen luminosity;
- QCD events containing muons $\mathrm{pp} \rightarrow \mu X$, scaled to $L = 10\ \mathrm{pb}^{-1}$.

4.7 Models for signal and backgrounds

Now, we deal with the final step of our analysis. We are going to build detailed fit models for both signal and backgrounds, in order to obtain, after the extraction of the signal from the backgrounds, directly from data:

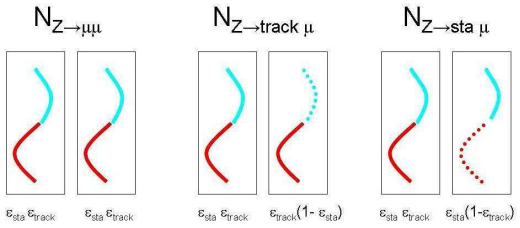

Figure 4.20: Reconstructed muon pairs contributing to the three categories of Z candidates defined for our analysis. The track in the central tracker is labelled with red, while the track in the muon detector is labelled with blue; if the track has been successfully reconstructed, the line is continuous, if the reconstruction fails, the line is dotted.

- the number of $Z \rightarrow \mu^-\mu^+$ signal events, from which, if we know the integrated luminosity L, we can determine the inclusive cross section $p + p \rightarrow Z + X \rightarrow \mu^+ + \mu^- + X$;

- the mean reconstruction efficiencies for muons in the central tracker (track muons) and in the muon detector (standalone muons).

In Figure 4.21 we show the invariant mass distributions after selection cuts. The contributions from the Monte Carlo background samples are shown with different colors. The level of the background for the Z reconstructed from global muon pairs is small ($\lesssim 0.1\%$). The main contribution comes from $t\,\bar{t}$ events.

For Z reconstructed from a global muon and a track muon unmatched to a standalone muon, background dominates: in particular, the main contributions come from QCD background and from W decay into muon and (unobserved) neutrino.

The distribution for Z reconstructed from a global muon and a standalone track muon unmatched to a track muon is statistically limited, so that the background subtraction is difficult. The background is still present, though not dominating: the main background component in this sample is the QCD background.

4.7.1 Shape parametrizations

Labelling with $N_{\mu\,\mu}$ the number of Z candidates reconstructed from a global muon pair, with $N_{\mu\,\mathrm{Tk}}$ the number of Z candidates reconstructed from a global muon and track muon unmatched to a standalone muon, and with $N_{\mu\,\mathrm{Sa}}$ the number of Z candidates reconstructed from a global muon and a

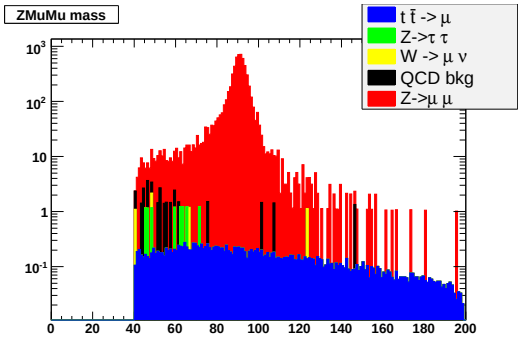

(a) *Z candidates from global muon pairs.*

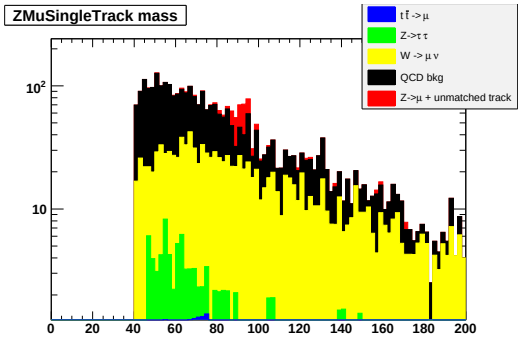

(b) *Z candidates from global muons and unmatched track muons.*

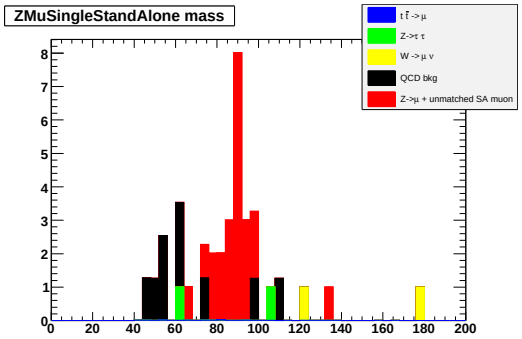

(c) *Z candidates from global muons and unmatched standalone muons.*

Figure 4.21: Invariant mass distribution for the Z candidates in signal and background events passing the Z → $\mu^+\mu^-$ selection including the isolation cut according to the different categories of candidates. Several contributions from background events are shown separately.

standalone track muon unmatched to a track muon, if we refer to Figure 4.20, we have:

$$N_{\mu\,\mu} = N_0 \cdot \epsilon_{\mathrm{Tk}}^2 \cdot \epsilon_{\mathrm{Sa}}^2 \tag{4.31a}$$

$$N_{\mu\,\mathrm{Tk}} = 2 \cdot N_0 \cdot \epsilon_{\mathrm{Tk}}^2 \cdot \epsilon_{\mathrm{Sa}}(1 - \epsilon_{\mathrm{Sa}}) \tag{4.31b}$$

$$N_{\mu\,\mathrm{Sa}} = 2 \cdot N_0 \cdot \epsilon_{\mathrm{Sa}}^2 \cdot \epsilon_{\mathrm{Tk}}(1 - \epsilon_{\mathrm{Tk}}) \tag{4.31c}$$

where N_0 is the number of $\mathrm{Z} \to \mu^+\mu^-$ decays, ϵ_{Tk} and ϵ_{Sa} are the efficiencies for reconstructing, respectively, track and standalone muon candidates, while the factor 2 in $N_{\mu\,\mathrm{Tk}}$ and $N_{\mu\,\mathrm{Sa}}$ arises from the fact that, as the muon candidate not globally reconstructed can be either the former or the latter in the muon pair from which a Z candidate is built, the two cases, being statistically independent, must be summed up.

The invariant mass distributions in the hypotheses of signal and background are modeled with phenomenological probability density functions using the results of the previous steps of the analysis (see section 4.4). We use different functional shapes for the three categories of Z candidates:

- For Z reconstructed from global muon pairs, the background being negligible ($\lesssim 0.1\%$), we can then fit only the signal. The signal distribution is modeled as the convolution of linear combination of the relativistic Breit-Wigner, of Z/γ^* interference term and of photon propagator with a Gaussian (reproduced here for convenience):

$$P(m) = C(M, \Gamma, \mu, \sigma) \int H(m') \cdot G(m - m'; \mu, \sigma_{\mu\,\mu}) dm' \tag{4.32}$$

  where $C(M, \Gamma, \mu, \sigma)$ is a normalization factor such that $P(m)$ is normalized to unity in the fit range,

$$H(m) = \left[\alpha \cdot f_{\mathrm{Z}}(m; M, \Gamma) + \beta \cdot f_{\mathrm{Z}/\gamma}(m; M, \Gamma) + \delta \cdot f_{\gamma}(m)\right] \tag{4.33}$$

  with $\alpha + \beta + \delta = 1$, and

$$f_{\mathrm{Z}}(m; M, \Gamma) = \frac{2}{\pi} \cdot \frac{\Gamma^2 M^2}{(m^2 - M^2)^2 + m^4(\Gamma^2/M^2)} \tag{4.34a}$$

$$f_{\mathrm{Z}/\gamma}(m; M, \Gamma) = M \cdot \frac{(m^2 - M^2)^2}{(m^2 - M^2)^2 + m^4(\Gamma^2/M^2)} \tag{4.34b}$$

$$f_{\gamma}(m) = \frac{1}{m^2}, \tag{4.34c}$$

  and

$$G(\Delta M; \mu, \sigma_{\mu\,\mu}) = \frac{1}{\sqrt{2\pi}\sigma_{\mu\,\mu}} \exp\left[-\frac{(\Delta M - \mu)^2}{2\sigma_{\mu\,\mu}^2}\right]; \tag{4.35}$$

and, taking into account the resolution effects, the mean value μ of the Gaussian is fixed to 0. Having neglected the backgrounds, and remembering the definition of the number of Z candidates reconstructed from a global muon pair $N_{\mu\ \mu}$, eq. (4.31), the invariant mass distribution can be modeled as:

$$F_{\mu\ \mu}(m) = N_0 \epsilon_{\mathrm{Tk}}^2 \epsilon_{\mathrm{Sa}}^2 P(m) \quad . \tag{4.36}$$

- When we consider Z reconstruced from a global muon and a track muon unmatched to a standalone muon, as the background dominates, we can empirically model it as the product of an exponential and a second order polynomial:

$$B_{\mu\ \mathrm{Tk}}(m) = N^{\mathrm{Bkg}}_{\mu\ \mathrm{Tk}} \cdot \exp[-\lambda m](1 + a_1 m + a_2 m^2). \tag{4.37}$$

The signal, instead, can be modeled with the same shape as the Z from global muon pairs. Taking into account the number of Z candidates reconstructed from a global muon and a track muon $N_{\mu\ \mathrm{Tk}}$, eq. (4.31), the invariant mass distribution can be modeled as:

$$F_{\mu\ \mathrm{Tk}}(m) = 2N_0 \epsilon_{\mathrm{Tk}}^2 \epsilon_{\mathrm{Sa}} (1 - \epsilon_{\mathrm{sa}}) P(m) + B_{\mu\ \mathrm{Tk}}(m) \quad . \tag{4.38}$$

- In the distribution for Z reconstructed from a global muon and a standalone track muon unmatched to a track muon, the not dominating background can be modeled as a a constant "offset" $N^{\mathrm{Bkg}}_{\mu\ \mathrm{Sa}}$. Besides, due to the small number of events, the resolution effects hide the Z peak, so we can model the signal with a Gaussian with Z mass peak as mean, while sigma will be an additional parameter:

$$G(m; M, \sigma_{\mu\ \mathrm{Sa}}) = \frac{1}{\sqrt{2\pi}\sigma_{\mu\ \mathrm{Sa}}} \exp\left[-\frac{(m-M)^2}{2\sigma^2_{\mu\ \mathrm{Sa}}}\right]. \tag{4.39}$$

When we take into account the number of Z candidates reconstructed from a global muon and a standalone muon $N_{\mu\ \mathrm{Sa}}$, the model we choose for the invariant mass distribution is then:

$$F_{\mu\ \mathrm{Sa}}(m) = 2N_0 \epsilon^2_{\mathrm{Sa}} \cdot \epsilon_{\mathrm{Tk}}(1 - \epsilon_{\mathrm{Tk}}) G(m; M, \sigma_{\mu\ \mathrm{Sa}}) + N^{\mathrm{Bkg}}_{\mu\ \mathrm{Sa}}. \tag{4.40}$$

4.7.2 Fit strategy and results

We determine the $Z \to \mu^-\mu^+$ event yield, the mean reconstruction efficiencies for muons in the central tracker ϵ_{Tk} and the muon detector ϵ_{Sa} by a simultaneous binned χ^2 fit to the invariant mass distributions for the three independent categories of the selected Z candidates. Starting from each invariant mass distribution, our fit strategy follows these steps:

1. We calculate the χ^2_k for each distribution:

$$\chi^2_k = \sum_{i=1}^{N_k^{\rm bin}} \frac{(n_i^k - f_k(m_i))^2}{n_i^k} \tag{4.41}$$

where k is the index of the Z candidate category ($k = \mu\ \mu, \mu$ Tk, μ Sa), $N_k^{\rm bin}$ is the number of bins, and n_i^k is the i-th bin content of the k-th Z candidate category invariant mass histogram, respectively;

2. We build the global χ^2:

$$\chi^2 = \chi^2_{\mu\ \mu} + \chi^2_{\mu\ \rm Tk} + \chi^2_{\mu\ \rm Sa} \quad ; \tag{4.42}$$

3. We minimize the global χ^2 using a statistical toolkit, built for our analysis and developed within the CMS framework, that allows to easily define in `C++` function models to be used in fit problems.

In Table 4.6 we report the mass range, the binning and the bin interval for the three histograms. The binning of each histogram has been defined in order to assure a sufficient statistics for each bin.

Table 4.6: Mass range $[m_{\rm min}, m_{\rm max}]$, binning $N_{\rm bins}$ and bin width ΔI for the simultaneous invariant mass fit.

Histogram	$m_{\rm min}$(GeV/c^2)	$m_{\rm max}$(GeV/c^2)	$N_{\rm bins}$	ΔI(GeV/c^2)
$m_{\mu\ \mu}$	60	120	60	1.0
$m_{\mu\ \rm Tk}$	60	120	30	2.0
$m_{\mu\ \rm Sa}$	60	120	15	4.0

The parameters M and Γ are not the Z physical mass and width. They are intended as phenomenological parameters which are left floating in the fit in order to obtain an accurate description of the signal peak, taking into account distortions from the ideal Z invariant mass shape. The result of the

simultaneous fit are listed in eq. (4.43).

$$\chi^2 = 103.446/87 = 1.19; \tag{4.43a}$$
$$N_0 = 6050 \pm 80 \tag{4.43b}$$
$$M = 91.23 \pm 0.05 \text{ GeV/c}^2 \tag{4.43c}$$
$$\Gamma = 3.91 \pm 0.16 \text{ GeV/c}^2 \tag{4.43d}$$
$$\beta = -0.0051 \pm 0.0018 \tag{4.43e}$$
$$\delta = 0.55 \pm 0.15 \tag{4.43f}$$
$$\epsilon_{\mathrm{Tk}} = 0.9992 \pm 0.0005 \tag{4.43g}$$
$$\epsilon_{\mathrm{Sa}} = 0.991 \pm 0.002 \tag{4.43h}$$
$$\mu = 0 \quad \text{(fixed)} \tag{4.43i}$$
$$\sigma_{\mu\,\mu} = 1.7 \pm 0.2 \text{ GeV/c}^2 \tag{4.43j}$$
$$\sigma_{\mu\,\mathrm{Sa}} = 4 \pm 3 \text{ GeV/c}^2 \tag{4.43k}$$
$$N^{\mathrm{Bkg}}_{\mu\,\mathrm{Tk}} = 200 \pm 90 \tag{4.43l}$$
$$\lambda = 0.022 \pm 0.009 \text{ GeV}^{-1}\text{c}^2 \tag{4.43m}$$
$$a_1 = -0.0014 \pm 0.0006 \text{ GeV}^{-1}\text{c}^2 \tag{4.43n}$$
$$a_2 = (-3 \pm 4) \cdot 10^{-5} \text{ GeV}^{-2}\text{c}^4 \tag{4.43o}$$
$$N^{\mathrm{Bkg}}_{\mu\,\mathrm{Sa}} = 0.37 \pm 0.14 \tag{4.43p}$$

Figure 4.22 shows the functions obtained from fit, superimposed to the mass distributions of the Z candidates reconstructed into the three categories of events: the signal contribution is plotted in red, while the background contribution in green.

Even if the χ^2 is satisfactory, M and Γ obtained from fit are larger than the PDG (Yao et al., 2006) values of the Z mass and width, while the width $\sigma_{\mu\,\mu}$ of the Gaussian accounting for the resolution effects is not consistent within 3σ with the value obtained from Monte Carlo models, being larger. This is expected from Monte Carlo studies, and is due to the effects of the initial and final state radiation, and the distortion deriving from the non-flat parton distribution functions in the region of the Z peak. Besides, a part of the Gaussian contributions to the invariant mass resolution is absorbed in the parameters of the signal shape, by increasing the values of the parameters M and Γ, and in the parameters of the resolution effects, by increasing $\sigma_{\mu\,\mu}$. We also see that we have a large uncertainty for the $\sigma_{\mu\,\mathrm{Sa}}$ in the signal shape of the Z candidates from global muons and unmatched standalone muons: this implies that we need higher statistics in order to resolve the resolution effects. The shape for resolution effects is quite inaccurate, since we use a symmetric Gaussian to model a distribution with outlayer tails

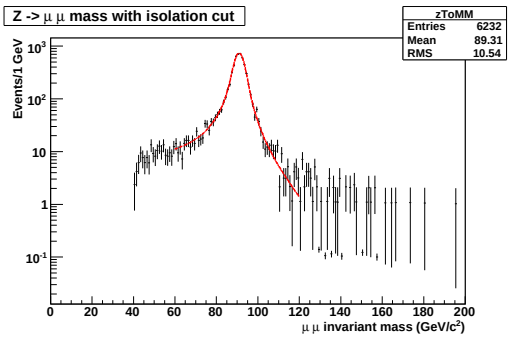

(a) *Z candidates from global muon pairs.*

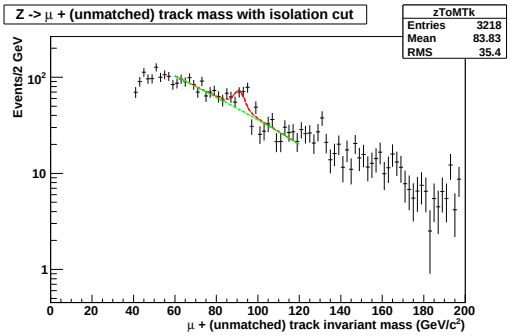

(b) *Z candidates from global muons and unmatched track muons.*

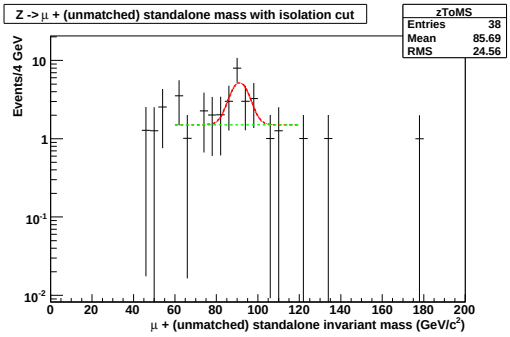

(c) *Z candidates from global muons and unmatched standalone muons.*

Figure 4.22: Invariant mass distributions and fit results for the Z candidates in signal and background(red) and background only (green) events passing the $Z \rightarrow \mu^+\mu^-$ selection including the isolation cut according to the different categories of candidates.

(see section 4.2.1, where the asymmetry of the data was taken into account by building a model with a linear combination of three Gaussians having different mean values), neglecting also other effects like initial and final state radiation. This implies that, with the information available, we cannot build a satisfactory model for the resolution effects. A new study, in which we extract the probability distribution function directly from the data, is in progress (see section 4.8.1).

Comparison with Monte Carlo truth

If we compare the values of the mean efficiencies deriving from the simultaneous fit with those obtained from Monte Carlo studies, see Table 4.7, the standalone efficiency obtained from the simultaneous fit is consistent within 1.5σ to the Monte Carlo prediction, while the track efficiency from fit is consistent within 3σ to its MC value.

Table 4.7: Comparison between the simultaneous fit results and the MC values of the mean reconstruction efficiencies.

Parameter	MC value	Fit estimate
ϵ_{Tk}	0.9963 ± 0.0006	0.9992 ± 0.0005
ϵ_{Sa}	0.9880 ± 0.0009	0.991 ± 0.002

4.8 Measurement of the inclusive cross section $\mathbf{p+p \rightarrow Z+X \rightarrow \mu^+\mu^- + X}$

Starting from the number of $\mathrm{Z} \rightarrow \mu^+\mu^-$ decays N_0 obtained from the simultaneous fit, we can measure the inclusive cross section $\mathrm{p}+\mathrm{p} \rightarrow \mathrm{Z}+X \rightarrow \mu^+\mu^- + X$:

$$\sigma = \frac{N_0}{\epsilon_{\mathrm{iso}}^{(\mathrm{MC})2}\left[1-\left(1-\epsilon_{\mathrm{trg}}^{(\mathrm{MC})}\right)^2\right]\epsilon_{\mathrm{kin}}^{(\mathrm{MC})}\epsilon_{\mathrm{gen}}L} \tag{4.44}$$

where

$\epsilon_{\mathrm{iso}}^{(\mathrm{MC})}$ is the Monte Carlo isolation efficiency, determined as (Alcaraz et al., 2008):

$$\epsilon_{\mathrm{iso}}^{(\mathrm{MC})} = 0.9613 \pm 0.0014 \tag{4.45}$$

$\epsilon_{\mathrm{trg}}^{(\mathrm{MC})}$ is the trigger efficiency, determined as:

$$\epsilon_{\mathrm{trg}}^{(\mathrm{MC})} = 0.9535 \pm 0.0030 \tag{4.46}$$

$\epsilon_{\mathrm{kin}}^{(\mathrm{MC})}$ is the Monte Carlo kinematical acceptance of muons, whose statistical error can be assumed as negligible, while its systematic error is of the order of a few %:

$$\epsilon_{\mathrm{kin}}^{(\mathrm{MC})} = 0.641 \tag{4.47}$$

ϵ_{gen} is the Monte Carlo generator filter efficiency (see Table 4.1):

$$\epsilon_{\mathrm{gen}} = 0.465 \tag{4.48}$$

L is the integrated luminosity: in our study, we have chosen

$$L \equiv \int \mathscr{L}\, dt = 10 \text{ pb}^{-1} \tag{4.49}$$

which is the integrated luminosity expected for the first data-taking period.

We obtain:

$$\sigma = 2.30 \pm 0.03 \text{ nb} \quad . \tag{4.50}$$

The value obtained is consistent within 1σ with the NLO cross section $\sigma_{\mathrm{NLO}} = 2.331$ nb, used for more detailed generator studies by the `MC@NLO` generator.

4.8.1 Updates and improvements

The method we have presented has been used for the CMS internal note for the `CSA07` exercise (Alcaraz et al., 2008). A new internal note, for `iCSA08` exercise (De Gruttola, Di Guida, Fabozzi, Lista, Noli, and Piccolo, 2008), is in preparation: it presents an extension of the method discussed in this thesis; the simultaneous fit is performed on four statistically independent categories of events with a reconstructed $\mathrm{Z} \to \mu^+\mu^-$: besides the already known $\mathrm{Z}_{\mu\,\mu}$, $\mathrm{Z}_{\mu\,\mathrm{t}}$, $\mathrm{Z}_{\mu\,\mathrm{s}}$ candidates, we build the new category of $\mathrm{Z}_{\mu\,\mu}^{\mathrm{no\ iso}}$ candidates, built from a pair of global muons, in which at least one is not isolated. These categories are mutually exclusive, in order to have four not-overlapping, hence statistically independent, event samples. After the production of binned muon invariant mass spectra for the four samples, a simultaneous binned χ^2 fit is performed, from which we extract, besides the Z yield and the average tracker and standalone efficiencies, the average isolation efficiency.

More accurate studies are in progress to obtain the trigger efficiency directly from data. In this case, we define these categories of$\mathrm{Z} \to \mu^+\mu^-$ candidates:

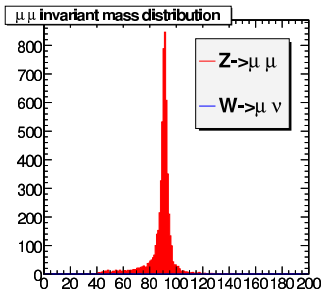

(a) *Z candidates from a global muon pair in which only one is triggered.*

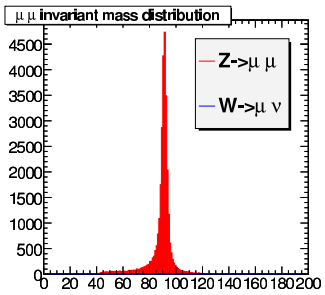

(b) *Z candidates from a global muon pair in which both are triggered.*

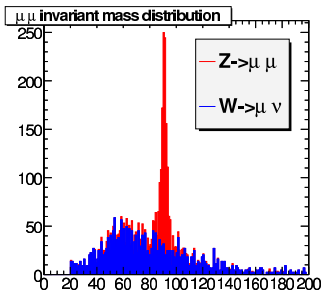

(c) *Z candidates from a triggered global muon and an unmatched track muon.*

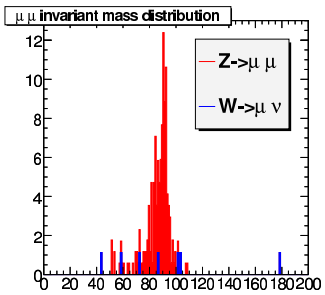

(d) *Z candidates from a triggered global muon and an unmatched standalone muon.*

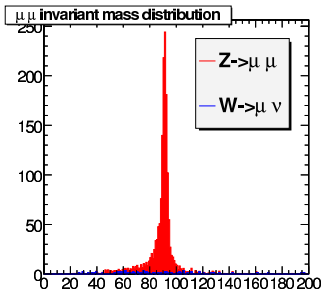

(e) *Z candidates from s global muon pair in which at least one is not isolated and at least onr is triggered.*

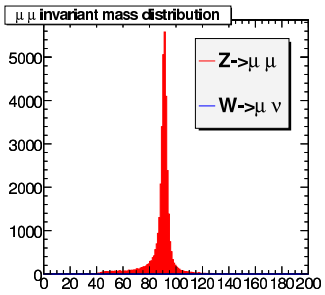

(f) *Z candidates from global muon pairs in which at least one muon is triggered.*

Figure 4.23: Invariant mass distributions for the Z candidates in signal and background events passing the selection for the improved analysis. Up to now, only the contribution from $W \rightarrow \mu\nu$ has been evaluated.

- $\mathrm{Z}^{1\ \mathrm{HLT}}_{\mu\ \mu}$ candidates, built from a pair of global muons in which *only one* is triggered;
- $\mathrm{Z}^{2\ \mathrm{HLT}}_{\mu\ \mu}$ candidates, built from a pair of global muons in which *both* are triggered;
- $\mathrm{Z}^{1\ \mathrm{HLT}}_{\mu\ \mathrm{t}}$ candidates, built from *one triggered* global muon and a track candidate;
- $\mathrm{Z}^{1\ \mathrm{HLT}}_{\mu\ \mathrm{s}}$ candidates, built from *one triggered* global muon and a standalone candidate;
- $\mathrm{Z}^{\text{no iso, at least 1 HLT}}_{\mu\ \mu}$ candidates, built from a pair of global muons in which at least one is not isolated *and at least one* is triggered.

These categories are again mutually exclusive, in order to have five not-overlapping, hence statistically independent, event samples. Besides, we build the category of $\mathrm{Z}^{\text{at least 1 HLT}}_{\mu\ \mu}$ candidates by summing up the $\mathrm{Z}^{1\ \mathrm{HLT}}_{\mu\ \mu}$ and $\mathrm{Z}^{2\ \mathrm{HLT}}_{\mu\ \mu}$ candidates. From the invariant mass distribution of $\mathrm{Z}^{\text{at least 1 HLT}}_{\mu\ \mu}$ candidates, we extract the probability distribution function. Finally, we use this model in a simultaneous binned χ^2 fit for the five distributions, thus determining, besides the $\mathrm{Z} \to \mu^+\mu^-$ yield and the reconstruction and isolation efficiencies, the HLT efficiency.

CONCLUSIONS

THIS thesis deals with a study on the inclusive production channel of the Z boson, subsequently decaying into two muons, to measure to inclusive cross section for the process $\mathrm{p} + \mathrm{p} \rightarrow \mathrm{Z} + X \rightarrow \mu^+\mu^- + X$ at the center of mass energy $\sqrt{s} = 14\,\mathrm{TeV}$ with the CMS detector at LHC. The Z production with subsequent decay into a muon pair will be studied starting from the LHC startup, since such events have relatively large cross section and a clear experimental signature, characterized by two isolated, high-p_{t} muons with an invariant mass consistent with the Z boson mass. Thus, this channel allows to monitor the LHC collider luminosity, to calibrate the CMS detector and, possibly, to discover new physics beyond the SM through the detection of events with two muons with high invariant mass peaking at a given mass resonance. In this thesis, we develop an analysis that, for a given integrated luminosity, will lead us to measure the Z inclusive cross section and the reconstruction efficiencies directly from data, with no assumption taken from Monte Carlo. This data-driven analysis can be performed just after the LHC startup, with only few pb^{-1} of integrated luminosity, and, being independent of Monte Carlo models, has reduced systematic uncertainties. In chapter 4, we have described the strategy used for this analysis in detail: after the study of the Z decay for Monte Carlo generated event samples (section 4.1), in order to build a satisfactory model of the Z mass peak shape (section 4.1.1), of its backgrounds (section 4.1.2), and of the Monte Carlo mass resolution (section 4.2), in order to describe resolution effects on real data (section 4.2.1), the kinematical characteristics of the muons, in which the Z decays, have been analyzed at the end of the full reconstruction chain (section 4.3). Therefore, several algorithms allowing the rejection of backgrounds from other channels with two final state muons and the identification of signal events have been implemented (sections 4.5 and 4.6): from them, through a robust fit model

based on a statistical toolkit developed within the CMS framework, both the number of signal events and the reconstruction efficiencies can be determined (section 4.7). Once known the integrated luminosity of the collider, the counting of the number of signal events, corrected by the reconstruction efficiencies, allows to measure the Z inclusive cross section (section 4.8). Actually, in order to obtain the cross section value, we need the isolation and triggering efficiencies for muon pairs, that, up to now, are known only from Monte Carlo studies. The method we have presented has been used for the CMS internal note for the `CSA07` exercise (Alcaraz et al., 2008). A new internal note, for `iCSA08` exercise (De Gruttola, Di Guida, Fabozzi, Lista, Noli, and Piccolo, 2008), is in preparation: it presents an extension of the method discussed in this thesis. New statistically independent categories of events with a reconstructed $Z \to \mu^+\mu^-$ are built, in order to determine also the isolation and triggering efficiencies for muon pairs directly for real data (see section 4.8.1).

APPENDIX A

THE CMS SOFTWARE PROJECT

THE analysis of physics processes, like the inclusive channel pp $\rightarrow$ Z+X $\rightarrow$ $\mu^+\mu^-$+X studied in this thesis, can be performed on both simulated and reconstructed event samples (The CMS Collaboration, 2006). The simulation of the CMS response to physics events — the "simulation chain" — follows these steps:

1. Physics processes are generated using Monte Carlo generators;

2. The simulation of the CMS detector and physics, with the generated events as input, taking into account geometrical and material information, produces persistent hits in the sensitive detectors, using the CMS framework;

3. These hit data, are then used as input to the subsequent digitization step, allowing for pile-up: this step converts hits into digitizations (also known as "digis") which correspond to the output of the CMS electronics, i.e. the detector response.

These steps are followed by the event reconstruction, in which information from sub-detectors are combined to identify physics objects in the final state. The data are therefore stored in one of the different formats available in CMS. The chosen format depends on the information required for offline analysis and on the physical disk space available.

In Figure A.1, the "simulation chain" and data analysis are sketched.

In this appendix, after an introduction to the CMS framework, we briefly review the steps that, starting from the event generation, lead to the production of datasets for offline analysis.

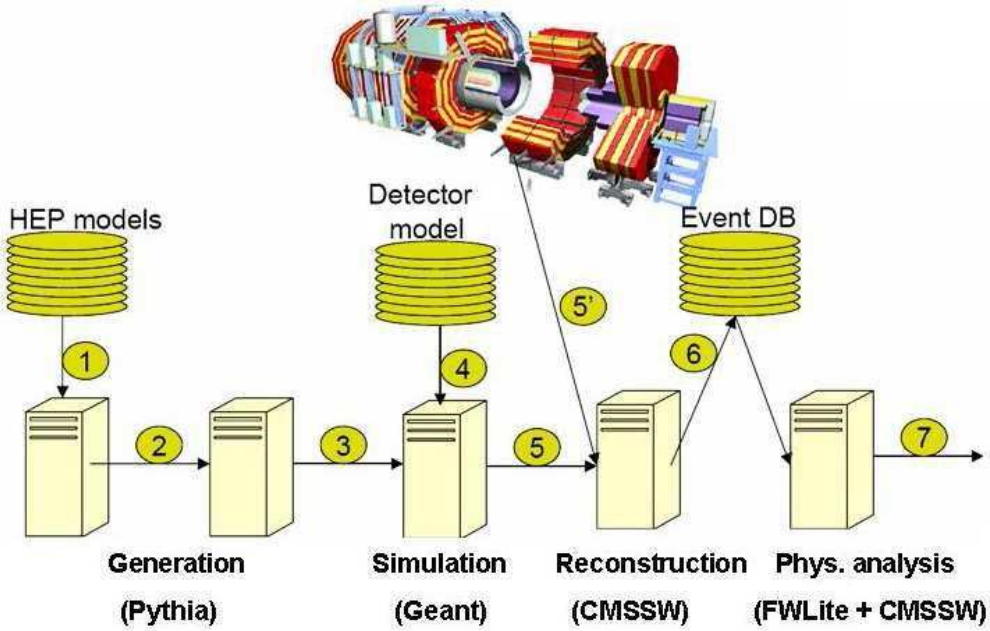

Figure A.1: Scheme of the simulation chain and data analysis in CMS.

A.1 CMS software architecture

The overall collection of software, referred to as `CMSSW` (CMS), is built around a Framework, an Event Data Model, and Services needed by the simulation, calibration and alignment, and reconstruction modules that process event data so that physicists can perform analysis.

The high-level goals of the CMS software are to process and select events, to deliver the processed results to experimenters within the CMS Collaboration, and to provide tools for them to analyze the processed information in order to produce physics results.

Many technical requirements should be considered such as the memory consumption and processing time per event necessary to meet financial constraints, and the physics performance requirements encompassing the ability to reproduce faithfully details of the underlying physics processes based on the detector data. These requirements imply that software should be developed keeping in mind not only performance but also modularity, flexibility, maintainability, quality assurance and documentation. CMS has adopted an object-oriented development methodology, based primarily on the `C++` programming language.

The requirements on the software architecture result in the following over-

all structure for the CMS software:

- an application framework customizable for each of the computing environments;
- physics software modules with clearly defined interfaces that can be plugged into the framework;
- services and utility toolkits that can be used by any of the physics modules.

The framework defines the top level abstractions, their behavior and collaboration patterns. It comprises two components: a set of classes that capture CMS specific concepts like detector components and event features and a control policy that orchestrates the instances of those classes taking care of the flow of control, module scheduling, input/output, etc. This control policy is tailored to the task at hand and to the computing environment.

The physics and utility modules can be plugged into the application framework at run time, independently of the computing environment. One can easily choose between different versions of various modules. The physics modules do not communicate with each other directly but only through the data access protocols that are part of the framework itself.

The service and utility toolkit consists of two major categories of services: physics type services (histogrammers, fitters, mathematical algorithms, geometry and physics calculation routines) and computer services (data access, inter module communication, user interface, etc.). Both the application framework and the service and utility toolkit shield the physics software modules from the underlying technologies which will be used for the computer services. This will ensure a smooth transition to new technologies with changes localized in the framework and in specific components of the service toolkit.

A.2 Framework

The primary goal of the CMS Framework and Event Data Model (EDM) is to facilitate the development and deployment of reconstruction and analysis software. Ease-of-use is very high in the design priorities; for example, developers are encouraged to make their stored data objects as simple as possible in order to remove the need for specialized private analysis data formats and the code used to make them. All reconstruction results should be made persistent in a format that can be directly used by an analysis without any additional layer.

Another way to ensure consistency and ease of use of the software is automation: the Framework provides ways to guarantee reproducibility by automatically maintaining and recording sufficient provenance information for all application results. This avoids developers having to record such information separately on how a particular reconstruction result was obtained.

A.2.1 Event Data Model-data access

The event data model is centered around the `Event`. The `Event` holds all data that was taken during a triggered physics event as well as all data derived from the taken data. Auxiliary information needed to process an Event is accessed via the `EventSetup`.

Events are processed by passing the `Event` through a sequence of modules. The exact sequence of modules is specified by the user. When an `Event` is passed to a module, that module can get data from the `Event` and put data back into the `Event`. When data is put into the `Event`, the provenance information about the module that created the data will be stored with the data into the `Event`.

The `Event` class[1] represents the observed and inferred products of a single triggered readout of the CMS detector. The `Event` is responsible for managing the lifetime of, and relationships between, it contents. The contents of the `Event` can include objects representing the raw detector output, reconstruction products, simulation products, and analysis objects relating to a single beam crossing or simulation thereof. The `Event` also contains "metadata" describing the configuration of the software used for the reconstruction of each contained data object and the conditions and calibration data used for such reconstruction.

A.2.2 Framework-module types and communication

The purpose of a "module" is to allow independent development and verification of distinct elements of triggering, simulation, reconstruction, and analysis. The concept of an event-processing module, each of which encapsulates a unit of clearly defined event-processing functionality, is introduced to support this goal. Such modules are not allowed to communicate directly with each other, which allows them to be independently tested and reused. Instead, modules communicate only through the `Event`.

The CMS framework executable (`cmsRun`) is configured, by `ParameterSets`, which are collections of named parameter/value pairs. These `ParameterSets`

[1] In `C++`, a class bundles together some amount of data with the set of functions relevant for manipulating those data.

are created from a user-written configuration file. The `ParameterSets` used to configure a job will be stored in the same file as the event data written by that job.

A.2.3 Framework services

The Framework identifies two categories of services based on whether or not the service can affect physics results. The two categories are handled by different system: the `ServiceRegistry` system and the `EventSetup` system.

The `ServiceRegistry` system provides services which are application extensions and, as such, their use should have no effect on physics results. Therefore, the `ServiceRegistry` is used to deliver services such as the error logger or a debugging service which provides feedback about the state of the Framework (e.g., what module is presently running).

To be able to fully process an `Event`, for example in an analysis, requires additional information outside of the `Event` itself (e.g., magnetic field measurements). These non-Event data are data whose "interval of validity" (IOV) is longer than one `Event`. The `EventSetup` system provides a unified access model for all services that deliver non-Event data.

The `EventSetup` provides a uniform access mechanism to all data/services constrained by an IOV. This will include all calibrations, alignments, geometry descriptions, magnetic field and run conditions recorded during data acquisition.

A.3 Event filter

The CMS Trigger and Data Acquisition System (TriDAS) is designed to inspect the detector information at the full crossing frequency and to select events at a maximum rate of $\mathcal{O}(10^2)$ Hz for archiving and later offline analysis. The required rejection power of $\mathcal{O}(10^5)$ is too large to be achieved in a single processing step, if a high efficiency is to be maintained for the physics phenomena CMS plans to study. For this reason, the full selection task is split into 2 steps. The first step (Level-1 Trigger) is designed to reduce the rate of events accepted for further processing to less than 100 kHz. The second step (High-Level Trigger, or HLT) is designed to reduce this maximum Level-1 Accept (L1A) rate of 100 kHz to a final output rate of approximately 100 Hz (see Figure A.2).

The functionality of the CMS DAQ/HLT system can be summarized in 4 points:

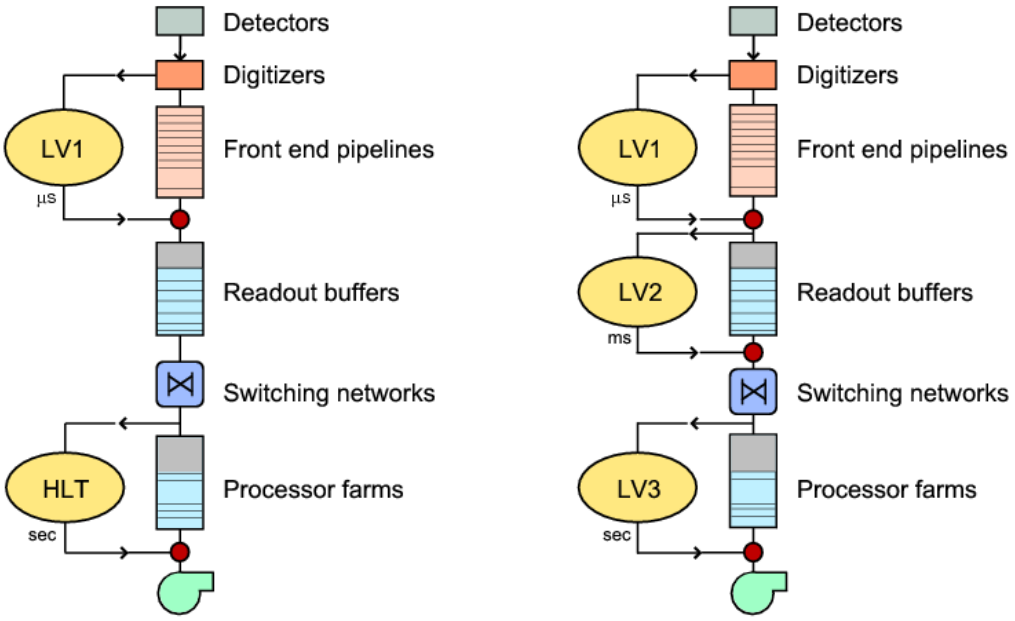

Figure A.2: Data flow in the Trigger/DAQ system. Left: the CMS choice, with a single entity, the High-Level Trigger (HLT) providing all filtering after the Level-1 decision. Right: the HLT function is split into two stages (LV2 and LV3).

- perform the readout of the front-end electronics after a Level-1 Trigger accept and assemble data from a given bunch-crossing in a single location (the memory of a computer);

- execute physics selection algorithms on the events read out, in order to accept the ones with the most interesting physics content;

- forward accepted events, as well as a small sample of the rejected ones, to online services monitoring the performance of the CMS detector;

- provide the means of archiving accepted events in mass storage.

A.4 Detector description

The CMS detector description includes geometrical shapes and dimensions, material information, and relative placements of each part of the detector in an ideal world. The software service providing this information uses a master source which can have derivatives. Sources derived from the master source can be databases, flat-file caches or other more optimized storage.

The Detector Description Database (DDD) (Case et al., 2001) provides access to the ideal geometry (geometry defined for the nominal placement of all geometrical objects) for CMS. Historically the DDD has referred to both a `C++` interface and ideal geometry data sources. The master data source is a collection of Extensible Markup Language (`XML`) files.

A.4.1 Geometry Service

The Geometry Service provides the necessary geometrical information for an event to be processed using the real geometry of detector elements as actually measured at the time of the event. Framework components are used to provide the ideal geometry from the Detector Description as well as Alignment corrections from the Conditions Service. Other framework components ensure the synchronization of the conditions to the event time. Subdetector specific software applies the alignments to the ideal geometry.

The CMS Geometry Service relies on the underlying software framework to provide the ideal geometry and alignment corrections necessary to deliver a user-level geometry for physics analysis.

A.5 Simulation

The detailed CMS detector and physics simulation is based on the GEANT4 (Agostinelli et al., 2003) simulation toolkit and the CMS object-oriented framework and event model. The simulation is implemented for all CMS detectors in both the central region (Tracker, Calorimeters and Muon Systems) and in the forward regions, including the field map from the 4 T solenoid. In addition, several test-beam prototypes and layouts have been simulated. The full simulation program implements the sensitive detector behavior, track selection mechanisms, hit collection and digitization (i.e. detector response).

The detailed simulation workflow is as follows:

- An appropriate Monte Carlo event generator (several are used) produces the data samples of physics events;
- A configuration for the GEANT4 simulation (detector configuration, physics cuts, etc.) is chosen;
- the GEANT4-based simulation of CMS, with generator events as input, produces (using the standard CMS framework) persistent hits in the sensitive detectors;
- These hit data are then used as input to the subsequent digitization step, allowing for pile-up. This step converts hits into digitizations ("digis") which correspond to the output of the CMS electronics.

A.5.1 Generation of physics events

There are several available Monte Carlo event generators for p p collisions, namely HERWIG (Corcella et al., 2001, 2002), HIJING (HIJ), ISAJET (Paige et al.), PYTHIA (Sjöstrand et al., 2006) and SHERPA (Gleisberg et al.). Each of these simulates a hadronic final state corresponding to some particular model of the underlying physics. The details of the implementation of the physics are different in each of these generators, however the underlying philosophy of the generators is the same (The CMS Collaboration, 2007). Most of the event generators that provide the collision events as input for the detector simulation are still written in FORTRAN, notably PYTHIA and HERWIG. Several projects to write event generators in C++ are ongoing (PYTHIA8, HERWIG++, SHERPA).

The cross section values and the differential distribution for almost all

processes are evalueated as follows:

$$\sigma(\mathrm{pp} \to CX) = \sum_{ij} \int f_i^{\mathrm{p}}(x_1, Q^2) f_j^{\mathrm{p}}(x_2, Q^2) \hat{\sigma}(ij \to C) dx_1 dx_2 \qquad \text{(A.1)}$$

where $f_i^{\mathrm{p}}(x, Q^2)$ are the Parton Distribution Functions (PDF) of i-th parton, that carried a fraction x of the initial proton momentum at a scale (Q^2), and $\hat{\sigma}(ij \to C)$ is the cross section for the hard process (i.e. describing two partons, i and j, interaction).

A general scheme of event generation assumes the evaluation of the hard process (the cross section value, the incoming and outgoing particle's momenta and colours), then evolves the event through a parton showering and hadronisation step, and the decay of the unstable particles. The event information contains the momenta of the final hadrons, leptons and photons and positions of their decay vertexes. Typically such information contains also the characteristics (momenta, colours, mother's and daughter's relations) of all intermediate partons (quarks, gluons, gauge bosons, unstable physical particles, etc) that provide a trace-back the history of particle production inside of an event. By using an acceptance-rejection methods weighted events can be returned.

Parton showering is based on the expansion around the soft and collinear evolution limits and is often ascribed to either the initial or final state. The algorithm used by `HERWIG` and `SHERPA` also include some effects due to quantum interference. The events that have more energy in the parton process have more showering, and consequently more jet activity.

The collection of quarks and gluons must then be hadronised into mesons and baryons. This is done differently in each of the event generators, but is described by a set of (fragmentation) parameters that must be adjusted to agree with experimental results. `HERWIG` looks for colour singlet collections of quarks and gluons with low invariant mass and groups them together; this set then turns into hadrons. `PYTHIA` splits gluons into quark-anti-quark pairs and turns the resulting set of colour singlet quark-anti-quark pairs into hadrons via a string model. `ISAJET` simply fragments each quark independently paying no attention to the colour flow.

The dominant cross-section at the LHC consists of events with no hard scattering. There is little detailed theoretical understanding of these minimum-bias events and the event generators must rely on present data. These minimum-bias events are important at LHC, particularly at design luminosity, as they overlap with interesting hard-scattering events. The generators use a different approach in this case. `HERWIG` uses a parametrisation of data mainly from the CERN p $\overline{\mathrm{p}}$ Collider. `PYTHIA` uses a mini-jet model where

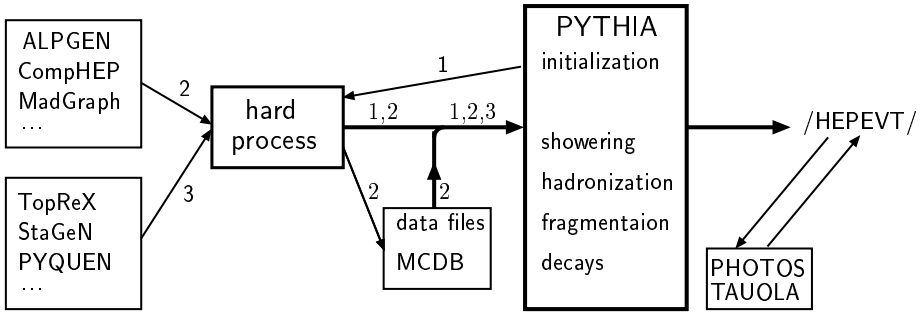

Figure A.3: Pure schematically data flow in `PYTHIA` and `HERWIG`.

the jet cross-section is used at very low transverse momenta, i.e the hard scattering process is extrapolated until it saturates the total cross-section. CMS has used the PYTHIA approach with dedicated modifications. The model of the hadronic interactions implemented in the physics generator has a direct impact on physical observables such as jet multiplicity, their average transverse momentum, internal structure of the jets and their heavy flavour content. This led to the choice to use PYTHIA for most processes, allowing for a consistent set of signal and background events to be generated.

Besides, the dedicated packages `CTEQ6L` (Pumplin et al., 2002) and `CTEQ6.5M` (Tung et al., 2007) are used for the calculation of the PDFs.

General scheme of generator usage in CMS

All event generators, included in CMS simulation software, can be separated into two groups.

The first group (`HERWIG`, `HIJING`, `ISAJET`, `PYTHIA`) provides the *full simulation* of events. The basic package explored in CMS is `PYTHIA` and only few specific processes were simulated with `HERWIG` or `HIJING`.

Pure schematically the data flow in `PYTHIA` and `HERWIG` is presented on Figure A.3.

After initialisation the package (`PYTHIA` or `HERWIG`) calls "hard process" routines (see "1" arrow lines on Figure A.3). Then information (the momenta of initial and final partons, the colours and so on) is passed to package for parton showering, hadronisation, fragmentation and decays of the unstable particles.

However, all these "full event simulation" generators have very limited number of the hard process matrix elements (typically for $2 \rightarrow 2$ reaction at

LO). Therefore, several special generators are used for simulation of many other LO processes. In fact, such packages generate the hard processes kinematic quantities, such as masses and momenta, the spin, the colour connection, and the flavour of initial- and final-state partons. The information is stored and is passed to full event simulation package like PYTHIA or HERWIG (see thick "output" line on Figure A.3).

Three generators, namely ALPGEN (Mangano et al., 2003), COMPHEP (Pukhov et al.), and MADGRAPH (Maltoni and Stelzer, 2003), are widely used for simulation of many processes, especially for the generation of the hard processes with multi-jet final states. For example, ALPGEN allows to generate $q\,\overline{q}$ pair production with up to 6 jets. As a result, the information with kinematics is stored in the output files (see "2" lines on Figure A.3). Then, like in a generic PYTHIA process, such information is passed to PYTHIA (see thick "output" line on Figure A.3).

There are several "*dedicated generators*", TOPREX (Slabospitsky and Sonnenschein, 2002), STAGEN, SINGLETOP, COSMIC, SIMUB, PHASE, PYQUEN (Lokhtin and Snigirev, 2000), HYDJET, EDDE. These generators are used for simulation of several specific process (see The CMS Collaboration (2007) for a short description of these codes). The information with hard processes kinematic quantities is stored and is passed to the "full event simulation" package (see "3" lines on Figure A.3).

After full simulation of event with PYTHIA or HERWIG the output information is stored. In addition two *special functionality* codes provide a better description of photon radiation from a charge final particles (PHOTOS (Barberio and Was, 1994)) and $\tau^{\pm}$-lepton decays (TAUOLA (Jadach et al., 1993)). Typically, these codes read the generator event information, perform simulation and then add generated information (new particles) into the event information again (see Figure A.3).

CMKIN

Almost all generators available in CMS could be used with the CMKIN package. Now the CMKIN is used for detector simulation input. This software package provides a common interface between physics event generators and CMS detector simulation. It also provides an environment to make physics plots of generated events. CMKIN provides an interface to a number of physics generators like PYTHIA, ISAJET and HERWIG. It also offers the possibility to use different "external generators" like ALPGEN (Mangano et al., 2003), COMPHEP (Pukhov et al.), MADGRAPH (Maltoni and Stelzer, 2003) and TOPREX (Slabospitsky and Sonnenschein, 2002). Cosmic muon simulation is available as well. Simple particle generation is also included, i.e. single and double

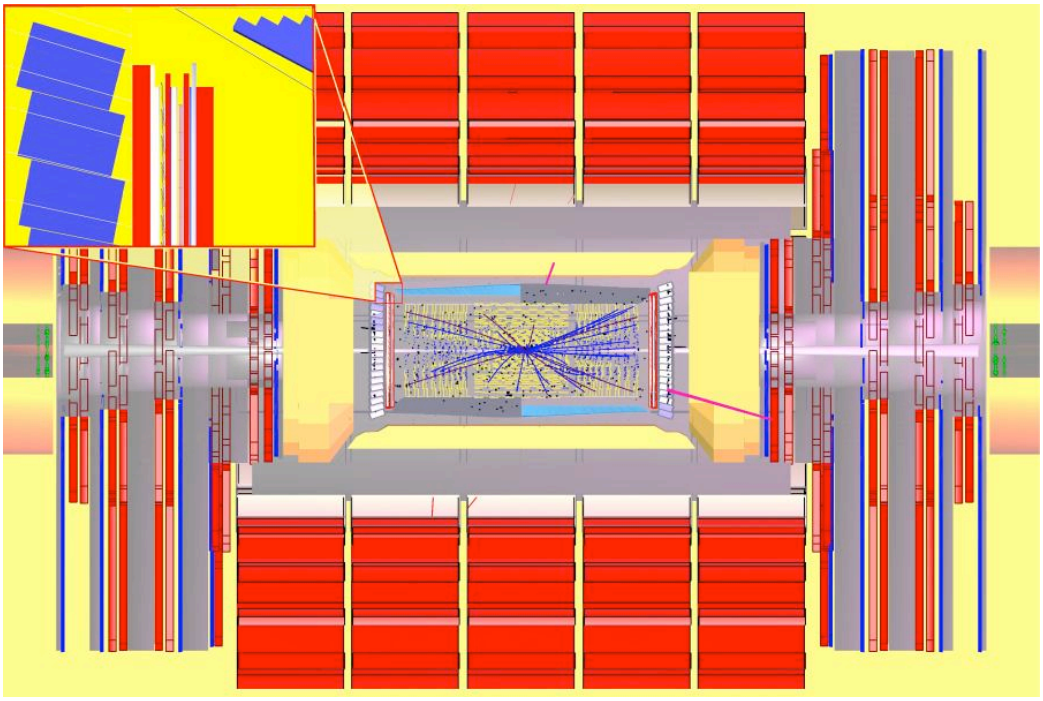

Figure A.4: CMS GEANT4-based simulation of the H $\rightarrow \gamma\gamma$ process showing the full CMS detector with the IGUANA-based interactive display. An inset zoom of the detector detail is also shown.

particles as well as simple multi particle events.

A.5.2 Detailed simulation framework

The full simulation relies on the GEANT4 toolkit (Agostinelli et al., 2003). GEANT4 provides a rich set of physics processes describing electromagnetic and hadronic interactions in detail. It also provides tools for modelling the full CMS detector geometry and the interfaces required for retrieving information from particle tracking through these detectors and the magnetic field. The CMS GEANT4-based simulation program uses the standard CMS software framework and utilities, as are used by the reconstruction programs.

A fully interactive (and non-CMS specific) GEANT4 visualization system has been established to debug the GEANT4 simulation, in particular the geometry modelling and magnetic field description. It is based on the IGUANA toolkit. Figure A.4 shows the IGUANA display of the full CMS detector as used for the GEANT4 simulation.

A.5.3 Pile-up treatment

During the low luminosity ($\mathscr{L} = 2 \times 10^{33}\,\mathrm{cm}^{-2}\,\mathrm{s}^{-1}$) and high luminosity ($\mathscr{L} = 10^{34}\,\mathrm{cm}^{-2}\,\mathrm{s}^{-1}$) phases of its operation, the LHC accelerator will produce, respectively, an average of about 3.5 and 17.5 inelastic (hard-core) p p collisions per bunch crossing that will "pile-up" on top of the signal collision firing the trigger. For the Monte Carlo simulations, diffractive collisions are also considered, which increases the pile-up total to 5.0 and 25 collisions, respectively, for low and high luminosity operation.

Moreover, in addition to the in-time pile-up, it is necessary to account in the simulation for out-of-time pile-up coming from bunch crossings before and after the triggered event. The number of crossings to consider before and after the nominal one depends on the front-end time response of the different subdetectors. Special cases such as bunch crossings with no pile-up either before or after the nominal one are also considered by the framework.

Since the addition of pile-up collisions occurs much faster than the detector simulation, and since it depends on the LHC luminosity and run conditions, pile-up collisions are simulated separately from the signal collisions. Both outputs are merged in a second step, using a luminosity dependent pile-up contribution. Generated signal collisions are therefore reused for producing samples corresponding to different luminosities.

The pile-up simulation is performed using the same `GEANT4` toolkit as for the signal simulation, producing simulated hits in exactly the same format. The pile-up collisions to be merged are randomly chosen from a pregenerated sample. In order to avoid correlations between event subsets overlapped to the same pile-up event sequence, a pile-up sample is never reused in the same order. Moreover, simulated pile-up collisions that pass trigger requirements are filtered out to avoid a low statistics bias in the many bunch crossings that would use such an event.

A.5.4 Digitization of simulated detector hits

The digitization step, following the hit creation step, constitutes the simulation of the electronic readout used to acquire data by the detector and DAQ systems. It starts from the hit positions and simulated energy losses in the sensitive detectors, and produces an output that needs to be as close as possible to real data coming from CMS. Information from the generation stage (e.g. particle type and momentum) is preserved in the digitization step.

Details on the digitization for the different CMS sub-detectors are given in chapter 2 of Volume I of the Physics Technical Design Report (The CMS Collaboration, 2006).

A.6 Event selection and reconstruction

Reconstruction is the operation of constructing physics quantities from the raw data collected in the experiment. As a software process, reconstruction is therefore the procedure of data reduction whose main client is the data analysis. The reconstruction process is seen as a collection of independent units, each one providing a set of corresponding reconstructed objects as output.

The reconstruction process can be divided into 3 steps, corresponding to local reconstruction within an individual detector module, global reconstruction within a whole detector, and combination of these reconstructed objects to produce higher-level objects.

The reconstruction units providing local reconstruction in a detector module use as input real data from the DAQ system or simulated data representing the real data. These data in either case are called "digis". The output from the reconstruction units are "`RecHits`", reconstructed hits which are typically position measurements (from times or clusters of strips or pixels) in tracking-type detectors (Muon and Tracker systems) and calorimetric clusters in Calorimeter systems. The `RecHits` are added to the event, and used as the input to the global reconstruction.

In the global reconstruction step information from the different modules of a subdetector are combined, although information from different subdetectors is not. For example, Tracker `RecHits` are used to produce reconstructed charged particle tracks and Muon `RecHits` are used to produce candidate muon tracks. Once again, the objects produced are added to the event.

The final reconstruction step combines reconstructed objects from individual subdetectors to produce higher-level reconstructed objects suitable for high-level triggering or for physics analysis. For example, tracks in the Tracker system and tracks in the Muon system are combined to provide final muon candidates, and electron candidates from the Calorimeter system are matched to tracks in the Tracker system. Figure A.5 shows how different units/products are combined to form a high level product.

A.6.1 Local reconstruction

Local reconstruction in individual detector modules leads to `RecHits`, which contain information about the energy deposition and positions of the particles interacting in the detectors.

In the Tracker detectors (strips and pixels), local reconstruction algorithms search for strips/pixels with a signal exceeding a threshold, and use these as seeds for clusters. Clusters are built by adding neighboring strips/pixels.

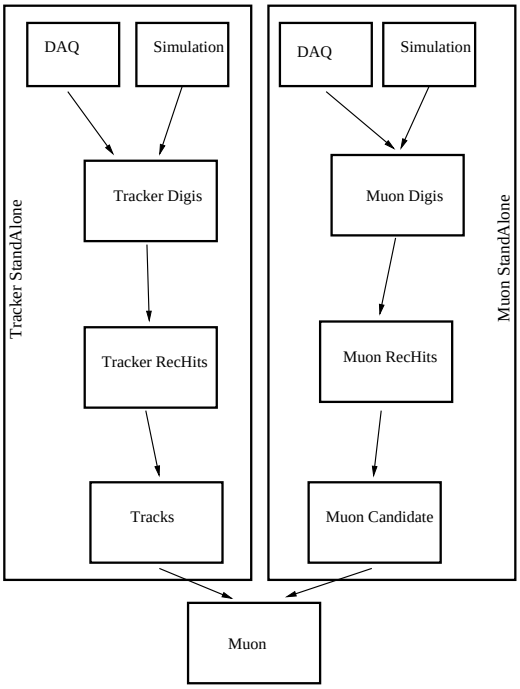

Figure A.5: Path to produce a Muon using information from Tracker and Muon Systems.

In the Muon Drift Chambers (DTs), local reconstruction provides the position of a muon hit in a drift cell, determined from the drift time measurement and the effective drift velocity. Three-dimensional track segments within a superlayer are built from hits in each component layer.

In the Muon Cathode Strip Chambers (CSCs), local reconstruction provides position and time of arrival of a muon hit from the distribution of charge induced on the cathode strips. Two-dimensional hits are obtained in each layer, and these can be combined to create three-dimensional track segments within each chamber (of 6 layers).

In the Muon Resistive Plate Chambers (RPCs), local reconstruction gives the position of a muon hit from the position of clusters of hit strips.

In the Electromagnetic Calorimeter (ECAL), local reconstruction identifies the position, time of arrival, and energy of localized electromagnetic energy depositions.

In the Hadron Calorimeter (HCAL), local reconstruction likewise identifies the position, time, and energy of localized hadronic energy depositions.

A.6.2 Global reconstruction

The global reconstruction algorithms use the objects created in the local reconstruction within a single detector module, combining them with the objects arising from other modules of the same subdetector to produce further objects which represent the best measurement from that subdetector. At this stage, no attempt is made to link the information from different subdetectors; this is part of the later Combined Reconstruction step.

Reconstruction in the Tracker system

In the high multiplicity charged-particle environment of p p collisions at LHC, a global tracking approach is unlikely to be an efficient use of computing resources. Instead, specialized approaches can serve different use cases, e.g. low/high p_{t} tracks, searches for displaced vertices, etc.

In order to satisfy multiple use cases, different reconstruction units must be permitted to run in parallel, each producing a set of tracks applicable to a specific use case. CMS has implemented and tested several different tracking algorithms, each implemented in a common framework in which the various components, from seed finding to propagation and final fit, are cleanly separated and modularized. More than one algorithm is usually available for each component, allowing an easy adaptation to different use cases. Additional information can be found in section A.7.

Reconstruction in the Calorimeter system

A Calorimetric Tower (`CaloTower`) links matching clusters in ECAL and HCAL to produce a projective tower in the calorimetry system. The towers have a definite position in the (η, ϕ) plane, and hence can be used as the basis for Jet reconstruction as described in section A.6.3.

Reconstruction in the Muon system

Global reconstruction in the Muon system is also called "Standalone muon" since it does not make use of Tracker hits; and it is also used in the Level 2 trigger algorithms. The reconstruction makes use of the track hits and track segments from the local reconstruction step in the individual muon subdetector modules of the CSC, DT, and RPC detectors. The algorithm starts from the locally-reconstructed muon track segments. A segment in one of the innermost detector stations (those closest to the interaction point) is used as a seed for a Kalman filter, which builds trajectories in the radially-increasing direction. A χ^2 cut is applied to reject hits unlikely to be associated with

the track, which can arise from showering, delta rays, and pair production. The trajectory is propagated using a detailed map of the magnetic field and taking account of energy loss in the detector material (mainly the steel of the magnet return yoke), until the outermost detector layer of the Muon system is reached. A backward Kalman filter is then applied, working from outside in, and the track parameters are defined at the innermost muon station. Finally, the track is extrapolated to the nominal interaction point and a vertex-constrained fit to the track parameters is performed. In this fit, since the magnetic field is inhomogeneous and nonuniform in the 2 endcap regions, the two-dimensional hits in CSC layers are used instead of the track segments which were used for seeding. Additional information can be found in section A.8.

A.6.3 Combined reconstruction: high-level objects

The final stage of reconstruction combines input objects created in the global reconstruction within each subdetector detector, creating objects based on the complete CMS detector. For example, a standalone muon candidate can be extrapolated into the Tracker detector, thus improving the measured muon track parameters using the high precision of the Tracker measurements. Another common example is matching of ECAL and HCAL clusters and their combination into jet candidates.

Photon and electron identification

Electron and photon showers deposit their energy in several crystals in the ECAL. Approximately 94% of the incident energy of a single electron or photon is contained in 3×3 crystals, and 97% in 5×5 crystals. The presence in CMS of material in front of the calorimeter results in bremsstrahlung and photon conversions. Because of the strong magnetic field the energy reaching the calorimeter is spread in ϕ. The spread energy is clustered by building a cluster of clusters, a "supercluster", which is extended in ϕ.

The global selection of electrons and photons proceeds in 3 steps. The first step uses the Calorimeter information only. The second step requires hits in the pixel detectors, consistent with an electron candidate. The success of the matching of an ECAL "supercluster" to hits in the pixel detector flags the candidate as an electron; otherwise, the candidate is flagged as a photon. In the final step, the selection of electrons uses full track reconstruction, seeded from the pixel hits obtained by the matching step. The selection of photons can instead use isolation cuts and rejection of π^0's based on lateral shower shape and the reconstruction of converted photons.

Additional information is given in the Volume I of the CMS Physics Technical Design Report (The CMS Collaboration, 2006, chapter 10, page 365).

Jet reconstruction

Jet reconstruction in p p collisions aims to reconstruct and identify jets arising from the hadronization of a scattered parton, in order to reconstruct its direction and energy. Many reconstruction algorithms exist in the literature, and vary in speed, efficiency, and resolution.

Most algorithms use a clustering technique, in which calorimetric towers close in (η, ϕ) to a high E_{t} tower are summed together, subject to some constraints. For example, in the cone algorithm, a seed tower is selected (typically according to high E_{t}) and then all objects sufficiently close in (η, ϕ) are used to form a proto-jet. The process of association is iterated until the parameters of the proto-jet have stabilized, and then the associated towers are considered to comprise a jet candidate. The procedure is repeated with the remaining unassociated towers, until no seeding tower with sufficiently high E_{t} remains.

See the Volume I of the CMS Physics Technical Design Report (The CMS Collaboration, 2006, chapter 11, page 404) for additional information.

Missing E_{t} reconstruction

Many channels of discovery at the LHC present as a clear signature for new physics a large missing transverse energy (for example, SUSY decays with a LSP escaping detection by CMS). A large effort has been placed on the design of calorimeters to have as complete η coverage as possible to allow for the needed measurement accuracy.

Muon identification

Global muon identification starts from the Standalone muon, adding associated silicon tracker hits and performing a final fit to the track.

Isolation criteria (see section 4.5) can also be applied to the muon candidates to provide additional rejection: at Standalone reconstruction using the calorimetric energy sum in a cone around the muon, and at Global reconstruction using the number of pixel tracks in a region around the projected muon trajectory. This suppresses non-prompt muons from b, c, π, and K decays.

Additional information is available in section A.8.

A.7 Track reconstruction

Track reconstruction in a dense environment needs an efficient search for hits during the pattern recognition stage and a fast propagation of trajectory candidates. In the CMS Tracker, the first task is simplified by the arrangement of sensitive modules in layers that are practically hermetic for a particle originating from the centre of the detector.

The second task uses the fact that the magnetic field is almost constant in a large part of the tracker volume and also that most of the support structure is concentrated on the layers, close to the sensors. During reconstruction the typical step length for propagation of track parameters is on the order of the distance between 2 layers and a helical track model is adequate. For reconstruction purposes the detailed distribution of passive material as used in the simulation is replaced by an attribution of material to layers. This model simplifies the estimation of energy loss and multiple scattering, which can be done at the position of the sensitive elements without requiring additional propagation steps.

The track reconstruction is decomposed into 5 logical parts:

- Hit reconstruction, which in turn consists of clustering of strips or pixels and estimating a position and its uncertainty;
- Seed generation;
- Pattern recognition or trajectory building;
- Ambiguity resolution;
- Final track fit.

A.7.1 Tracker clusterization

Silicon strip tracker clusterization

Clusters are reconstructed in the strip tracker by searching for a seed strip with a signal to noise ratio $S/N > 3$. Nearby strips are included in the cluster if they satisfy $S/N > 2$. Holes are allowed inside clusters only if they are assigned to highly inclined tracks. The total signal size of the cluster must exceed 5 times the square-root of the sum of the RMS-noise-squared of the individual strips inside it.

The cluster position is usually determined from the centroid of the signal heights. The large interchannel coupling in the strip tracker makes it non-trivial to determine the position from the cluster edges, as is done for the

pixel tracker. Nonetheless, this is done for very wide clusters (containing at least 4 strips).

The position resolution is parameterized as a quadratic function of the projected track width on the sensor in the plane perpendicular to the strips. The parameters are also dependent on whether the observed cluster width is compatible with the track width and cluster position.

Pixel tracker clusterization

The cluster reconstruction algorithm for the pixel detector starts from a cluster seed, defined as a pixel with $S/N > 6$. It then adds pixels adjacent to the cluster if they have $S/N > 5$, continuing this process until no more adjacent pixels are found. Diagonally adjacent pixels are considered adjacent. Finally the cluster is retained if its total charge has $S/N > 10.1$. The same algorithm is applied to the barrel and forward pixel detectors.

The position of pixel clusters is estimated independently in both dimensions. It is based on the relative charges of the pixels at the edges of the cluster and the associated reconstructed track angle. Depending on the detector module orientation, both the track inclination and the Lorentz shift can contribute to the charge sharing.

The algorithm used needs as an input parameter the expected width of the charge distribution collected on the sensor surface. A precise charge width estimate is performed if the impact angles of the particle on the detector are known from the partial track reconstruction, otherwise the track impact angles are estimated from the polar and azimuthal angles of the hit modules with all tracks assumed to originate from the nominal interaction point.

The error on the reconstructed position is estimated from the spatial displacement between simulated and reconstructed hits (residuals) and error parameterization is performed as a function of the cluster size and the rapidity. An additional and more precise error parameterization is performed when the track impact angles are available from the partial or complete track reconstruction.

The reconstruction inefficiency is defined as the fraction of simulated hits that do not have any associated reconstructed hit. For the pixel detectors this is below 0.5%. The fraction of reconstructed hits that is not associated with any simulated hit (ghost hits) is less than 0.01%. Both the reconstruction efficiency and the ghost rate quoted here do not take into account readout inefficiencies.

Typical simulated resolutions, for unirradiated sensors, are better than 15 μm in the barrel in the transverse direction and vary between $15 - 30$ μm for the barrel longitudinal direction and for the endcap disks.

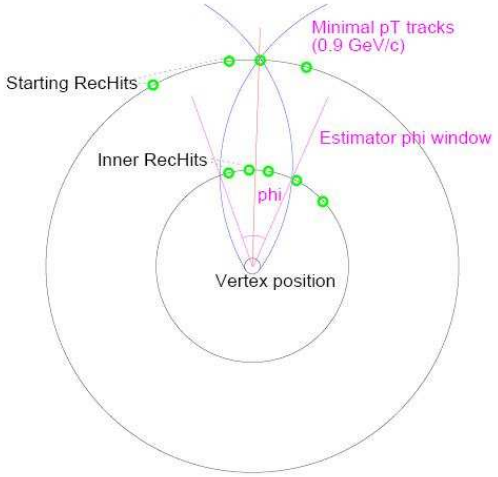

Figure A.6: Principle of operation of the Pixel seed generator.

A.7.2 Seed generation

Seed generation provides initial trajectory candidates for the full track reconstruction. A seed must define initial trajectory parameters and errors. They can be obtained externally to the Tracker, using inputs from other detectors, but the precision of initial trajectory parameters obtained in such a way is, in general, poor. Another way is to construct seeds internally. In this case each seed is composed from the set of reconstructed hits that are supposed to come from 1 charged particle track. Since 5 parameters are needed to start trajectory building, at least 3 hits, or 2 hits and a beam constraint, are necessary. If the beam constraint is used it is removed during the final fit. Hits that are seed constituents are provided by the dedicated reconstruction.

Regional seed generation

Although the external information is usually not sufficient for full seed definition it is still useful to constrain the search area for its constituents.

A major improvement in the current implementation is the possibility to do the reconstruction in the region of interest only (*regional reconstruction*). The key concept for the new regional reconstruction software is called the `TrackingRegion`. It is meant to be an abstract definition of the region of interest with kinematical constraints. The `TrackingRegion` specifies the direction around which the region is defined, the (signed) inverse transverse momentum range, and the allowed position of the track impact point (vertex along beam line and maximum allowed distance from vertex in the transverse

plane and along the beam line). Two concrete implementations are provided: `GlobalTrackingRegion` and `RectangularEtaPhiTrackingRegion`. The latter allows the direction to be constrained within a given range of η and ϕ. Regional seed generation reconstructs sets of hits which are compatible with a track passing the kinematical requirements of the `TrackingRegion`.

Choise of the layers for hit finding

In the baseline, seeds are defined by pairs of pixel hits. The pixel detector is well suited for seeding purposes because of its low occupancy. Furthermore, pixel hits are the most precise, close to the beam pipe, and have both $r-\phi$ and $z-r$ coordinate measurements. To assume maximal efficiency for finding hit pairs in each direction, 3 combinations of layer pairs are used.

Conversion of hit pairs to seeds

Seed creation is much more computationally intensive than just the 2 (at least) hits used for its definition. Seed construction involves computation of the `FreeTrajectoryState`, construction of an error matrix, and definitions of the first 2 `TrajectoryMeasurements` and a `TrajectoryStateOnSurface`, which contains the local and global position and direction of the track together with the curvature and the covariance matrix of track parameters.

Additional seed generators

Another type of seed generator is the generator based only on hits from the strip tracker. It can be especially useful for the detector at start-up, when the pixel detector will not be installed in an incomplete configuration. The hit-pair finding algorithm described above is applied to pairs of layers of silicon-strip detectors.

It is also possible to combine the pixel layers with some silicon layers.

A.7.3 Pattern recognition

The pattern recognition is based on a combinatorial Kalman filter method. The filter proceeds iteratively from the seed layer, starting from a coarse estimate of the track parameters provided by the seed, and including the information of the successive detection layers one by one. On each layer, i.e., with every new measurement, the track parameters are known with a better precision, up to the last point, where they include the full tracker information.

First, a dedicated navigation component determines which layers are compatible with the initial seed trajectory. The trajectory is then extrapolated to these layers according to the equations of motion of a charged particle in a magnetic field, accounting for multiple scattering and energy loss in the traversed material.

Since several hits on the new layer may be compatible with the predicted trajectory, several new trajectory candidates are created, 1 per hit. In addition, 1 additional trajectory candidate is created, in which no measured hit is used, to account for the possibility that the track did not leave any hit on that particular layer. This fake hit is called an "invalid hit".

Each trajectory is then "updated" with the corresponding hit according to the Kalman filter formalism. This update can be seen as a combination of the predicted trajectory state and the hit in a weighted mean, as the weights attributed to the measurement and to the predicted trajectory depend on their respective uncertainties.

All resulting trajectory candidates are then grown in turn to the next compatible layer(s), and the procedure is repeated until either the outermost layer of the tracker is reached or a "stopping condition" is satisfied. In order not to bias the result, all trajectory candidates are grown in parallel. To avoid an exponential increase of the number of trajectory candidates, the total number of candidates is truncated at each layer. To limit the number of combinations, and hence to avoid an exponential increase thereof, only a limited number of these are retained at each step, based on their normalized χ^2 and number of valid and invalid hits.

Tunable parameters, regional and partial tracking

This algorithm is configurable through several parameters.These main parameters are (default values are given in brackets) the following:

- the maximum number of candidates that are propagated at each step (5);
- the inclusion of an invalid hit in the list of compatible hits, when the latter is not empty (always include invalid hit);
- the maximum χ^2 of the hits considered compatible with the predicted track state (30);
- the maximum number of invalid hits, i.e., crossings of sensitive detectors without a measurement (1);
- the maximum number of consecutive invalid hits (1);

- the minimum transverse momentum (0.9 GeV/c);
- the minimum number of hits per track (5).

In addition, it is possible to specify an arbitrary stopping condition, in which case the pattern recognition is interrupted before the end of the tracker is reached (*partial track reconstruction*).

If the track reconstruction is constrained to a region, the constraint affects mostly the seed generation phase. The only constraint that can be applied effectively at the pattern recognition stage is the transverse momentum cut.

When a trajectory is propagated to a given layer, the uncertainty of the predicted state has a direct effect on pattern recognition, since it determines the compatibility between the trajectory and nearby hits. The number of compatible hits found on a layer determines the increase of the number of trajectories to be propagated, as the initial trajectories are multiplied by the number of hits found.

A.7.4 Ambiguity resolution

Ambiguities in track finding arise because a given track may be reconstructed starting from different seeds, or because a given seed may result in more than 1 trajectory candidate. These ambiguities, or mutually exclusive track candidates, must be resolved in order to avoid double counting of tracks.

The ambiguity resolution is applied twice: the first time on all track candidates resulting from a single seed, and the second time on the complete set of track candidates from all seeds.

A.7.5 Track fitting and smoothing

For each trajectory, the building stage results in a collection of hits and in an estimate of the track parameters. However, the full information is only available at the last hit of the trajectory and the estimate can be biased by constraints applied during the seeding stage. Therefore the trajectory is refitted using a least-squares approach, implemented as a combination of a standard Kalman filter and smoother.

The Kalman filter is initialized at the location of the innermost hit with an estimate obtained during seeding. The corresponding covariance matrix is scaled by a large factor in order to avoid any bias. The fit then proceeds in an iterative way through the list of hits. For each valid hit the position estimate is re-evaluated using the current values of the track parameters: information about the angle of incidence increases the precision of the measurement especially in the pixel modules. The track parameters and their covariance

matrix are updated with the measurement and the trajectory is propagated to the surface associated with the next hit. The track parameters and their covariance matrix are modified according to the estimates for energy loss and multiple scattering at the target surface and the sequence is repeated until the last hit is included.

This first filter is complemented with a smoothing stage: a second filter is initialized with the result of the first one —except for the covariance matrix, which is scaled with a large factor — and run backward toward the beam line. At each hit the "updated" parameters of this second filter, which contain all information from the outermost hit up to and including the current hit, are combined with the "predicted" parameters of the first filter, i.e., the information from the innermost hit outward, but excluding the current hit.

This filtering and smoothing procedure yields optimal estimates of the parameters at the surface associated with each hit and, specifically, at the first and the last hit of the trajectory. Estimates on other surfaces, e.g., at the impact point, are then derived by extrapolation from the closest hit.

A.7.6 Influence of tracker material on track reconstruction

Track reconstruction is based upon the equations of motion of a charged particle in a magnetic field. In the standard Kalman filter the evolution of the state vector and its covariance matrix is determined. This simple model has to be modified in the presence of matter. Two kinds of effects are taken into account: energy loss (for electrons due to bremsstrahlung, for all other particles due to ionization), and multiple scattering. Ionization energy loss is described according to the Bethe-Bloch formula without density corrections; the average and variance of the fractional energy loss of electrons due to radiation are computed based on the PDF given by Bethe and Heitler. The effect of multiple scattering is calculated using the approximation for the gaussian core given by Highland (Yao et al., 2006, chapter 27).

The simplified treatment of the material is valid only inside the Tracker volume. Propagation to the Muon system requires detailed knowledge of the passive material. Currently the propagations outside of the tracker volume are performed with the `GEANE` package (Innocente et al., 1991), which uses the full simulation geometry.

A.8 Muon reconstruction

The muon reconstruction software is able to perform reconstruction in the muon system and the silicon tracker. The software has been designed using the concept of *regional reconstruction* in order to allow its use in both the offline reconstruction and the High-Level Trigger (The CMS Collaboration, 2000) (online event selection).

Employing regional reconstruction results in very small parts of the detector actually needing to be reconstructed before a physics object is validated. As an example, the amount of information needed to reconstruct a muon track in the silicon tracker represents less than a few per cent of the total tracker data volume. The software does not reconstruct tracks in the entire tracker, but only in that part which can possibly be involved in the reconstruction of a charged particle track compatible with the hits in the muon chambers. This results in savings on the overall CPU power needed to process the events. The method depends strongly on the identification of a good "seed", providing initial values of the 5 trajectory parameters and their errors, that can start the reconstruction with high efficiency and reliability. In the online environment these seeds are provided by the Level-1 Trigger system (The CMS Collaboration, 2002).

The muon reconstruction algorithm used by the HLT is seeded by the muon candidates found by the Level-1 muon trigger, including those candidates that did not necessarily lead to a Level-1 trigger accept. These seeds define a region of interest in the muon system, in which local reconstruction is performed. For offline reconstruction a different seed-generation algorithm has been developed, which performs local reconstruction in the entire muon system and uses patterns of segments reconstructed in the CSC and/or DT chambers as initial seeds. Muon reconstruction is performed in 3 stages: local reconstruction (local-pattern recognition), standalone reconstruction and global reconstruction. Starting from a seed, the chambers compatible with the seed are identified and local reconstruction is performed only in these chambers. Standalone muon reconstruction uses only information from the muon system, while global-muon reconstruction uses also silicon tracker hits. The HLT standalone and global reconstruction are called Level-2 and Level-3 reconstruction, respectively.

A.8.1 Local muon reconstruction

Position reconstruction and track-segment reconstruction in the drift tubes

The information stored in a DT digi is a TDC measurement, representing a drift time. The primary objects that result from the DT local reconstruction are, therefore, points in the cell volume: their distances with respect to the wire are computed by converting drift times to drift distances.

Starting from a time-to-distance parameterization obtained using a `GARFIELD` (Veenhof, 1994) simulation of the cell behaviour, the measured coordinate x_{drift} is computed using a function of the drift time; $B_{\parallel}$ and $B_{\perp}$, the components of the B field parallel and perpendicular, respectively, to the wire in the radial direction; and α, the incidence angle with respect to the normal direction to the chamber:

$$x_{\text{drift}} = x_{\text{drift}}(t_{\text{drift}}, B_{\parallel}, B_{\perp}, \alpha). \tag{A.2}$$

The component of the magnetic field parallel to the drift lines can be neglected since it has no measurable effect on the drift time.

Since $B_{\parallel}$, $B_{\perp}$ and α are not known at the level of the individual hit, a 3-step reconstruction procedure is implemented. The first step assumes a crude estimate of the impact angle and the hit position along the wire. The hit is then updated twice: after it has been used to build a 2D $r-\phi$ or $r-z$ segment (second step) and after it has been used in the 3D segment fit.

By default, the errors on the reconstructed hit positions are obtained from a Gaussian fit of the residual distributions (the difference between simulated and reconstructed distances from the wire).

The reconstruction algorithm, which uses a constant drift velocity to compute the hit distance from the wire using a constant drift velocity, neglects any dependency on the magnetic field or the track angle.

The segment reconstruction works on the $r-\phi$ and $r-z$ projections independently: only at the end of the procedure are the 2 projections combined and a three-dimensional segment is built. The reconstruction in each projection is an exercise in pattern recognition and linear fitting, with the complication of left-right ambiguity. The reconstruction is performed in 3 steps:

1. a segment candidate is built from a set of aligned hits;
2. the best segments among those sharing hits are selected;
3. the hit reconstruction is then updated using the information from the segment and the segments themselves are eventually refitted.

The first step begins by selecting 2 hits in different layers, starting from the most separated. Both hypotheses, left and right, are considered. The pair is kept if the angle of this protosegment is compatible with a track pointing to the nominal interaction point. For each pair, additional compatible hits are searched for in all layers. It is possible that the left and right hypotheses are both compatible with the segment. In this case, the ambiguity is solved later. At this stage, a linear fit is performed using the hit positions and errors for each collection of hits. The segment with the maximum number of hits and the minimum χ^2 is retained; all the others are rejected. Finally, a quality criterion is applied, requiring the number of hits ≥ 3 and the $\chi^2/\mathrm{ndf} < 20$. The same algorithm is applied for a single superlayer $r-z$ or, in the case of the $r-\phi$ projection, for 2 SLs, considering all 8 layers together. In all cases, a protection against the detector being too noisy is applied, so the reconstruction is not attempted if the number of hits is greater than a predefined number.

The pattern recognition described above produces a set of segment candidates. A consistency check is performed in order to test whether 2 segments share the same hit. Conflicts are solved on the basis of the number of hits and the χ^2 of the segment.

The hits from the leftover candidates are updated, taking into account the incidence angle as reconstructed by the segment. The segment linear fit is then redone using the updated hits.

Up to this point, the $r-\phi$ and $r-z$ projections are treated independently. As the 2 projections are orthogonal, a segment in 1 projection cannot be used to validate or invalidate a segment in the other. By construction, all combinations of segments from the 2 projections are kept. In practice, more than 1 segment is found for either projection in a given chamber in less than 1% of the cases.

Knowledge of the position along the wire, as well as the angle with respect to the drift cell, are provided to the hit reconstruction algorithm before combining the 2 projections performing the final fit of the segment. The result is a segment with parameters in space, suitable for use in the global reconstruction.

Clusterization and track-segment reconstruction in the cathode strip chambers

The inputs to the local reconstruction are the detected signals from the cathode strips and anode wires. The information about these signals are contained in the strip and wire digis, respectively. In the simulation software, the digis are the output of the preceding simulation of the electronics

response of the detector to the passage of generated particles. In the real world, the digis will be derived from the actual DAQ output stream.

The charge distribution due to the passage of a single charged particle through a chamber layer is typically distributed over 3 to 5 strips.

The basic procedure for local reconstruction in the endcap muon CSCs is to obtain the pulse height in each strip (in a strip digi), and then to cluster neighbouring strips to determine the probable position of incidence of the incident muon.

Each of the 6 layers of a chamber is considered independently. A two-dimensional `RecHit` is created at each intersection of a 3-strip cluster and a wire group. At a later stage of local reconstruction, the `RecHits` in the 6 layers of a chamber are fit to form a "track segment" for use in the first stage of the muon track reconstruction.

The final stage of the local reconstruction in the CSCs is to build track segments within each CSC from the `RecHits` reconstructed in each of the 6 layers. The algorithm starts with the first and last `RecHit` in a chamber (the hit with the most negative local x in layer 1 and the hit with the most positive local x in layer 6) and constructs a straight line between them. The starting and ending points are required to have an $r-\phi$ separation of at most 1 cm. Then for each intermediate layer, we successively attempt to add 1 hit and update the linear fit accordingly. Only hits reasonably close (within 2.5 mm in $r-\phi$) to the line are considered, and the χ^2/ndf of the updated fit must be reasonable. The hit giving the best fit from all compatible hits on a layer is kept. A track segment is defined only if there are at least 4 hits on such a line. The associated hits are then flagged as 'used', and the procedure is iterated starting with another pair of unused hits for the end points of a line. The fit is performed simultaneously in the local z projections for x and y. If no segment is built using the default hit-association windows, a second pass is allowed in which the windows are broadened.

Clusterization in resistive plate chambers

In the RPCs, the results of the local reconstruction are points in the plane of the detector. A clustering procedure is first performed, using all the strips that have a signal. The procedure combines all adjacent fired strips into a cluster. Once all the clusters are formed, the reconstructed point for each is defined as the "center of gravity" of the area covered by that cluster of strips. In the barrel, where the strips are rectangular, this point is simply the center of a rectangle. In the endcap, the computation is more complicated since the area covered by the clusters are trapezoids of variable shape. The assumption is that each group of strips is fired as the result of a single particle crossing the

chamber plane, and that this crossing can have taken place anywhere with flat probability over the area covered by the strips of that cluster. Errors are computed under the same assumption of flat probability. Therefore, they are simply $\sigma_i = L_i/\sqrt{12}$ $(i = 1, 2)$, where L_i is the length of the i-th side of the rectangle.

A.8.2 Standalone muon reconstruction

The standalone/Level-2 muon reconstruction uses only data from the muon detectors — the silicon tracker is not used. Both tracking detectors (DT and CSC) and RPCs participate in the reconstruction. Despite the coarser spatial resolution, the RPCs complement the tracking chambers, especially where the geometrical coverage is problematic, mostly in the barrel-endcap overlap region.

The reconstruction starts with the track segments from the muon chambers obtained by the local reconstruction. The state vectors (track position, momentum, and direction) associated with the segments found in the innermost chambers are used to seed the muon trajectories, working from inside out, using the Kalman-filter technique (Fruhwirth, 1987). The predicted state vector at the next measurement surface is compared with existing measurements and updated accordingly. In the barrel DT chambers, reconstructed track segments are used as measurements in the Kalman-filter procedure. In the endcap CSC chambers, where the magnetic field is inhomogeneous, the individual reconstructed constituents (three-dimensional hits) of the segments are used instead. Reconstructed hits from the RPC chambers are also included. A suitable χ^2 cut is applied in order to reject bad hits, mostly due to showering, delta rays and pair production. In case no matching hits (or segments) are found, e.g. due to detector inefficiencies, geometrical cracks, or hard showering, the search is continued in the next station. The state is propagated from one station to the next using the `GEANE` package, which takes into account the muon energy loss in the material, the effect of multiple scattering, and the nonuniform magnetic field in the muon system. The track parameters and the corresponding errors are updated at each step. The procedure is iterated until the outermost measurement surface of the muon system is reached. A backward Kalman filter is then applied, working from outside in, and the track parameters are defined at the innermost muon station. Finally, the track is extrapolated to the nominal interaction point (defined by the beam-spot size: $\sigma_{xy} = 15$ μm and $\sigma_z = 5.3$ cm) and a vertex-constrained fit to the track parameters is performed.

A.8.3 Global muon reconstruction

The global/Level-3 muon reconstruction consists in extending the muon trajectories to include hits in the silicon tracker (silicon strip and silicon pixel detectors). Starting from a standalone reconstructed muon, the muon trajectory is extrapolated from the innermost muon station to the outer tracker surface, taking into account the muon energy loss in the material and the effect of multiple scattering. The `GEANE` package is currently used for the propagation through the steel, the coil and the calorimeters. Silicon layers compatible with the muon trajectory are then determined, and a region of interest within them is defined in which to perform regional track reconstruction. The determination of the region of interest is based on the track parameters and their corresponding uncertainties of the extrapolated muon trajectory, obtained with the assumption that the muon originates from the interaction point. The definition of the region of interest has a strong impact on the reconstruction efficiency, fake rate, and CPU reconstruction time: well measured muons are reconstructed faster and with higher efficiency than poorly measured ones.

Inside the region of interest, initial candidates for the muon trajectory (regional seeds) are built from pairs of reconstructed hits. The 2 hits forming a seed must come from 2 different tracker layers, and all combinations of compatible pixel and double-sided silicon strip layers are used in order to achieve high efficiency. In addition, a relaxed beam-spot constraint is applied to track candidates above a given transverse momentum threshold to obtain initial trajectory parameters. Starting from the regional seeds, a track-reconstruction algorithm, based on the Kalman-filter technique, is used to reconstruct tracks inside the selected region of interest. The track-reconstruction algorithm consists of the following steps: trajectory building (seeded pattern recognition), trajectory cleaning (resolution of ambiguities) and trajectory smoothing (final fit). In the first step, the trajectory builder transforms each seed into a set of trajectories. Starting from the innermost layer, the trajectory is propagated to the next tracker reachable layer, and updated with compatible measurements found on that layer. In the second step, the trajectory cleaner resolves ambiguities between multiple trajectories that may result from a single seed on the basis of the number of hits and the χ^2 of the track fit. In the final step, all reconstructed tracks are fitted once again, without a beam-spot constraint, using the hits in the muon chambers from the original standalone reconstruction together with the hits in the silicon tracker. To resolve possible ambiguities a second cleaning step is performed which selects the final muon candidates on the basis of a χ^2 cut.

A.9 Event data tiers

CMS defines different standard data tiers corresponding to different levels of detail required by various applications. These range from alignment, calibration and detector studies, to Physics analysis:

`FEVT` (Full EVenT) contains the full event content, including many outputs produced by intermediate processing steps;

`RECO` (RECOnstructed Data) contains the output of the reconstruction including enough information to be able to apply new calibrations and alignments and reprocess many of the components;

`AOD` (Analysis Object Data): this is a subset of the reconstructed data (RECO) chosen to satisfy the needs of a large fraction of physics analysis studies and which should be contained in a size of roughly 100 kilo-bytes per event.

BIBLIOGRAPHY

CMS Software Home Page. https://cmsdoc.cern.ch/cms/cpt/Software/html/General/. (Cited on page 138.)

HIJING web site. http://www-nsdth.lbl.gov/xnwang/hijing/index.html. (Cited on page 144.)

S. Abachi et al. Search for High Mass Top Quark Production in p $\overline{\text{p}}$ Collisions at $\sqrt{s}$ = 1.8 TeV. *Phys. Rev. Lett.*, 74(13):2422–2426, Mar 1995a. doi: 10.1103/PhysRevLett.74.2422. The D0 Collaboration. (Cited on page 22.)

S. Abachi et al. Observation of the Top Quark. *Phys. Rev. Lett.*, 74(14): 2632–2637, Apr 1995b. doi: 10.1103/PhysRevLett.74.2632. The D0 Collaboration. (Cited on page 22.)

G. Abbiendi et al. Search for the Standard Model Higgs Boson at LEP. *Physics Letters B*, 565:61–75, Jul 2003. The ALEPH Collaboration, the DELPHI Collaboration, the L3 Collaboration and the OPAL Collaboration, The LEP Working Group for Higgs Boson Searches. arXiv:hep-ex/0306033. (Cited on page 35.)

F. Abe et al. Evidence for Top Quark Production in p $\overline{\text{p}}$ Collisions at $\sqrt{s}$ = 1.8 TeV. *Phys. Rev. D*, 50(5):2966–3026, Sep 1994a. doi: 10.1103/PhysRevD.50.2966. The CDF Collaboration. (Cited on page 22.)

F. Abe et al. Evidence for Top Quark Production in p $\overline{\text{p}}$ Collisions at $\sqrt{s}$ = 1.8 TeV. *Phys. Rev. Lett.*, 73(2):225–231, Jul 1994b. doi: 10.1103/PhysRevLett.73.225. The CDF Collaboration. (Cited on page 22.)

F. Abe et al. Observation of Top Quark Production in p $\overline{\text{p}}$ Collisions with the Collider Detector at Fermilab. *Phys. Rev. Lett.*, 74(14):2626–2631, Apr

1995. doi: 10.1103/PhysRevLett.74.2626. The CDF Collaboration. (Cited on page 22.)

S. Agostinelli et al. GEANT4: A simulation toolkit. *Nucl. Instrum. and Methods A*, 506:250–303, 2003. The GEANT4 Collaboration. (Cited on pages 144 and 148.)

I. Aitchison and A. Hey. *Gauge Theories in Particle Physics.* Graduate Student Series in Physics. IOP Publishing, third edition, 2002. (Cited on page 7.)

J. Alcaraz et al. A Combination of Preliminary Electroweak Measurements and Constraints on the Standard Model, 2006. URL http://lepewwg.web.cern.ch/LEPEWWG/. The LEP Collaborations ALEPH, DELPHI, L3, OPAL, and the LEP Electroweak Working Group. arXiv:hep-ex/0612034. (Cited on pages 29, 32 and 34.)

J. Alcaraz et al. Precision Electroweak Measurements and Constraints on the Standard Model, 2007. URL http://lepewwg.web.cern.ch/LEPEWWG/. The LEP Collaborations ALEPH, DELPHI, L3, OPAL, and the LEP Electroweak Working Group. arXiv:0712.0929 [hep-ex]. (Cited on pages 29, 32 and 33.)

J. Alcaraz et al. Towards a measurement of the inclusive $W \to W\nu$ and $Z \to \mu^-\mu^+$ cross sections in p p collisions at $\sqrt{s} = 14$ TeV. Internal Note CMS AN-2007/062, CMS, Aug 2008. (Cited on pages 130, 131 and 136.)

G. Altarelli and G. Isidori. Lower Limit on the Higgs Mass in the Standard Model: An Update. *Physics Letters B*, 337(1–2):141–144, Oct 1994. (Cited on page 29.)

J. J. Aubert et al. Experimental Observation of a Heavy Particle *J*. *Phys. Rev. Lett.*, 33(23):1404–1406, Dec 1974. doi: 10.1103/PhysRevLett.33.1404. (Cited on page 22.)

J. E. Augustin et al. Discovery of a Narrow Resonance in e^- e^+ Annihilation. *Phys. Rev. Lett.*, 33(23):1406–1408, Dec 1974. doi: 10.1103/PhysRevLett.33.1406. (Cited on page 22.)

E. Barberio and Z. Was. PHOTOS: A Universal Monte Carlo for QED radiative corrections. Version 2.0. *Comput. Phys. Commun.*, 79:291–308, 1994. (Cited on page 147.)

D. Bardin and G. Passarino. Upgrading of Precision Calculations for Electroweak Observables. `arXiv:hep-ph/9803425`. (Cited on page 88.)

D. Bardin, G. Passarino, and M. Grünewald. Precision Calculation Project Report. `arXiv:hep-ph/9902452`. (Cited on page 88.)

D. Bardin, M. Bilenky, T. Riemann, M. Sachwitz, H. Vogt, and P. Christova. `DIZET` — Electroweak one-loop corrections for $e^+e^- \to f^+f^-$ around the Z peak. *Comp. Phys. Comm.*, 59(2):303–312, Jun 1990. (Cited on page 88.)

D. Bardin, M. Bilenky, A. Chizhov, A. Sazonov, O. Fedorenko, T. Riemann, and M. Sachwitz. Analytic approach to the complete set of QED corrections to fermion pair production in e^+ e^--annihilation. *Nucl. Phys. B*, 351 (2):1–48, Mar 1991a. (Cited on page 88.)

D. Bardin, M. Bilenky, Y. Sedykh, T. Riemann, and M. Sachwitz. QED corrections with partial angular integration to fermion pair production in e^+ e^- annihilation. *Phys. Lett. B*, 255(2):290–296, Feb 1991b. (Cited on page 88.)

D. Bardin, M. Bilenky, P. Christova, M. Jack, L. Kalinovskaya, A. Olchevski, S. Riemann, and T. Riemann. `ZFITTER v.6.21`: A semi-analytical program for fermion pair production in e^+ e^- annihilation. *Comp. Phys. Comm.*, 133(2–3):229–395, Jan 2001. (Cited on page 88.)

F. A. Berends et al. Z line shape. In G. Altarelli, R. H. P. Kleiss, and C. Verzegnassi, editors, *Z Physics at LEP 1*, volume 1, page 89, Geneva, 1989. CERN. (Cited on page 88.)

K. Bleuler. Eine neue Methode zur Behandlung der longitudinalen und skalaren Photonen (A New Method for the Treatment of Longitudinal and Scalar Photons). *Helvetica Physica Acta*, 23(5):567–586, Sep 1950. (Cited on page 16.)

A. Borrelli, M. Consoli, L. Maiani, and R. Sisto. Model independent analysis of the Z line shape in e^+ e^- annihilation. *Nucl. Phys. B*, 333(2):357–379, Mar 1990. (Cited on page 88.)

R. Budny. Detailed W^0 effects in $e^+e^- \to e^+e^-$. *Phys. Lett. B*, 55(2):227–231, Feb 1975. (Cited on page 85.)

G. Burgers et al. Δr or the relation between the electroweak couplings and the weak vector boson masses. In G. Altarelli, R. H. P. Kleiss, and C. Verzegnassi, editors, *Z Physics at LEP 1*, volume 1, page 55, Geneva, 1989. CERN. (Cited on page 89.)

N. Cabibbo. Unitary Symmetry and Leptonic Decays. *Phys. Rev. Lett.*, 10(12):531–533, Jun 1963. doi: 10.1103/PhysRevLett.10.531. (Cited on pages 22 and 24.)

N. Cabibbo, L. Maiani, G. Parisi, and R. Petronzio. Bounds on the Fermions and Higgs Boson Masses in Grand Unified Theories. *Nuclear Physics B*, 158(2–3):295–305, Oct 1979. (Cited on page 31.)

R. N. Cahn. Analytic forms for the $e^+ e^-$ annihilation cross section near the Z including initial-state radiation. *Phys. Rev. D*, 36(9):2666–2670, Nov 1987. doi: 10.1103/PhysRevD.36.2666. (Cited on page 88.)

R. N. Cahn. *Semi-Simple Lie Algebras and Their Representations.* Benjamin/Cummings, Menlo Park, 1984. (Cited on page 26.)

P. A. Carruthers. *Introduction to Unitary Symmetry.* John Wiley and Sons, New York, 1966. (Cited on page 26.)

J. A. Casas, J. R. Espinosa, and M. Quiros. Improved Higgs Mass Stability Bound in the Standard Model and Implications for Supersymmetry. *Physics Letters B*, 342(1–4):171–179, Jan 1995. (Cited on page 31.)

J. A. Casas, J. R. Espinosa, and M. Quiros. Standard Model Stability Bounds for New Physics within LHC Reach. *Physics Letters B*, 382(4):374–382, Aug 1996. (Cited on page 31.)

M. Case et al. Detector Description Domain Architecture and Data Model. *CMS Note 2001-057*, 2001. (Cited on page 143.)

E. D. Commins and P. Bucksbaum. *Weak Interactions of Quarks and Leptons.* Cambridge University Press, Cambridge, 1983. (Cited on page 18.)

G. Corcella, I. G. Knowles, G. Marchesini, S. Moretti, K. Odagiri, P. Richardson, M. H. Seymour, and B. R. Webber. `HERWIG 6`: an event generator for hadron emission reactions with interfering gluons (including supersymmetric processes). *Journal of High Energy Physics*, 2001(01):010–010, Jan 2001. doi: 10.1088/1126-6708/2001/01/010. URL `http://stacks.iop.org/1126-6708/2001/i=01/a=010`. `arXiv:hep-ph/0011363`. (Cited on pages 96 and 144.)

G. Corcella, I. G. Knowles, G. Marchesini, S. Moretti, K. Odagiri, P. Richardson, M. H. Seymour, and B. R. Webber. `HERWIG 6.5` Release Note, Oct 2002. `arXiv:hep-ph/0210213`. (Cited on pages 96 and 144.)

J. M. Cornwall, D. N. Levin, and G. Tiktopoulos. Uniqueness of Spontaneously Broken Gauge Theories. *Phys. Rev. Lett.*, 30(25):1268–1270, Jun 1973. doi: 10.1103/PhysRevLett.30.1268. (Cited on page 29.)

J. M. Cornwall, D. N. Levin, and G. Tiktopoulos. Derivation of Gauge Invariance from High-energy Unitarity Bounds on the S Matrix. *Phys. Rev. D*, 10(4):1145–1167, Aug 1974. doi: 10.1103/PhysRevD.10.1145. (Cited on page 29.)

M. Cvetic and P. Langacker. Implications of Abelian extended gauge structures from string models. *Phys. Rev. D*, 54(5):3570–3579, Sep 1996. doi: 10.1103/PhysRevD.54.3570. (Cited on page 82.)

M. De Gruttola, S. Di Guida, F. Fabozzi, L. Lista, P. Noli, and D. Piccolo. Determination of $\mathrm{p+p} \to \mathrm{Z}+X \to \mu^+ + \mu^- + X$ inclusive cross section with a simultaneous fit of Z yield and muon reconstruction efficiencies. Internal Note CMS AN-2008/062, CMS, Sep 2008. (Cited on pages 131 and 136.)

J. F. de Trocóniz and F. J. Ynduráin. Precision Determination of the Pion Form Factor and Calculation of the Muon $g-2$. *Phys. Rev. D*, 65(9): 093001, Apr 2002. doi: 10.1103/PhysRevD.65.093001. (Cited on page 33.)

A. Djouadi. The Anatomy of Electro-Weak Symmetry Breaking, May 2005. `arXiv:hep-ph/0503172`, `arXiv:hep-ph/0503173`. (Cited on pages 29, 30, 31 and 71.)

A. Djouadi, J. Kalinowski, and M. Spira. `HDECAY`: a Program for Higgs Boson Decays in the Standard Model and its Supersymmetric Extension. Technical Report DESY 97-079, DESY, 1997. `arXiv:hep-ph/9704448`. (Cited on page 73.)

S. D. Drell and T.-M. Yan. Partons and their applications at high energies. *Ann. Phys.*, 66(2):578–623, Aug 1971. (Cited on page 92.)

J. Ellis, M. K. Gaillard, and D. V. Nanopoulos. A Phenomenological Profile of the Higgs Boson. *Nucl. Phys. B*, 106:292, 1976. (Cited on page 73.)

J. R. Espinosa and M. Quiros. Improved Metastability Bounds on the Standard Model Higgs Mass. *Physics Letters B*, 353(2–3):257–266, Jun 1995. (Cited on page 32.)

G. Feinberg, P. Kabir, and S. Weinberg. Transformation of Muons into Electrons. *Phys. Rev. Lett.*, 3(11):527–530, Dec 1959. doi: 10.1103/PhysRevLett.3.527. especially footnote 9. (Cited on page 28.)

S. Frixione and B. R. Webber. Matching NLO QCD Computations and Parton Shower Simulations. *Journal of High Energy Physics*, 2002(06):029–029, June 2002. doi: 10.1088/1126-6708/2002/06/029. URL `http://stacks.iop.org/1126-6708/2002/i=06/a=029`. `arXiv:hep-ph/0204244`. (Cited on page 96.)

S. Frixione, P. Nason, and B. R. Webber. Matching NLO QCD and Parton Showers in Heavy Flavour Production. *Journal of High Energy Physics*, 2003(08):007–007, August 2003. doi: 10.1088/1126-6708/2003/08/007. URL `http://stacks.iop.org/1126-6708/2003/i=08/a=007`. `arXiv:hep-ph/0305252`. (Cited on page 96.)

R. Fruhwirth. Application of Kalman Filtering to Track and Vertex Fitting. *Nucl. Instrum. and Methods A*, 262:444, 1987. (Cited on page 166.)

H. M. Georgi, S. L. Glashow, M. E. Machacek, and D. V. Nanopoulos. Higgs Bosons from Two-Gluon Annihilation in Proton-Proton Collisions. *Phys. Rev. Lett.*, 40(11):692–694, Mar 1978. doi: 10.1103/PhysRevLett.40.692. (Cited on page 69.)

S. L. Glashow. Partial Symmetries of Weak Interactions. *Nucl. Phys.*, 22(4):579–588, February 1961. (Cited on page 7.)

S. L. Glashow, J. Iliopoulos, and L. Maiani. Weak Interactions with Lepton-Hadron Symmetry. *Phys. Rev. D*, 2(7):1285–1292, Oct 1970. doi: 10.1103/PhysRevD.2.1285. (Cited on page 22.)

S. L. Glashow, D. V. Nanopoulos, and A. Yildiz. Associated production of Higgs bosons and Z particles. *Phys. Rev. D*, 18(5):1724–1727, Sep 1978. doi: 10.1103/PhysRevD.18.1724. (Cited on page 72.)

T. Gleisberg et al. Event generator for the LHC. `arXiv:hep-ph/0508315`. (Cited on page 144.)

J. Goldstone. Field Theories with 'Superconductor' Solutions. *Il Nuovo Cimento*, 19:154–164, 1961. (Cited on page 12.)

J. Goldstone, A. Salam, and S. Weinberg. Broken Symmetries. *Phys. Rev.*, 127(3):965–970, Aug 1962. doi: 10.1103/PhysRev.127.965. (Cited on page 12.)

M. W. Grunewald. Combined Electroweak Analysis, 2007. `arXiv:0709.3744 [hep-ph]`. (Cited on page 29.)

S. N. Gupta. Theory of Longitudinal Photons in Quantum Electrodynamics. *Proceedings of the Royal Society A*, 63(7):681–691, 1950. (Cited on page 16.)

F. Halzen and A. D. Martin. *Quarks and Leptons: an Introductory Course in Modern Particle Physics*. John Wiley and Sons, 1984. (Cited on page 7.)

T. Hambye and K. Riesselmann. Matching Conditions and Higgs Boson Mass Upper Bounds Reexamined. *Phys. Rev. D*, 55(11):7255–7262, Jun 1997. doi: 10.1103/PhysRevD.55.7255. (Cited on page 31.)

T. Han, H. E. Logan, B. McElrath, and L.-T. Wang. Phenomenology of the little Higgs model. *Phys. Rev. D*, 67(9):095004, May 2003. doi: 10.1103/PhysRevD.67.095004. (Cited on page 82.)

P. W. Higgs. Broken Symmetries, Massless Particles and Gauge Fields. *Phys. Lett.*, 12(2):132–133, Sep 1964a. doi: 10.1016/0031-9163(64)91136-9. (Cited on page 7.)

P. W. Higgs. Broken Symmetries and the Masses of Gauge Bosons. *Phys. Rev. Lett.*, 13(16):508–509, Oct 1964b. doi: 10.1103/PhysRevLett.13.508. (Cited on page 7.)

P. W. Higgs. Spontaneous Symmetry Breakdown without Massless Bosons. *Phys. Rev.*, 145(4):1156–1163, May 1966. doi: 10.1103/PhysRev.145.1156. (Cited on page 7.)

C. T. Hill and E. H. Simmons. Strong dynamics and electroweak symmetry breaking. *Phys. Rept.*, 381:235–402, 2003. `arXiv:hep-ph/0203079`. (Cited on page 82.)

R. Hofstadter, H. R. Fechter, and J. A. McIntyre. High-energy electron scattering and nuclear structure determinations. *Phys. Rev.*, 92(4):978–987, Nov 1953. doi: 10.1103/PhysRev.92.978. (Cited on page 5.)

V. Innocente, M. Maire, and E. Nagy. `GEANE`: Average Tracking and Error Propagation Package. Technical Report IT-ASD W5013-E, CERN Program Library, 1991. (Cited on page 161.)

G. Isidori, G. Ridolfi, and A. Strumia. On the Metastability of the Standard Model Vacuum. *Nuclear Physics B*, 609(3):387–409, Aug 2001. (Cited on page 32.)

S. Jadach, Z. Was, R. Decker, and J. H. Kuhn. The tau decay library TAUOLA: Version 2.4. *Comput. Phys. Commun.*, 76:361–380, 1993. (Cited on page 147.)

G. L. Kane. *Perspective on Higgs Physics*, volume 13 of *Advanced Series on Directions in High Energy Physics*, chapter The Standard Model Intermediate Mass Higgs Boson by S. Dawson. World Scientific, 1997. arXiv:hep-ph/9703387. (Cited on page 29.)

G. L. Kane, W. Repko, and W. Rolnick. The Effective $W^{\pm}$, Z Approximation for High-Energy Collisions. *Phys. Lett. B*, 148:367, 1984. (Cited on page 72.)

M. Kobayashi and K. Maskawa. CP-Violation in the Renormalizable Theory of Weak Interaction. *Prog. Theor. Phys.*, 49(2):652–657, Feb 1973. doi: 10.1143/PTP.49.652. (Cited on page 24.)

M. Kramer, E. Laenen, and M. Spira. Soft gluon radiation in Higgs boson production at the LHC. *Nucl. Phys. B*, 511:523, 1998. arXiv:hep-ph/9611272. (Cited on page 71.)

Z. Kunszt. Associated Production of Heavy Higgs Boson with Top Quarks. *Nucl. Phys. B*, 247:339, 1984. (Cited on page 72.)

K. D. Lane. Technicolor 2000. arXiv:hep-ph/0007304. (Cited on page 83.)

C. M. G. Lattes, H. Muirhead, G. P. S. Occhialini, and C. F. Powell. Processes Involving Charged Mesons. *Nature*, 159:694–697, May 1947. (Cited on page 5.)

L. M. Lederman et al. Observation of a Dimuon Resonance at 9.5 GeV in 400 GeV Proton-Nucleus Collisions. *Phys. Rev. Lett.*, 39(5):252–255, Aug 1977. doi: 10.1103/PhysRevLett.39.252. (Cited on page 22.)

B. W. Lee, C. Quigg, and H. B. Thacker. Weak Interactions at Very High Energies: The Role of the Higgs-boson Mass. *Phys. Rev. D*, 16(5):1519–1531, Sep 1977. doi: 10.1103/PhysRevD.16.1519. (Cited on page 29.)

A. Leike. The phenomenology of extra neutral gauge bosons. *Phys. Rept.*, 317:143–250, 1999. arXiv:hep-ph/9805494. (Cited on page 82.)

C. H. Llewellyn Smith. High Energy Behaviour and Gauge Symmetry. *Physics Letters B*, 46(2):233–236, Sep 1974. (Cited on page 29.)

I. P. Lokhtin and A. M. Snigirev. Nuclear geometry of jet quenching. *Eur. Phys. J. C*, 16:527–536, 2000. (Cited on page 147.)

F. Maltoni and T. Stelzer. `MadEvent`: Automatic event generation with `madgraph`. *JHEP*, 02:027, 2003. (Cited on page 147.)

M. L. Mangano, F. Piccinini, A. D. Polosa, M. Moretti, and R. Pittau. `ALPGEN`, a generator for hard multiparton processes in hadronic collisions. *Journal of High Energy Physics*, 2003(07):001–001, Jul 2003. doi: 10.1088/1126-6708/2003/07/001. URL `http://stacks.iop.org/1126-6708/2003/i=07/a=001`. `arXiv:hep-ph/0206293`. (Cited on pages 104 and 147.)

S. P. Martin. A supersymmetry primer. `arXiv:hep-ph/9709356`, 2006. (Cited on page 81.)

G. P. S. Occhialini and C. F. Powell. Nuclear Disintegrations Produced by Slow Charged Particles of Small Mass. *Nature*, 159:186–190, Feb 1947. (Cited on page 5.)

F. E. Paige, S. D. Protopopescu, H. Baer, and X. Tata. `ISAJET 7.69`: A Monte Carlo Event Generator for p p, p $\overline{\text{p}}$, and e^+ e^- Reactions. `arXiv:hep-ph/0312045`. (Cited on page 144.)

A. Pukhov et al. `CompHEP`: A package for evaluation of Feynman diagrams and integration over multi-particle phase space. User's manual for version 33. `arXiv:hep-ph/9908288`. (Cited on page 147.)

J. Pumplin, D. R. Stump, J. Huston, H.-L. Lai, P. Nadolsky, and W.-K. Tung. New Generation of Parton Distributions with Uncertainties from Global QCD Analysis. *Journal of High Energy Physics*, 2002(07):012–012, Jul 2002. doi: 10.1088/1126-6708/2002/07/012. URL `http://stacks.iop.org/1126-6708/2002/i=07/a=012`. `arXiv:hep-ph/0201195`. (Cited on pages 104 and 146.)

L. Randall and R. Sundrum. Large Mass Hierarchy from a Small Extra Dimension. *Phys. Rev. Lett.*, 83(17):3370–3373, Oct 1999. doi: 10.1103/PhysRevLett.83.3370. (Cited on page 83.)

V. Ravindran, J. Smith, and W. van Neerven. NNLO corrections to the total cross section for Higgs boson production in hadron hadron collisions. *Nucl. Phys. B*, 665:325, 2003. `arXiv:hep-ph/0302135`. (Cited on page 71.)

P. Renton. *Electroweak Interactions*. Cambridge University Press, Cambridge, 1990. (Cited on page 18.)

L. Resnick, M. K. Sundaresan, and P. J. S. Watson. Is There a Light Scalar Boson? *Phys. Rev. D*, 8(1):172–178, Jul 1973. doi: 10.1103/PhysRevD.8.172. (Cited on page 75.)

G. D. Rochester and C. C. Butler. Evidence for the Existence of New Unstable Elementary Particles. *Nature*, 160:855–857, Dec 1947. (Cited on page 5.)

L. H. Ryder. *Quantum Field Theory*. Cambridge University Press, second edition, 1996. (Cited on pages 7 and 25.)

A. Salam. Weak and Electromagnetic Interactions. In N. Svartholm, editor, *Elementary Particle Theory: Relativistic groups and Analiticity*, volume 8 of *Nobel Symposium*, pages 367–377, Aspenasgarden, Sweden, July 19-25, 1968, 1968. Almqvist and Wiksells, Stokholm. (Cited on page 7.)

T. Sjöstrand, L. Lönnblad, and S. Mrenna. `PYTHIA 6.4` Physics and Manual. *Journal of High Energy Physics*, 2006(26):026, May 2006. doi: 10.1088/1126-6708/2006/05/026. URL `http://stacks.iop.org/1126-6708/2006/i=05/a=026`. `arXiv:hep-ph/0603175`. (Cited on pages 96 and 144.)

S. R. Slabospitsky and L. Sonnenschein. `TopReX` generator (version 3.25). Short manual. *Comput. Phys. Commun.*, 148:87, 2002. (Cited on page 147.)

M. Spira. `HIGLU`: A Program for the Calculation of the Total Higgs Production Cross Section at Hadron Colliders via Gluon Fusion Including QCD Corrections. Technical Report DESY T-95-05, DESY, 1995. `arXiv:hep-ph/9510347`. (Cited on pages xi and 70.)

The ALEPH Collaboration, The DELPHI Collaboration, The L3 Collaboration, The OPAL collaboration, The SLD Collaboration, The LEP Electroweak Working Group, and The SLD Electroweak and Heavy Flavour Groups. Precision Electroweak Measurements on the Z Resonance. *Phys. Rept.*, 427:257, 2006. URL `http://lepewwg.web.cern.ch/LEPEWWG`. `arXiv:hep-ex/0509008`. (Cited on pages xi and 85.)

The ALICE Collaboration. A Large Ion Collider Experiment Technical Proposal Design. Technical Report CERN/LHCC 95-71, LHCC/P3, CERN, Geneva, Oct 1995. (Cited on page 38.)

The ATLAS Collaboration. Atlas Technical Proposal for a General Purpose p p Experiment at the Large Hadron Collider at CERN. Technical Report CERN/LHCC 94-43, LHCC/P2, CERN, Geneva, Dec 1994. (Cited on page 37.)

The CMS Collaboration. CMS Physics TDR, Volume I: Detector Performance and Software. Technical Report CERN-LHCC-2006-001; CMS-TDR-008-1, CERN, Geneva, 2006. URL `http://cms.cern.ch`. (Cited on pages 43, 137, 149 and 154.)

The CMS Collaboration. CMS Physics Technical Design Report, Volume II: Physics Performance. *J. Phys. G*, 34(6):995–1579, 2007. URL `http://cms.cern.ch`. (Cited on pages 69, 144 and 147.)

The CMS Collaboration. The TriDAS Project Technical Design Report, Volume 2: Data Acquisition and High-Level Trigger. Technical Report CERN-LHCC-2002-026, CERN, Geneva, 2002. URL `http://cms.cern.ch`. (Cited on page 162.)

The CMS Collaboration. The TriDAS Project Technical Design Report, Volume 1: The Trigger System. Technical Report CERN-LHCC-2000-038, CERN, Geneva, 2000. URL `http://cms.cern.ch`. (Cited on page 162.)

The CMS Collaboration. The Compact Muon Solenoid. Technical Report CERN/LHCC 94-38, LHCC/P1, CERN, Geneva, Dec 1994. (Cited on page 37.)

The LHC Project. LHC Design Report, Volume I: the LHC Main Ring. Technical Report CERN-2004-003-V-1, CERN, Geneva, 2004a. `lhc.web.cern.ch/lhc/`. (Cited on pages xv, 37 and 40.)

The LHC Project. LHC Design Report, Volume II: the LHC Infrastructure and General Services. Technical Report CERN-2004-003-V-2, CERN, Geneva, 2004b. `lhc.web.cern.ch/lhc/`. (Cited on page 37.)

The LHC Project. LHC Design Report, Volume III: the LHC Injector Chain. Technical Report CERN-2004-003-V-3, CERN, Geneva, 2004c. `lhc.web.cern.ch/lhc/`. (Cited on page 37.)

The LHCb Collaboration. A Large Hadron Collider Beauty Experiment for Precision Measurements of CP-Violation and Rare Decays LHCb Technical Proposal. Technical Report CERN/LHCC 98-04, LHCC/P4, CERN, Geneva, Feb 1998. (Cited on page 38.)

W.-K. Tung, H.-L. Lai, A. Belyaev, J. Pumplin, D. R. Stump, and C.-P. Yuan. Heavy Quark Mass Effects in Deep Inelastic Scattering and Global QCD Analysis. *Journal of High Energy Physics*, 2007(02):053, Feb 2007. doi: 10.1088/1126-6708/2007/02/053. URL `http://stacks.iop.org/1126-6708/2007/i=02/a=053`. `arXiv:hep-ph/0611254`. (Cited on pages xi, 70, 104 and 146.)

A. I. Vainshtein, M. Voloshin, V. I. Zakharov, and M. A. Shifman. Low-energy Theorems for Higgs Boson Couplings to Photons. *Sov. J. Nucl. Phys.*, 30:711, 1979. (Cited on page 76.)

R. Veenhof. `GARFIELD`, a Drift Chamber simulation program user's guide. Technical Report W5050, CERN Program Library, 1994. (Cited on page 163.)

S. Weinberg. Current Algebra and Gauge Theories I. *Phys. Rev. D*, 8(2): 605–625, Jul 1973. doi: 10.1103/PhysRevD.8.605. especially footnote 8. (Cited on page 28.)

S. Weinberg. A Model of Leptons. *Phys. Rev. Lett.*, 19(21):1264–1266, Nov 1967. doi: 10.1103/PhysRevLett.19.1264. (Cited on page 7.)

K. Winter. *Neutrino Physics*. Cambridge University Press, Cambridge, second edition, 2000. (Cited on page 18.)

W.-M. Yao et al. Review of Particle Physics. *Journal of Physics G*, 33:1+, 2006. URL `http://pdg.lbl.gov`. (Cited on pages 18, 19, 29, 82, 87, 90, 128 and 161.)